



## Fundamental investigations of catalyst nanoparticles

Elkjær, Christian Fink

*Publication date:*  
2016

*Document Version*  
Publisher's PDF, also known as Version of record

[Link back to DTU Orbit](#)

*Citation (APA):*  
Elkjær, C. F. (2016). *Fundamental investigations of catalyst nanoparticles*. Department of Physics, Technical University of Denmark.

---

### General rights

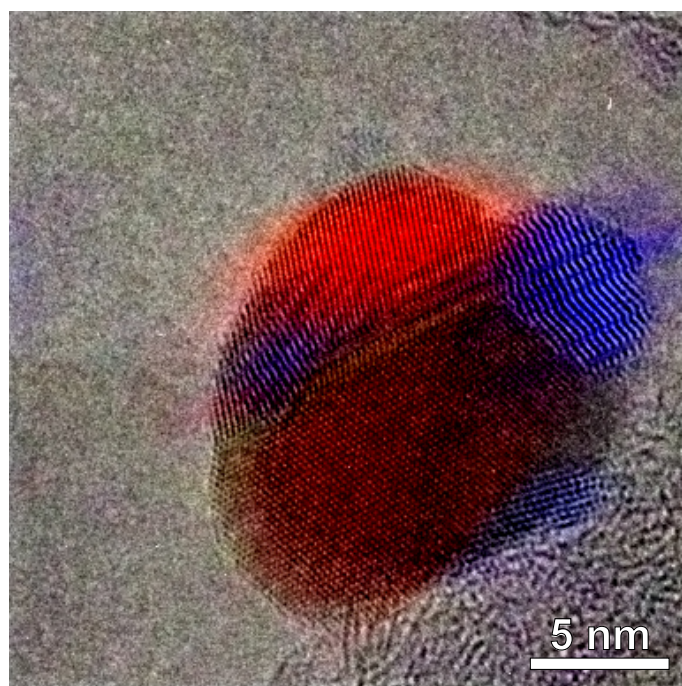
Copyright and moral rights for the publications made accessible in the public portal are retained by the authors and/or other copyright owners and it is a condition of accessing publications that users recognise and abide by the legal requirements associated with these rights.

- Users may download and print one copy of any publication from the public portal for the purpose of private study or research.
- You may not further distribute the material or use it for any profit-making activity or commercial gain
- You may freely distribute the URL identifying the publication in the public portal

If you believe that this document breaches copyright please contact us providing details, and we will remove access to the work immediately and investigate your claim.

# FUNDAMENTAL INVESTIGATIONS OF CATALYST NANOPARTICLES

CHRISTIAN FINK ELKJÆR



Imaging Catalyst Dynamics

Center for Individual Nanoparticle Functionality  
Department of Physics  
Technical University of Denmark

Haldor Topsøe A/S

January 2016

TITLE

Fundamental investigations of catalyst nanoparticles  
*Imaging Catalyst Dynamics*

SUBMITTED

January 2016

SUPERVISORS

Professor Ib Chorkendorff, CINF DTU

Senior Research Scientist Stig Helveg, Haldor Topsøe A/S

Senior Research Scientist Jens Sehested, Haldor Topsøe A/S

COVER ILLUSTRATION

Cu/ZnO nanoparticle imaged *in situ* in 1 mbar H<sub>2</sub> at 300 °C.

PhD Thesis • Christian Fink Elkjær © January 2016

## PREFACE

---

This thesis is submitted in the candidacy of the PhD degree from the Technical University of Denmark (DTU). Funding was provided by Haldor Topsøe A/S, DTU Physics and the Danish Ministry of Science, Technology and Innovation through the Catalysis for Sustainable Energy initiative. I gratefully acknowledge them for their support.

The work was carried out from August 2011 to December 2015. In the period June 2012 - June 2013 I was on a leave of absence from the PhD studies while I worked at Haldor Topsøe on the development and use of Nanoreactor technology for high pressure *in situ* TEM.

Thanks to my supervisors Ib Chorkendorff, Stig Helveg and Jens Sehested for excellent supervision and many good discussions. It has been a pleasure to experience and benefit from your extensive knowledge within your fields of expertise. Special thanks to Stig for day-to-day advice and discussions and for your commitment to my professional development.

At Haldor Topsøe, I have enjoyed a professional and warm environment and the vast knowledge and experience gathered there. It has been a privilege to work with state of the art equipment in one of the best microscopy facilities in the world and it is inspiring to experience a private company dedicated to the advancement of science. Thanks to my colleagues in the Microscopy Department for creating a pleasant and inspiring working environment and for your help with different aspects of my project. Special thanks to Sven Ullmann for your help with experiments and for many interesting technical discussions. Thanks to Charlotte Appel for your support as department manager and your efforts to make us external students part of the team. Thanks to the methanol group for providing materials and for help and input on the parts of my project related to Cu catalysts.

At CINF DTU I have enjoyed the lively environment and thriving academic setting among the many PhD students and Postdocs. Thanks to everyone for creating a fun and stimulating working environment and thank you for your dedicated research and effort to invent the technologies of tomorrow. Thanks to Anders Nierhoff and Christian Holse for fruitful collaboration and to Anders for preparing TEM samples throughout my entire project.

A special thanks to my dear wife Julie for your continuous support throughout the project and during the final writing process. I dedicate this thesis to you and Ellen.

*Kgs. Lyngby, January 2016*

---

Christian Fink Elkjær



## ABSTRACT

---

Heterogeneous catalysis, the conversion of chemicals by the use of a suitable solid state catalyst, is a very important technology in modern society and it is involved in the production of up to 90% of all chemicals. Catalysis has in this way played a significant role in the technological and economic development in the 20th century. There is however a downside to this development and we are seeing significant pollution and pressure on resources. Catalysis therefore has an increasingly important role in limiting pollution and optimizing the use of resources. This development will depend on our fundamental understanding of catalytic processes and our ability to make use of that understanding.

This thesis presents fundamental studies of catalyst nanoparticles with particular focus on dynamic processes. Such studies often require atomic-scale characterization, because the catalytic conversion takes place on the molecular and atomic level.

Transmission electron microscopy (TEM) has the ability to image nanostructures with atomic resolution and reveal the atomic configuration of the important nanoparticle surfaces. In the present work, TEM has been used to study nanoparticles *in situ* at elevated temperature and with gas present in the microscope in order to recreate the conditions found in a chemical reactor. This is very important because we know that particles may change shape as their surfaces respond to a changing gas atmosphere. To obtain quantitative and credible information *in situ*, it is very important that we only study intrinsic structures and phenomena and not those that may be induced by the high energy electrons used to image the specimen. This requires careful consideration of the influence of the electron beam in order to understand, control and minimize that influence.

I present four different topics, each related to different aspects of nanoparticle dynamics and catalysis.

The first topic is the reduction of a homogeneous solid state precursor to form the catalytically active phase which is metal nanoparticles on an inert support. Here, we have reduced Cu phyllosilicate to Cu on silica and imaged the process *in situ*. The data obtained established the foundation for modeling work which revealed that the reduction proceeded by an autocatalytic route. Here, the initial nucleation of Cu is slow and the subsequent growth in size is fast because the Cu particles themselves catalyze further reduction.

The second topic treated the active state of a methanol synthesis catalyst. This work was performed by a parallel approach, where we investigated identically created nanoparticles both with TEM and X-

ray photoelectron spectroscopy (XPS). The methanol synthesis catalyst is a complex high surface area Cu/ZnO/Al<sub>2</sub>O<sub>3</sub> structure that is difficult to study by TEM. We therefore created size-selected CuZn alloy nanoparticles that were transformed by oxidation and reduction into Cu nanoparticles decorated with ZnO. This represents a simplified model system for the high surface area catalyst. The interplay between Cu and ZnO and the exact role of ZnO as a promoter for catalytic activity is not yet fully understood. Our work revealed that the surface of the reduced catalyst consists mainly of Cu decorated with well defined ZnO crystals. It was demonstrated by XPS that a fraction of the ZnO is reduced simultaneously with the Cu under H<sub>2</sub> atmosphere, presumably forming a surface alloy in the Cu.

The third topic studied the sintering of Cu nanoparticles supported on silica. Sintering is the main deactivation mechanism for the methanol synthesis catalyst and so this topic is of great interest to the development of better catalysts. It was found that sintering proceeded via Ostwald ripening, i. e. the migration of atomic species between particles, with a net flow from small to larger particles resulting in an overall growth in particle size. The presence of CO increased the rate of sintering significantly and the presence of H<sub>2</sub>O slowed it down.

The fourth topic investigated the oxidation of CO on a Pt catalyst in the special case where the reaction displays temporal rate oscillations under fixed conditions. This is a well-known phenomenon, but the mechanism driving the oscillations on nanoparticles has hitherto been unknown. We used nanoreactor technology which allows for simultaneous TEM imaging and activity measurement, also referred to as an *Operando* experiment. With this we revealed that the shape of the Pt nanoparticles changed in phase with changes in global reaction rate. By the use of reactor modeling it was possible to show that the oscillations were possible due to the coupling between the self-poisoning nature of the CO oxidation reaction on Pt and gas flow and diffusion in the reactor. Our work showed that shape changes can drive global rate oscillations.

## RESUMÉ

---

Heterogen katalyse, omdannelsen af kemiske forbindelser på en passende katalysator, er en meget vigtig teknologi i det moderne samfund og det er estimeret at katalyse er involveret i produktionen af op til 90% af alle kemikalier. Katalyse har således spillet en vigtig rolle i både den teknologiske og økonomiske udvikling af vores samfund igennem det 20. århundrede. Denne udvikling har dog også en bagside og har medført en stærkt øget forurening og pres på globale ressourcer. Det er derfor helt oplagt at katalyse i fremtiden skal spille en vigtig rolle i reduktion af forurening og i bedre udnyttelse af de tilgængelige ressourcer. En sådan udvikling kræver at vi øger vores fundamentale forståelse af katalysatorer og katalytiske processer og at vi formår at udnytte den viden bedst muligt.

Denne afhandling præsenterer fundamentale studier af nanopartikler i relation til katalytiske processer og med særlig fokus på dynamik. Sådanne studier kræver ofte at vi kan beskrive katalysatorens atomare struktur fordi den kemiske omdannelse sker på molekylært og atomart niveau.

Ved hjælp af transmissionselektronmikroskopi (TEM) er vi i stand til at tage billeder af nanostrukturer med atomar opløsning og på den måde afdække den atomare struktur af de katalytisk vigtige overflader. I denne afhandling har jeg brugt TEM til at studere nanopartikler *in situ*, altså med en omgivende gas og ved høj temperatur, for på den måde at skabe betingelser der minder om dem i en katalytisk reaktor. Dette kan være særdeles væsentligt, da vi ved at partiklerne kan skifte form som funktion af det omgivende miljø. For at få troværdig information når vi opererer *in situ*, er det vigtigt at studere de intrinsiske strukturer og fænomener og ikke fænomener som eventuelt sker som funktion af elektronstrålen. TEM er nemlig baseret på at elektroner med høj energi skydes igennem prøven for at danne billedet og disse kan i høj grad påvirke prøven. Dette kræver overvejelse og omtanke, men hvis eksperimentet udføres rigtigt er det muligt at finde betingelser hvor intensiteten af elektronstrålen er tilstrækkelig lav, så der ydes begrænset eller ingen indflydelse på prøven.

I denne afhandling præsenterer jeg resultater under fire forskellige emner, som alle relaterer sig til nanopartikler og katalyse.

Det første emne omhandler reduktion af et homogent oxidmateriale der omdannes til en aktiv katalysator som består af metalliske nanopartikler på en bærer. Konkret har vi reduceret en Cu-silikat for at danne Cu partikler på siliciumdioxid og fulgt processen *in situ* med TEM. Resultatet viser fremkomst og vækst af nanopartikler optaget

med en høj tidslig opløsning og disse data blev brugt som basis for en modellering af partikelvæksten.

Det andet emne omhandler katalysatorer til fremstilling af metanol og i særdeleshed den atomare struktur i den reducerede tilstand. Dette arbejde blev udført med en parallel tilgang hvor vi studerede ens nanopartikler med TEM og XPS (X-ray Photoelectron Spectroscopy). Den industrielle katalysator består af Cu, ZnO og Al<sub>2</sub>O<sub>3</sub> og har en høj strukturel kompleksitet der gør det vanskeligt at studere den med TEM. Derfor lavede vi et modelsystem baseret på nanopartikler af Cu og Zn. Disse blev oxideret og reduceret for at danne Cu nanopartikler med små krystaller af ZnO siddende på overfladen. Sådanne partikler kan ses som en strukturelt simplificeret model for den industrielle katalysator. Interessant nok er samspillet imellem Cu og ZnO endnu ikke fuldt forstået for disse systemer, særligt måden hvorpå ZnO øger aktiviteten af Cu er til stadighed et emne der bliver diskuteret. Vores arbejde kunne vise at størstedelen af partiklernes overflade består af Cu når de er reduceret og desuden viste XPS at en del af zinken bliver reduceret samtidig med kobberet under en atmosfære af H<sub>2</sub>. Det antages dermed at der bliver dannet en overfladelegering mellem Cu og Zn og at den spiller en rolle for aktiviteten.

Det tredje emne omhandler stabilitet og sintring af Cu på en plan overflade af SiO<sub>x</sub>. Sintring, vækst i partikelstørrelse over tid, er den vigtigste grund til at metanolkatalysatorer ældes og deaktiverer. Derfor er dette emne særdeles interessant i forhold til at udvikle bedre katalysatorer. Mine resultater sandsynliggør at sintringen af Cu sker igennem udvekslingen af atomare specier hvor nettostrømmen går fra små til store partikler, såkaldt Ostwald ripening. Over tid vil det øge den gennemsnitlige partikelstørrelse. Desuden så jeg at tilstedeværelsen af CO dramatisk øgede hastigheden af sintringen, hvor tilstedeværelsen af H<sub>2</sub>O bremsede den.

Det fjerde emne omhandler CO oxidation på en Pt katalysator under forhold hvor den globale rate oscillerer. Dette er et velbeskrevet fænomen i litteraturen, men det har hidtil ikke været kendt hvilken mekanisme der driver sådanne oscillationer på nanopartikler. Vi brugte en miniaturiseret reaktor, den såkaldte nanoreaktor, som gør det muligt at optage TEM billeder samtidig med at den katalytiske omsætning måles. Ved hjælp af denne teknik kunne vi iagttage hvordan Pt partiklerne skiftede form synkront med ændringer i omsætningsgraden af CO. Et omfattende arbejde med at modellere reaktionen med baggrund i disse observationer viste at sådanne formændringer er tilstrækkeligt til at forklare oscillationerne i omsætning.

## LIST OF PAPERS RELATED TO THIS WORK

---

### PAPER I

Visualization of oscillatory behaviour of Pt nanoparticles catalysing CO oxidation

Søren Vendelbo, Christian F. Elkjær, Hanne Falsig, Indra Puspitasari, P. Dona, Luigi Mele, Bart J. Nelissen, Richard van Rijn, Patricia J. Kooymann and Stig Helveg.

*Nature Materials* **13**, 884-890 (2014).

Paper included (page 193).

### PAPER II

The dynamic behavior of CuZn nanoparticles under oxidizing and reducing conditions

Christian Holse, Christian F. Elkjær, Anders Nierhoff, Jens Sehested, Ib Chorkendorff, Stig Helveg, Jane H. Nielsen.

*The Journal of Physical Chemistry C* **119**, 2804-2812 (2015).

Paper included (page 201).

### PAPER III

Revealing the formation of copper nanoparticles from a homogeneous solid precursor by electron microscopy

Roy van den Berg, Christian F. Elkjær, Cedric J. Gommès, Ib Chorkendorff, Jens Sehested, Petra E. de Jongh, Krijn P. de Jong, Stig Helveg. *Submitted.*

Paper included (page 211).

### PAPER IV

The effect of gas atmosphere on the sintering rate of Cu nanoparticles supported on silica

Christian F. Elkjær, Jens Sehested, Ib Chorkendorff, Stig Helveg, *In preparation.*



# CONTENTS

---

Thesis	1
1 INTRODUCTION	3
1.1 Heterogeneous catalysis	3
1.1.1 Transition metal catalysis	5
1.1.2 The active site	8
1.1.3 In situ catalyst characterization	9
1.1.4 Catalysis and society	10
1.2 Thesis outline	11
2 METHODS	13
2.1 Transmission electron microscopy	13
2.1.1 The microscope	14
2.1.2 Beam-sample interactions	16
2.1.3 Image contrast	18
2.1.4 High resolution imaging	18
2.2 <i>In situ</i> TEM, concept and hardware	24
2.2.1 Grids and holder	26
2.3 Operation	28
2.3.1 Controlling dose rate	28
2.3.2 Beam influence	31
2.4 Image handling and analysis	33
2.4.1 2D Fast Fourier Transform	34
2.4.2 Cross correlation and image summation	36
2.5 Chapter conclusion	38
3 CATALYST ACTIVATION. REDUCTION OF CU-SILICATE	41
3.1 Particle formation from a homogeneous precursor	41
3.2 Methods	42
3.2.1 TEM imaging	42
3.2.2 Image analysis	42
3.3 Precursor material	43
3.4 Reduced material	44
3.5 Assessing the beam effect	47
3.5.1 Beam in H <sub>2</sub>	47
3.5.2 Beam pre-reduction	48
3.6 Imaging the reduction process <i>in situ</i>	52
3.7 Particle growth modeling	56
3.8 Chapter conclusion	60
4 CATALYST ACTIVITY. THE METHANOL SYNTHESIS CATALYST	61
4.1 The methanol synthesis reaction	61
4.1.1 The active site	62
4.2 Model system preparation	63

4.3	Experimental setup and methods	65
4.3.1	UHV system: deposition, temperature treatment and spectroscopy	65
4.3.2	XPS	66
4.3.3	In situ TEM	67
4.4	Results	68
4.4.1	From CuZn to Cu/ZnO	68
4.4.2	TEM image analysis	71
4.4.3	Oxidation-reduction cycles	73
4.4.4	H <sub>2</sub> pressure dependence	78
4.4.5	Zn reduction	80
4.4.6	Activity	81
4.5	Chapter conclusion	86
5	CATALYST STABILITY. SINTERING OF CU	89
5.1	Deactivation of Cu catalysts	89
5.1.1	Routes to deactivation of Cu/ZnO/Al <sub>2</sub> O <sub>3</sub>	90
5.1.2	Correlation between surface area and activity	90
5.1.3	Stability of Cu/ZnO/Al <sub>2</sub> O <sub>3</sub>	90
5.1.4	Effect of the gas environment	92
5.1.5	Sintering mechanisms	96
5.2	Sintering of Cu nanoparticles in the TEM	97
5.2.1	Wet impregnation of Cu	98
5.2.2	Experimental procedure	99
5.2.3	Varying gas environment	99
5.2.4	Conclusions from wet impregnated samples	105
5.3	Deposition by cluster source	105
5.3.1	Sample preparation	106
5.3.2	Measurement procedure	109
5.3.3	Automated particle measurement	109
5.3.4	Varying gas environment	111
5.3.5	Sintering mechanism	111
5.3.6	Sintering simulation	113
5.3.7	Effect of electron beam	118
5.4	Chapter conclusion	120
6	CO OXIDATION AND HIGH PRESSURE OPERANDO TEM	123
6.1	High pressure <i>in situ</i> TEM and CO oxidation	123
6.2	The CO oxidation reaction	123
6.3	The nanoreactor system	125
6.3.1	Nanoreactor loading	127
6.3.2	Nanoreactor temperature	128
6.3.3	Associated equipment	130
6.4	Treatment of data	131
6.4.1	Data synchronization	132
6.4.2	Mass spectrometry quantification	135
6.4.3	Reaction heat and flow rate measurement	135
6.5	Oscillations in CO oxidation	136

6.5.1	Mass spectrometry and calorimetry, global information	136
6.5.2	TEM during oscillations, local information	138
6.6	Reactor modeling	143
6.6.1	Steady state reactor model	144
6.7	Time-dependent reactor model	148
6.8	Chapter conclusion	153
7	SUMMARY AND CONCLUSION	155
	<b>Appendix</b>	157
A	COLORING OF TEM IMAGES	159
B	AUTOMATIC PARTICLE SIZE MEASUREMENT	161
C	QUANTIFICATION OF MS SIGNALS FOR NANOREACTOR EXPERIMENTS	165
	<b>BIBLIOGRAPHY</b>	171
	<b>Papers</b>	191
	Paper I	193
	Paper II	201
	Paper III	211

## ACRONYMS

---

BET	Surface area measurement by N <sub>2</sub> physisorption. Based on the Brunauer, Emmett and Teller theory
CTF	Contrast transfer function
DFT	Density functional theory
DOS	Density of states
EDS	Energy dispersive x-ray spectroscopy
EELS	Electron energy loss spectroscopy
FFT	Fast Fourier transform
fps	Frames per second
HRTEM	High resolution transmission electron microscopy
MS	Mass spectrometry
PSD	Particle size distribution
QMS	Quadrupole mass spectrometer
SNR	Signal to noise ratio
TEM	Transmission electron microscopy
TMP	Turbo molecular pump
TOF	Turnover frequency
TPR	Temperature programmed reduction
UHV	Ultra high vacuum
XRD	X-ray diffraction
XPS	X-ray photoelectron spectroscopy

# THESIS



## INTRODUCTION

---

This thesis presents work on heterogeneous catalyst systems, mainly studied using electron microscopy techniques. It has been carried out in a close collaboration between Haldor Topsøe A/S and CINF DTU. Here we have been able to combine the strong competences in electron microscopy and catalysis at Haldor Topsøe with the expertise in sample preparation and ultra high vacuum techniques at CINF. Part of the work has also been carried out in collaboration with researchers from Utrecht University.

My research has been divided into four topics, which is also reflected in the structure of this thesis. All four topics have been concerned with nanoparticle catalyst systems and the dominant experimental technique has been transmission electron microscopy (TEM). For most experiments, the catalysts have been imaged under *in situ* conditions, which entails elevated temperature and pressure. This opens up the possibility of studying nanoparticles under conditions that resemble a chemical reactor in order to reveal the true atomic structure of a catalyst. *In situ* experiments have also allowed me to study the nanoparticles during dynamic transformations such as reduction, oxidation and sintering. Using this technique, I have worked with several important aspects of nanoparticles and their role as catalysts in the conversion of chemicals. Specifically, I have been concerned with three stages of catalyst life: particle formation, nano-scale structure during operation and catalyst aging.

My research has had two goals: first, to expand our knowledge of nanoparticle catalysts, particularly with respect to fundamental aspects and atomic structure, and second to further develop the experimental techniques related to *in situ* TEM. I hope, with the work I present in this thesis, that I have helped advance our understanding and capabilities within the field.

### 1.1 HETEROGENEOUS CATALYSIS

Catalysis is the enabling of a chemical conversion by the use of a catalyst. The catalyst can be an enzyme, a chemical substance or a solid. The catalyst is not consumed in the reaction, but is left unchanged, ready for the next conversion. A chemical reaction proceeds because there is a decrease in potential energy associated with it, but the barrier for conversion may be too high for it to ever happen without the catalyst. An example is a mixture of a combustible gas with air. There is a significant energy gain associated with the combustion process

(reaction with oxygen from the air), but the mixture is stable at room temperature. In order for the reaction to happen, the molecules must be brought in close contact and sufficient energy must be transferred to break or activate internal bonds, which can happen by heating up the gas mixture or on the surface of a suitable catalyst.

The present thesis will only be concerned with the sub topic of heterogeneous catalysis, where the reacting molecules and the catalyst are in different phases. Specifically, for all reactions studied here reactants and products are gases and the catalyst is a solid, typically in the form of metal nanoparticles.

Schematically the role of the catalyst can be depicted as in Figure 1.1 for the reaction between reactants A and B to form the product C. The gas phase reaction is associated with a high barrier (high potential energy for the transition state), which is significantly reduced if the reaction takes place on the surface of a catalyst. The surface catalyzed reaction proceeds over three steps. Bonding: the reactants bond to the catalyst, resulting in a gain in energy (lowering of potential energy). Reaction: the reactants are both bonded to the catalyst, they are brought in close proximity and intramolecular bonds are weakened, and hence the barrier for reaction to the product C is lowered. Separation: the product leaves the catalyst surface.

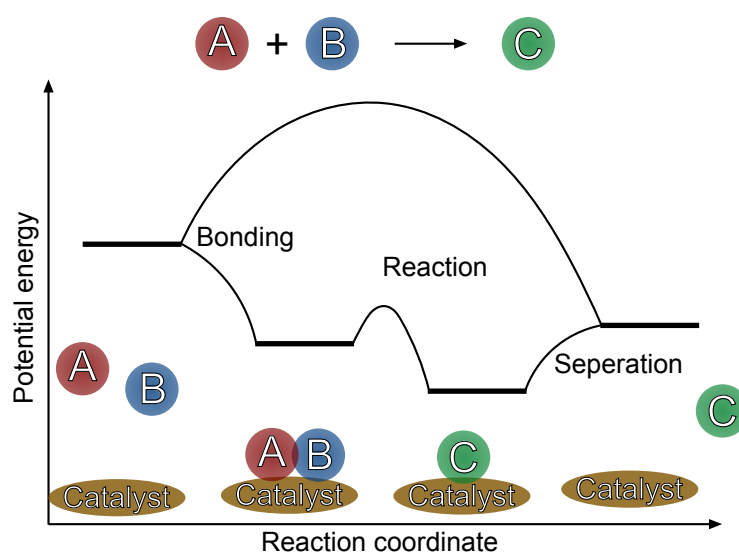


Figure 1.1: Potential energy diagram for a catalytic reaction where reactants A and B combine to form product C. Figure inspired by [1]

Any catalyst will not work for any reaction, rather the catalyst must specifically match a given chemical reaction. From Figure 1.1 we can deduce some information about how good a catalyst is. The possible catalyst candidates are divided into three regimes: i) The reactants A and B will not bind to the catalyst, i.e. there is no energy gained from bonding to the catalyst. In this case the reaction will be slow or not proceed at all. ii) Reactant, intermediates or the products bind too strongly to the surface and the catalyst surface will be occupied

and not ready to accept new reactants. In this case the reaction will also be slow or not proceed at all. iii) The binding is just right, meaning that reactants will bind to the catalyst and products will separate at an acceptable rate. This is a qualitative explanation of Sabatier's principle, which states that there is an optimum rate of reaction as a function of the heat of adsorption[1]. In the following, a more quantitative explanation of the binding of molecules and atoms to surfaces will be given in relation to transition metal catalysts.

### 1.1.1 Transition metal catalysis

The most important elements for heterogeneous catalysis are the transition metals. When a molecule or atom is adsorbed on the surface of a catalyst, there will be an interaction between the electronic states of the catalyst and the adsorbate. It is therefore important to consider the electronic properties of the catalyst, in this case a transition metal. A schematic drawing of the density of states (DOS) for a transition metal is shown in Figure 1.2. The DOS is characterized by a broad sp-band and a narrow d-band. An adsorbate will interact strongly with the d-band, which functions almost like a molecular orbital, giving rise to bonding and antibonding electronic orbitals for the adsorbate-metal complex[1]. As we move across the periodic table, the filling degree of the d-band will change, which will impact the properties and catalytic reactivity of the transition metals[2-4].

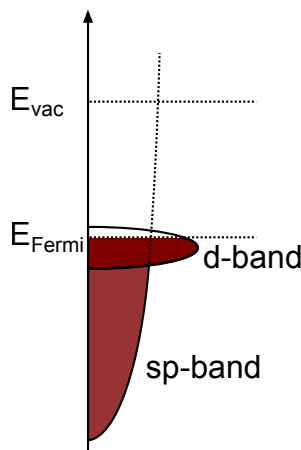


Figure 1.2: Schematic density of state (DOS) diagram for a transition metal. The electronic structure is characterized by a broad sp-band and a narrow localized d-band.

A description of the interaction between adsorbate and metal is given by the Newns-Anderson model[5, 6]. Here, I will qualitatively describe what happens when a molecule approaches a transition metal surface. This will explain why the molecule will bind to the surface and why intermolecular bonds may be weakened in this process[1].

Figure 1.3 presents a schematic diagram of the electronic interaction between adsorbate and catalyst, as a molecule approaches the surface. Here we consider the simple case of an  $H_2$  molecule with bonding and antibonding orbitals  $\sigma$  and  $\sigma^*$ , and where both electrons are located in the bonding orbital. As the molecule gets closer, the electron wave functions will start to overlap. The interaction with the sp-band leads to a broadening and a shift to lower energies for the molecular orbitals, resulting in a net energy gain and binding to the metal. The interaction with the narrow d-band resembles the interaction with an atom or molecule and results in a splitting of the  $\sigma$  and  $\sigma^*$  orbitals into bonding and anti-bonding orbitals. The filling of the bonding orbitals will further strengthen the bond to the surface, and as seen from Figure 1.3, both the  $\sigma$  and  $\sigma^*$  orbitals can contribute to this bonding, also referred to as chemisorption. The filling of the molecular antibonding orbital  $\sigma^*$  effectively moves electronic density in the molecule from the bonding to the anti-bonding orbital, which serves to weaken the internal molecular bond. This is key to understanding how a transition metal surface can dissociate a molecule and here we are getting close to the core of heterogeneous catalysis.

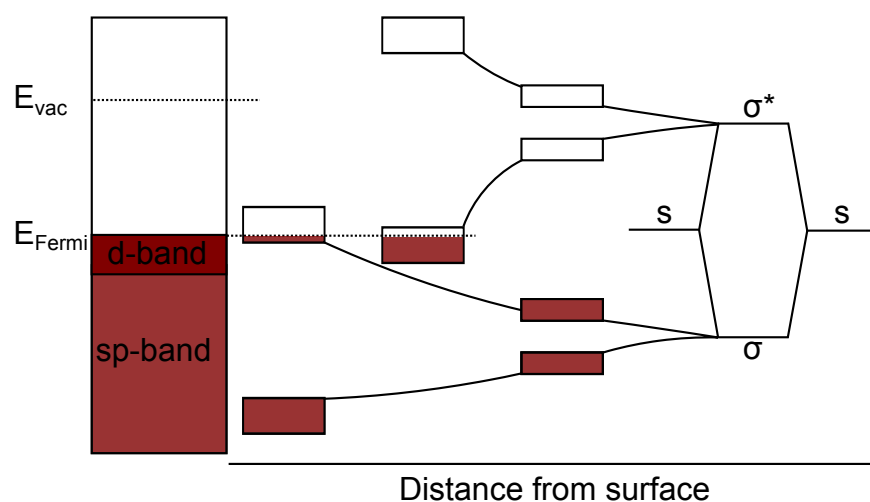


Figure 1.3: Schematic drawing of the interaction between the molecular bonding ( $\sigma$ ) and anti-bonding ( $\sigma^*$ ) orbitals of an  $H_2$  molecule with the s-p and d-band of a transition metal. The interaction with the sp-band leads to a lowering and broadening of the bands, whereas the interaction with the narrow d-band gives rise to a splitting into bonding and anti-bonding orbitals. If electrons fill the anti-bonding orbital of the molecule, then the molecular bond is weakened, which may lead to dissociation. Figure inspired by [1].

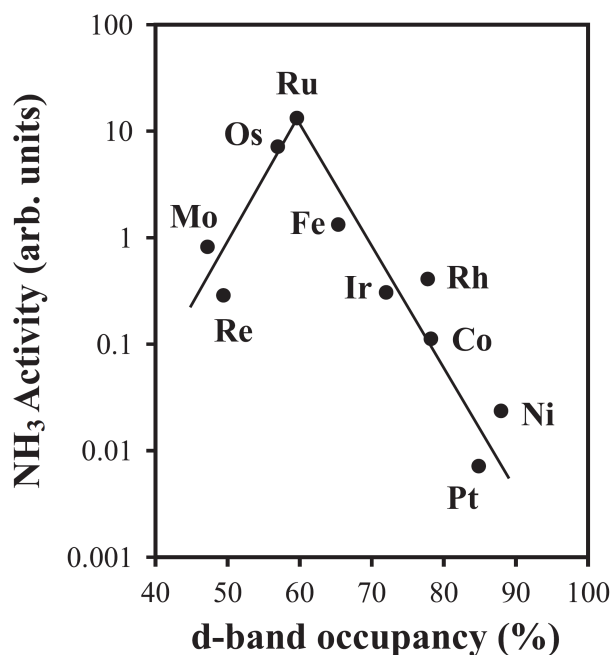


Figure 1.4: Ammonia synthesis activity as a function of d-band occupancy for a range of transition metals. This is a volcano curve demonstrating Sabatier's principle. Adapted from [1], originally from [7]

The importance of the d-band for chemisorption and dissociation also explains why material properties as well as catalytic properties vary across the periodic table. Moving from left to right through the transition metals, the d-band filling degree increases. Figure 1.4 shows the rate of ammonia synthesis for a range of metals, plotted as a function of the d-band occupancy. This is a good illustration of the previously mentioned Sabatier's principle; metals to the left will readily dissociate  $N_2$  but will bind the N atoms too strongly. The metals to the right are less reactive and will not be able to dissociate  $N_2$ . The optimum is found for Ru with a d-band occupancy of around 60%. A plot of the type shown in Figure 1.4 is referred to as a volcano plot due to the shape. In Figure 1.4 the d-band occupancy is used as a descriptor for the catalytic activity and it is one of the simplest we can think of. The interaction between adsorbates and metal surfaces may however be more complicated than the simple picture drawn here and finding appropriate descriptors for catalytic activity will be more complicated. A tremendous work has been done in the development of methods to calculate adsorption and transition state energies using density functional theory (DFT) and micro-kinetic modeling [2, 4, 8, 9]. This has secured an extensive theoretical framework for the description of heterogeneous catalysis, to a point where it is possible to accurately calculate the rate of catalytic conversion based purely on theory [10]. Furthermore, this theoretical framework is now successfully applied to predict and screen for entirely new classes

of catalysts[11–13]. In Chapter 6, DFT and micro-kinetic modeling is used to calculate the surface specific rate for CO oxidation on Pt.

### 1.1.2 *The active site*

So far we have only discussed catalytic activity as a function of the elemental composition of the catalyst. This is however only part of the story; local structural differences may have a significant impact on the catalytic activity which is known as structure sensitivity. In some cases a certain structure, which may only comprise a fraction of the catalyst surface, can be responsible for all catalytic conversion because the activity here is orders of magnitude higher than for other structures[14]. If that is the case, then that structure is typically referred to as the active site. Much of the fundamental research in catalysis can be described as a search for the active site, or more generally; the coupling of structure and activity. It is however not simple at all to determine whether a catalytic reaction is structure sensitive and what is the active site under operating conditions. An excellent tutorial review of structure sensitivity and the nature of the active site in catalysis is given by Nørskov et al.[15]. The following discussion is largely based on that paper.

In a typical catalyst the active element will be present as crystalline nanoparticles. These particles will expose terraces of various types, but there will also be a number of edges, steps, and corners where the atoms have lower coordination numbers. There are two ways in which the catalytic properties of these sites may be different from the flat surfaces; the electronic and the geometrical effect. The origin of the electronic effect is the different local electronic structure of an under coordinated atom. For the late transition metals, the d-band tends to lie higher for under coordinated surface atoms, which results in a stronger interaction with adsorbates. Comparing with the volcano plot in Figure 1.4, this corresponds to moving to the left towards stronger binding. Depending on the position of the element on the volcano, this may lead to an increase or a decrease in catalytic activity[15]. The geometrical effect arises because the different surface structures provide alternative geometries for binding of adsorbates and may be very important as e. g. seen for ammonia synthesis[14].

The local electronic properties may also be changed by alloying, either in the bulk[13], the surface[16] or as a subsurface alloy[17]. This will change the local electronic environment and will thereby change binding energies of adsorbates, which may lead to increased activity. Chapter 4 is concerned with the methanol synthesis catalyst, where the active site was suggested to be a step in the Cu surface with a Zn atom incorporated[16].

The idea of structure sensitivity and active site is very important in the experimental catalysis work, such as that presented in this thesis.

In order to unravel the relationship between structure and catalytic activity, it is necessary to measure both structure and catalytic conversion. Due to the many types of surfaces exposed by a nanoparticle catalyst, it is preferred to have a simplified structural model where only a single type of surface is exposed. Traditionally this has been done in well controlled experiments under ultra high vacuum (UHV) conditions. Here, different surface types are studied by the use of single crystals of different orientation and possibly aligned such that a number of step sites are exposed[18]. An indirect way of demonstrating structure sensitivity is by a site dependent blocking, by e. g. gold[19] or sulfur[14]. In UHV experiments, the catalytic conversion is typically not measured for the full reaction, rather a simpler test reaction is chosen as a descriptor for the full reaction. Examples of this is the sticking coefficient for  $N_2$  as a test reaction for ammonia synthesis[14] or dissociation of CO as a test reaction for methanation[18, 20].

The experiments mentioned here are typical for traditional surface science. They operate on idealized surfaces and at low pressures to guarantee a high degree of control and provide very specific structure-activity information. The downside to this is that the conditions are quite different from those in the industrial process. First of all, the catalyst is an idealized structure far from the more complicated industrial catalyst, which is typically in the form of supported nanoparticles. This discrepancy is referred to as the materials gap. Also the environment in the UHV experiment is very different from the inside of a chemical plant, where the pressure can be up to hundreds of bar depending on the process. This is referred to as the pressure gap.

### 1.1.3 *In situ* catalyst characterization

My research has been devoted to narrowing the material and pressure gaps by working with nanoparticle catalysts at elevated temperature and pressure, referred to as *in situ* conditions[21].

It is often of great interest to study a catalyst under conditions similar to those in the industrial reactor because nanoparticles respond dynamically to changes in the surrounding gas environment due to changes in the surface free energies stemming from the interaction with adsorbates[22–25]. In the extreme case, this would mean that the active site is only present under operating conditions, which makes it absolutely necessary to characterize the system *in situ*.

*In situ* implementations have been developed for many of the classic characterization tools[21]. The implementation is most straight forward with photon based techniques due to the relatively low interaction with matter. These include infrared, raman and x-ray absorption spectroscopy as well as x-ray diffraction[21, 26]. Electrons interact

much stronger with matter, but regardless of this, it is now possible to perform the electron based techniques X-ray photoelectron spectroscopy (XPS)[27, 28] and electron microscopy[29, 30] at mbar pressures. My work has revolved around *in situ* TEM which is described in further detail in Chapter 2.

The investigation of the relationship between structure and activity not only requires good, sometimes *in situ*, structural characterization, but also a good mean of measuring catalytic activity. The latest frontier within advanced catalysis research technology is simultaneous measurements of structure and activity. This has been coined *in Operando*[21, 31, 32]. In Chapter 6 I will present our work on *Operando* TEM, where atomic resolution imaging and measurement of catalytic conversion are performed simultaneously[33].

#### 1.1.4 *Catalysis and society*

The impact of heterogeneous catalysis on our modern life can hardly be overestimated with 85-90% of the products of the chemical industry made in catalytic processes. Catalysis is indispensable in the production of transportation fuels and bulk and fine chemicals as well as for the removal of pollution from power plants and cars[1].

Because catalysis is involved in so many products, it has a tremendous impact on our lives and the development of the modern western life style over the past hundred years, even if it is not something we see directly. Polymers for example, are produced in catalytic processes and plastics are now found literally everywhere. The process to produce ammonia and thereby make nitrogen available as a synthetic fertilizer has had a big impact on the efficiency of our agricultural production and we would not be able to sustain the global population if not for this.

With these examples, we invariably also get a feeling for the double-edged sword that is our modern lifestyle: Plastics are an enormous pollutant, the synthetic polymers are not broken down and will remain in the environment for literally millions of years. Although the production of fertilizers supports billions of people, the large global population exercises a huge pressure on the environment and available resources. Finally, all the big industrial processes involve the use of fossil resources as fuel and feedstock, and they thereby contribute significantly to global CO<sub>2</sub> release and anthropogenic global warming.

It is unquestionable that we will have to change much about the way we produce chemicals and our lives in general in this century, particularly in the developed countries. Our current way of life is quite simply not sustainable in the long run and it is the responsibility of my generation to support and drive such a development. Here, heterogeneous catalysis will undoubtedly play an important part, both

in terms of limiting pollution in the short term, but also through the development of new processes that use sustainable feedstocks instead of oil and natural gas.

A very important new field that is already opening up now, is the binding of sustainably produced energy in chemicals and fuels. This can be through the processing of biomass to chemicals and fuels and by hydrogen or synthesis gas production from electricity through electrolysis. It is likely that we will see a combination where biomass is upgraded with hydrogen from electrolysis in order to fully utilize the carbon bound by the plants[34]. Synthesis gas produced from electrolysis can be further processed to e. g. methanol, which has been suggested as a future fuel and energy carrier[35, 36]. These processes will be indispensable if we are to produce sustainable transportation fuels and they rely heavily on catalysis.

All in all there will be plenty to do within the field, and the technology to convert chemicals and store energy by catalysis will be as important as ever. This further emphasizes the need to understand our current catalysts and processes and to develop new ones to help us overcome the challenges that lie ahead. Here fundamental research, such as that presented in this thesis, will remain important and will hopefully help us move towards a more sustainable future.

## 1.2 THESIS OUTLINE

CHAPTER 1 Introduction to heterogeneous catalysis and relevant research topics.

CHAPTER 2 Methods used in this work. This is mainly in relation to transmission electron microscopy (TEM) and particularly *in situ* TEM.

CHAPTER 3 Catalyst activation. *In situ* imaging of the formation of a nanoparticle catalyst from a solid precursor by reduction with hydrogen.

CHAPTER 4 Catalyst structure and activity. The study of a Cu/ZnO model catalyst for methanol synthesis.

CHAPTER 5 Catalyst deactivation. The sintering of Cu nanoparticles supported on a flat surface.

CHAPTER 6 A dynamic structure-activity relation. Simultaneous TEM and reactivity measurements during oscillatory CO oxidation on Pt nanoparticles. *In situ* TEM at atmospheric pressure.



METHODS

---

In this chapter I will introduce some of the equipment and methods used in this work. In the following chapters, I will describe 4 different sub projects so it is difficult to introduce all methods here. Instead, I will describe some of the subjects that apply to all projects, and then methods and equipment that are specific to the individual experiments will be described where it is appropriate.

In terms of equipment, all experiments have been carried out on the same microscope, they have been *in situ* at high temperature and with gases present. They all concerned nanostructured catalysis systems and the fundamental understanding of these. Here, I will first present a section about the hardware, then the human aspect; how the hardware is operated and finally the treatment we need to interpret the images.

## 2.1 TRANSMISSION ELECTRON MICROSCOPY

All experiments have been carried out using a transmission electron microscope (TEM). The TEM relies on electrons to form a two-dimensional image of a three-dimensional structure, equivalently to the optical microscope which rely on photons. The important difference is the wavelength which determines the resolution of the image, and thereby the size of the features that can be resolved. The wavelength of visible light is 400-700 nm, setting the resolution limit to around 300 nm[37]. Our world however, contains many interesting objects and phenomena below this length scale, and the electron microscope has made it possible to image these. The wavelength of the electron  $\lambda$ , is a function of its momentum  $p$ , as given by the de Broglie equation[37]:

$$\lambda = \frac{h}{p} \quad (2.1)$$

where  $h$  is Planck's constant. In the TEM, the electrons are accelerated in a high voltage electrical field, and for a typical acceleration voltage of 300 kV (as used in my work), the wavelength is 0.00197 nm[37]. With such a short wavelength it becomes possible to resolve objects less than a nm in size, and the electron microscope thus provides means of studying a world that is otherwise hidden for us. From its invention in the early 1930s, the electron microscope has continuously provided new insight within e. g. biology and the physical sciences, and today it is an indispensable tool for research and development

within e. g. nanomaterials, semiconductor devices and heterogeneous catalysts.

The limit for maximum obtainable resolution has been constantly pushed through the history of TEM. In past days, the ultimate resolution was found in microscopes operated at above 1000 kV, which adds enormously to both size and prize. Today these are no longer needed; with the development of clever electron optics it is possible to resolve features down to less than 0.1 nm [38, 39] and with single atom sensitivity [39, 40]. In essence, this provides all we need when it comes to studying catalyst nanostructures.

A parallel development has also taken place; the development of *in situ* methodology, allowing us to image catalyst nanoparticles with atomic resolution during exposure to gas and at elevated temperature [29, 41–44]. With closed gas cell systems, it is even possible to raise the pressure above 1 bar [45, 46].

With the above, many important technical issues have been solved, and we have an amazing range of tools at our disposal. As scientists, our job is to ask the right questions and put these tools to the best possible use. In this way, electron microscopy will keep providing better understanding of the world and help bring ideas and technology forward.

### 2.1.1 *The microscope*

I used the FEI Titan 80-300 TEM<sup>1</sup> at Haldor Topsøe A/S for my experiments (Figure 2.1). This microscope is equipped with an image corrector that brings the maximum resolution down to 0.1 nm. Furthermore, it is fitted with an environmental cell (e-cell), so it can be used with gases, at pressures up to approximately 20 mbar.

The transmission electron microscope works by passing a broad and parallel beam of high energy electron through the sample and the image is formed by the interaction of these electrons with the specimen. The strong interaction of the electrons with matter puts some limitations on the microscope: first it must be operated in high vacuum and second, the specimen must be very thin, typically no more than 100 nm. The TEM relies on the use of electromagnetic lenses to spread or condense the electron beam, much like glass lenses will spread or condense light. In an optical microscope, the optical conditions can be changed by moving optically fixed lenses, whereas in the electron microscope, the position of the lenses is fixed, but their optical properties can be changed.

The microscope can be divided into three sections: illumination system, image forming system and projection system. Physically these form the top, middle and bottom part of the microscope column (Figure 2.1).

---

<sup>1</sup> www.fei.com

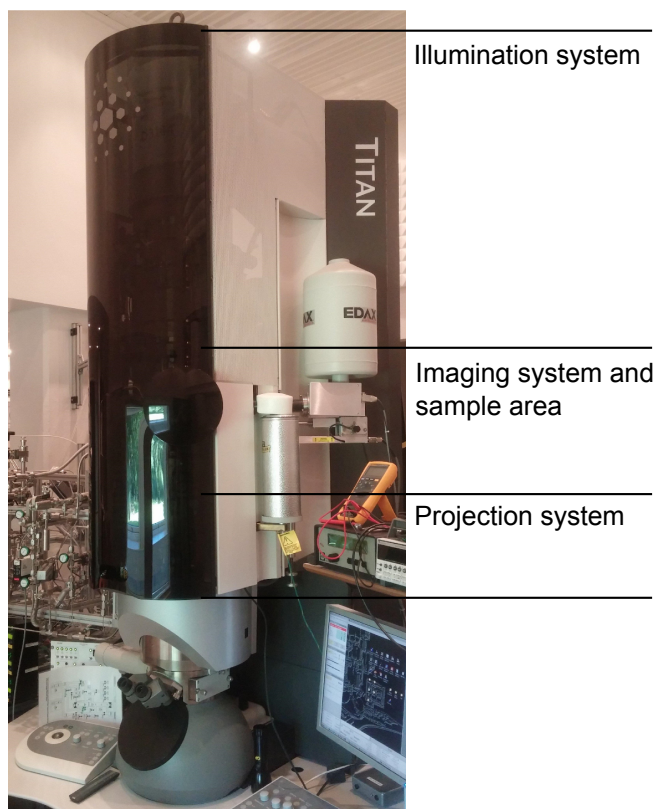


Figure 2.1: FEI Titan environmental microscope at Haldor Topsøe A/S.

The illumination system generates electrons from an electron source, accelerates the electrons in a high voltage field and finally sends a parallel beam through the sample region. In the Titan, the electron source is a field emission gun (FEG) of the Schottky type. This type of source produces electrons with a very low energy spread, which is important to achieve high resolution images. A TEM can also be fitted with a filament source, which will limit the microscope resolution due to a higher energy spread. In the Titan microscope, the high voltage can be adjusted between 80 kV and 300 kV. For the work presented in this thesis, only 300 kV was used. The Titan has three condenser lenses which form the beam incident on the sample. The condenser system is used to control the current and size of the beam. When we later talk about a certain dose rate or illumination area, this is set by the condenser system.

TEM is a broad beam technique, where the entire imaged area is illuminated simultaneously when acquiring an image. The coherency of the beam is a very important parameter, which is in part determined by the electron source and condenser system. Spatial and temporal coherence in the beam are crucial for high resolution imaging because the contrast is based on the phase of the electrons. This will be elaborated on in Section 2.1.4.

The image system is located in the sample region in the center of the microscope. Here a TEM grid, containing the sample, is placed on the tip of a sample holder. The sample region is contained in the objective lens, which is responsible for forming the image. A principle sketch of the image formation by the objective lens is shown in Figure 2.2.

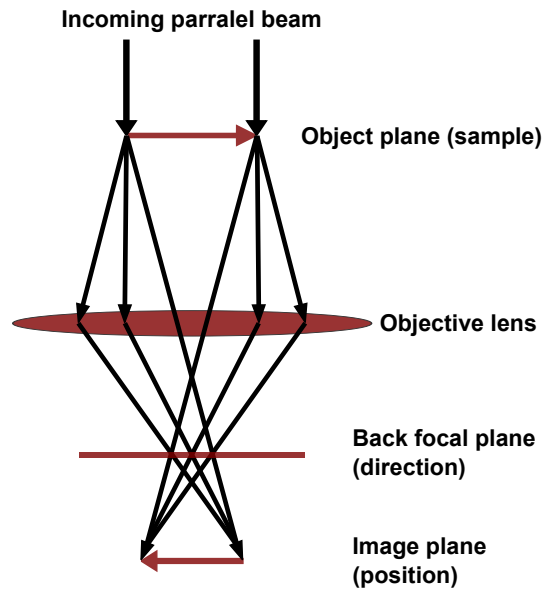


Figure 2.2: Image formation by the objective lens. A diffraction image is formed in the back focal plane (electrons scattered at the same angle ends in the same spot) and the image is formed in the image plane (electrons scattered from the same point ends in the same spot).

When electrons are scattered elastically by the specimen, they will leave at different angles depending on the object they are scattered from. The objective lens acts as a convex lens, which will focus the electrons onto the image plane, creating a magnified image of the sample. Electrons scattered from the same position in the object plane, will also end in the same position in the image plane. Electrons scattered in the same direction, or angle, will end in the same position in the back focal plane. An image of the back focal plane is called a diffraction image and contains information of the crystalline structure of the specimen equivalent to X-ray diffraction (XRD).

After the objective lens, the image is further magnified and projected onto a fluorescent viewing screen (seen in the bottom of the column in Figure 2.1) or onto a CCD camera.

*In fact this is not entirely true; the lens is not perfect and suffers from spherical aberration. This is important for high resolution imaging, which we will get back to.*

### 2.1.2 Beam-sample interactions

Figure 2.3 shows the interactions between the beam of incoming electrons and the sample. These interactions are the underlying mechanism behind both the creation of images and the analytical tools the

microscope may be equipped with. Depending on the sample thickness, a large fraction of the electrons will pass the sample unaffected, this is the direct beam, as illustrated in Figure 2.3. Other electrons are scattered, and here we distinguish between either elastic (no loss of energy) or inelastic scattering (energy transfer to the sample).

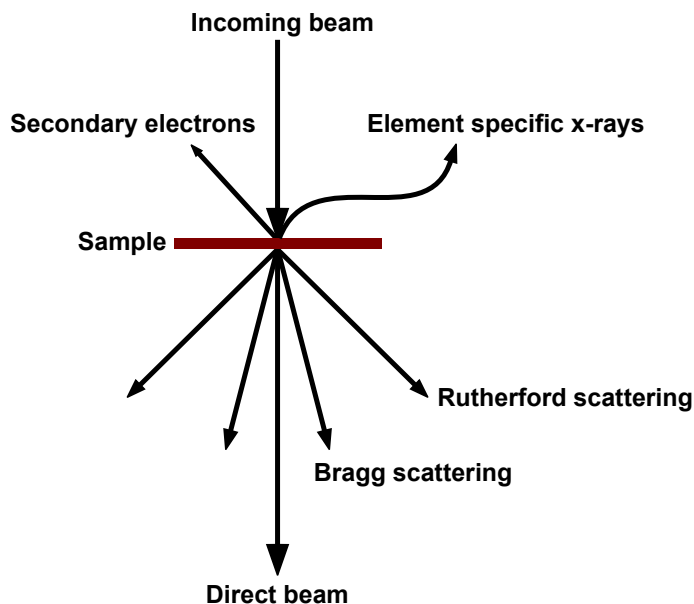


Figure 2.3: Beam sample interactions. Electrons may be transmitted with no scattering (direct beam) or be elastically (Bragg, Rutherford) or inelastically scattered. Inelastic scattering transfers energy to the sample, energy that may be emitted as secondary electrons or element specific x-rays.

When elastically scattered, the electrons will change direction from interaction with the potential of the atomic nuclei in the sample. Elastic events are divided into Bragg scattering, where the scattering angle is determined by the crystal structure of the sample, and Rutherford scattering, where the scattering angle depends on the atomic number of the elements in the sample. Image contrast can be formed in different ways, as we will get back to, but it will always stem from elastic scattering events.

Electrons may also undergo inelastic scattering due to various loss processes where energy is transferred to the sample, e.g. in the form of electronic or plasmonic excitations or phonons. Due to these excitations, the transmitted beam will carry information about the thickness and composition of the sample. This is the principle behind electron energy loss spectroscopy (EELS). When an excited atom in the sample decays, it may be by emitting a photon, an element specific x-ray. The analysis of these x-rays is the principle behind energy dispersive x-ray spectroscopy (EDS). Both of these methods will give information about the elemental composition of the sample. In this thesis, I do not present spectroscopic data acquired in the microscope, so these techniques will not be described further.

### 2.1.3 *Image contrast*

We have established how the lenses will create an enlarged image of the sample, but how is contrast created in the image? Let us first consider what is meant by the term contrast[37]. Contrast essentially means the difference in intensity between two areas of the image. If these have intensity  $I_1$  and  $I_2$ , the contrast  $C$  is defined as:

$$C = \frac{I_2 - I_1}{I_1} = \frac{\Delta I}{I_1} \quad (2.2)$$

Our eyes are not able to detect intensity differences below 5-10 % so if we just look at the raw image intensity, we wont see anything, since the contrast is often well below these levels[37]. In practice, the contrast is enhanced when the digital image is presented, such that the recorded intensities are expanded to the entire bit depth. This enhances contrast significantly.

When we talk about image formation, we view the transmitted electrons as a wave. The wave is defined by an amplitude and a phase, and it is convenient to divide contrast mechanisms into amplitude and phase related. Amplitude contrast shall be discussed briefly here, and phase contrast, particularly in relation to High resolution transmission electron microscopy (HRTEM) is discussed in the next section.

Amplitude contrast is formed when the electron wave from different areas of the sample have different amplitude, i.e. a different number of electrons reach the camera. This is achieved by actively excluding electrons that have been scattered at angles above a certain value. This is done with an aperture located in the back focal plane (Figure 2.2).

Mass-thickness contrast is generated when electrons diffracted by Rutherford scattering are removed from the image, either by the objective aperture or by the TEM column. Since the cross section for Rutherford scattering increases with atomic number and sample thickness, thick areas and areas of heavier elements will appear darker in the image. Mass-thickness contrast is by far the dominating contrast mechanism in biological sciences[37].

The second type of amplitude contrast is diffraction contrast, which relies on the scattering by crystalline objects in the sample. Scattering from a single crystal will form diffraction spots in the back focal plane. By selecting or excluding these spots, bright field or dark field images can be formed based on diffraction contrast.

### 2.1.4 *High resolution imaging*

Phase contrast relies on the phase changes imposed on the electron wave when it is scattered by the sample. This mechanism provides

the high resolution information in the image and is responsible for the imaging of atomic columns and lattices.

To describe the phase contrast from high spatial frequencies, i. e. at high resolution, we need a description of the interaction of the electron wave with the sample, as well as the microscope's ability to transfer the wave function to an image. The following is based on the description by Williams and Carter[37]:

In real space, the image  $g(\mathbf{r})$  is related to the specimen  $f(\mathbf{r})$  as:

$$g(\mathbf{r}) = f(\mathbf{r}) \otimes h(\mathbf{r} - \mathbf{r}') \quad (2.3)$$

where  $h(\mathbf{r} - \mathbf{r}')$  is a weighting term, called the point-spread function, describing how much each point in the specimen contributes to each point in the image.  $h(\mathbf{r} - \mathbf{r}')$  describes the imperfect information transfer of the image system, i. e. a point in the specimen will be transferred to a disk in the image, and hence each point in the image will have overlapping contributions from many points in the specimen.

We can conveniently represent  $g(\mathbf{r})$  in reciprocal, or Fourier space, by applying a Fourier transform. This is a representation of the function in the frequency domain, where the coordinate  $\mathbf{u}$  is the reciprocal lattice vector, or the spatial frequency for a particular direction. In Fourier space we have:

$$G(\mathbf{u}) = H(\mathbf{u})F(\mathbf{u}) \quad (2.4)$$

here,  $H(\mathbf{u})$  is called the contrast transfer function and is described as the product of three separate contributions:

$$H(\mathbf{u}) = A(\mathbf{u})E(\mathbf{u})B(\mathbf{u}) \quad (2.5)$$

$A(\mathbf{u})$  is the aperture function, describing the spatial frequency cut-off by a possible objective aperture.  $E(\mathbf{u})$  is the envelope function, describing the attenuation of the wave at high frequencies. This will also act as a frequency cut-off, and is determined by the properties of the electron source and the objective lens.  $B(\mathbf{u})$  is the aberration function and describes the effect of the objective lens on the transmitted wave as[37]:

$$B(\mathbf{u}) = \exp(i\chi(\mathbf{u})) \quad (2.6)$$

For a microscope without aberration corrector, we can ignore higher order aberrations and  $\chi(\mathbf{u})$  will then only depend on the defocus and spherical aberration. The latter is an inherent property of a round electromagnetic lens and means that the focus depends on the scattering angle. Both defocus and spherical aberration are rotationally

symmetric, so  $\mathbf{u}$  is reduced to a scalar  $u$  and the one-dimensional  $\chi(\mathbf{u})$  is expressed as:

$$\chi(\mathbf{u}) = \pi\Delta f\lambda u^2 + \frac{1}{2}\pi C_s\lambda^3 u^4 \quad (2.7)$$

Here,  $\Delta f$  is the defocus, which is set by the operator,  $C_s$  is the spherical aberration,  $\lambda$  is the wavelength of the electrons and  $u$  is the spatial frequency.

We now turn to the description of the specimen and how it will affect the phase of the transferred wave function. The electrons exiting the specimen will be described by the specimen transfer function  $f(\mathbf{r})$ . The phase change will depend only on the potential function  $V(x, y, z)$ . Assuming that the sample is thin, we can replace  $V$  with a projected potential by integrating over the sample thickness  $t$ :

$$V_t(x, y) = \int_0^t V(x, y, z) dz \quad (2.8)$$

Using the projected potential to describe the phase change and including a term for absorption in the sample  $\mu(x, y)$ , the specimen transfer function is expressed as:

$$f(x, y) = \exp[-i\sigma V_t(x, y) - \mu(x, y)] \quad (2.9)$$

where  $\sigma$  is an interaction constant that depends on the energy of the primary electrons. If the specimen is sufficiently thin, we can assume that there is no absorption. This is called the phase object approximation, POA. For very thin specimens, the exponential function can be expanded, ignoring higher order terms, and the approximation is then called the weak phase object approximation, or WPOA. Here, the specimen transfer function is simplified to:

$$f(x, y) = 1 - i\sigma V_t(x, y) \quad (2.10)$$

Applying the WPOA (Equation 2.10) to Equation 2.3 the wave function as seen in the image is given by:

$$\psi(x, y) = [-i\sigma V_t(x, y)] \otimes h(x, y) \quad (2.11)$$

and intensity of the wave function on the sample is:

$$I = \psi\psi^* \quad (2.12)$$

Here it can be shown that only the imaginary part of  $B(\mathbf{u})$  contributes, so that  $H(\mathbf{u})$  (Equation 2.5) can be redefined as the intensity transfer function  $T(\mathbf{u})$  (as described by Williams and Carter[37]):

$$T(\mathbf{u}) = A(\mathbf{u})E(\mathbf{u})2\sin(\chi(\mathbf{u})) \quad (2.13)$$

In the weak phase approximation,  $T(\mathbf{u})$  is identical to the contrast transfer function (CTF).

If we ignore the aperture and envelope functions  $A(\mathbf{u})$  and  $E(\mathbf{u})$  we can consider only the contrast transferred by the aberration function  $\sin(\chi(\mathbf{u}))$ . The function is periodic in  $u$  for non-zero values of  $\Delta f$  and  $C_s$ , but we are interested in obtaining a constant contrast over the largest possible interval of spatial frequencies. Recalling the one dimensional form of  $\chi(\mathbf{u})$  (Equation 2.7), we see that it should be possible to offset the effect of the large positive spherical aberration by applying a negative defocus.

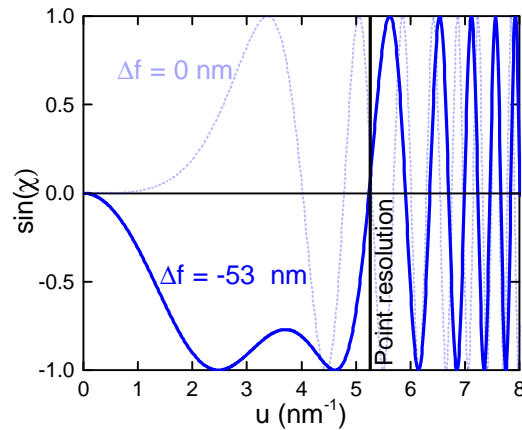


Figure 2.4:  $\sin(\chi(u))$  for a microscope with  $C_s = 1$  mm at defocus 0 and -53 nm. -53 nm is the extended Scherzer defocus, which represents the optimum balance between  $C_s$  and  $\Delta f$  which maximizes the point resolution and provides a flat information transfer.

Figure 2.4 shows the CTF (disregarding the envelope functions) for a 300 kV microscope with a spherical aberration of 1 mm. The plot shows the contrast transfer as a function of spatial frequency for two defocus settings; 0 nm and -53 nm. -53 nm is the extended Scherzer defocus, which optimizes the CTF to move the first cross-over to the highest possible  $u$  and provides a nearly constant contrast to the first cross-over. For the negative defocus setting, the defocus term in Equation 2.7 is dominating the CTF up until the cross over where the two terms are equal. At higher values of  $u$ ,  $C_s$  will dominate Equation 2.7 and the CTF takes on the shape of a normal sine function. At the cross over, when  $\sin(\chi)$  is zero, there is no contrast, and spatial frequencies with this value will not be shown in the image. The first cross over therefore defines the point resolution of the microscope. For  $u$  higher than the the point resolution, information may still be transferred, but the information is not directly interpretable due to the periodically changing sign of the contrast.

At high values of  $u$ , the envelope function  $E(\mathbf{u})$ , defined by spatial and temporal incoherencies in the microscope, kicks in and attenuates the contrast transfer. Figure 2.5 shows the same  $\sin\chi$  as Figure 2.4

but including envelope functions for the spatial and temporal incoherence. These were calculated using the software CTFExplorer<sup>2</sup>. Values that define the temporal incoherencies are chromatic aberration ( $C_c$ ), energy spread and high tension ripple. The spatial coherence is defined by the convergence angle. The exact values used for these are quoted in Figure 2.5 and are based on values relevant for the Titan 80-300 used in this work, except for the spherical aberration that is set to 1 mm here.

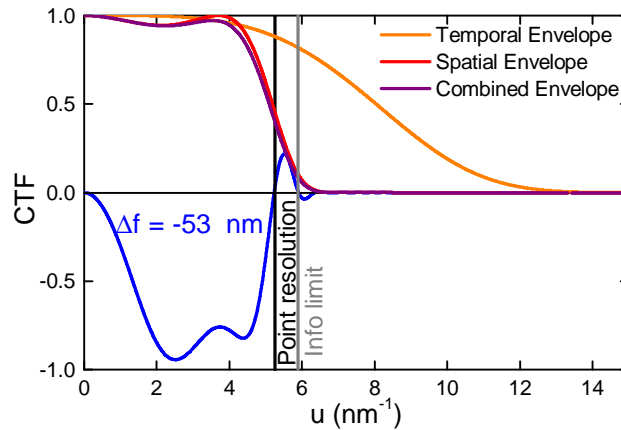


Figure 2.5: CTF for a microscope with  $C_s = 1$  mm at defocus  $-53$  nm. Here the spatial and temporal envelope functions are included. Point resolution is  $0.19$  nm ( $u = 5.26$ ) and information limit is  $0.17$  nm ( $u = 5.88$ ) Calculated using CTFExplorer for  $C_s = 1$  mm,  $C_c = 1.4$  mm, Energy spread =  $1.1$  eV, high tension ripple =  $1$  ppm, convergence angle  $1$  mrad. Calculated focal spread is  $3$  nm.

In Figure 2.5, the envelope functions do not change the point resolution, which is maintained at  $0.19$  nm ( $u = 5.26$ ) at the extended Scherzer defocus. We now see that the information limit is set to  $0.17$  nm ( $u = 5.88$ ), which is mainly an effect of the spatial envelope function. The effect of the spatial incoherence is enhanced by the spherical aberration of the microscope as we will see when we look at the CTF of the aberration corrected instrument.

The microscope I have used, is equipped with a spherical aberration, or  $C_s$ , corrector[38, 47]. This is an advanced device located below the objective lens. It uses a number of hexapole lenses to correct for spherical aberrations, which allows the user to control  $C_s$  and essentially set it to zero. This moves the cross over of the CTF significantly and increases the point resolution of the microscope. At high spatial frequencies, higher order aberrations become important and the aberration function will no longer be spherically symmetric. The two dimensional CTF is measured by dedicated software on the basis of a tilt-series and used to optimize, or tune, the settings of the image

<sup>2</sup> <http://www.maxsidorov.com/ctfexplorer/>

corrector. The tuning is standard operation prior to any experiment requiring high resolution.

Even if the CTF is not spherically symmetric, it may still be instructive to see a one-dimensional transfer function, in order to get a sense of some general traits of the  $C_s$ -corrected microscope.

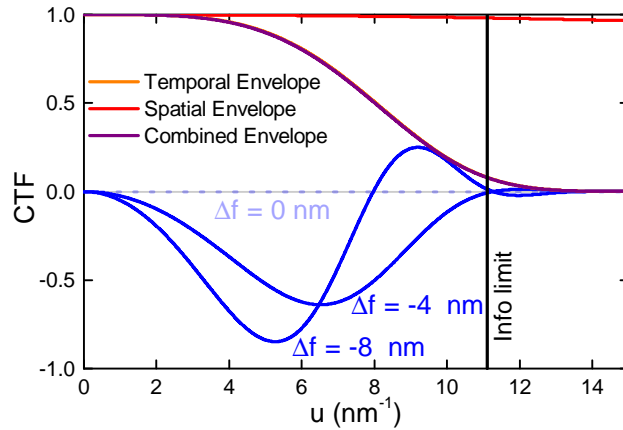


Figure 2.6: CTF for a microscope with  $C_s = 0$  mm at defoci 0, -4 and -8 nm. Information limit is 0.09 nm ( $u = 11.1$ ). With no spherical aberrations, it is possible to set the point resolution equal to the information limit ( $\Delta f = -4$  nm). Contrast can be enhanced by further defocusing ( $\Delta f = -8$  nm). Calculated using CTFExplorer<sup>3</sup> for  $C_s = 0$  mm,  $C_c = 1.4$  mm, Energy spread = 1.1 eV, HT Ripple = 1 ppm, convergence angle 1 mrad. Calculated focal spread is 3 nm.

Figure 2.6 shows the CTF calculated for the same parameters as Figure 2.5 with the only exception that  $C_s$  is now zero. If we first compare the envelope functions, we see that the temporal envelope is unchanged, whereas the spatial envelope no longer has a significant influence because of the lack of  $C_s$ . This moves the information limit dramatically to 0.09 nm ( $u = 11.1$ ), and we can see how such a microscope is able to obtain the previously quoted 0.1 nm resolution. To increase this value further, the microscope must be optimized mechanically as well as electronically and the energy spread of the beam must be reduced[48].

The lack of  $C_s$  has some implications on the phase contrast that requires a slightly different operation than for the uncorrected TEM. In the uncorrected microscope, there is a wide band of flat information transfer at the Scherzer defocus. In the  $C_s$ -corrected microscope, the first cross-over moves towards infinitely high  $u$  as the defocus goes towards zero. The contrast however also goes to zero for  $\Delta f \rightarrow 0$ , which is of course not an ideal situation for imaging. It is therefore necessary to adjust the defocus in order to obtain satisfactory contrast. Figure 2.6 shows the CTF for three defoci; 0, -4 and -8 nm. For -4 nm, the cross-over is placed at the information limit but here the contrast is still quite low, particularly for low values of  $u$ . This has the

implication that larger features, such as the overall particle outline and shape may be very weak in the image, for conditions where the atomic lattice displays well. In practice it may be beneficial to move the cross-over down in order to enhance the contrast at an interesting band of  $u$ -values, but lowering the the point resolution as for  $\Delta f = -8$  nm in Figure 2.6.

An advantage of the  $C_s$ -corrected microscope that should be mentioned here is the lack of delocalization for the phase contrast. For an uncorrected microscope, delocalization means e. g. that the atomic lattice fringes resolved in a nanoparticle will extend over the edge of the particle. This is not the case for a  $C_s$ -corrected; here the edges of nanoparticles will be razor-sharp which may make it possible to resolve and interpret the surface structure[49].

With the explanation above, we have seen how a high resolution image is formed in the TEM and how contrast is generated from the phase change induced on the electron wave by the potential of the atomic nuclei in the sample. An example of a HRTEM image of a Cu crystal can e. g. be seen in Figure 2.11 (page 30). Given the discussion of how contrast is transferred to the image, it is important to note that when we image a periodic structure such as a metal particle, we are not creating a direct image of the atomic lattice. Instead, the image represents contrast generated by the periodic arrangement of the atoms and the image therefore contains information about lattice spacing and orientation. For that reason, the periodic structure seen in a HRTEM image is referred to as lattice fringes and not lattice planes[37].

## 2.2 *in situ* TEM, CONCEPT AND HARDWARE

As pointed out in the introduction to this thesis, it is often of great interest to study catalysts and nanoparticle system *in situ* under conditions different from vacuum, typically meaning elevated temperature and pressure. *In situ* TEM experiments can be divided into two categories. i) Equilibrium experiments, where we look at some equilibrium structure under the influence of gas and temperature, as e.g. Cu on ZnO in different gas environments[22] or ii) Dynamic (or non-equilibrium) experiments e.g. growth of carbon fibers[42]. Both categories may have the same requirements in terms of temperature and pressure, whereas dynamic experiments may have other requirements as e.g. video rate imaging or alignment with other experimental data.

There is one overall concept that all *in situ* TEM instrumentation is build upon, and that is the confinement of the experimental conditions to the sample region, allowing the microscope to operate under its normal vacuum conditions. This concept is sketched in Figure 2.7.

In addition to the confinement, there must be ways to control and monitor temperature and pressure.

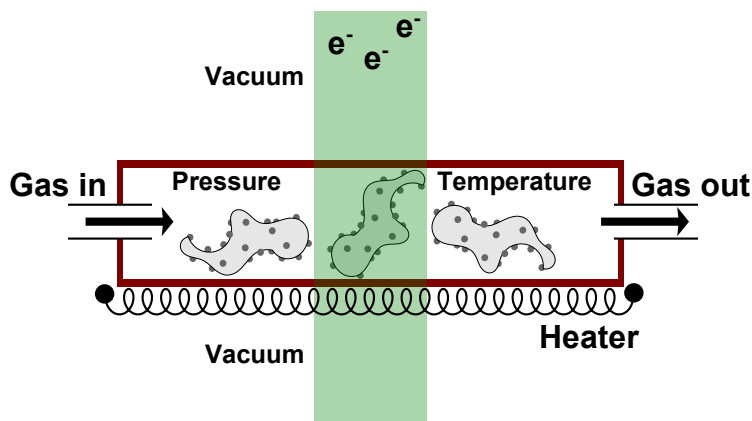


Figure 2.7: Basic principle behind an *in situ* TEM experiment. Gas pressure and high temperature is confined to a narrow region around the sample in order to maintain high vacuum in the rest of the microscope. The separation between *in situ* region and vacuum must allow the electron beam to pass.

The *in situ* concept may be implemented either by the principle of differential pumping[29] or by a closed gas cell[45]. The latter will be described in detail in Chapter 6 so here we will concentrate on the former. The Titan microscope (Figure 2.1) is based on differential pumping and this is the concept behind the experiments described in Chapter 3, Chapter 4 and Chapter 5.

A schematic drawing of the instrument is shown in Figure 2.8 (from Jinschek and Helveg[50]). The concept is based on the design by Boyes and Gai[29]. Here, the sample area is called the environmental cell, or e-cell. The top and bottom of the e-cell has small pin holes, apertures, where the gas leaks out to the vacuum of the microscope column. The apertures must be small to limit the gas flow, but large enough for the electron beam to pass through. The vacuum on the other side of the e-cell is pumped by Turbo molecular pump (TMP)s to remove the flowing gas and maintain vacuum. To maintain sufficiently high vacuum at the electron source in the top of the microscope, a second differential pumping stage is added, with another set of apertures and TMPs. The height of the environmental cell, the same as the pole piece gap, is 5.4 mm, which is the height of the gas column that the electron beam must pass. The atomic density of a solid is around 1000 times that of an ideal gas at 1 bar, so at 1 mbar, the density is around  $10^{-6}$  times that of a solid. What this means is that 5.4 mm gas at 1 mbar contains roughly the same number of atoms as 5 nm of solid. At 20 mbar this has increased to 100 nm, and we approach the point where the gas becomes a limiting factor in terms of resolution. Even if it is possible to maintain a high resolution at these high pressures[50], the scattering of electrons on the gas phase

will always limit the differentially pumped TEM to the mbar regime, since the height of the pole piece gap must remain several mm in order to accommodate the sample. This is not a limitation for closed gas cell systems, which we will get back to in Chapter 6.

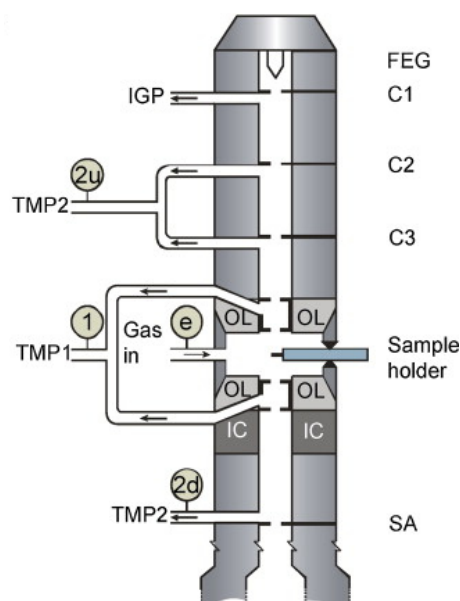


Figure 2.8: Titan ETEM schematic drawing. Reproduced from Jinschek and Helveg[50]

### 2.2.1 Grids and holder

In the investigation of heterogeneous catalysts, *in situ* will usually require elevated temperatures. This is implemented by a special sample holder for the microscope, which contains a resistive heater and a temperature probe. Specifically, I have used a Gatan model 628 heating holder, shown in Figure 2.9. This was used for experiments reported in Chapter 3, Chapter 4 and Chapter 5.

The holder is designed for regular TEM grids, typically circular and 3 mm in diameter. The grid is placed in a furnace and heat is transferred to the sample through the grid, and by radiation at high temperatures. The furnace is suspended between two ceramic balls as shown in Figure 2.9a to thermally isolate it from the rest of the holder. The grid rests in the recess and is fixed by a hollow screw mounted from the top. Figure 2.9b shows the underside of the holder. Here, the four cables used for temperature control are seen. Two are connected to the resistive heater inside the furnace and two are connected to a temperature probe placed on the outside. The temperature is controlled by a Gatan SmartSet Hot Stage Controller, using active feedback control. Typically my experiments have been run in the 'Temperature ramp' mode, where the temperature controller con-

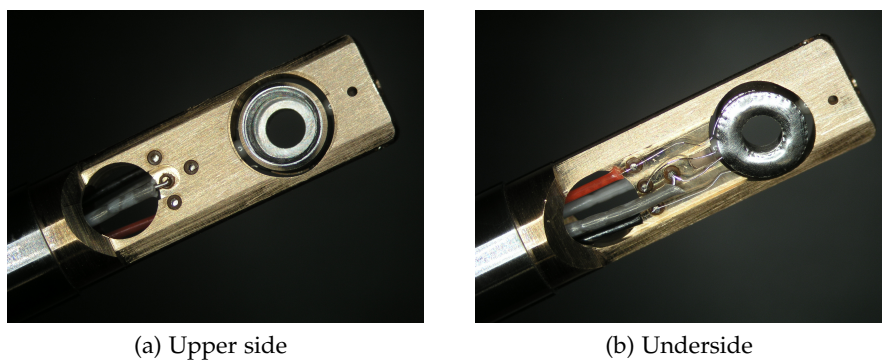


Figure 2.9: Gatan heating holder model 628. The holder is designed for use with standard circular 3 mm TEM grids. The holder features a small furnace mounted between two ceramic balls.

**(a)** Top side. Here the grid is placed inside the furnace, in the recess, and is fixed by a hollow screw mounted from the top.  
**(b)** Under side. There are four electrical connections; two for the resistive heater inside the furnace, and two for the temperature probe mounted on the outside of the furnace.

trols the output power to get a certain ramp rate (typically  $30\text{ }^{\circ}\text{C}/\text{min}$ ) and target temperature.

The holder works in vacuum or at mbar pressures. At higher gas pressure, the convective cooling will be too high, and the output power of the holder is insufficient.

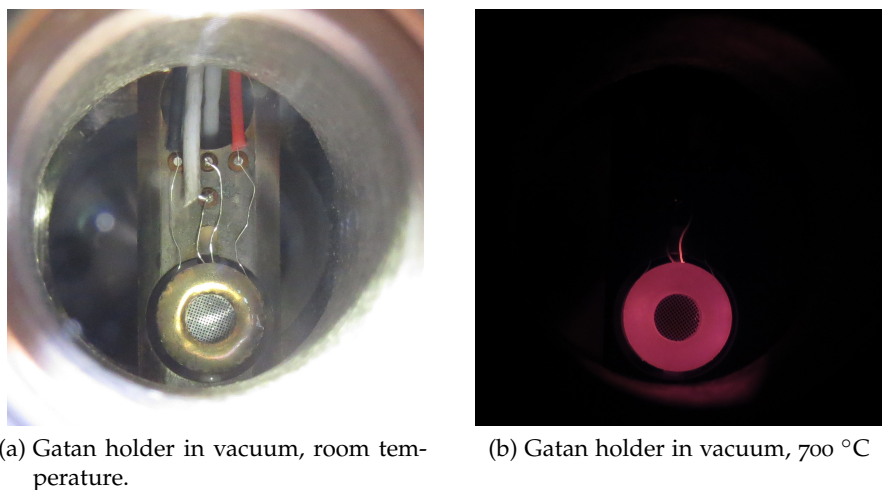


Figure 2.10: Gatan heating holder hot

Figure 2.10 shows the holder in a windowed vacuum cell at room temperature and with light (Figure 2.10a) and heated to  $700\text{ }^{\circ}\text{C}$  imaged in darkness (Figure 2.10b) where the holder is emitting visible light.

Whereas the temperature of the furnace is known, the grid may have a different temperature, depending on the transport of heat to

and away from the grid. Mølgaard Mortensen et al. recently did an impressive effort in modeling flow and temperature in the e-cell and on and around the heated holder[51]. The main conclusion is that the gradients are limited, the temperature on the grid is typically no more than 10 °C lower than on the furnace. This temperature difference is however affected by the heat conductance of the grid material as well as of the surrounding gas. Generally higher heat conductance of the grid material should result in a lower temperature difference, whereas higher heat conductance of the gas results in higher temperature difference due to more efficient heat removal from the sample region[51]. This is in line with observations made in relation to this study. For the results presented in Chapter 3, we reduced a Cu phyllosilicate in H<sub>2</sub> which has a high heat conductance. Here we saw a tendency to more efficient reduction when using gold grids (high heat conductance) compared to stainless steel grids (low heat conductance).

All implications of the choice of grid material for *in situ* experiments is not yet fully understood and possible effects must be evaluated for the individual experiment and sample type.

### 2.3 OPERATION

This section will discuss some important aspects of operating the TEM during an *in situ* experiment, specifically in relation to control of the illumination conditions and unwanted beam-sample interactions. This will also include the handling and analysis of TEM images.

#### 2.3.1 Controlling dose rate

There are several parameters to control with respect to the illumination conditions in an *in situ* TEM experiment; electron energy, electron flux and illumination area comes to mind. Electrons interact strongly with matter, that is why the TEM is so great for imaging and analysis, but the interaction may also lead to adverse or undesired effects, often referred to as beam effects. These will tend to scale with the flux of electrons, and that is why good control of illumination conditions is paramount in controlling beam effects[52–54].

The high tension, or electron primary energy, has a strong effect on the beam sample interaction. Knock-on damage, i. e. removal of atoms from the specimen by the electrons, increases with increasing primary energy. For light sample types, such as graphene or biological specimens, this is very important. A primary energy tension however also increases the cross section for inelastic scattering, which means that ionization damage increase with lower primary energy. A decrease in primary energy will in turn also increase image contrast so the net ef-

fect may be zero because the dose rate can be lowered accordingly[55, 56].

Traditionally, a high primary energy has been used for *in situ* experiments to limit gas and sample ionization and to increase the penetration depth through the gas-sample layer. For my experiments, I have operated the Titan at 300 kV and it has not been a goal to evaluate the effect of lowering the primary electron energy.

When we talk about controlling beam effects and electron flux, we often discuss both dose rate and total dose, in this work measured in  $e^-/(\text{\AA}^2\text{s})$  and  $e^-/\text{\AA}^2$  respectively. In the literature these are often reported as  $\text{A}/\text{cm}^2$  and  $\text{As}/\text{cm}^2$ . Here, the total dose is simply the number of electrons or charge accumulated in the sample or dose rate multiplied by time. For everything reported here, dose rate has been measured by the fluorescent screen of the microscope. Usually I would start the day by measuring a set of dose rates I want to use, e.g. 1, 5, 50, 100  $e^-/(\text{\AA}^2\text{s})$  and then write down the settings of the condenser system for these dose rates. This makes it easy to change back and forth between settings. It also ensures that the incident dose rate is independent of gas in the *in situ* experiment, since scattering on the gas may lower the current on the fluorescent screen.

So how do we find the right dose rate to use, or more generally, the right settings to use for a given experiment? This is not necessarily easy, and it will always be a compromise between image quality (SNR), possible exposure time, resolution and of course beam effects. The SNR of a given image is often measured as the ratio between mean pixel intensity  $n_{\text{mean}}$  and the standard deviation of the pixel intensities  $\sigma_n$ :

$$\text{SNR} = \frac{n_{\text{mean}}}{\sigma_n} \quad (2.14)$$

According to the Rose condition, the SNR should be at least 3-5 in order to have a significant signal.

Figure 2.11 shows three HRTEM images acquired at three different dose rates.  $n_{\text{mean}}$ ,  $\sigma_n$  and SNR are quoted in the figure. Dose rates of 50, 100 and 300  $e^-/(\text{\AA}^2\text{s})$  were measured in vacuum on the fluorescent screen before the experiment. The images were recorded with a pixel size of 0.063 nm. Using this and the calibration of the camera, 1 electron gives 3.8 counts, the measured average image intensities corresponds to 32, 66, 211  $e^-/(\text{\AA}^2\text{s})$ . The discrepancy is mainly due to a different calibration of fluorescent screen and camera. In the following chapters, I will report numbers recorded on the fluorescent screen.

The three images in Figure 2.11 are representative of typical dose rates used for acquiring HRTEM images in this work and should give some idea of what image quality to expect and what HRTEM images look like at SNR of 7, 10 and 19. 50  $e^-/(\text{\AA}^2\text{s})$  is typically the

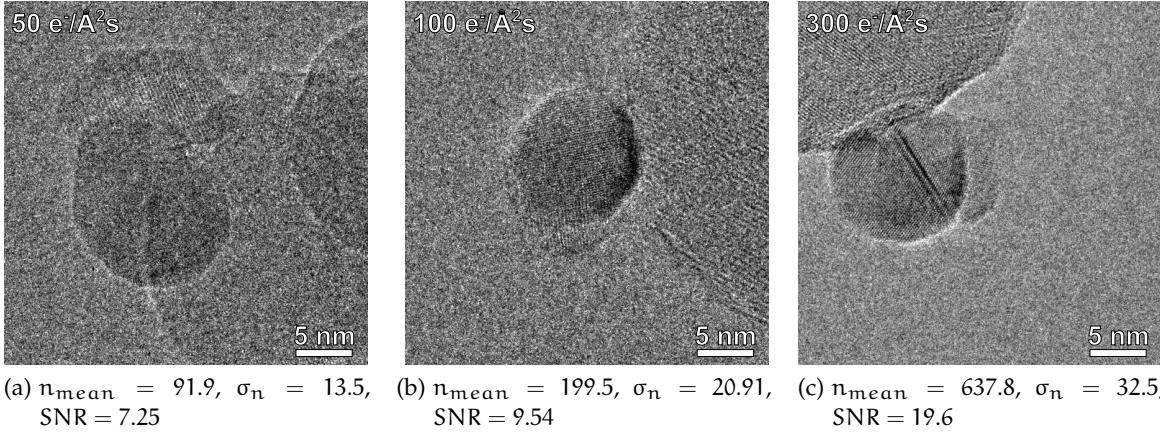


Figure 2.11: CuZn nanoparticles on  $\text{Al}_2\text{O}_3$  recorded *in situ* in 1 mbar  $\text{H}_2$  at 250 °C. Pixel size 0.063 nm, quoted dose rates recorded on fluorescent screen.

lowest practical dose rate for getting sufficient contrast and resolution, whereas  $300 \text{ e}^-/(\text{\AA}^2\text{s})$  has been a typical upper limit in my experiments in terms of beam effects. This is however highly dependent on the specific experiment. The standard deviation,  $\sigma_n$  in Equation 2.14, is expected to scale with a power of 0.5 according to Poisson statistics[57] and so the SNR will scale with  $n^{0.5}$  according to Equation 2.14. The SNR from Figure 2.11 is plotted as function of dose rate (numbers from the camera calibration) in Figure 2.12. A power law fit shows a scaling of  $n^{0.58}$ .

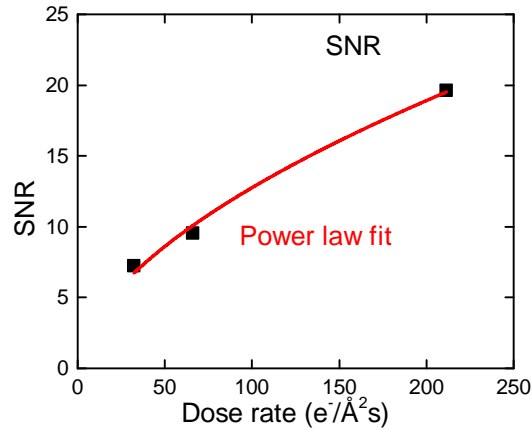


Figure 2.12: Signal to noise ratio as a function of total dose rate (same exposure time) for the three images in Figure 2.11

The SNR is thus determined by the number of electrons  $n$  incident on each pixel of the camera. Here we will consider what parameters determine  $n$ :

$$n = \text{DR} \times A_{\text{pixel}} \times t_{\text{exposure}} \quad (2.15)$$

DR is the dose rate measured in  $e^-/(\text{\AA}^2\text{s})$ ,  $A_{\text{pixel}}$  is the corresponding area of one pixel measured in  $\text{\AA}^2$ ,  $t_{\text{exposure}}$  is the exposure time in s.

Dose rate was already discussed, the limiting factor here is often beam effects, which will be discussed in more detail in the following section. The selection of dose rate may however also have other adverse effects in an *in situ* experiment. Jinschek and Helveg[50] has demonstrated that a high dose rate is detrimental to the resolution when gas is present in the e-cell. This further emphasizes the need to use a low dose rate, and the importance of controlling how the electrons are delivered. Instead of a high dose rate, it will thus be necessary to adjust the other parameters in Equation 2.15 to arrive at a sufficient SNR

$A_{\text{pixel}}$  is the square of the pixel size. The pixel size determines the maximum achievable resolution, and it is often worth it to optimize on this parameter, since  $n$  scale with the square of the pixel size. According to the Nyquist criterion, the sampling rate (equivalent to pixel size) should be at least twice the frequency that is measured (equivalent to the feature/crystal lattice spacing that is imaged). In reality for TEM, you often want the pixel size to be 3-4 times smaller than the feature to resolve. This means, that even if I am operating a microscope capable of 0.1 nm resolution, I might only be interested in resolving e. g. Pt(220) at 1.4  $\text{\AA}$ , and the pixel size should be adjusted accordingly in order to maximize  $n$ . In practice, pixel size is chosen by adjusting the magnification of the microscope. This is mainly important due to restrictions on DR, the images will always look better with smaller pixel size/higher magnification. Finally we have the exposure time  $t_{\text{exposure}}$ . Under most circumstances, exposure time is limited by sample drift. Even the best TEM holders will have a slight random drift, and this will blur the image/cap the resolution. The typical drift rate is of a magnitude that present only a problem at high resolution. In Section 2.4.2 a measurement of drift rate will be shown. In special cases, such as the one presented in Chapter 6, a very fast dynamic process is recorded. Here, this will put a limit to the exposure time.

### 2.3.2 Beam influence

When discussing beam influence, it is important to state that the beam will most likely *always* have an effect on the sample. Also in high vacuum imaging, it is often an overlooked fact, that the beam current may strongly affect the structure that is imaged[58, 59]. So how do we deal with this? Recently, the concept of 'Divide and Conquer' has been presented for traditional TEM/non-*in situ* experiments[59, 60]. This builds on a similar approach presented by Jinschek and Helveg[50]; to use a low dose rate and long exposure time in order

to minimize and control the beam-sample interactions. The idea behind 'Divide and Conquer'[60] is to deliver the probing particles, in this case electrons, one-by-one. Then, if the dose rate is sufficiently low, a structure that is distorted or excited by an incoming electron, will have time to relax to the original configuration before the next electron comes. Kisielowski[59] demonstrate this by acquiring a large stack of images using an extremely low dose rate of  $10 e^-/(\text{\AA}^2\text{s})$  and aligning and summing post acquisition using the method of exit-wave reconstruction[61]. This allowed imaging of the inherent structure of Au nanoparticles, contrary to a much more dynamic structure during high dose rate (standard) imaging[59].

For the *in situ* experiments presented here, the guiding idea has been a similar 'Divide and conquer' approach; that it is possible to find a dose rate and illumination scheme that allow for the imaging of inherent structure or phenomena. It may sound like an obvious way to view an *in situ* experiment, but that is not necessarily the case. The literature also has examples of the study of beam induced phenomena and the attempt to relate that to e. g. thermally induced phenomena outside the microscope[62].

So how do we know if we image an inherent structure or phenomenon and not a beam effect? Earlier I divided *in situ* experiments into equilibrium and non-equilibrium experiments and I will discuss it in the context of these two.

**EQUILIBRIUM EXPERIMENTS** The goal is to image the inherent structure of a nanoparticle system *in situ* under some external influence. The question thus becomes, how do we know if it is the inherent structure? In practice, this is often answered by mapping out the effect of the beam at varied doses and dose rates[53]. The logic is, that if you know what the effect of the beam is, it is also possible to find a dose rate where this effect is not seen. Possible beam effects could be change in shape[59], growth or change in support or particle[53], growth of contamination or beam induced reduction or oxidation.

This is an empirical and effective method, that can often be implemented simply by recording time lapsed images of the specimen at various dose rates.

**NON-EQUILIBRIUM EXPERIMENTS** Assessing the beam effect in a non-equilibrium experiment might be slightly more difficult. The reason is that we are studying a dynamic effect, so a change in the specimen is the expected outcome. Examples of such dynamic experiments are; reduction and oxidation[63], sintering[52, 64–66], electromigration[67] and shape changes in a dynamic reaction[33]. The common denominator for these experiments is an external stimuli, e. g. temperature or gas environment that is driving the system towards equilibrium. To control beam effects in this situation, it is important

to know what effect the electrons have on the process. There are no general rules here, it is individual for each experiment, and it is necessary to make this assessment for each new system. Some examples of possible beam effects in non-equilibrium experiments from the literature and the present thesis are; speeding up reduction[54](Chapter 3), causing particle shrinkage in parallel with thermally driven sintering[52] (Chapter 5), causing particle mobility (Chapter 6) or affecting the Particle size distribution (PSD) in a reduction experiment[54] (Chapter 3).

For the non-equilibrium experiments, we have also worked with an empirical approach, where the beam effects are measured and reduced, but where the more fundamental aspects are not necessarily understood. There are two main tools to assess and circumvent beam effects. First, we need quantitative metrics to evaluate the system. That could be e.g. particle positions (track movement), PSD or speed of a given process. When such quantitative metrics are established, the beam effects are investigated by evaluating the measures as function of dose rate and total dose. This will also, when possible, include experiments performed in the absence of the electron beam. In this way, it is determined, first how the beam affects the process, and second at what illumination conditions the effect is below the detection limit.

In the two paragraphs above, I have presented some thoughts on beam effects, and how we work to circumvent adverse effects of the electron beam. With the empirical approach we do not try to understand all details of the beam-sample interactions and adverse beam effects[55, 56]. Instead it works to reveal, control and minimize the sample and gas specific beam influence by recording quantitative metrics as a function of dose rate and total dose. When possible, this includes non-illuminated areas.

These guidelines are hopefully reflected in the work presented in the following chapters and any details specific to the individual systems will be described when appropriate.

## 2.4 IMAGE HANDLING AND ANALYSIS

Image handling and analysis has been very important in this work, and I have developed a range of routines using Matlab<sup>4</sup>. In the following chapters, Matlab has been used for image summation (Chapter 4), drift correction (Chapter 6), particle size measurement/segmentation (Chapter 5) and for plotting and aligning data in videos (Chapter 6).

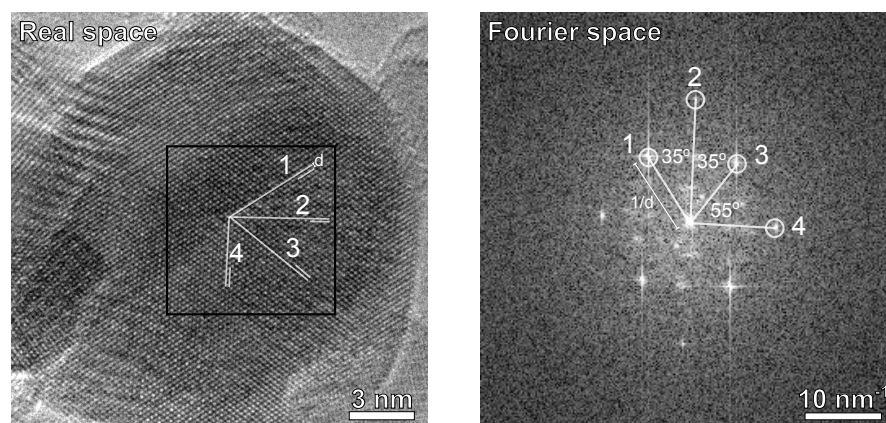
---

<sup>4</sup> [www.mathworks.com](http://www.mathworks.com)

## 2.4.1 2D Fast Fourier Transform

A key method for analyzing HRTEM images is the two-dimensional Fourier transform. By applying the transform, we can view the image represented in reciprocal or frequency space, which gives a direct measure of the periodic structures present in the image. In Fourier space, a periodic structure is represented by the reciprocal lattice vector  $\mathbf{u}$  that was discussed in relation to the contrast transfer function.

A two-dimensional Fourier transform of a HRTEM image is called a diffractogram because it corresponds to the diffraction pattern from a crystal of identical type and orientation as the imaged structure. In this thesis, diffractograms will be called FFTs after the method with which they are created; the Fast Fourier Transform. The analysis of the FFT is analogous to the analysis of a diffraction pattern. In the following we will take a brief look at the extraction of some key values from the HRTEM image and corresponding FFT of a face centered cubic crystal. We will look at the resolved lattice fringes and the angles between the planes. For a cubic crystal, the angles between the real space planes are identical to the angles between the corresponding reciprocal lattice vectors. This makes the interpretation relatively straight forward. For other crystal types, simulation tools can be used to calculate the diffraction pattern.



(a) Real space image of Cu nanoparticle (b) Fourier space representation of the image area in the black square in (a)

Figure 2.13: Cu crystal in a Cu/ZnO catalyst represented by (a) the real space image and (b) the Fourier space image. Periodic structures in (a) are represented as bright dots in (b) at the corresponding spatial frequency and direction.

Figure 2.13a shows a Cu crystal in a Cu/ZnO/Al<sub>2</sub>O<sub>3</sub> catalyst. In this image, lattice fringes are resolved in many directions and the real space image thus corresponds to the atomic columns in the crystal oriented parallel with the electron beam. Four lattice planes, 1, 2, 3 and 4, are marked by lines following rows of atomic columns in

Figure 2.13a. The lattice spacing for these planes is indicated by a second shorter line on the neighboring plane, and for 1 by the value  $d$ . Already from the real space image we would be able to measure the lattice spacings indicated in Figure 2.13a, but the uncertainty would be significant. The great advantage of the FFT is that it takes into account all the lattice fringes in a given direction when calculating the corresponding spatial frequency, thereby significantly increasing the accuracy of the measurement.

Figure 2.13b shows the FFT of the area marked by a black square in Figure 2.13a. Here we see a range of bright spots, where each spot corresponds to a spatial frequency of a periodic structure in the image. Each pixel in the FFT has a real and an imaginary value and the image in Figure 2.13b is the real part. This is sufficient for analyzing the period (lattice spacing) and direction of the resolved lattice planes in Figure 2.13b. The imaginary part carries information about the spatial origin of the individual frequencies and can be used to determine the location of a given lattice spacing in the real space image. This will be used later in Chapter 4.

The spots corresponding to the four lattice planes in Figure 2.13a has been marked in Figure 2.13a, where the distance from the center to the spot is  $1/d$  where  $d$  is the lattice spacing. The relationship between  $d$  and the given lattice plane indicated by the Miller indices  $(h, k, l)$  of the lattice vector is given by[57]:

$$d = \frac{a}{\sqrt{h^2 + k^2 + l^2}} \quad (2.16)$$

where  $a$  is the lattice parameter for the given crystal (0.361 nm for Cu[68]).

Selection rules which are valid for electron diffraction also applies for HRTEM images. The selection rules dictates that some lattice planes will not give rise to lattice fringes in the image just as they will not give rise to spots in the diffraction pattern. This is a further emphasis of the previously made point: the HRTEM image is not an image of the crystal structure, it is the contrast generated by the periodic arrangement in the structure[37]. For a face centered cubic crystal only lattice planes where all indices  $(h, k, l)$  are either odd or even result in spots in the diffraction pattern. This means that the three largest spacings that are resolved for Cu are Cu(111) at  $d = 0.21$  nm, Cu(200) at  $d = 0.18$  nm and Cu(200) at  $d = 0.13$  nm.

To retrieve the lattice spacing of the four planes marked in Figure 2.13a we must measure the distance from the center to the four spots in Figure 2.13b. Here we get that  $1/d$  is 5.07, 7.95, 4.87 and 5.65  $\text{nm}^{-1}$  for spots 1, 2, 3 and 4, which corresponds to lattice spacings  $d$  of 0.20, 0.13, 0.20 and 0.18 nm respectively. From this, it is possible to identify the resolved lattice planes as belonging to the families Cu{111}, Cu{200} and Cu{220}.

Because the resolved lattice extends to the surface, we can use the bulk crystal information to identify the types of surfaces that are exposed by the particle. This is crucial for the discussion about active site and structure-activity in relation to heterogeneous catalysis and it will be important in the interpretation of data presented in Chapter 6.

Finally the angles between the spots in the FFT are a direct measure of the angles between the corresponding real space lattice planes for a cubic crystal such as Cu. The angle  $\theta$  between two lattice vectors with Miller indices  $(h_1, k_1, l_1)$  and  $(h_2, k_2, l_2)$  is given by[37]:

$$\cos(\theta) = \frac{h_1 h_2 + k_1 k_2 + l_1 l_2}{\sqrt{h_1^2 + k_1^2 + l_1^2} \sqrt{h_2^2 + k_2^2 + l_2^2}} \quad (2.17)$$

An analysis of the angles in Figure 2.13b by the use of Equation 2.17 can identify the indices of the lattice planes, not just the families, and can be used to determine the zone axis, which is the crystal direction parallel with the electron beam. For the image in Figure 2.13 the zone axis belongs to the  $\{110\}$  family because this is the only direction that can form a  $90^\circ$  angle with the identified lattice planes.

In Chapter 4 non-cubic oxide crystals are imaged. Here, the identification of lattice planes is performed based on XRD-references[68] and the angles are not taken into consideration.

#### 2.4.2 Cross correlation and image summation

Cross-correlation is a key technique used to calculate the spatial displacement between two different images of the same object[69]. In the context of this work, this has been important for aligning long sequences of images, either for videos (Chapter 6) or for image summation (Chapter 4).

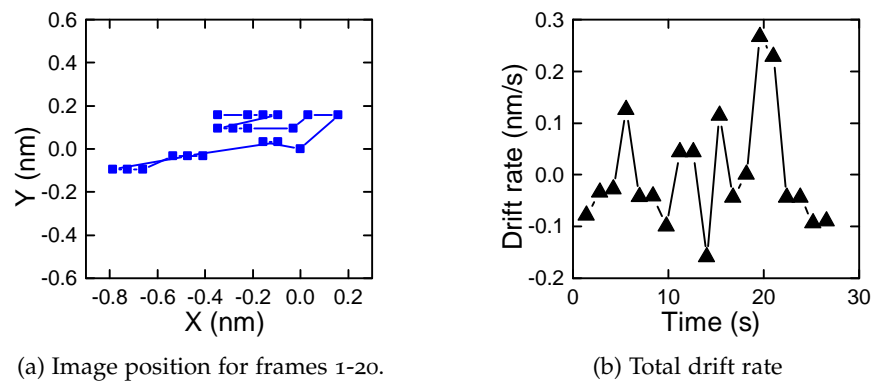


Figure 2.14: Displacement and drift rate for a series of 20 images acquired with 1 s exposure time and 1.4 s/frame.

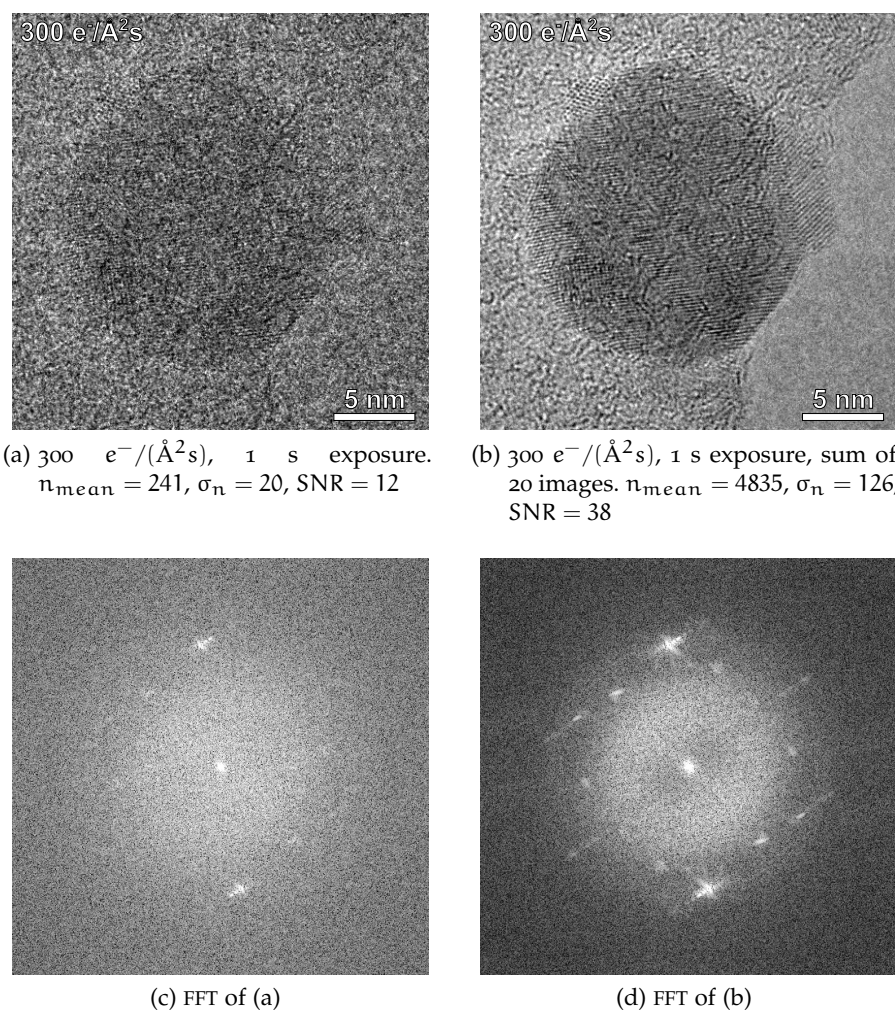
**(a)** Displacement of each frame relative to frame 10 (0,0). **(b)** Drift rate in nm/s calculated by differentiating the absolute displacement.

Figure 2.14 shows the displacement and drift rate calculated using cross correlation for a stack of 20 images. The images were acquired in 2 mbar  $\text{H}_2 : \text{CO} = 1:1$  at 260 °C. Acquisition parameters were 1 s exposure time, 1.4 s per frame (0.4 s used for camera readout) and a dose rate of  $300 \text{ e}^-/(\text{\AA}^2\text{s})$ . For reference, a single frame from this series is shown in Figure 2.15a. Figure 2.14a shows image position on the X and Y axis relative to the central image of the stack positioned at (0,0). The drift is mainly in the X-direction, which is the direction parallel with the holder rod. Image displacement seen as drift, can be caused by charging of the sample, movement of the individual area of the sample being viewed or movement of the entire holder. The drift seen here, a random movement in the direction of the holder rod, suggests that the holder is the cause. The displacement is on the order of 1 nm over an acquisition period of approximately 30 s. For the 20 cm holder rod, 1 nm is a relative movement of  $5 \times 10^{-9} \text{ m/m}$ . Keeping in mind that the thermal expansion coefficient of Inconel (the rod material) is  $12 \times 10^{-6} \text{ m/(m K)}$  and that this was recorded with a sample temperature of 260 °C it is really not too bad!

Figure 2.14b shows the frame-to frame drift rate in nm/s. This should give some idea about how sample drift limits the maximum attainable resolution. For many frames, the rate is below 0.1 nm/s but for some frames the rate is significantly higher at up to 0.3 nm/s.

There may also be drift in the Z-direction which will be seen as a change in focus. Contrary to X,Y-drift this is not easy to correct for, but usually not a problem within the time of a series acquisition such as the one shown here. If however there is a significant Z-drift then it will not be meaningful to acquire a series for summation such as the one shown here. Z-drift can be measured from the FFT of an amorphous material.

After calculating the image drift, the stack of images can be aligned according to the relative image position. In the present case, 20 frames were recorded in order to perform summation and increase the SNR. Figure 2.15a shows a single frame and Figure 2.15c shows the corresponding FFT. The atomic lattice of the Cu particle is certainly visible in Figure 2.15a, as also clearly seen in the FFT, but the overall contrast appears weak. Summation of 20 consecutive frames results in a vast improvement as seen from Figure 2.15b. Interestingly, there is also an improvement in the lattice information in the image as seen from the FFT in Figure 2.15d. This comes from a higher SNR, but also because the drift rate, and thereby maximum resolution, is different for the 20 frames. As seen from Figure 2.14b, some frames show a drift rate above 0.1 nm/s, which then starts to be detrimental for the resolution. By averaging we get a resolution in the summed image similarly to the best frames in the series, equivalent of actively selecting the best images from a series.



(a)  $300 \text{ e}^-/\text{\AA}^2\text{s}$ , 1 s exposure.  
 $n_{\text{mean}} = 241$ ,  $\sigma_n = 20$ , SNR = 12

(b)  $300 \text{ e}^-/\text{\AA}^2\text{s}$ , 1 s exposure, sum of  
 20 images.  $n_{\text{mean}} = 4835$ ,  $\sigma_n = 126$ ,  
 SNR = 38

Figure 2.15: The effect of image summation to improve SNR and image contrast. A series of 20 images were aligned and summed.

**(a)** A single frame from the series. **(b)** The summed image shows a dramatic improvement in contrast and resolution.

## 2.5 CHAPTER CONCLUSION

This chapter has introduced some basic concepts of transmission electron microscopy; how the instrument is constructed and how it is able to form images of nanostructures with atomic resolution. This capability is very important in catalysis research, because the basic functionality of the catalyst nanoparticles is so closely interlinked with the atomic structure. The nanostructures imaged under vacuum conditions is not necessarily representative of the relevant structure during operation because the shape of nanoparticles may respond dynamically to the surrounding environment. In order to counter this limitation, TEMs have been developed to accommodate gas and high temperature, which allows us to image catalysts under *in situ* condi-

tions. I have briefly explained how that is implemented in a modern Titan environmental microscope, both in terms of the instrument itself and the accompanying furnace holder.

When the microscope is operated *in situ*, it is very important to pay close attention to the effect of the electron beam. This is important because the electrons interact strongly with both the sample and the surrounding gas, which may cause various changes to the specimen under study. In an *in situ* experiment, we may want to follow the same particle over time, which makes it even more important to limit the effect of the electron beam. Our overall goal is always to image inherent structures and processes and not those induced by our measuring probe, so it is of uttermost importance to control and limit these effects.

I have given a simple example of how to interpret HRTEM images by considering the Fourier space representation of the image in order to identify lattice planes in an atomically resolved crystal. Finally, by the use of cross correlation, we are able to align and sum large series of images in order to increase contrast. This makes it possible to acquire images with a high total dose, even if the dose rate is limited in order to minimize the effect of the electron beam.



## CATALYST ACTIVATION. REDUCTION OF CU-SILICATE

---

This chapter describes the *in situ* TEM imaging of the reduction of a Cu phyllosilicate precursor to form Cu nanoparticles supported on SiO<sub>2</sub>. This work is submitted for publication at the time of writing[54] and this chapter is based on that paper. There will be references to the paper in this chapter and the manuscript can be found attached to this thesis as Paper III (page 211). The scope of the work has been to provide quantitative data on the particle formation during reduction, as input for modeling of the particle growth kinetics. The reduction of Cu phyllosilicate is very sensitive to the electron beam, and it was therefore important to understand the nature of this influence in order to minimize it before acquiring quantitative kinetic data of the growth process. Modeling was performed by C. Gommès and R. van den Berg, and I was not closely involved in the details of this. The focus of this chapter is thus on the microscopy. Particle size measurements from TEM images were performed by R. van den Berg.

### 3.1 PARTICLE FORMATION FROM A HOMOGENEOUS PRECURSOR

Many catalytic systems are formed from a homogeneous precursor. Here the precursor contains a solid structure that is decomposed and transformed into support and active phase. This transformation happens during a calcination (usually heating in oxidizing gas) or reduction (heating in a reducing gas). A class of catalysts with a solid precursor step in the preparation are the industrially important coprecipitated catalysts, one of these being the methanol synthesis catalyst Cu/ZnO/Al<sub>2</sub>O<sub>3</sub> described later. For that catalyst, the precursor consists of crystals of mixed Cu,Zn,Al hydroxycarbonates, formed after precipitation[70–72]. During calcination, these are broken down to CuO, ZnO and Al<sub>2</sub>O<sub>3</sub>, and finally the CuO can be reduced to Cu.

The process to form the active material is thus a complicated one, but with a significant impact on the properties of the final catalyst. Despite the widely used, and highly optimized preparation from solid precursors, the details known of the formation of the active system are limited [73]. Here we attempt to follow the development of nanoparticles *in situ*, by TEM imaging during the transformation from a homogeneous material to supported nanoparticles. The TEM is particularly well suited for this purpose, because the high spatial resolution gives us the ability to follow the appearance, growth and position of individual nanoparticles. This is contrary to ensemble

averaging techniques such as XRD, which can also be used to follow particle development *in situ* during calcination and reduction [74]. The quantitative information about individual nanoparticles provided by the TEM, will allow a much more detailed modeling, where the model can be fitted to the development of these specific particles rather than ensemble averaged data.

## 3.2 METHODS

### 3.2.1 TEM imaging

All samples were ground in a mortar and dry loaded on to metal TEM grids. For this work we used grids of either stainless steel or gold. After loading, samples were mounted in the Gatan heating holder and inserted into the microscope. For *in situ* experiments, gas was allowed into the e-cell of the microscope and the sample was heated with a rate of 30 °C/min to the desired temperature. Several different experiments were performed, first to evaluate and quantify the effect of the electron beam, and later to acquire quantitative data of particle growth. The exact details of each experiment will be described in the relevant sections.

To minimize the effect of the electron beam under *in situ* conditions, most experiments were run at a very low dose rate of  $1 \text{ e}^-/(\text{\AA}^2\text{s})$ . To get a sufficient signal to noise ratio in the images, they were acquired at relatively low magnification. Images were acquired as 1024 by 1024 pixels and with a pixel size of 0.56 nm/pixel. Total image width was thus 573 nm, allowing for a typical Cu phyllosilicate agglomerate (such as Figure 3.1 on page 44) to fit within one image. For this pixel size and dose rate, the average number of incident electrons on each pixel, for a 1 s exposure time, was 32. The standard deviation in these images was measured to 8, resulting in a SNR of 4. Images in Figure 3.8a on page 54 represent this condition. Due to the low SNR, only particles with diameters larger than approximately 3.4 nm (6 pixels) were clearly distinguishable in the present experiment. Sample areas were also imaged with a higher dose rate of  $5 \text{ e}^-/(\text{\AA}^2\text{s})$  in vacuum after the reduction. Figure 3.8d on page 54 represent this condition.

### 3.2.2 Image analysis

Particles sizes were measured manually using ImageJ. For a typical reduced sample, see Figure 3.3b on page 46. The particles are clearly visible in the image, but due to the inhomogeneity of support and sample, it is difficult to use an automated routine for particle measurements. There are ways to accomplish this[75], but it is more difficult than on planar supports. For a manual counting, typically only

particles positioned in the outermost layers of the agglomerate are measured, since the thicker areas leads to a diffuse contrast and a blurring of the particles.

For a measurement of particle size, typically several hundred particles were measured in different agglomerates. We calculated the optimal bin size for plotting the PSD according to [76, 77] as:

$$\text{bin} = 2 \times (Q_3 - Q_1) \times N^{-1/3} \quad (3.1)$$

where  $Q_3$  and  $Q_1$  are the third and first quartile respectively and  $N$  is the number of particles measured.

The average size and PSD were compared between different samples. To quantify the similarity, we calculated the probability that two PSDs had the same mean value. Such a statistical evaluation is a necessary because there is a limited number of particles available for measurement in the *in situ* regions. The probability was calculated using the ANOVA method<sup>1</sup>. If the probability for the same mean was lower than 2.5% the PSDs were determined to differ significantly. Comparison of PSDs was thus used as a quantitative measure to determine whether the reduction behavior was similar for two different samples reduced under different conditions (pressure, temperature, electron beam).

In order to follow the reduction process in the regions where time-lapsed images were recorded, we developed the measure 'Stage of particle evolution'. Here, 25 particles were selected in the last frame of the time series, and these 25 particle were then traced and measured back in time. At each time step, the 'Stage of particle evolution' was calculated as the mean size, where particles that had not yet emerged, were included in the average with 0 nm.

### 3.3 PRECURSOR MATERIAL

The homogeneous solid precursor used for this experiment was Cu phyllosilicate,  $\text{Cu}_2\text{Si}_2\text{O}_5(\text{OH})_2$  [78]. Our material was prepared by the homogeneous deposition-precipitation procedure as described by Van Der Grift et al.[79]. The material was prepared from colloidal  $\text{SiO}_2$  and Cu nitrate. A detailed description of the preparation is found in [54].

A TEM image of the as-prepared material is shown in Figure 3.1. It is a plate structure, with plates 5-20 nm wide and up to 100 nm long. No CuO particles were seen with these imaging conditions.

<sup>1</sup> ANOVA method in Microsoft Excel's analysis toolpack

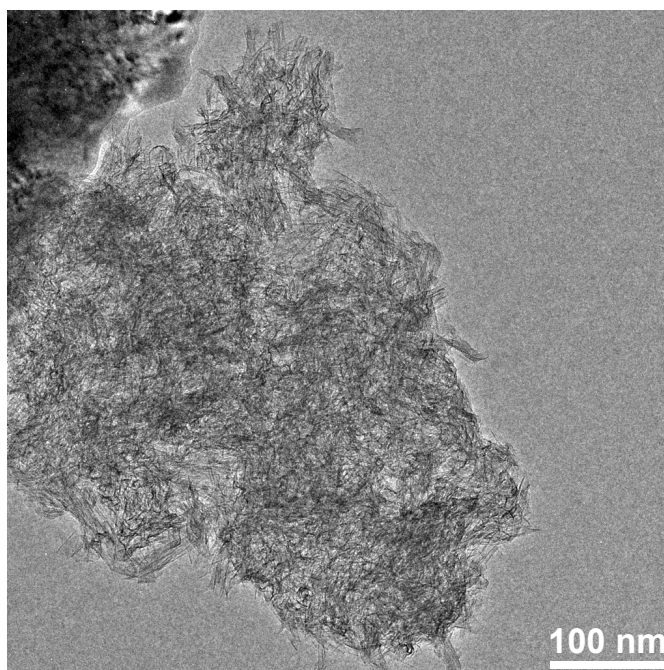


Figure 3.1: TEM micrograph of as-prepared Cu phyllosilicate.

The Cu phyllosilicate was examined with XRD, surface area measurement by  $N_2$  physisorption (BET) and TEM. XRD (Figure 3.2b) showed a mainly amorphous material as expected[78], with a weak peak from chrysocolla, a form of Cu phyllosilicate[78]. Here it is important to note, that no traces of  $CuO$  or  $SiO_2$  were found, meaning that the synthesis resulted in a pure Cu phyllosilicate phase. BET showed a surface area of  $550 \text{ m}^2/\text{g}$ , a sharp increase from the  $100 \text{ m}^2/\text{g}$  for the colloidal  $SiO_2$  ingredient. Both these measurements confirmed that the reaction was completed and that we had the desired material.

#### 3.4 REDUCED MATERIAL

For all experiments, the Cu phyllosilicate was reduced in  $H_2$  gas. First, a temperature programmed reduction (TPR) was performed in a regular plug flow reactor to determine the reduction properties of the material. The result of this is shown in Figure 3.2a.

The Cu phyllosilicate was reduced in a gas of 20%  $H_2$  in Ar by ramping up the temperature at  $2 \text{ }^\circ\text{C}/\text{min}$  to  $500 \text{ }^\circ\text{C}$ . During reduction, the  $H_2$  signal was monitored by mass spectrometry (MS). The hydrogen consumption started at  $220 \text{ }^\circ\text{C}$ , peaked at  $255 \text{ }^\circ\text{C}$  and ceased above  $270 \text{ }^\circ\text{C}$ . In another case, the reduction was performed in a plug flow reactor at a fixed temperature of  $250 \text{ }^\circ\text{C}$  in 20%  $H_2$  in Ar. After reduction the sample was passivated by slowly letting in air, and then transferred to XRD analysis. This clearly showed the appearance of both  $SiO_2$  and Cu crystals (Figure 3.2b).

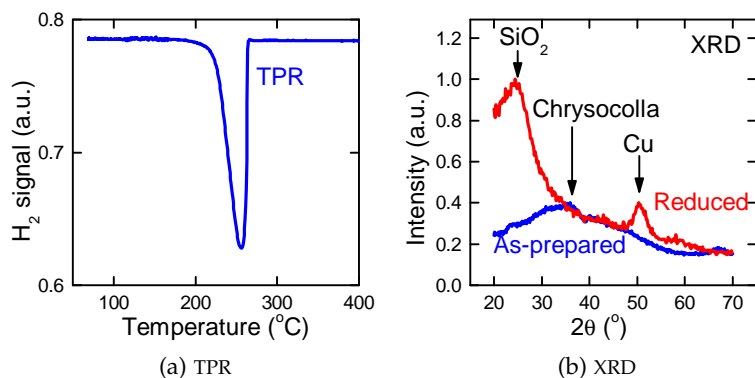


Figure 3.2: Characterization of the reduction behavior of Cu-phyllsilicate. **(a)** Temperature programmed reduction (TPR). **(b)** XRD analysis. The as-prepared sample (blue) shows a weak peak from chrysocolla, a form of Cu-phyllsilicate. After reduction, peaks from SiO<sub>2</sub> and Cu are seen.

With *in situ* TEM, the gas pressure is limited, in this case we used 1 mbar H<sub>2</sub>. This is significantly lower than the 200 mbar used in the plug flow reactor. The lower pressure may entail that a higher temperature is necessary[63]. To investigate this, we first heated four different samples in 1 mbar H<sub>2</sub> to 150, 200, 250 and 280  $^{\circ}C$ . No visible changes were seen after heating to 150  $^{\circ}C$  (4 hours) and 200  $^{\circ}C$  (30 min). At 250  $^{\circ}C$ , after 30 min, nanoparticles clearly started to form, with an average diameter of approximately 5 nm. After 2 hours at 250  $^{\circ}C$ , the particles had grown to an average size of approximately 8 nm. At 280  $^{\circ}C$ , particles had reached the final size of 8 nm after 30 min. Neither maintaining the temperature longer at 280  $^{\circ}C$  or further increasing it to 310  $^{\circ}C$  led to any sample changes. It was therefore concluded that the reduction proceeds to completion after 30 min in the microscope in 1 mbar H<sub>2</sub> at 280  $^{\circ}C$  [54].

The possibility of reducing the sample, and knowing at what temperature to do it, was the first necessary step for proceeding with the experiment. In order to verify the reduction behavior, we compared the end result of reduction in the microscope with the result of reduction in the plug flow reactor. The result of this is shown in Figure 3.3.

To make sure that we were comparing two reduced samples, the sample from the reactor was re-reduced and imaged *in situ* in the microscope (Figure 3.3a). This was done, in case the Cu particles had oxidized after transfer and storage in air. The sample reduced from Cu phyllsilicate inside the microscope is shown in Figure 3.3c. The image was acquired in vacuum, after reduction at 280  $^{\circ}C$  for 30 minutes. The two samples look very similar, with similar particle sizes and density. The edge structure is different though; the sample reduced in the microscope has maintained more of the plate structure, as seen around the edge. This difference is most likely due to the

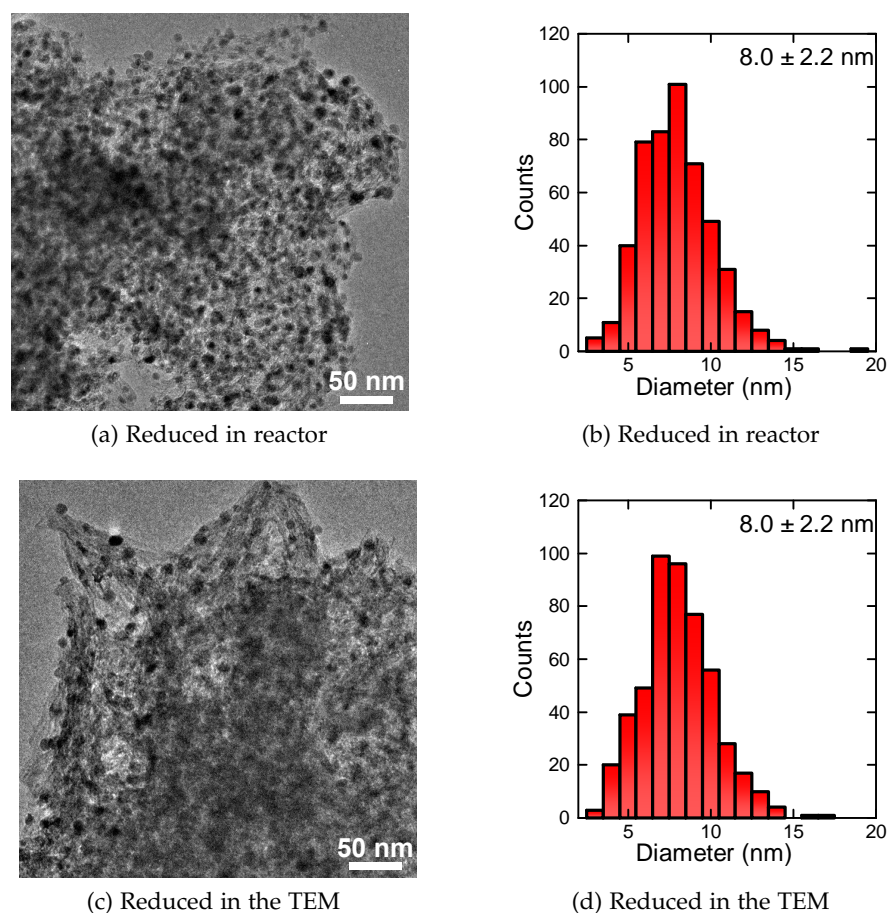


Figure 3.3: Comparison between reduction in a plug flow reactor and in the microscope.

**(a)** TEM micrograph of Cu phyllosilicate after reduction in plug flow reactor (20 % H<sub>2</sub> in Ar, 250 °C) and re-reduction in the TEM (1 mbar H<sub>2</sub>, 250 °C). **(b)** Histogram of particle diameters measured in 17 images of the same sample as (a). **(c)** TEM micrograph of Cu-phyllosilicate after reduction in the TEM (1 mbar H<sub>2</sub>, 280 °C). **(d)** Histogram of particle diameters measured in 17 images of the same sample as (c).

mechanical forces and different local environment in the plug flow reactor.

To quantitatively compare the reductions, 500 particles were measured in images from 17 regions for each sample. The histograms are shown in Figure 3.3b and Figure 3.3d. These show that mean particle diameter (8.0 nm) and standard deviation (2.2 nm) were identical. The final Cu nanoparticle characteristics are thus independent of H<sub>2</sub> pressure and temperature for reduction in these two setups.

With the information above, appropriate pressure and temperature for reduction in the microscope were determined, and it was validated that reduction under 'microscope conditions' is representative for conditions endured in the plug flow reactor. This is the first prereq-

quisite for the *in situ* experiment, where the process is to be recorded with time-lapsed TEM images. The second prerequisite is to find conditions where the influence of the electron beam is minimized. This will be the subject of the next section.

### 3.5 ASSESSING THE BEAM EFFECT

In the following I will explain how we developed a routine for safe operation with minimal influence of the electron beam. To evaluate the effect of the electron beam, it is necessary to have quantitative metrics to evaluate it from. Here we have chosen two: The first quantitative metric is the possible observation of visible changes during illumination by electrons. If this is observed, the illuminated area is compared to a non-illuminated in order to evaluate if the electron beam is responsible for the observed changes. In the present case, we study a dynamical phenomena, so the sample is expected to change between consecutive images, and it is therefore necessary to compare with a non-illuminated reference area. We expect particle formation during the experiment, so the second quantitative metric is a comparison of the final PSD for illuminated and non-illuminated sample areas. This is a way to assess whether the electron beam has influenced the reduction process.

#### 3.5.1 *Beam in H<sub>2</sub>*

In the first experiment, we assessed the direct effect of the electron beam on the sample in an H<sub>2</sub> atmosphere. In order to decouple the effect of the electron beam from thermal reduction, this was done at 150 °C. At this temperature, no particle formation was seen in non-illuminated reference areas[54].

After heating to 150 °C and waiting for drift stabilization, 5 different areas were investigated with 5 different dose rates. Each region was continuously illuminated for approximately 20 minutes while time lapsed TEM images were acquired. This was done for electron dose rates of 1, 5, 10, 20 and 100 e<sup>-</sup>/(Å<sup>2</sup>s).

At these conditions, particles quickly started to emerge under the electron beam. For an identical experiment with no H<sub>2</sub>, particle formation was very limited. This indicates that the mechanism behind beam induced reduction is activation and presumably dissociation of H<sub>2</sub> molecules by the high energy electrons, and not direct reduction by the electron beam. In another study, we have demonstrated reduction of Cu by atomic hydrogen[63]. This will be discussed in Chapter 4.

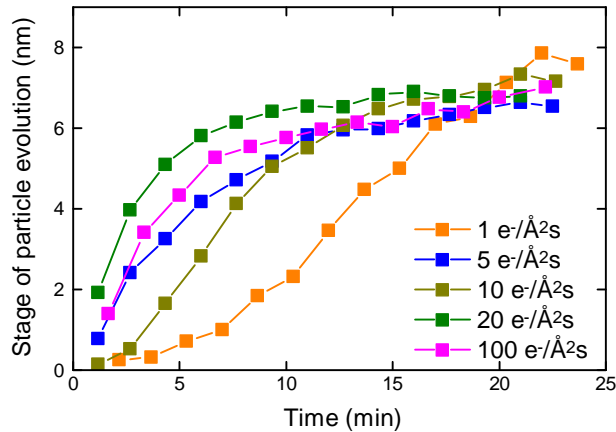


Figure 3.4: Evolution of particle size during beam induced reduction. Stage of particle evolution for dose rates 1, 5, 10, 20 and 100  $e^-/(\text{\AA}^2\text{s})$ . 1 mbar  $\text{H}_2$ , 150 °C.

The stage of particle evolution is plotted in Figure 3.4. For the dose rates 5, 10, 20 and 100  $e^-/(\text{\AA}^2\text{s})$ , the particle evolution was similar regardless of dose rate. Only the lowest dose rate of 1  $e^-/(\text{\AA}^2\text{s})$  differs with a significantly lower rate of particle nucleation and growth. This could indicate that for any dose rate at or above 5  $e^-/(\text{\AA}^2\text{s})$ , a sufficient amount of excited  $\text{H}_2$  or H-radicals is generated in order for another step in the reduction process to become rate-limiting.

The conclusion to take from this experiment is that it is impossible to completely remove beam induced reduction for this sample in the presence of  $\text{H}_2$  gas. The strategy must therefore be to minimize it by first of all using the lowest possible dose rate, in this case 1  $e^-/(\text{\AA}^2\text{s})$ . A dose rate lower than this would compromise the image SNR or require the use of even lower magnification. Since we cannot completely remove the beam contribution, it must be ensured that the thermal reduction proceeds significantly faster in order to minimize the influence of the electron beam on the process.

### 3.5.2 Beam pre-reduction

TEM acquisition *in situ* during the reduction process requires the use of a very low electron dose rate. A typical approach would therefore be to acquire high quality images of the region of interest before and after the reduction. High quality could mean higher dose rate, or perhaps longer exposure time. Illuminating the sample before reduction could however have an effect on the reduction process, if the interaction with the electron beam in vacuum would alter the Cu phyllosilicate.

To investigate the effect of electron illumination prior to reduction, we illuminated and imaged 5 different regions in one sample, with dose rates of 1, 5, 10, 20 and 100  $e^-/(\text{\AA}^2\text{s})$ . Each region was illumi-

nated for approximately 2 min. No visual changes were seen during the 2 minutes for dose rates at or below  $20 \text{ e}^-/(\text{\AA}^2\text{s})$  [54]. After this, 1 mbar  $\text{H}_2$  was allowed into the e-cell and the temperature was raised to  $280 \text{ }^\circ\text{C}$  and held for 30 min before cooling down and evacuating. Each region was imaged again, as well as reference regions for comparison. Images of all regions are shown in Figure 3.5. By comparison to the reference (Figure 3.5a), it is clear that pre-illumination results in larger Cu particles, particularly evident for pre-illumination with the highest dose rate (Figure 3.5f).

Figure 3.6 shows PSDs from the images in Figure 3.5. For the reference (a), particles were measured in multiple regions. As the dose rate is increased, the PSDs show an increase in average size, as well as a broadening towards larger particles (b-f). For pre-illumination with a dose rate of  $100 \text{ e}^-/(\text{\AA}^2\text{s})$  (Figure 3.6f) there is a significant number of large nanoparticles with sizes of 15 nm and above.  $100 \text{ e}^-/(\text{\AA}^2\text{s})$  is the highest applied dose rate here and the effect of it is significant, but it is worth noting that  $100 \text{ e}^-/(\text{\AA}^2\text{s})$  still be considered very low dose for normal TEM operation.

The implication of this finding is quite significant. What Figure 3.5 and Figure 3.6 show, is that illumination in vacuum, even with a very low dose rate of  $1 \text{ e}^-/(\text{\AA}^2\text{s})$ , will strongly alter the end result of the reduction, even if no changes are seen to the sample during vacuum imaging. This underlines several important aspects worth remembering for *in situ* TEM. First, that each sample type is individual when it comes to beam effects, and that it is import to investigate these as part of the experiment. Second, for *in situ* experiments such as this where we want to follow a region over time, it important to have a metric for comparison with unilluminated areas. In the present case, it is the final average size and the shape of the PSD.

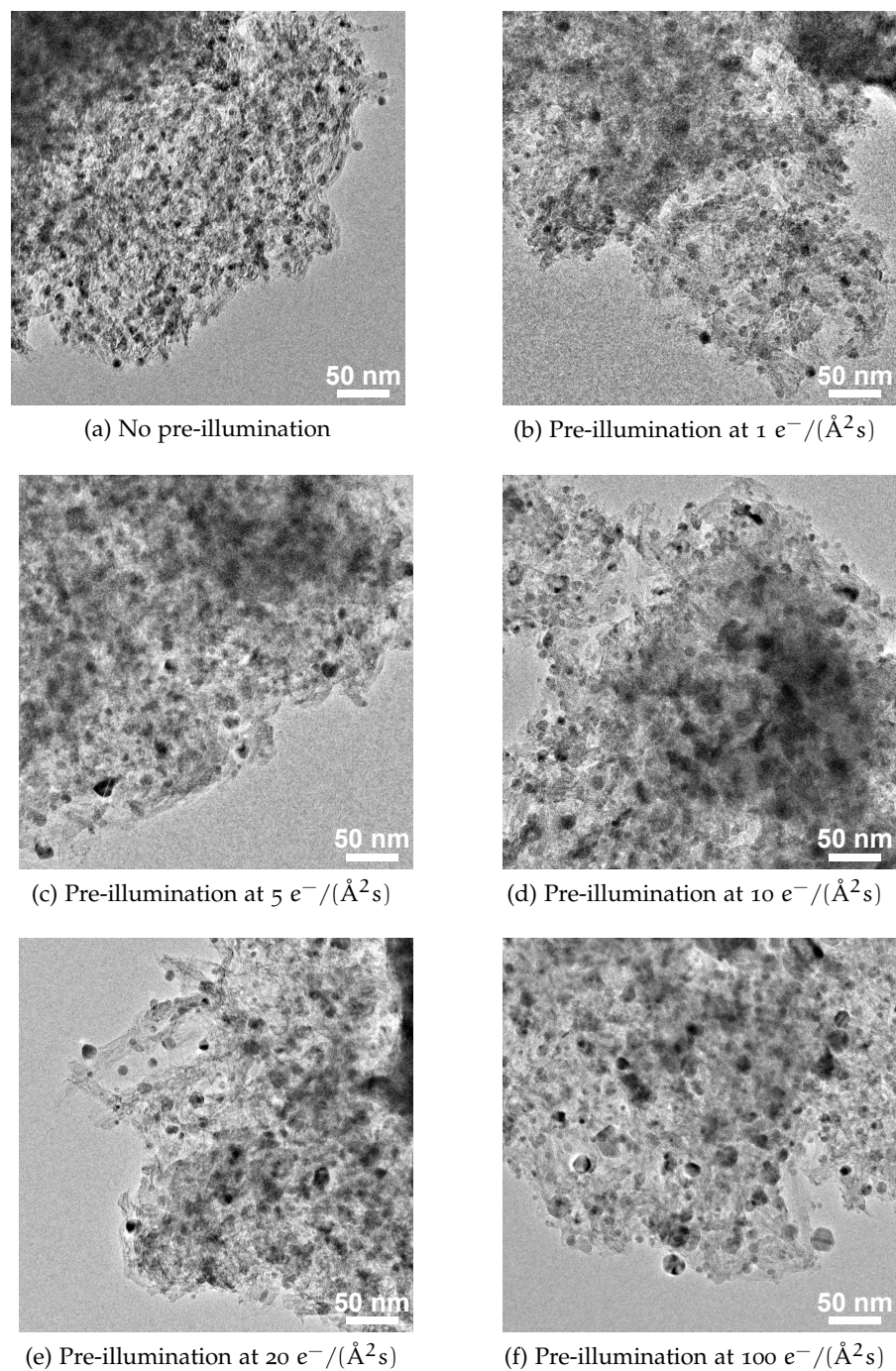


Figure 3.5: The effect of electron illumination prior to reduction. All images from different regions of the same sample. Each region was illuminated for 2 minutes in vacuum, then the sample was reduced in 1 mbar  $\text{H}_2$  at  $280^\circ\text{C}$  for 30 min. No electron illumination during reduction.

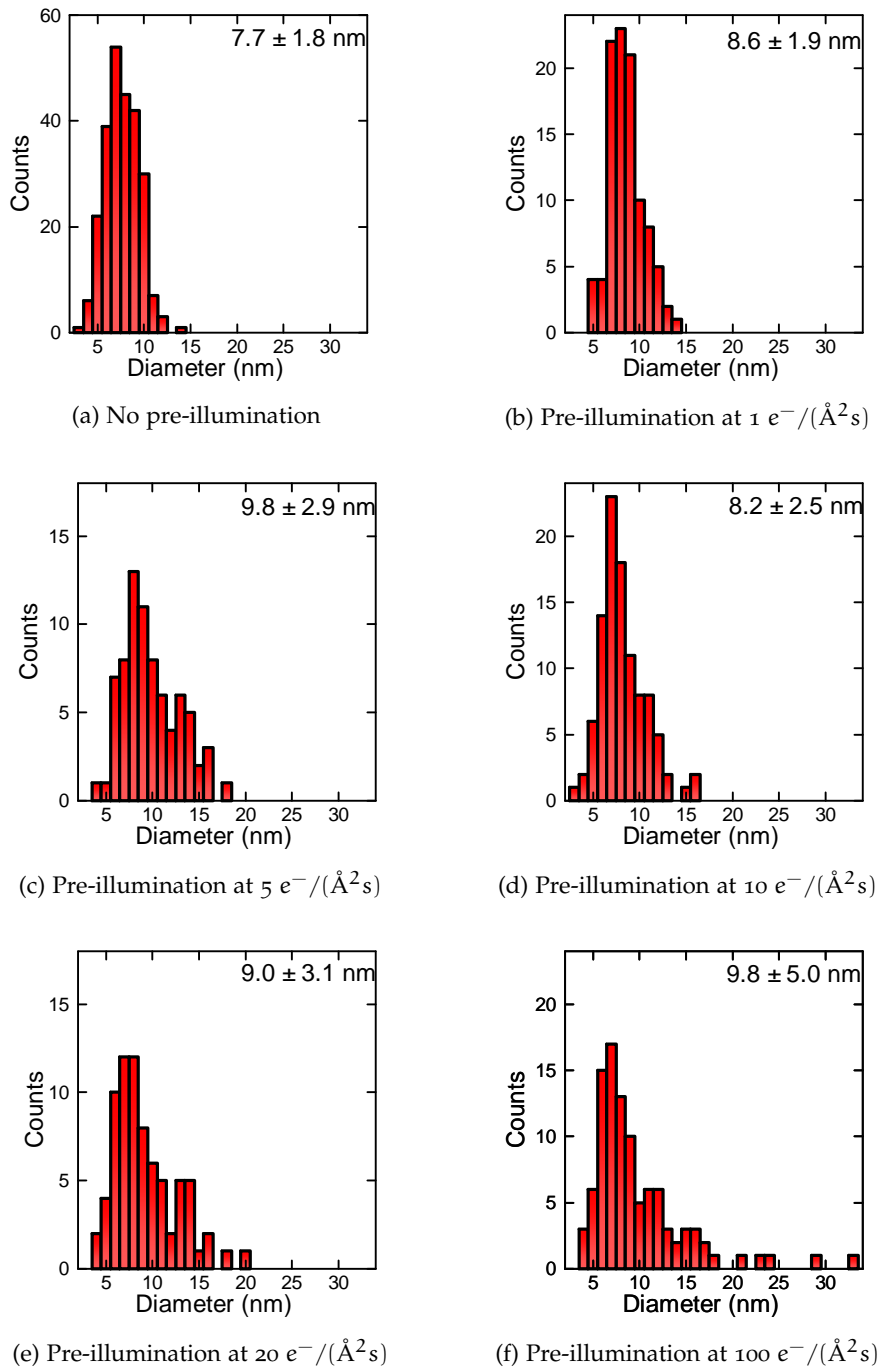


Figure 3.6: The effect of electron illumination prior to reduction. PSDs measured from the images in Figure 3.5 Each region was illuminated for 2 minutes in vacuum, then the sample was reduced in 1 mbar  $\text{H}_2$  at 280 °C for 30 min. No electron illumination during reduction.

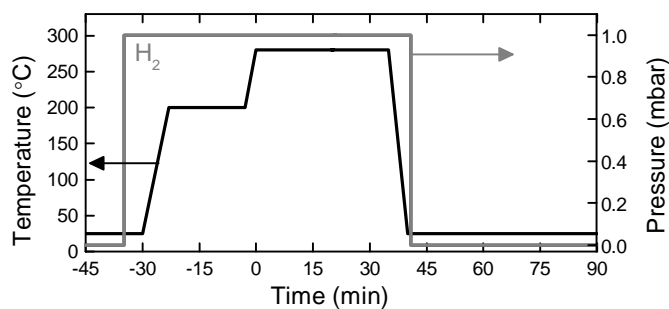
3.6 IMAGING THE REDUCTION PROCESS *in situ*

With the experiments listed above, we start to have an idea of some important properties that characterize the effect of the electron beam on the reduction of Cu phyllosilicate:

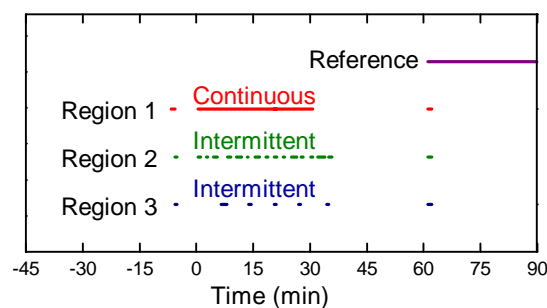
- Reduction at 280 °C in 1 mbar H<sub>2</sub> proceeds to completion in 30 minutes.
- Beam induced reduction is inevitable in H<sub>2</sub> atmosphere. At 1 e<sup>-</sup>/(Å<sup>2</sup>s) the rate is limited.
- Illumination in vacuum will have a profound effect on the end result.

With this information, we can set up a measurement scheme that will allow us to track the reduction over time, while still keeping the effects of the electron beam to a minimum. The measurement scheme is presented in Figure 3.7, for gas and temperature (Figure 3.7a) and electron illumination (Figure 3.7b). Time 0 is when the temperature reaches 280 °C.

After inserting the sample in the microscope, 1 mbar H<sub>2</sub> is allowed into the e-cell and the temperature is increased to 200 °C. At this temperature, no reduction of the Cu phyllosilicate takes place[54]. At 200 °C regions of interest are located at very low magnification and extremely low dose rate (<0.1 e<sup>-</sup>/(Å<sup>2</sup>s)). The reason to go to 200 °C first is to allow the holder to stabilize at this temperature, which limits the drift after the final temperature step. The temperature is then increased to 280 °C (30 °C/min) and immediately after this, imaging is started with a dose rate of 1 e<sup>-</sup>/(Å<sup>2</sup>s). In the first few minutes after the temperature increase, slight drift was experienced, but acquisition times shorter than 1 s was not possible, due to the low dose rate. Three regions were imaged in two samples. In the first sample one region ('Region 1') was continuously illuminated while time lapsed TEM images were acquired. In the other sample, two regions were illuminated intermittently, one with high frequency ('Region 2') and one with low frequency ('Region 3'). The actual illumination times were recorded and are plotted in Figure 3.7b. The idea behind varying the illumination time in the dynamic experiment, is that this will give a clear idea whether the observations are affected by beam induced reduction. If it is the case, a correlation between particle formation and illumination time/total dose would be expected.



(a) Pressure and temperature



(b) Electron illumination

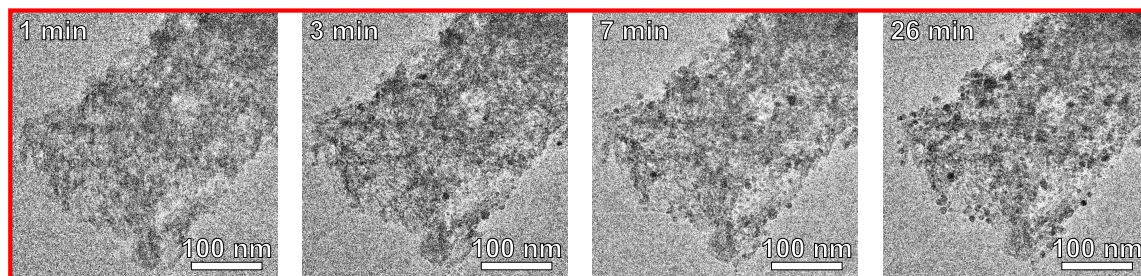
Figure 3.7: Experimental procedure for the reduction of Cu phyllosilicate in 1 mbar  $\text{H}_2$  with minimum beam influence. Temperature is raised to 200 °C, drift is stabilized, then temperature is raised to 280 °C where the reduction process initiates. Three regions are followed in two samples. Dose rate is  $1 \text{ e}^-/(\text{\AA}^2\text{s})$  during  $\text{H}_2$  exposure. Region 1 is continuously illuminated, Region 2 and 3 are intermittently illuminated. After cooling all regions, as well as reference regions, are imaged with  $5 \text{ e}^-/(\text{\AA}^2\text{s})$ .

For all three regions, time lapsed images resulted in movies of the particle formation<sup>2</sup>. Figure 3.8 shows selected frames from these movies. Figure 3.8a shows frames from Region 1, where the first frame was recorded after 1 min. At this time, no nanoparticles have formed. In the second frame, recorded after 3 min, particles are clearly visible. After 7 min most particles have formed and after 26 min, they have grown to their final size. Region 2 (Figure 3.8b) shows a similar pattern, with a few particles formed already after 1 min. This concerns particles larger than the detection limit of approximately 3 nm, so particles smaller than that may have formed already at 1 min without being resolved in the images. The first frame of Region 3 (Figure 3.8a) was recorded after 7 min where a significant number of particles had formed. Finally, Figure 3.8d shows a previously unilluminated reference area after 30 min at 280 °C.

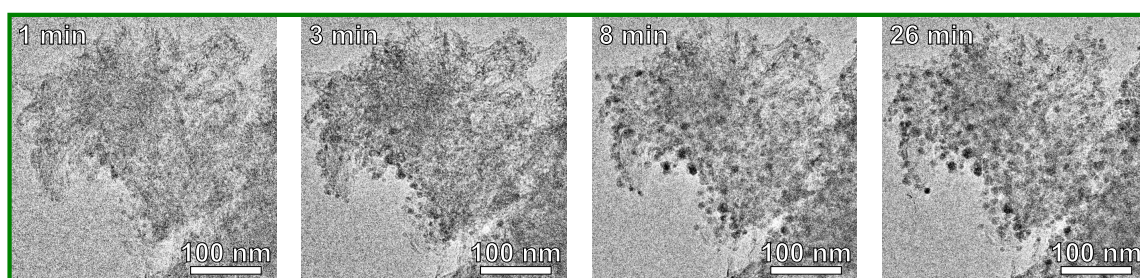
Some important conclusion to take from the dynamic experiment are the following: The critical diameter for nucleation is 3 nm (detection limit) or smaller. Once particles have nucleated, as seen from the

<sup>2</sup> Movies will be available online when the paper is published.

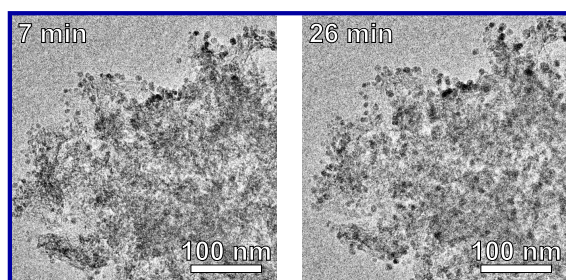
images, they are immobile, which implies that particle growth does not proceed via particle migration and coalescence, but rather via attachment of smaller Cu species that are able to diffuse on the support. Cu particles form homogeneously over the sample, with no preferred sites for nucleation.



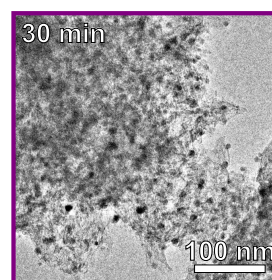
(a) Region 1 (Continuous illumination)



(b) Region 2 (Intermittent illumination)



(c) Region 3 (Intermittent illumination)



(d) Reference region (No illumination)

Figure 3.8: Frames from time-lapsed movies acquired during reduction of Cu phyllosilicate in 1 mbar  $H_2$  at 280 °C.

**(a)** Region 1 observed with continuous illumination at  $1 e^-/(\text{\AA}^2s)$ . **(b)** Region 2 observed with intermittent illumination at  $1 e^-/(\text{\AA}^2s)$ . Time interval approximately 2 min. **(c)** Region 3 observed with intermittent illumination at  $1 e^-/(\text{\AA}^2s)$ . Time interval approximately 6 min, first frame acquired after 7 min. **(d)** Reference area, previously unilluminated. Final PSDs for these areas are shown in Figure 3.10

In order to quantify and compare the development during reduction, the stage of particle evolution was calculated for each region during the process. As previously described, this was done by selecting 25 particles in the final frame of the experiment. These 25 particles were then tracked back in time, and in each frame their diameter was measured. The stage of particle evolution was calculated as the aver-

age particle size where particles that had not yet emerged were taken as 0 nm. The result of this is plotted in Figure 3.9. We immediately notice that all three regions develop in exactly the same way. In particular, it should be noted that when Region 3 is imaged the first time after 7 min, it has reached the same stage as Regions 1 and 2. This is a very strong evidence that the effect of the electron beam in these experiments is negligible. If that was not the case, we would have seen a difference between the three regions depending on the accumulated dose. For comparison, Figure 3.9 also shows the development in particle evolution for the purely beam induced reduction at 150 °C, also for a dose rate of  $1 \text{ e}^-/(\text{\AA}^2\text{s})$ . Here the particle formation is much slower than for the thermally induced reduction.

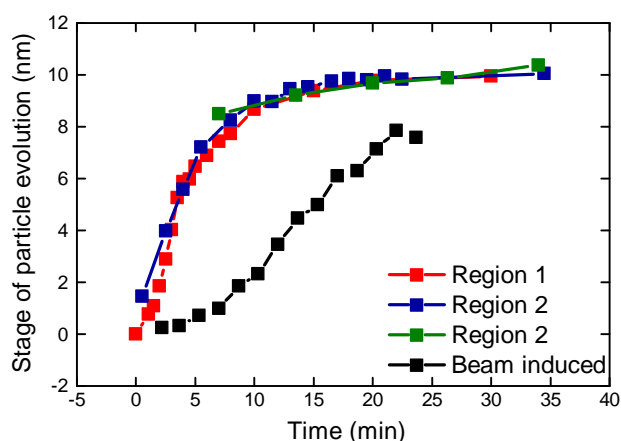


Figure 3.9: Stage of Cu particle evolution during reduction in 1 mbar  $\text{H}_2$  at 280 °C. Measured from TEM images acquired *in situ* as presented in Figure 3.8. For comparison, the purely beam induced reduction at the same dose rate is shown (taken from Figure 3.4)

As a final evaluation of the possible beam influence, we look at the resulting PSD of the three regions and at reference regions on one sample (Figure 3.10). All regions had similarly shaped PSD and the deviations of the mean value were within the statistical error for these limited ensembles.

With this experiment we have provided high quality time lapsed data of the reduction process. Due to careful considerations of the effect of the electron beam, this data is inherent to the thermally driven reduction process in  $\text{H}_2$  gas. The beam influence was not detectable for either continuous or intermittent illumination. We have therefore used the data from Region 1 (continuous illuminations) as a basis for modeling, since this data provides the highest possible time resolution of the process.

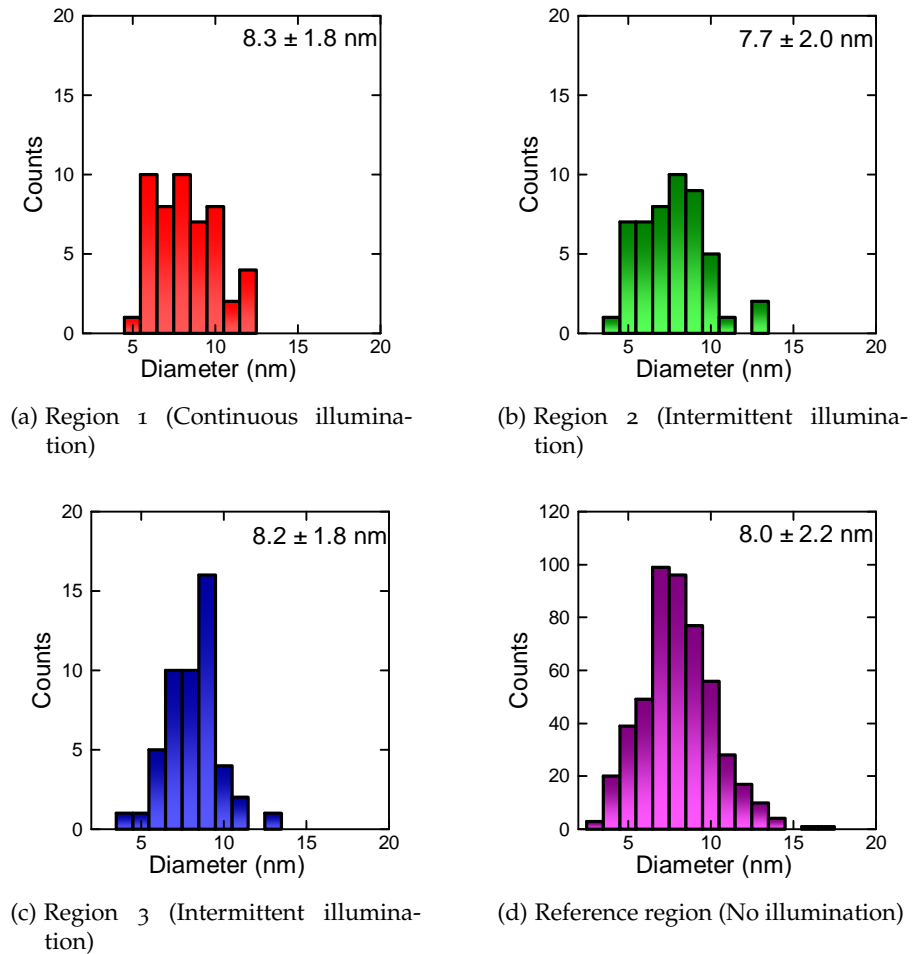


Figure 3.10: PSDs for the three regions imaged *in situ*, as well as reference regions from one sample. Images for size distributions were acquired in vacuum with  $5 e^-/(\text{\AA}^2\text{s})$  after reduction.

(a) Region 1 observed with continuous illumination at  $1 e^-/(\text{\AA}^2\text{s})$ . (b) Region 2 observed with intermittent illumination at  $1 e^-/(\text{\AA}^2\text{s})$ . Time interval approximately 2 min. (c) Region 3 observed with intermittent illumination at  $1 e^-/(\text{\AA}^2\text{s})$ . (d) Reference area, previously unilluminated.

### 3.7 PARTICLE GROWTH MODELING

This section describes some key results from the particle growth modeling[54]. The sizes of 25 individual particles were tracked in Region 1 over time and used as the basis for modeling growth. The *in situ* data provides information about the nucleation time of each individual particle as well as the subsequent growth. The information obtained from the microscopy was compared with two kinetic models; a classical nucleation and growth model and an autocatalytic model.

The nucleation-and-growth model[80] assumes that Cu is reduced from the phyllosilicate and fed to a reservoir of mobile copper species

that is described by a mean field. Particles then nucleate when the concentration of Cu species on the support exceeds a saturation level and these particles grow by the addition of Cu species from the reservoir. This model is based on a mean-field approximation; that the concentration of Cu species is uniform over the support, except for a boundary layer around each particle. The size evolution of all particles was fitted to the model with the two adjustable parameters: kinetic constant and diffusion coefficient (Figure 3.11).

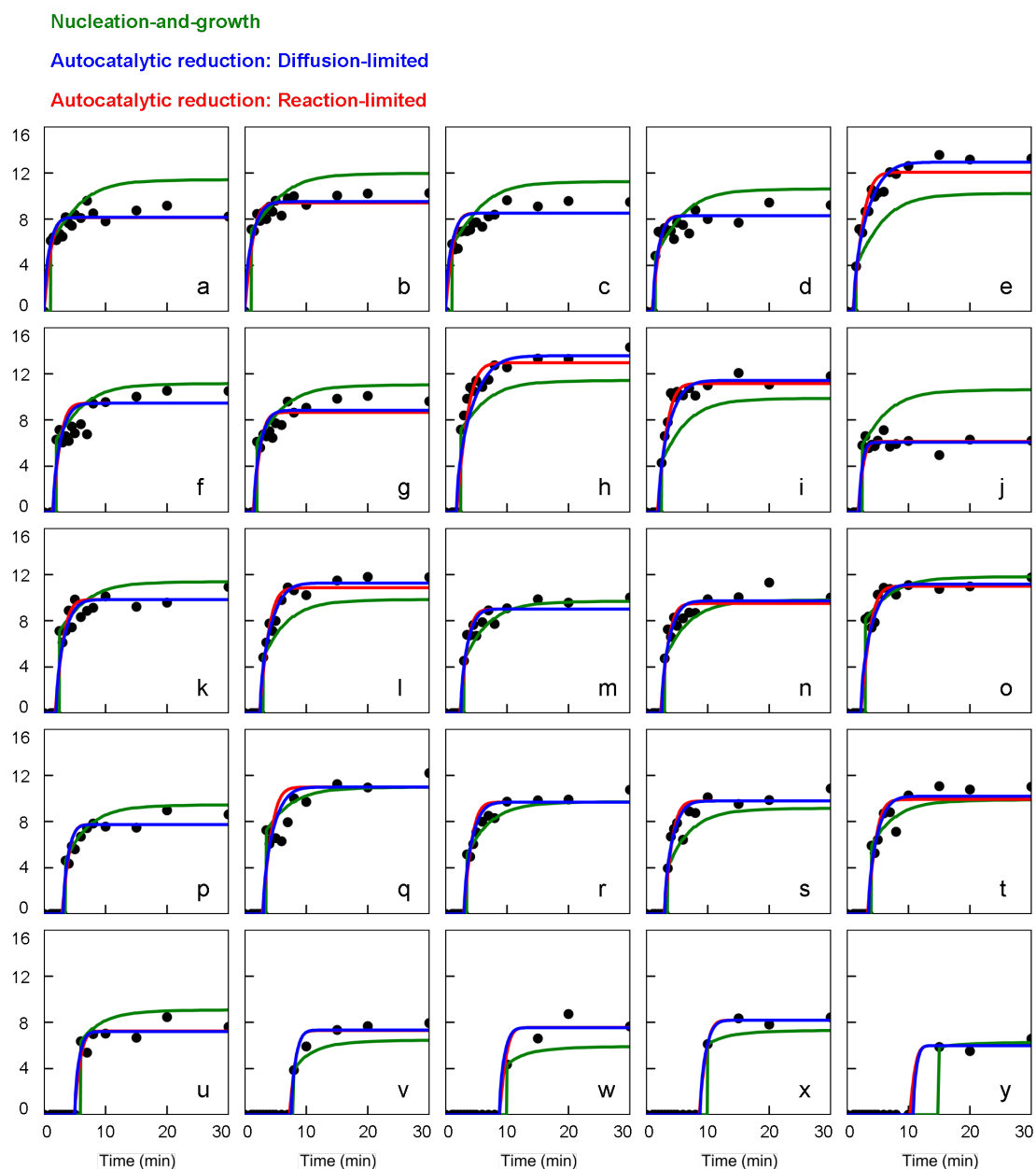


Figure 3.11: Size evolution of 25 particles in Region 1. The measured particle sizes are shown as black dots. The fitted nucleation and growth model is shown in green and the fitted autocatalytic model is shown in red (reduction-limited) and blue (diffusion-limited).

The fitted nucleation-and-growth model describes the data reasonably well as seen in Figure 3.11, where the fitted data (green lines) is plotted together with the measured particle sizes (black dots). The result of the fit however has some physically improbable implications. We observe the first nucleation events after a few minutes, but in the model, the reduction takes place from time zero. This has the consequence that the concentration of Cu species reaches a very high value of approximately one monolayer in the early phase of the experiment. Moreover, the fitted diffusion coefficient is very small ( $\sim 5 \times 10^{-19}$  m<sup>2</sup>/s) compared to typical values for surface diffusion which are  $10^{-5}$  -  $10^{-8}$  m<sup>2</sup>/s [54]. Another inconsistency between the model and our data is the relationship between final size and nucleation time. The nucleation-and-growth model builds on a mean field approximation, which implies that the final particle will depend only on the nucleation time. This is however not what we observe; there is a considerable scatter in the final particle size as a function of nucleation time. Examples of this is Figure 3.11e and Figure 3.11j where the final particle size is much larger and smaller than what the model predicts based on the nucleation time.

To respond to the inconsistencies in the simple nucleation-and-growth model, a second model was developed based on autocatalytic reduction of Cu[81]. Here, the reduction is slow during the nucleation period and fast during the growth period, because the metallic particles themselves dissociate hydrogen to catalyze the reduction of Cu from the phyllosilicate. Since the mean field approximation clashes with the observed scatter between nucleation time and size, it was assumed that each particle is associated with a limited capture zone, a so-called box, which will define its final size. This is consistent with the structure of the Cu phyllosilicate that consists of plates 5-20 nm wide and up to 100 nm long. It seems logical that diffusion is easier within such a plate than over the interface between adjacent plates. By using the density of Cu in the phyllosilicate structure, it can be calculated that an 8 nm particle contains an amount of Cu corresponding to a box size of 17 nm.

Before nucleation, it is assumed that all Cu ions in a box have an equal probability for reduction and subsequent nucleation. This type of phenomena can be described by Poisson statistics, so it is assumed that the nucleation time as a function of box (particle) size follows a Poisson distribution. A result of this is that particles of larger final size have a higher probability to nucleate early than smaller particles. Figure 3.12 shows the cumulative probability that a particle has nucleated at a specific time as a function of its final size. This is plotted together with the experimental data and we see that most of the particles have a probability between 0.1 and 0.9 of having nucleated at the observed time. The Poisson model therefore captures both the re-

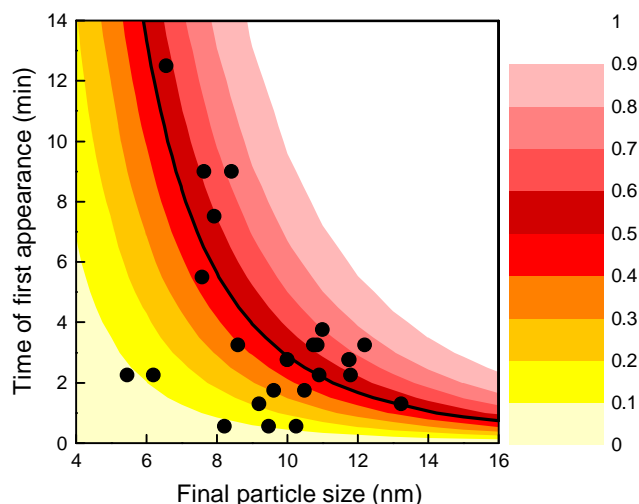


Figure 3.12: Plot of time of first appearance as a function of the final particle size as measured in the *in situ* TEM data from Region 1. The colored regions indicate the cumulative probability, according to Poisson statistics, for nucleation to occur at a specific time for a given final particle size.

lation between nucleation time and final size as well as the scatter in the data.

As soon as a nucleus has formed, the autocatalytical reduction is assumed to start and from there on the development in particle size is described by a growth model. Two parameters could be limiting the growth: i) diffusion of Cu ions in the solid to the particle (diffusion-limited model) or ii) reduction at the particle-support interface[82]. The model was fitted for both cases and the result is shown in Figure 3.11 as blue and red lines for the diffusion and reaction limited model respectively.

In the reaction limited model, the rate of reduction is assumed to be proportional to the concentration of  $\text{Cu}^{2+}$  ions in the box. Here, the kinetic constant was  $0.45 \text{ nm/min}$  for the best fit which corresponds to a growth rate of about 2 atomic layers per minute.

In the diffusion limited model the diffusion constant was found to be  $4.5 \times 10^{-19} \text{ m}^2/\text{s}$  which is typical for solid state diffusion[83].

Both versions of the auto-catalytic model describes the observations well (Figure 3.11) and the fitted parameters are of reasonable value. It is therefore not possible to distinguish between the two. From Figure 3.11 we see that the autocatalytic model described our observations better than the classical nucleation-and-growth model. Based on our observations and modeling it is therefore suggested that the mechanism behind the reduction of Cu phyllosilicate to Cu nanoparticles on silica is autocatalytic. It is plausible that the initial growth phase is reaction limited due to the high concentration of  $\text{Cu}^{2+}$  ions at this time. Then as the particle grows and the concentration of  $\text{Cu}^{2+}$  decreased, the mechanism is likely to become diffusion limited.

## 3.8 CHAPTER CONCLUSION

*In situ* TEM was used to follow the reduction of Cu phyllosilicate in  $H_2$  at 280 °C to form Cu particles supported on  $SiO_2$ . This is representative for a class of catalyst systems where the active nanoparticle phase is formed from a solid homogeneous precursor. The reduction inside the microscope was found to be representative of the reduction in a plug flow reactor at higher pressure, because the final particle size distribution (PSD) was identical for the two methods. The electron beam was found to have a profound effect on the reduction inside the microscope. The temporal development of the sample (particle formation) and the final PSD was used as quantitative measures to assess the effect of the electron beam and the effect of temperature on the reduction process. The conclusions from this was the following:

- No particle formation at 150 or 200 °C in 1 mbar  $H_2$ . At 250 °C particles formed slowly and the process was not complete after 30 min. At 280 °C the reduction proceeds faster and particle formation was complete after 30 min.
- At 150 °C in 1 mbar  $H_2$  particles formed during illumination by the electron beam. For dose rates 5, 10, 20 and 100  $e^-/(\text{Å}^2\text{s})$  particles formed quickly and completed within 10 min. At 1  $e^-/(\text{Å}^2\text{s})$ , particle formation was significantly slower.
- Little or no particle formation was observed during electron illumination in vacuum.
- Electron illumination at room temperature in vacuum before reduction increased the mean particle size after reduction. This was the case for dose rates 1, 5, 10, 20 and 100  $e^-/(\text{Å}^2\text{s})$ . Mean particle size increased with increasing dose rate.

Based on these findings, we developed a procedure that allowed us to image the thermally driven reduction process with minimal influence of the electron beam. The key points were to avoid illumination in vacuum and to reduce under conditions where the thermal reduction was significantly faster than the beam induced. Following this procedure allowed us to obtain quantitative time resolved data of particle formation and growth. This was done for three illumination schemes of varying total dose and the particle formation was found to be independent of this. This directly shows that the process proceeded with minimal influence of the electron beam.

The particle formation was modeled by fitting to the experimentally observed nucleation and growth of 25 individual particles. The process was found to be well described by an autocatalytic model where the initial nucleation is slow and subsequent growth is fast because the already formed particles catalyze further reduction by  $H_2$ .

## CATALYST ACTIVITY. THE METHANOL SYNTHESIS CATALYST

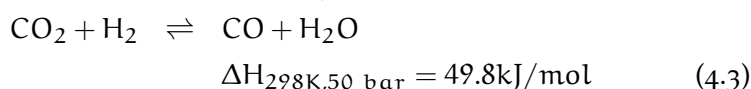
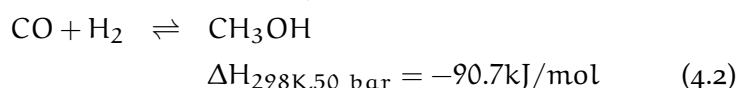
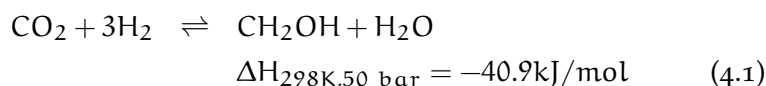
---

This chapter presents investigations of the atomic structure and catalytic activity of the methanol synthesis catalyst. Experiments were performed in collaboration with Christian Holse and Anders Nierhoff at DTU. They performed specialized sample preparation and spectroscopy at UHV conditions which we found to be a fantastic complement to *in situ* TEM. This chapter is mainly based on our recent paper attached to this thesis[63].

### 4.1 THE METHANOL SYNTHESIS REACTION

Methanol, CH<sub>3</sub>OH or MeOH, is the simplest alcohol and a very important industrial chemical with a yearly production of over 40 megaton[84]. Methanol is an important precursor chemical in the production of other chemicals such as formaldehyde which is again used in the production of e. g. plastics and paints.

The modern methanol synthesis process was developed in the 1960s by ICI. It proceeds over a Cu/ZnO/Al<sub>2</sub>O<sub>3</sub> catalyst at 230 °C and 50 to 100 bar[70, 84], and produces MeOH from a synthesis gas (syngas) containing CO, CO<sub>2</sub> and H<sub>2</sub>. The methanol synthesis reaction can be described by the three reactions[70]:



where Equation 4.1 and Equation 4.2 describe methanol synthesis from CO<sub>2</sub> and CO respectively, and Equation 4.3 is the reverse water gas shift reaction. The three reactions are inter-dependent and any two of the three gives a complete thermodynamical description of the system.

Figure 4.1 shows *in situ* TEM images of the catalyst at low and high magnification. It is comprised of spheres of metallic Cu interlinked by more irregular crystals of ZnO.

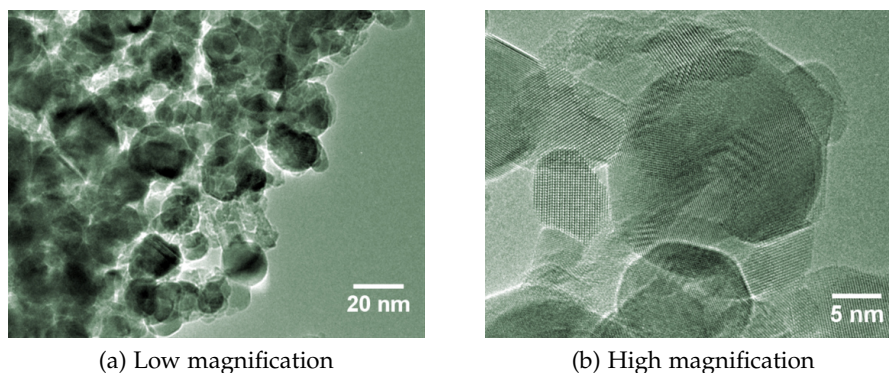


Figure 4.1: The Cu/ZnO/Al<sub>2</sub>O<sub>3</sub> methanol synthesis catalyst. This is the high surface area industrial catalyst prepared by co-precipitation. Imaged in 1 mbar H<sub>2</sub> at 300 °C.

#### 4.1.1 *The active site*

Despite its long history as a commercial catalyst and a high amount of scientific research over the years, key issues about the methanol synthesis catalyst remain controversial. In particular, the following points are still debated[70]:

- The nature of the active site
- The role of ZnO
- The reaction mechanism, especially whether CO or CO<sub>2</sub> is the dominating reactant.

The intention with the work presented in this chapter is in particular to investigate the two first points; the nature of the active site and the role of ZnO. Since Zn is assumed to be a constituent in the active site[16], these two points are closely related.

ZnO plays an important role for the catalyst structure, acting as a spacer between the Cu crystals, which allows for a very high Cu loading and surface area in the catalyst. The CuO/ZnO framework is created from crystals of Cu,Zn,Al-hydroxycarbonates, e. g. zincian malachite[85], and the role of the Zn in this process is well understood.

Today, it seems widely accepted that ZnO also has an important promoting effect on the methanol synthesis activity[16, 86], although it has previously been suggested, and shown, that activity only scales with Cu area for various supports[84, 87]. In that paper, the measurements of Cu surface area was done by N<sub>2</sub>O reactive frontal chromatography[88, 89], a method we now know can underestimate the surface area due to Zn incorporation in the Cu surface[90].

Even if it is accepted that ZnO has a promoting effect, many different explanations has been on the table. The Klier group promoted the

idea that the active site was  $\text{Cu}^{+1}$  ions incorporated in the  $\text{ZnO}$ [91]. From Topsøe, it was shown that the shape of the Cu particles was gas dependent[22, 92, 93] and that this dynamic behavior could be satisfactorily incorporated in a micro-kinetic model[94]. Finally, a Cu-Zn surface alloy was suggested as the active site[95]. Recently, it was shown that such a surface alloy is present in an industrial-type catalyst even under mild reducing conditions[90], and theoretical calculations suggest that Zn incorporated in a step in the Cu surface is the active site for MeOH synthesis[16]. Along with this, Behrens et al. suggest that ZnO migrates to the Cu surface during reduction[16] and that it may even completely cover the Cu surface[96].

In the following, we have focused on the interplay between Cu and ZnO during oxidation and reduction, both with an emphasis on the exact location on Cu and ZnO relative to each other[16, 96] as well as the possibility of reduction of Zn and the formation of a Cu-Zn surface alloy[90]. We have acquired global chemical information using XPS and local structural information using TEM.

#### 4.2 MODEL SYSTEM PREPARATION

In order to decrease the level of complexity, one often makes use of model systems. Essentially, this is a representative model of the catalyst and process, but it is simplified to varying degree in order to isolate parameters and obtain better control. For the MeOH synthesis catalyst, examples of this is  $\text{Al}_2\text{O}_3$ -free systems[22], Cu single crystals at UHV conditions[97] and  $\text{CO}$ - or  $\text{CO}_2$ -free synthesis gas[91, 98].

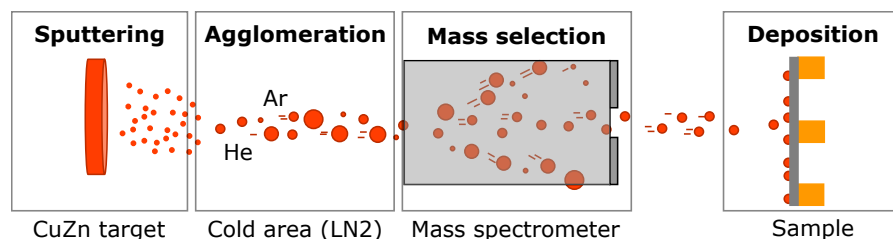


Figure 4.2: Deposition of size selected nanoparticles by cluster source. Cu and Zn atoms are sputtered off the target and agglomerate in the cold zone. Nanoparticles are size selected in the QMS and move on to the sample where they are deposited.

Our model system was made from size selected CuZn alloy nanoparticles. The cluster deposition technique allows us to create nanoparticles of well-defined size[99, 100] and composition[101]. Figure 4.2 shows the working principle of the cluster source apparatus. The cluster formation proceeds under vacuum conditions in three steps; sputtering, agglomeration and mass selection. These take place in three dedicated zones. The sputtering zone contains a metal target, in this case CuZn in a predefined composition. The target is sputtered with  $\text{Ar}^+$  ions by a magnetron sputter head, releasing a gas of atoms. Next

is the agglomeration zone, which has an Ar and/or He pressure of ca 1 mbar and is cooled by liquid nitrogen. Here, the atoms released from the target agglomerate, forming nanoparticles of varying size. The temperature, gas types and pressures will define the size distribution of the nanoparticles. Next, the nanoparticles pass through a QMS that will filter the nanoparticles according to their mass/charge ratio. This typically produces a very narrow PSD, for example, as shown by Nielsen et al., Ru nanoparticles of  $10.8 \pm 0.8$  nm[100]. Finally the nanoparticles move into the deposition chamber where they land on the sample. In the present work we used either a Ti single crystal or a TEM grid. The Ti single crystal was used for XPS and the TEM grids for *in situ* TEM.

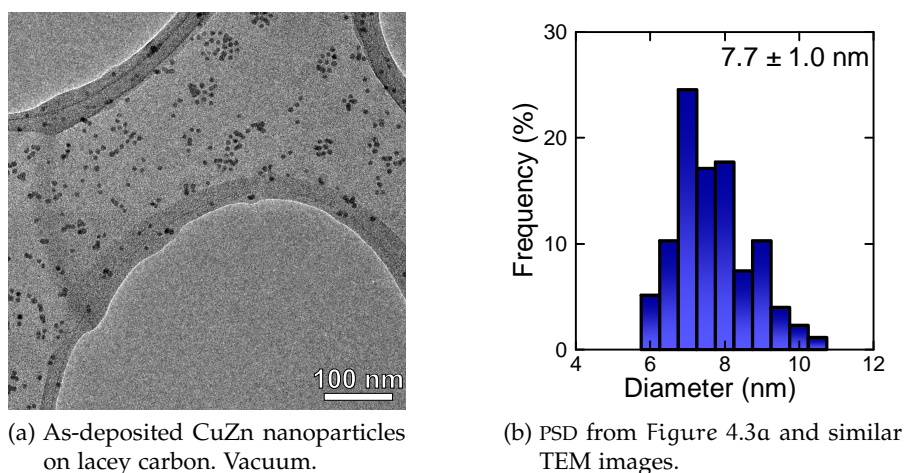


Figure 4.3: As-deposited CuZn nanoparticles. Target size 6.5 nm.

(a) Agglomeration seen by TEM, suggesting that particles are able to move after deposition. (b) PSD from 175 particles measured in (a) and similar images from the same sample.

For the work published in [63], I used standard lacey carbon Cu grids, where the CuZn particles were deposited directly on the amorphous carbon support. Figure 4.3a shows a TEM image acquired in vacuum of the as-deposited nanoparticles. The average diameter measured from this and similar images was  $7.7 \pm 1.0$  nm. For this deposition, the target size was 6.5 nm, assuming a spherical geometry. The particles may change shape due to interaction with the support, which would cause an increase in the projected diameter. The formation of a surface oxide at this point, may also increase the size slightly. Furthermore, we see that the particles are clustered, in a systematic manner, suggesting that they are able to move on the carbon film after deposition. The particles are expected to bind stronger to oxide surfaces and therefore not move on the  $\text{TiO}_2$  crystal where they were deposited for XPS analysis. This was confirmed by STM where no clustering was observed[102]. Figure 4.3b shows the PSD for this sample and a tail towards larger sizes is evident. Larger particles may be cre-

ated if particles coalesce on the support at deposition. Examples of particle grouping are also seen directly from the TEM image in Figure 4.3a.

Having created size selected CuZn nanoparticles, these must be transformed into a suitable model system for the MeOH catalyst. The CuZn alloy phase, brass, is not present in the MeOH catalyst during operation as a bulk phase, so our model system must be transformed to Cu/ZnO. Figure 4.4 shows the basic principle of formation of model system from CuZn as it has been employed here. First, the CuZn is oxidized, creating separate phases of CuO and ZnO, thus segregating Cu and Zn because there is no mixed oxide phase for these two elements. A reduction at low temperature ( $<300\text{ }^{\circ}\text{C}$ ) will reduce the Cu without the complete reduction of Zn and a return to a bulk alloy phase. The alloy formation is primarily limited by the diffusion of Zn in Cu, the rate of which will increase with temperature[103].

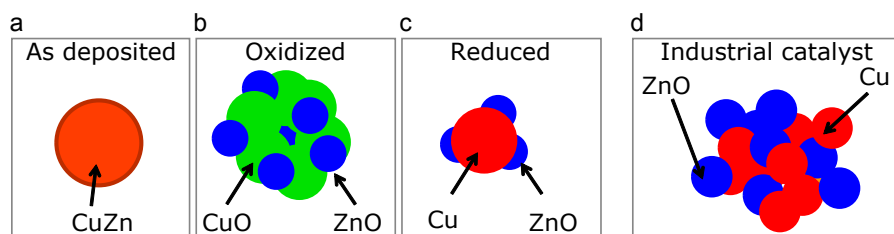


Figure 4.4: Formation of Cu/ZnO from CuZn nanoparticles. First the CuZn particle (a) is oxidized in  $\text{O}_2$  at elevated temperature. This segregates CuO and ZnO (b), because there is no mixed oxide phase for Cu and Zn. A mild reduction will reduce the Cu, whereas ZnO will stay in the oxide phase (c). The model Cu/ZnO nanoparticle created this way may be viewed as a unit cell of the industrial catalyst (d).

### 4.3 EXPERIMENTAL SETUP AND METHODS

Cluster synthesis, high pressure treatments and XPS were all performed in the same UHV setup[63, 102] at CINF DTU. *In situ* TEM was performed on the Haldor Topsøe Titan 80-300.

#### 4.3.1 UHV system: deposition, temperature treatment and spectroscopy

We employed a parallel approach of similar gas and temperature treatments in the UHV setup and in the TEM. In the UHV setup, these treatments were done in a high-pressure cell attached to the vacuum system. Here, the  $\text{TiO}_2$  crystal was heated under gas pressures from 1 to 900 mbar, and it is thus possible to achieve significantly higher pressure than the few mbar available in the TEM. After these treatments, the sample was transferred to the main vacuum chamber where XPS-analysis was performed. The typical mode of operation was a 1 hour

treatment in the high pressure cell, followed by spectroscopic analysis. This could be followed by another 1 hour treatment at a higher temperature. In this way we studied the development in a 'quasi-*in situ*' manner[77].

#### 4.3.2 XPS

X-ray photoelectron spectroscopy (XPS) is a classic surface sensitive spectroscopic technique widely used for the analysis of materials. It relies on the photoelectric effect first described by Einstein. Since catalysis takes place on material surfaces, XPS is an obvious choice for the study of such materials, and beneficial as a complementary technique to TEM. XPS provides accurate information about sample averaged surface composition, whereas TEM provide information about the spatial organization of the sample. In the current project, we relied on both to explain our observations.

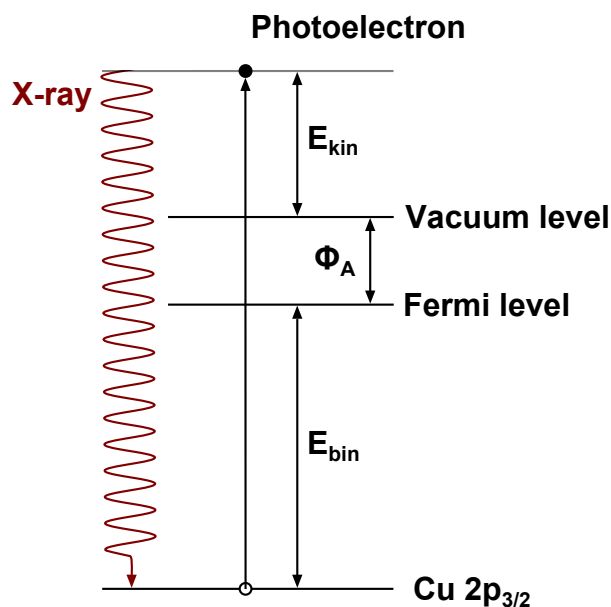


Figure 4.5: The XPS technique for the measurement on the Cu 2p<sub>3/2</sub> core level. The XPS technique relies on an incoming x-ray photon which may excite a core level electron to leave the sample. The binding energy is measured as the difference between the energy of the incoming x-ray and the kinetic energy of the outgoing electron and the work function of the the analyzer  $\Phi_A$ . Drawing inspired by[1]

The principle behind XPS is illustrated in Figure 4.5. An incoming photon of energy  $h\nu$  excites a core level electron, e.g. Cu 2p<sub>3/2</sub>, into vacuum. The kinetic energy,  $E_{kin}$  of the electron is measured

by an electron energy analyzer (in the present case a hemispherical analyzer) and the binding energy  $E_{\text{bin}}$  can be calculated as:

$$E_{\text{bin}} = h\nu - \Phi_A - E_{\text{kin}} \quad (4.4)$$

where  $h$  is Planck's constant and  $\Phi_A$  is the work function of the analyzer. The energy of the emitted electron will thus depend on the energy of the x-ray source and the binding energy of the emitted electron. This produces a specific fingerprint of the element from which the electrons are emitted because the binding energies are element specific. In the present case we used an  $\text{AlK}\alpha$  source where  $h\nu$  is 1486.6 eV. The kinetic energy of the emitted electrons typically fall in the range of 0-1000 eV. At these energies, the mean free path of the electron in the material is low, less than 1 nm, which is the origin of the surface sensitivity of XPS; even if the x-rays penetrate deeply into the material, the photoelectrons can only escape from the outermost layer[1].

The photo-emission process will leave a hole in one of the inner shells of the atom. This may be filled by an electron from a higher shell. This process will release energy, which may be transferred to another electron such that it is released with a specific energy. This is called the Auger process and the released electron an Auger electron. In this work we have both utilized photoelectrons and Auger electrons.

The binding energies not only depend on the element, but also on the chemical state, because the energies of the core electrons is slightly shifted depending on the state of the valence electrons. This is called the chemical shift and it is typically in the range of 0-3 eV[1]. Here we have used chemical shifts to distinguish between oxidized and metallic Cu and Zn.

### 4.3.3 *In situ* TEM

Particles were deposited either directly on a lacey carbon/Cu grid[63] or on top of spherical  $\text{Al}_2\text{O}_3$  particles deposited on Au grids. After deposition, the grids were removed from the UHV setup and either transferred directly to the TEM or to a glove box. The transfer included exposure to ambient air for a maximum of 30 minutes.

For the *in situ* experiment, a grid was placed in the Gatan heating holder and inserted in the microscope. For oxidation, the sample was exposed to 1 mbar  $\text{O}_2$  and heated to 300 °C with a rate of 30 °C/min. Reduction was performed in 1 mbar  $\text{H}_2$  at 300 °C, where the sample was imaged *in situ* at various time steps until full reduction was seen by an inspection of the lattice fringes in the images. Electron illumination was maintained at levels at or below 300 °C in order to minimize the effect of the electron beam and avoid or minimize beam assisted reduction. Most HRTEM images were acquired with a pixel

size of 0.063 nm, sufficient to resolve Cu(111) and Cu(200) at 0.21 and 0.18 nm respectively. Typically, a series of 10-20 images were acquired and alignment and summation was used to increase the SNR (Section 2.4.2). All TEM images shown in the following represent such summed image series.

#### 4.4 RESULTS

Particles were produced from a target containing Cu and Zn in the ratio Cu:Zn 90:10. For deposition on TiO<sub>2</sub>, particles were produced with a mass filter setting corresponding to a size of 9 nm. For deposition on the TEM grids and microreactors, particles were produced from two targets with composition Cu:Zn 90:10 and 97:3.

##### 4.4.1 From CuZn to Cu/ZnO

The formation of Cu/ZnO nanoparticles from CuZn was followed in parallel by XPS and *in situ* TEM. Figure 4.6 shows XPS data from the Zn 2p<sub>2/3</sub> (a) and Cu 2p<sub>2/3</sub> (b) lines for the as-deposited, oxidized and reduced samples. The amount of Cu and Zn in the particle surface was quantified based on the 2p<sub>2/3</sub> lines taking into account sensitivity factors[63]. The Cu amount (Cu/(Cu + Zn)) is shown in percent in Figure 4.6c.

In the as-deposited state, the shape and position of the Cu L<sub>3</sub>VV (not shown here) and the Zn L<sub>3</sub>M<sub>4,5</sub>M<sub>4,5</sub> Auger line (Figure 4.16 on page 80) reveal that the particles are metallic after deposition, as expected. The target is metallic and the deposition takes place in an oxygen free environment. The surface composition based on the 2p line intensities shows a ratio between Cu and Zn of ~75:25. This is different from the target composition which was 90:10. It is however not unusual to see these differences when using binary systems[101]. The nanoparticle composition is expected to be homogeneous in the as-deposited state, and the composition measured here is thus assumed to be representative of the bulk composition.

Oxidation of the nanoparticles in 200 mbar O<sub>2</sub> at 200 °C results in a drastic lowering of the Zn concentration in the surface, such that Cu:Zn is ~95:5. The shape of the Cu 2p line, specifically the feature at 491 eV, reveals that the Cu is fully oxidized to CuO [104]. A shift in the Zn L<sub>3</sub>M<sub>4,5</sub>M<sub>4,5</sub> Auger line (Figure 4.16 on page 80) also reveals that the Zn is fully oxidized to ZnO at this point.

Reduction in 200 mbar H<sub>2</sub> at 200 °C completely changes the surface composition and lowers the amount of Cu, such that Cu:Zn ~45:55. This corresponds to an enrichment of Zn in the surface compared to the bulk composition measured in the as-deposited sample.

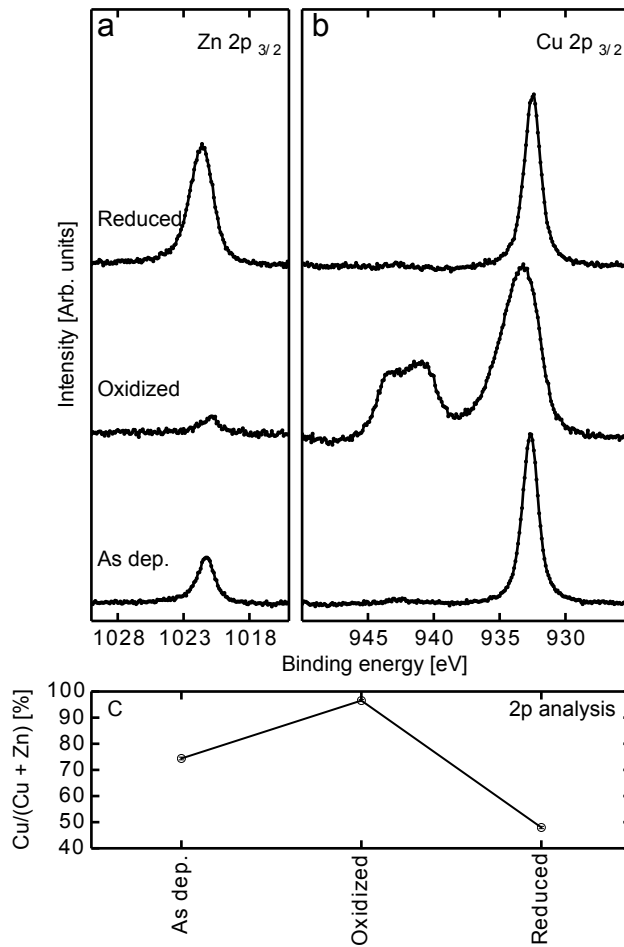


Figure 4.6: Analysis of surface composition for as deposited, oxidized and reduced CuZn nanoparticles.

(a) Zn 2p<sub>3/2</sub> line, background subtracted. (b) Cu 2p<sub>3/2</sub> line, background subtracted. (c) Cu surface concentration as a percentage of total metal amount. Particles were synthesized from a target with composition Cu:Zn 90:10 and the deposition size was 9 nm.

To understand the results from XPS and relate them to structural transformations, we imaged the three situations, as-deposited, oxidized and reduced.

HRTEM images are shown in Figure 4.7. In the as-deposited state (a), particles are spherical and polycrystalline. The spherical shape indicates that the morphology has equilibrated at room temperature. Ru nanoparticles deposited in a similar way were observed to have 'cauliflower'-shape, suggesting a non-equilibrated shape after deposition[100]. Remarkably, there is no indication of a surface oxide as seen from HRTEM images. Pure Cu particles deposited and transferred under similar conditions has been observed to oxidize during transfer, indicating that the brass is more resistant to oxidation, possibly because the Zn helps form a passivating layer. There is an amorphous overlayer, but this is ascribed to carbon deposition in the microscope

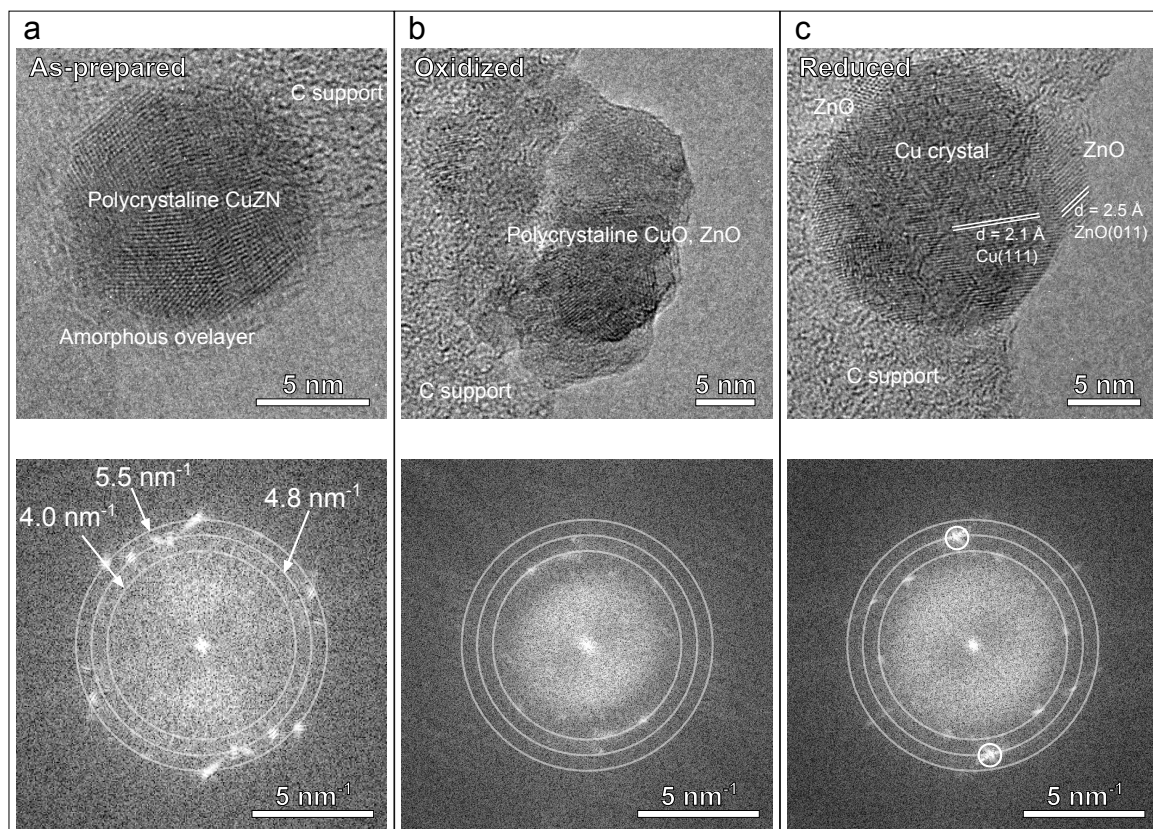


Figure 4.7: HRTEM images and FFTs of as deposited, oxidized and reduced CuZn nanoparticles. Three specific lattice spacings of  $4.0 \text{ nm}^{-1}$  ( $2.5 \text{ \AA}$ ),  $4.8 \text{ nm}^{-1}$  ( $2.1 \text{ \AA}$ ) and  $5.5 \text{ nm}^{-1}$  ( $1.8 \text{ \AA}$ ) are marked with circles in the FFTs. These correspond to a common distance in CuO, Cu<sub>2</sub>O and ZnO ( $2.5 \text{ \AA}$ ), Cu(111) ( $2.1 \text{ \AA}$ ) and Cu(200) ( $1.8 \text{ \AA}$ ). (a) As-deposited particle, imaged in vacuum at room temperature. Spherical particle with multiple crystal domains. Amorphous overlayer is ascribed to carbon contamination building up under the electron beam. Resolved lattice spacings correspond to Cu(111) and Cu(200). (b) Oxidized, imaged in 1 mbar O<sub>2</sub> at 300 °C. Irregularly shaped and multicrystalline. Resolved lattice spacings corresponding to CuO(-1-11), Cu<sub>2</sub>O (111) and ZnO(011). (c) Reduced, imaged in 1 mbar H<sub>2</sub> at 300 °C. Spherical Cu particle decorated with ZnO. Resolved lattice spacings correspond to Cu(111) and ZnO(011).

deposited under the electron beam when the sample is at room temperature and vacuum. This was never a problem under *in situ* conditions.

Polycrystallinity is seen directly in the HRTEM image, as well as in the FFT below. Here we see spacings at  $2.1 \text{ \AA}$  ( $4.8 \text{ nm}^{-1}$ ) and  $1.8 \text{ \AA}$  ( $5.5 \text{ nm}^{-1}$ ) corresponding to Cu(111) and Cu(200). Incorporation of Zn in the Cu lattice leads to a slight increase in the lattice constant, e.g. the 111 direction has a table value of  $2.08 \text{ \AA}$  for Cu and  $2.12 \text{ \AA}$  for a Cu<sub>75</sub>Zn<sub>25</sub> alloy[68]. This is however below the precision of HRTEM so we cannot, based on the images in Figure 4.7, say that the Cu and Zn is alloyed in the as-deposited particles. XPS data has however convincingly shown that. The polycrystallinity is also seen directly from the FFT in Figure 4.7 because there are multiple close-

lying spots at the same distances. It is also noted that no spots are seen at distances below  $4.8 \text{ nm}^{-1}$ , i. e. there is no indication of oxides in the as-deposited particles.

After oxidation in 1 mbar  $\text{O}_2$  at  $300^\circ\text{C}$ , only irregular shaped particles were seen. An example is shown in Figure 4.7 b. The FFT reveals that the resolved lattice is mainly seen at distances around  $4.0 \text{ nm}^{-1}$ , corresponding to a lattice spacing of  $2.5 \text{ \AA}$ . This distance can come from the (011) direction of ZnO or the (-1-11) direction of CuO. Based on the lattice information in Figure 4.7b, it is not possible to distinguish between crystals of ZnO and CuO. The imaged particle is not the same as shown in the as-deposited state, due to the contamination (amorphous overlayer), that build up during imaging in vacuum.

Figure 4.7c shows a particle after reduction in 1 mbar  $\text{H}_2$  at  $300^\circ\text{C}$ . After reduction, particles are spherical and with large Cu domains. They are not necessarily single crystals, but have fewer domains than the as-deposited particles. In the particle shown in Figure 4.7c, we see the Cu(111) direction in the 'north-south' direction resolved in most of the particle. On the surface, small crystals of ZnO are seen; the ZnO (011) direction is indicated in the figure for one of these.

The *in situ* TEM at the final stage reveals a morphology comparable to the intended structure (Figure 4.4). In the projected TEM images, ZnO appears to be located only on the surface of the Cu particle. This in turn explains why a Zn enrichment is measured by XPS in the final reduced state compared to the as-deposited particles. Because XPS is surface sensitive and only probes the outermost ca 2 nm, the final measurement will measure all Zn in the sample because it is present as small crystallites, whereas the Cu is in larger particles, where the Cu located in the center does not enter into the measurement and quantification. With this complementary use of XPS and TEM we are able to obtain a better structural description of the particles and confirm that we have the desired structure.

#### 4.4.2 TEM image analysis

FFTs were used to identify lattice spacings present in HRTEM images. The FFT however also carries information about the spatial origin of the periodicities in its imaginary term. We can utilize this to map which areas of the image certain lattice spacings originate from. This can be done for a specific spot in the FFT, but in the following I will present a generalized approach to identify and indicate certain lattice spacings in TEM images.

Figure 4.8a shows a frame averaged TEM image of a Cu/ZnO particle imaged *in situ* in 1 mbar  $\text{H}_2$  at  $300^\circ\text{C}$  and corresponding FFT. Lattice spacings of Cu and ZnO are identified and named in the FFT. By applying two circular masks in the FFT and performing an inverse Fourier transformation it is possible to identify the spatial origin of

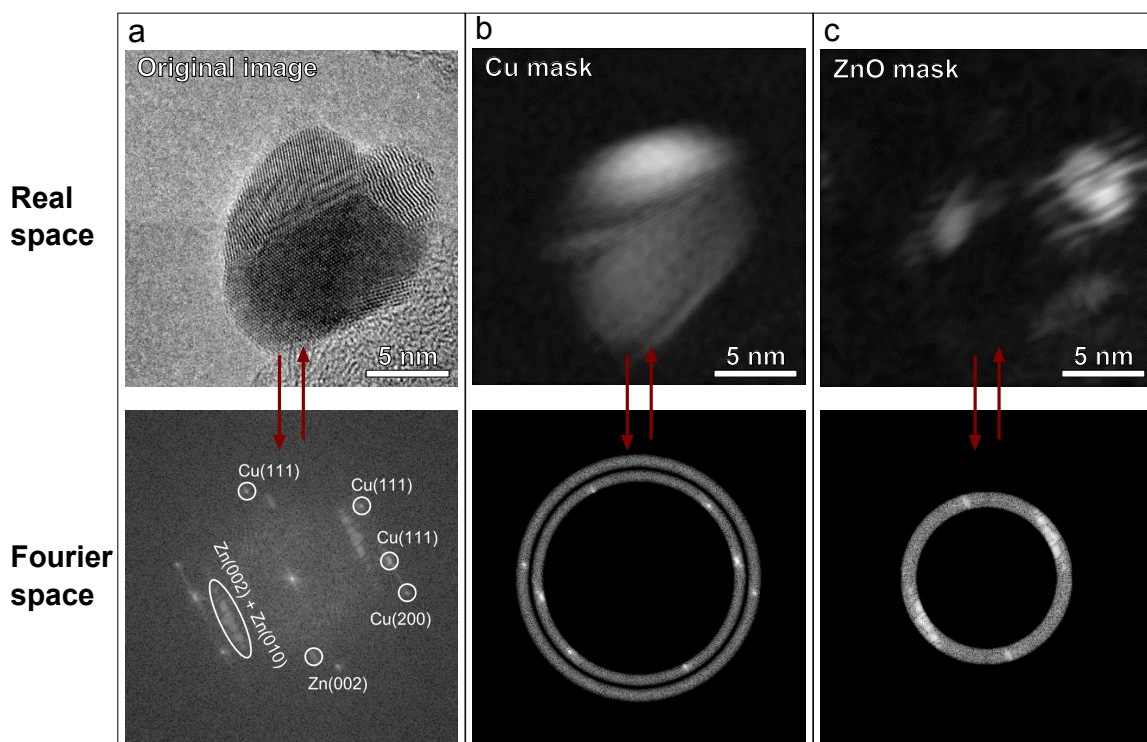


Figure 4.8: Identification of crystal phases in HRTEM images using FFT, masking and inverse FFT. **(a)** TEM image of a Cu crystal decorated with smaller ZnO crystallites. Acquired *in situ* in 1 mbar  $\text{H}_2$  at 300 °C. **(b)** Annular masks applied to Cu(111) at  $1/2.08 \text{ \AA}^{-1}$  and Cu(200) at  $1/1.81 \text{ \AA}^{-1}$ . Inverse FFT identifies the spatial origin of these spacings. **(c)** Annular masks applied to ZnO(010) at  $1/2.81 \text{ \AA}^{-1}$  and ZnO(002) at  $1/2.60 \text{ \AA}^{-1}$ . Inverse FFT identifies the spatial origin of these spacings. Mask width is  $1/0.03 \text{ \AA}^{-1}$  for both cases.

the spots in the FFT coming from Cu(111) and Cu(200) (Figure 4.8b). This directly shows that the large central crystal is metallic Cu. This is done similarly for ZnO, and from Figure 4.8b it is evident that the three crystals on the Cu surface are ZnO.

To make a general treatment for all images, a range of lattice spacings were chosen in order to identify Cu, CuO,  $\text{Cu}_2\text{O}$  and ZnO. These are shown in Table A.1 (Appendix A, page 159). Here it is important that each spacing is unique to the associated phase, which e. g. rules out  $d = 2.5 \text{ \AA}$ , mentioned in Figure 4.7, because it is found in all relevant oxides in the Cu-Zn system. This is a limitation for the generalized approach, but the identification can also be used more specifically, i. e. to identify ZnO in the reduced system, if it can be confirmed that no CuO or  $\text{Cu}_2\text{O}$  is present. It is also possible to manually identify the individual spots in the FFT and color according to this. Here it was however decided to attempt a general and completely automated approach.

Each crystal phase and corresponding lattice spacings define annular masks that are shown superimposed on the FFT in Figure 4.9a, each with a unique color. Each masked image is inversely transformed

and the real space image (such as those in Figure 4.8) is added with a weighting in the three RGB channels given by its specified color. Cu was added in the red channel, CuO in the green channel and ZnO in the blue channel. Cu<sub>2</sub>O was added with 50 % in red and 50 % in blue, resulting in a purple color. The result is seen in Figure 4.9a.

The particle, now with colors, shown in Figure 4.9b illustrates the structure of this model catalyst. It consists of a large central Cu particle, the red area, divided in two crystal domains. The Cu particle is decorated with three smaller crystallites of ZnO as indicated by the blue color.

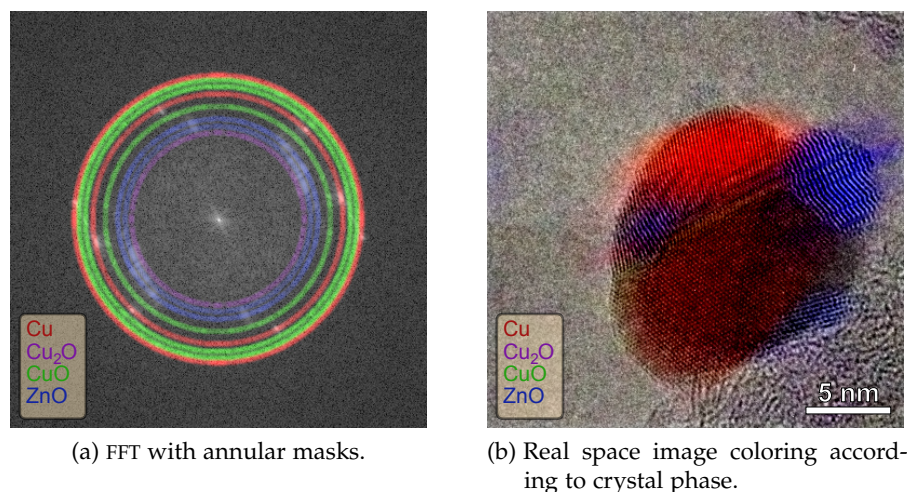


Figure 4.9: Coloring of HRTEM images according to crystal phase.

**(a)** Annular masks for Cu, CuO, Cu<sub>2</sub>O and ZnO overlaid on the FFT. Lattice spacings and crystal phases defined in Table A.1 (Appendix A, page 159). **(b)** Real space TEM image with colored crystal domains superimposed.

#### 4.4.3 Oxidation-reduction cycles

The oxidation and subsequent reduction of Cu/ZnO has previously been used to observe structural transformations and draw conclusions about the active state of the catalyst[16]. We have also investigated these transformations by repeatedly cycling the catalyst between an oxidized and reduced state. This was done multiple times in the UHV-setup with the same sample and for one cycle in the TEM.

The TEM images in Figure 4.10a-Figure 4.10d were acquired *in situ* in 1 mbar H<sub>2</sub> and 1 mbar O<sub>2</sub> for reducing and oxidizing conditions respectively. In all cases the temperature was 300 °C. The Cu decorated with ZnO is the now well known condition seen in the reduced state in Figure 4.10a. The outline of the initial particle was drawn around it and superimposed on images (a)-(d). Upon oxidation (Figure 4.10b) lattice fringes corresponding to CuO are resolved,

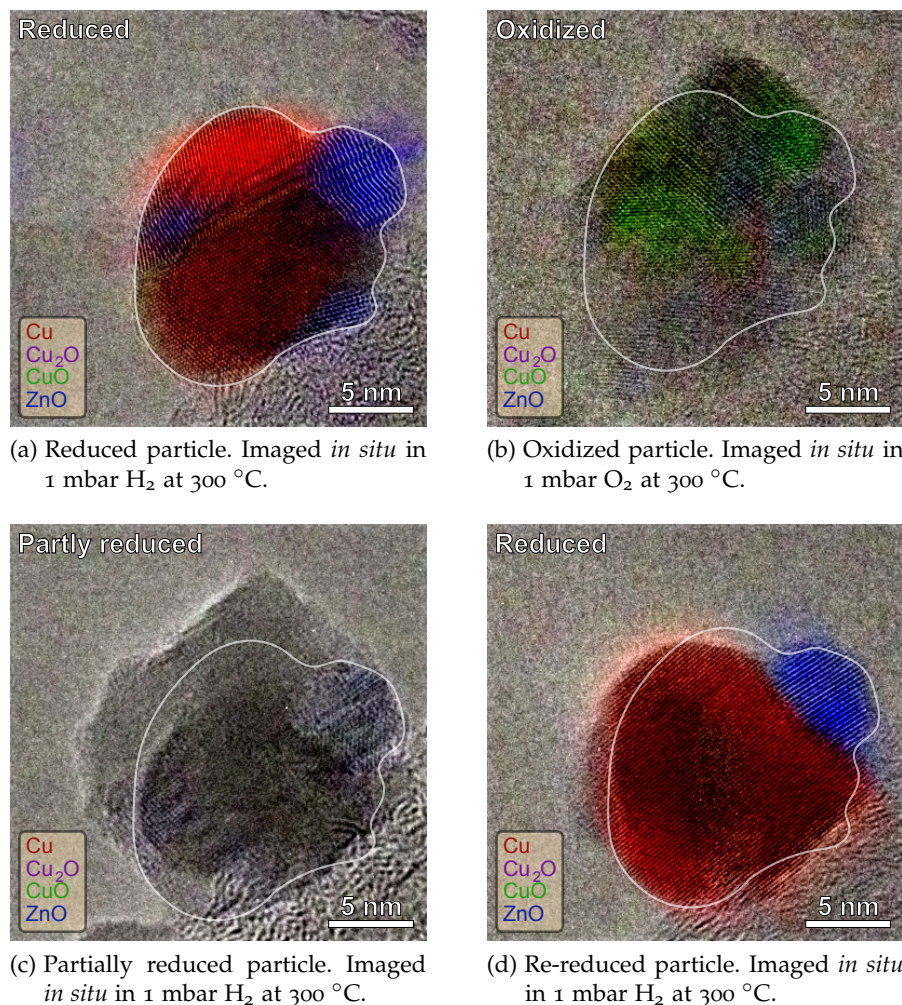


Figure 4.10: *In situ* TEM imaging of Cu/ZnO nanoparticles during reduction and oxidation cycles.

(a) Reduced particle in 1 mbar H<sub>2</sub> at 300 °C. (b) Oxidized particle imaged *in situ* after 1 hour in 1 mbar O<sub>2</sub> at 300 °C. (c) Partly reduced particle imaged after 0.5 h in 1 mbar H<sub>2</sub> at 300 °C. (d) Re-reduced particle after 1.5 h in 1 mbar H<sub>2</sub> at 300 °C.

as seen by the green color. The oxidation is associated with an increase in the projected area, and comparing with the outline from the initial particle, it is clear that the oxidation has resulted in an expansion that covers the previous position of the ZnO. The surface of the oxidized particle is smooth, i. e. no protruding ZnO crystallites, suggesting that these are now encapsulated by CuO. The lattice fringes of the ZnO are not resolved inside the particle. By measuring the projected area of the particle in Figure 4.10a and Figure 4.10b, an apparent volume increase was calculated to 88%, which is in line with the expected volume increase upon oxidation from Cu to CuO. Similarly, 88 particles were measured in overview images of the same area and showed a similar increase[63]. Figure 4.10c shows the particle af-

ter 30 min in 1 mbar  $H_2$  at 300 °C. The particle is still significantly larger than in the reduced state, but has changed shape compared to the fully oxidized state in Figure 4.10b. This suggests a partial reduction to  $Cu_2O$  at this point. The image lacks coloring because only faint lattice contrast was seen here, which will depend on the specific orientation and crystal phase. A faint blue coloring is seen in the position where the largest ZnO crystallite is expected to be. Here the encapsulation by the CuO or  $Cu_2O$  is evident. Finally, after 1.5 hours in 1 mbar  $H_2$  at 300 °C full reduction has occurred as seen in Figure 4.10d. There is now only a single Cu crystal, and the largest ZnO crystal is located in its original position and the morphology of the original particle is thus partly recreated.

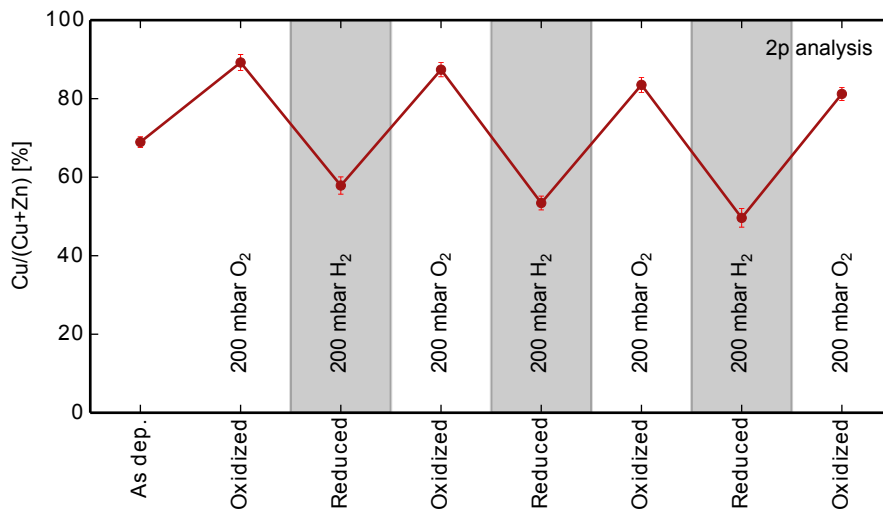
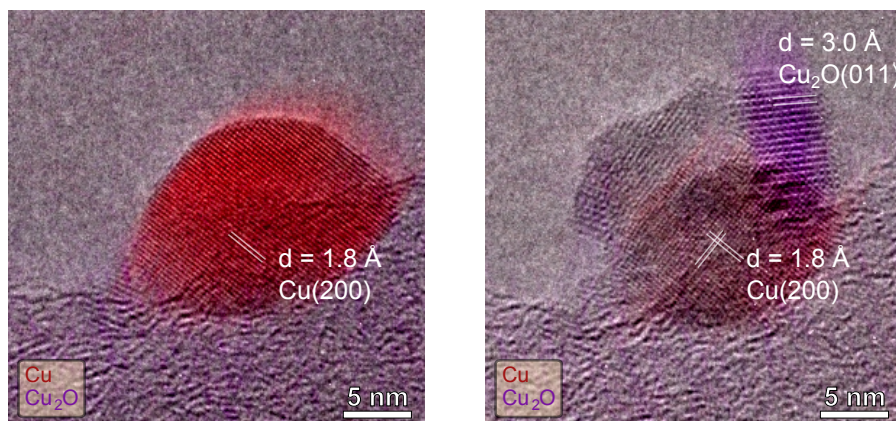


Figure 4.11: Quasi-*in situ* XPS of Cu/ZnO nanoparticles during reduction and oxidation cycles. Surface composition calculated from Cu and Zn 2p lines shows a reversible increase and decrease in Cu content after oxidation and reduction respectively. This is in line with the apparent encapsulation by CuO observed by TEM (Figure 4.10).

The XPS data in Figure 4.11 shows the Cu concentration ( $Cu/(Cu+Zn)$ ) during several cycles of oxidation and reduction. As it was already discussed and seen in Figure 4.6, oxidation is associated with a decrease in the Zn signal such that the ratio Cu:Zn is increased to around 95:5. By taking into account the TEM images during oxidation, we can explain the reduction in Zn signal as an encapsulation by CuO during oxidation. The encapsulation is due to the way Cu oxidizes. Because the diffusion rate of Cu in CuO/ $Cu_2O$  is higher than the diffusion rate of O, the oxide will tend to grow on the outside of the existing oxide. This is the driver behind the Kirkendall effect which can form hollow oxide nanoparticles under certain conditions[105].

To illustrate the initial oxide growth, Cu/ZnO nanoparticles were exposed to mild oxidation conditions with  $3.2^{-3}$  mbar  $O_2$  at room

temperature. This induced a rapid growth of a disordered oxide layer of a few nm. At these conditions, only  $\text{Cu}_2\text{O}$  and not  $\text{CuO}$  is expected. A similar sample was oxidized in the UHV-setup in 200 mbar  $\text{O}_2$  at room temperature in order to obtain a reference spectrum for  $\text{Cu}_2\text{O}$  [104] which XPS confirmed [63] in agreement with literature [104].



(a) Cu/ZnO nanoparticle.  $\text{H}_2 : \text{CO} = 1:1$ , 2 mbar, 260 °C.

(b) Cu/ZnO nanoparticle. Oxidized in  $3.2 \times 10^{-3}$  mbar  $\text{O}_2$  at 25 °C.

Figure 4.12: Growth of  $\text{Cu}_2\text{O}$  at mild oxidation conditions.

- (a) Cu/ZnO nanoparticle imaged *in situ* in a gas mix of  $\text{H}_2 : \text{CO} = 1:1$ , 2 mbar, 260 °C. Cu(200) lattice is resolved in one direction.  
 (b) Cu/ZnO nanoparticle imaged in vacuum after oxidation in  $3.2 \times 10^{-3}$  mbar  $\text{O}_2$  at 25 °C. Cu(200) is resolved in two directions (90 ° angle).  $\text{Cu}_2\text{O}$  is unequivocally identified by the

It is difficult to pinpoint the  $\text{Cu}_2\text{O}$  phase in HRTEM images because many lattice spacings overlap with  $\text{CuO}$  and  $\text{ZnO}$ . The  $\text{Cu}_2\text{O}$  (011) spacing at 3.02 Å is however unique, and can unequivocally identify  $\text{Cu}_2\text{O}$  if the sample is oriented correctly. Figure 4.12a shows a Cu/ZnO particle at reducing conditions ( $\text{H}_2 : \text{CO} = 1:1$ , 2 mbar, 260 °C.) and Figure 4.12b shows the same particle imaged in vacuum after the mild oxidation. Here, the coloring procedure was adjusted to identified only lattice spacings belonging to Cu and  $\text{Cu}_2\text{O}$ . It is evident that the Cu area has been reduced and that other crystal domains are protruding from the particle surface. One of these is aligned with the (011) direction parallel to the electron beam, and can thus be identified as  $\text{Cu}_2\text{O}$ . Based on XPS and HRTEM we conclude that the initial oxide growing on the surface of the Cu at room temperature is  $\text{Cu}_2\text{O}$ . In the following,  $\text{CuO}$  will be omitted as a possible candidate for crystals observed in the HRTEM images.

Figure 4.13 is another example of a particle before and after mild oxidation. Figure 4.14 shows the same images, colored according to phases. For Figure 4.14a, Cu and ZnO were identified and for Figure 4.14b, Cu,  $\text{Cu}_2\text{O}$  and ZnO were identified. Crystals of ZnO are seen on top of the Cu for the reduced particle in Figure 4.13b, colored blue in Figure 4.14b. One ZnO crystal is positioned on the

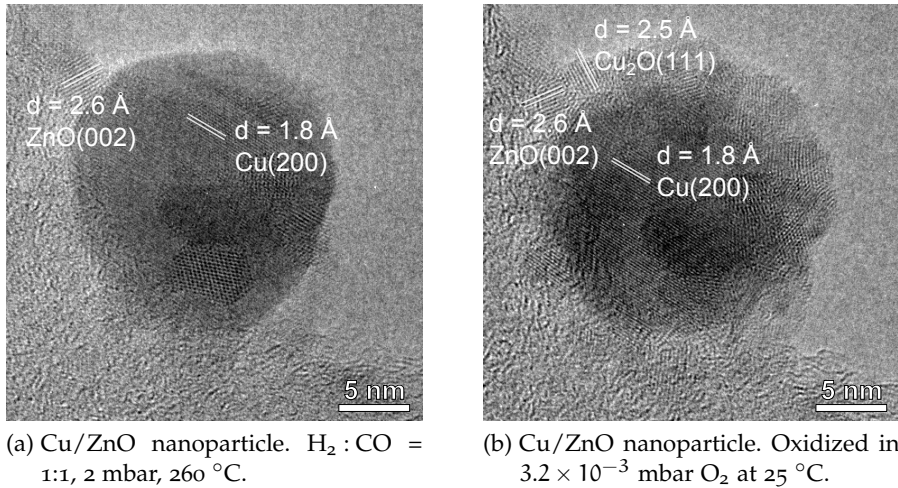


Figure 4.13: Growth of  $Cu_2O$  at mild oxidation conditions.

(a) Cu/ZnO nanoparticle imaged *in situ* in a gas mix of  $H_2 : CO$  1:1, 2 mbar, 260 °C. ZnO(011) plane is marked in a protruding ZnO crystal. (b) Cu/ZnO nanoparticle imaged in vacuum after oxidation in  $3.2 \times 10^{-3}$  mbar  $O_2$  at 25 °C. The previously protruding ZnO crystal is now partly covered by the outwards growing oxide.

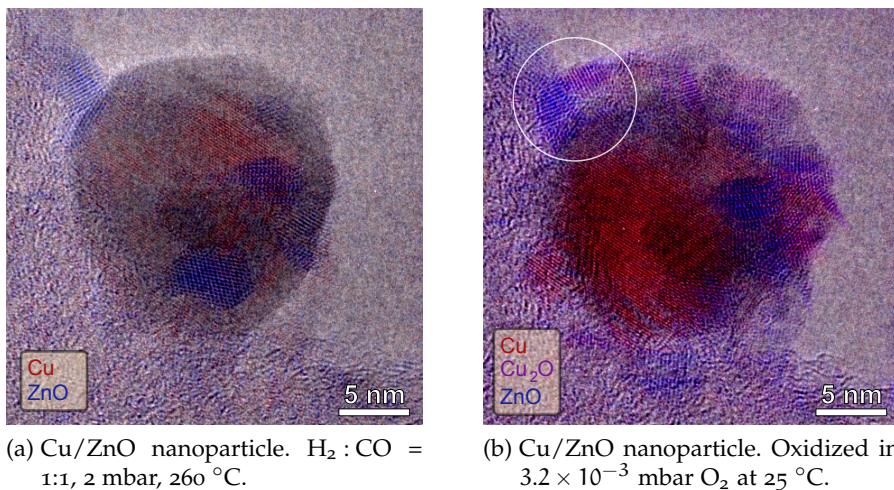


Figure 4.14: Same images as Figure 4.13. Colored according to lattice spacings of (a) Cu(111+200) and ZnO(002+010) (b) Cu(111+200),  $Cu_2O$  (111) and ZnO(002+010). See Table A.1 for lattice spacings. The white circle indicates an example of encapsulation of ZnO by  $Cu_2O$ .

carbon support and in close contact with the Cu particle (lattice spacing of ZnO(002) as marked in Figure 4.13b).

After oxidation (Figure 4.13b and Figure 4.14b), the Cu crystal is maintained in the central region, but a very disordered, 2-3 nm thick, oxide layer extends from the Cu surface on the entire particle. Looking

at the image in Figure 4.14b, this is colored purple, showing that it is  $\text{Cu}_2\text{O}$ , as expected.

The white circle in Figure 4.14b indicates an example of the postulated encapsulation of ZnO by  $\text{Cu}_2\text{O}$ . Here the ZnO located on the support, in close proximity to the Cu, is still seen, but now  $\text{Cu}_2\text{O}$  has grown next to it, covering at least some of the ZnO surface. This shows exactly why the XPS signal is lowered upon oxidation of these samples.

#### 4.4.4 $\text{H}_2$ pressure dependence

Different pressures were used in the parallel experiments for oxidation and reduction. In the UHV-setup the pressure was 200 mbar in the high pressure cell, whereas the pressure was 1 mbar in the TEM. This difference also affected the temperature required for reduction; where 200 °C was sufficient for reduction in the high pressure cell, it was necessary to go to 300 °C in the TEM in order to fully reduce the Cu. We are looking at the reaction:



And the equilibrium constant of this reaction is:

$$K = \frac{\text{H}_2\text{O}}{\text{H}_2} \quad (4.6)$$

At 200 °C,  $K$  is  $10^{12}$ , which means that the reaction is thermodynamically favored regardless of a possible background water pressure as long as there is  $\text{H}_2$  present. Reduction of CuO is however kinetically limited and will need a certain elevated temperature to proceed. The limitation is assumed to be either diffusion in the solid, or dissociation of  $\text{H}_2$ . If  $\text{H}_2$  dissociation is a limiting factor, this would explain why increasing the pressure, and hence the chemical potential of  $\text{H}_2$  decreases the reduction temperature.

In the following we have investigated the reduction behavior for the Cu/ZnO particles depending on  $\text{H}_2$  pressure. Prior to reduction, the sample was oxidized in 200 mbar  $\text{O}_2$  at 200 °C. Reduction was carried out as a temperature programmed reduction, where the sample was held for one hour at a constant temperature, then analyzed by XPS. This was repeated for a 25 °C temperature increase. Based on the 2p analysis, it was established that the ratio  $\text{Cu}/(\text{Cu}+\text{Zn})$  is a useful measure of the reduction of the sample, and so this is shown in Figure 4.15 as a function of temperature for  $\text{H}_2$  pressures of 1, 5, 200 and 900 mbar. A steep decrease in Cu concentration upon reduction of Cu was also reported by Behrens et al.[16].

At 1 mbar, the transition from high to low Cu surface concentration is seen at 250 °C, confirming the need for higher temperature at

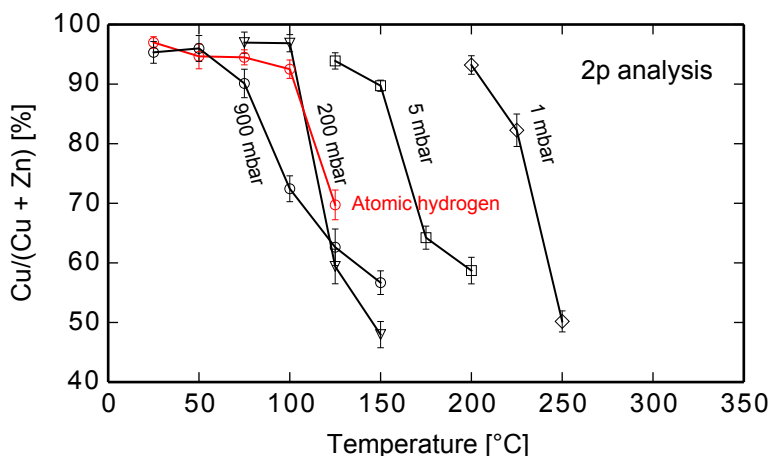


Figure 4.15: Cu surface concentration as measured by XPS at Cu and Zn 2p lines. Each point corresponds to 1 hour at constant temperature. Cu reduction is associated with a steep decrease in Cu surface concentration. The reduction is pressure dependent and the temperature needed for reduction increases with decreasing  $H_2$  pressure.

the TEM operating pressure. 300 °C was required in the TEM for the specific configuration with Cu/carbon film grids in 1 mbar  $H_2$ . This may depend on the local temperature distribution in the grid, i. e. the local temperature at the catalyst particle was lower than the temperature of the sample holder. For all  $H_2$  pressures, there is a specific temperature where the Cu:Zn ratio drops steeply and where the Cu is reduced within the 1 hour treatment in the high pressure cell. This critical temperature decreases as the pressure is increased.

Defining the critical temperature  $T_c$  to be the temperature for which the Cu is completely metallic, we get, based on an analysis of the Cu  $L_2$  VV line[102], that  $T_c = 100, 125, 175, 250$  °C for  $p_{H_2} = 900, 200, 5, 1$  mbar respectively. These temperatures coincide with the point where the ratio  $Cu/(Cu+Zn) < 75\%$  in Figure 4.15.

Besides raising the pressure, the chemical potential of hydrogen can also be increased by dissociation to form atomic hydrogen[106]. The atomic hydrogen was formed by a hot filament positioned in line of sight of the sample, while  $H_2$  gas was dosed at a low pressure of  $1 \times 10^{-6}$  mbar. The reduction temperature under these conditions was 125 °C as seen in Figure 4.15. This is further evidence that the dissociation of  $H_2$  gas is the limiting factor for the reduction of Cu/ZnO particles. The electron beam is assumed to have a similar effect, and a high beam current will facilitate a reduction[54](Chapter 3). In our experiments, 300 °C was needed to fully reduce Cu in the microscope, suggesting that the influence of the beam was limited. Behrens et al. observed reduction of a co-precipitated Cu/ZnO/ $Al_2O_3$  catalyst at 125 °C during an ambient pressure XPS measurement in 0.25 mbar  $H_2$ , which is contradictory to our results. The most likely explanation

for the difference is that the high power x-ray beam has activated or dissociated the  $H_2$  gas, such that the reduction could proceed at low temperature, as we see with pre-dissociated  $H_2$  in Figure 4.15.

#### 4.4.5 Zn reduction

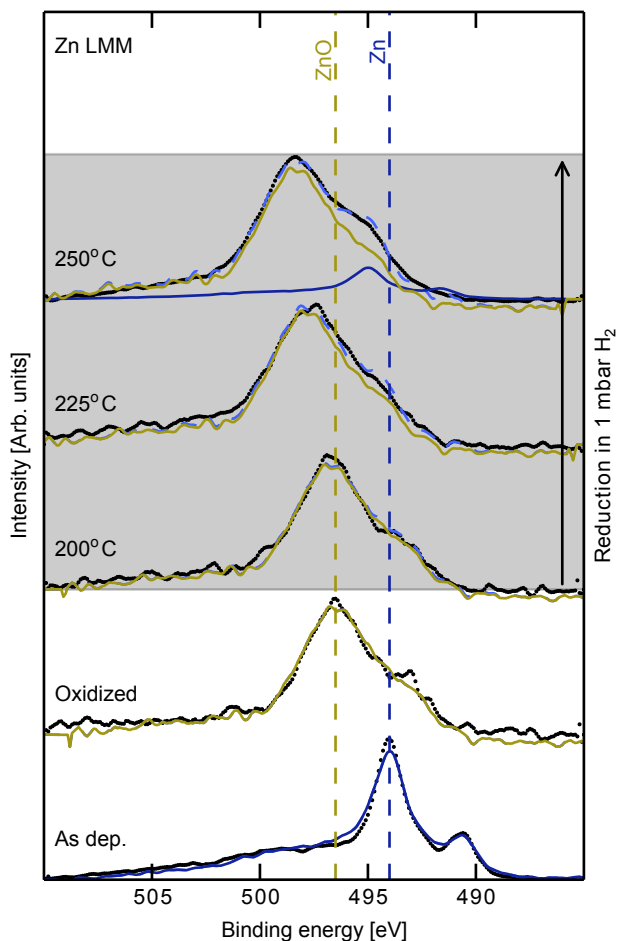


Figure 4.16: Zn  $L_2M_{4,5}M_{4,5}$  Auger line obtained during reduction in 1 mbar  $H_2$ . The dotted line is 7 point smoothed XPS data and the dashed line is a fit with metallic and oxidized Zn used as reference. The components of the fit are shown by a blue (metallic) and yellow (oxidized) line.

The chemical state of Zn was addressed with XPS by considering the Zn  $L_2M_{4,5}M_{4,5}$  Auger line as shown in Figure 4.16 for the as deposited and oxidized particles, as well as during reduction in 1 mbar  $H_2$ . The as deposited and oxidized spectra were used as references for the Zn in metallic (blue) and oxidized (yellow) state. These were fitted as a linear combination to the spectra obtained during reduction. At 200 and 225 °C, where the Cu is still not reduced (Figure 4.15), Zn is only seen in the oxidized state. At 250 °C however, a shoulder emerges on the spectrum, and the fit shows that a fraction of the Zn has been

reduced. This result is similar to that obtained by Kuld et al.[90]. The entire spectrum shifts left at 225 and 250 °C, which may be related to charging of the TiO<sub>2</sub> support. The distance between the peaks from Zn and ZnO was kept fixed when fitting. The magnitude of the signal from metallic Zn was found to correspond to 0.5-1 monolayer if alloyed in the Cu surface[102].

Reduction of ZnO happens concurrently with the reduction of Cu and was observed at all H<sub>2</sub> pressures and in atomic hydrogen. H<sub>2</sub> readily dissociates on Cu[107] and the concurrent reduction of Cu and ZnO could mean that the reduction happens via hydrogen spillover from Cu to ZnO present on the Cu surface[108, 109], since these are in close proximity in the present system. Another important point is that surface alloying of Zn in Cu is associated with a gain in energy which makes reduction of ZnO thermodynamically feasible[103, 110] in gas atmospheres where ZnO would otherwise not reduce.

#### 4.4.6 Activity

The ultimate goal of investigating the properties of the Cu/ZnO nanoparticles, is to measure their activity and correlate it with structure. The synthesis method should give us very good control over both size and Zn content. The latter by varying the composition of the metal target in the cluster source. In the following I will describe activity measurement for varying sizes of Cu/ZnO particles and for two compositions, one with 30% Zn and one with 9% Zn.

The particles were tested in the  $\mu$ -reactor system at CINF, which is specially designed for testing very small amounts of catalyst material[111–113]. The experiments were carried out by Anders Nierhoff who also quantified the experimental data shown in figures Figure 4.17, Figure 4.18 and Figure 4.19. The results are not yet conclusive and more work is needed. A detailed description of the experimental setup and procedure is found in Anders Nierhoff's PhD thesis[113].

Nanoparticles were deposited inside the  $\mu$ -reactor under UHV conditions and the reactor was then taken out in air and sealed with a Pyrex lid. The reactor volume where the particles were deposited is made from SiO<sub>2</sub>. The reactor was then transferred to the test setup. First the nanoparticles were oxidized in 200 mbar O<sub>2</sub> and then reduced in 2 bar H<sub>2</sub>. Finally the catalytic activity was tested in the MeOH synthesis reaction in a gas of CO<sub>2</sub> : H<sub>2</sub> = 1 : 4 at 2 bar total pressure. The outlet gas was monitored by MS and the methanol conversion was measuring as mass 31. A turnover frequency (TOF), MeOH molecules created per surface Cu atom per second, was calculated by taking into account the mass 31 signal, the flow rate through the reactor and the number of nanoparticles deposited[113].

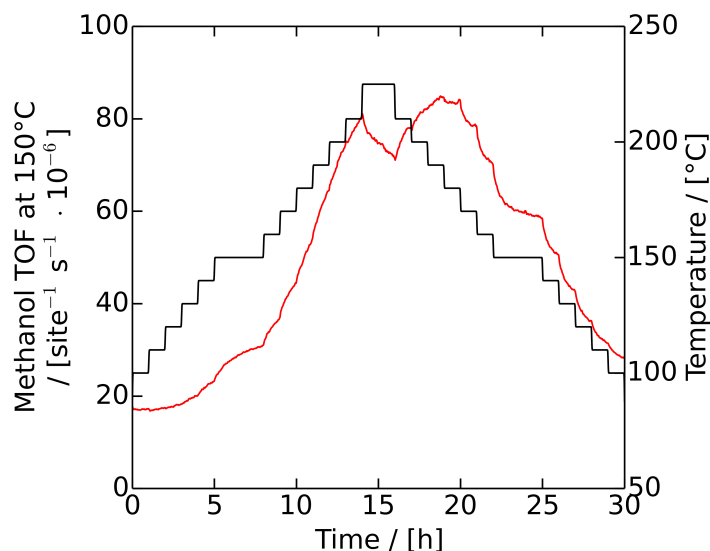


Figure 4.17: CO<sub>2</sub> hydrogenation to MeOH on size-selected Cu/ZnO nanoparticles in the  $\mu$ -reactor. Temperature is ramped from 100 °C to 225 °C in steps of 10 °C (last step 15 °C) and down again. MeOH is measured by MS as mass 31 and recalculated to a TOF.

Figure 4.17 shows a typical temperature ramp and MeOH synthesis. The temperature is ramped from 100 to 225 °C in steps of 10 °C (last step 15 °C) and down to 100 °C again. Each temperature is held for 1 hour, and 150 °C is held for 3 hours to allow the signal to further stabilize. From Figure 4.17 it is evident that there is a significant time delay in the MeOH signal, which is ascribed to a very long time constant in the transport of MeOH molecules from the reactor volume to the MS, possibly due to a strong interaction/sticking of the polar MeOH molecule in the tubing. As the temperature is increased, the TOF increases, until the last step to 220 °C where the conversion starts to decrease. This is because the reaction reaches equilibrium at this point. This shows why the industrial MeOH synthesis reaction is run at high pressures to increase the reaction equilibrium. In order to compare different catalysts, the TOF was compared at 150 °C for the ramp down.

Figure 4.18 shows TOF and Zn content as measured by XPS, as a function of particle size for 7 different samples. Evidently activity is divided in two groups, where the samples with the lowest Zn content (ca 9%) show by far the highest activity. There is no apparent dependence on size, except for the point at 8 nm. This measurement was not repeated to confirm or disprove its validity. Most likely, the oddly low activity 8 nm is due to an error in preparation or measurement. Looking at the Zn content, we see that the particle synthesis is very reproducible, resulting in more or less the same amount of Zn for the same target.

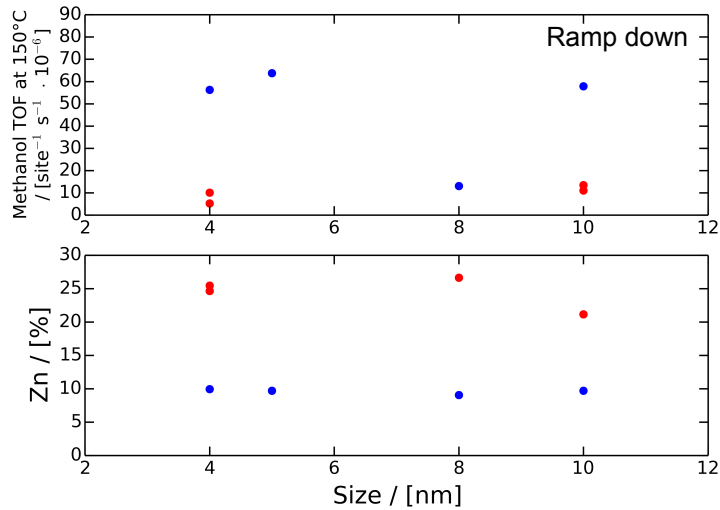


Figure 4.18: MeOH activity and Zn content as a function of particle size for 7 samples. TOF is compared at 150 °C for the ramp down. No size dependence is seen, but clearly the group of particles with the lowest Zn content show the highest activity.

It is an interesting conclusion that the activity is independent of particle size. This is in agreement with results by Prieto et al.[114] who found similar specific activity for a wide range of Cu particle sizes for a Cu/ZnO catalyst supported on SiO<sub>2</sub>. In another study, the MeOH reaction was claimed to proceed on Cu-Zn steps[16], which suggests that there should be a size dependency, since the amount of steps will increase as the particle size is lowered.

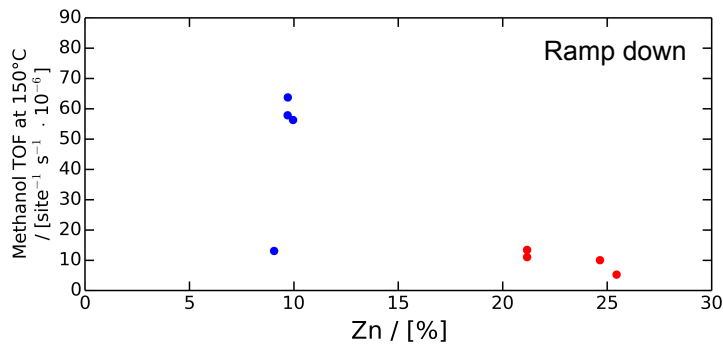


Figure 4.19: MeOH activity as a function of Zn content for 7 samples. TOF is compared at 150 °C for the ramp down. The trend towards higher activity for lower Zn content is evident.

Figure 4.19 shows the activity plotted as a function of Zn content rather than particle size. Here it is clear that the samples are divided in two groups depending on Zn content. Apparently the high Zn content has a detrimental effect on the MeOH activity. It is well known that Zn strongly promotes the activity of Cu, so the trend seen in Figure 4.20 must end once the Zn content is lowered further.

While the absolute ratio between Cu and Zn is constant for particles prepared from the same target, the ratio between Cu surface area and Zn will also depend on size. This will further complicate the interpretation of the data shown in Figure 4.18 and Figure 4.19.

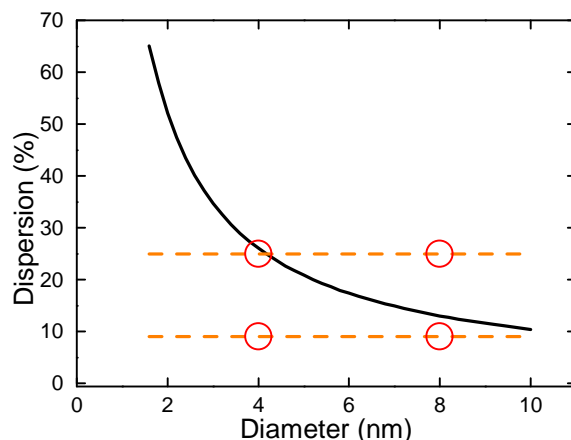


Figure 4.20: Dispersion (fraction of atoms located in the surface) for Cu particles as a function of diameter. Samples were made with Zn contents of 9% and 25% (orange lines). Particles were produced for TEM at sizes 4 and 8 nm (red circles). Images shown in Figure 4.21. At 4 nm, the Zn content corresponds to ca 1 and 0.5 monolayer for 25% and 9% respectively. At 8 nm, 9% corresponds to ca 1 monolayer and 25% corresponds to about two monolayers.

To quantify the relationship between Zn content and Cu surface area, the dispersion (surface atoms as percentage of total amount of atoms) was calculated for Cu particles as a function of size. For a particle of radius  $r$ , the volume and surface area are (assuming a spherical geometry):

$$V = 4/3\pi \times r^3 \quad (4.7)$$

$$A = 4\pi \times r^2 \quad (4.8)$$

The total number of atoms in the particle ( $\text{atoms}_{\text{particle}}$ ) and in the surface ( $\text{atoms}_{\text{surf}}$ ) can then be estimated as:

$$\text{atoms}_{\text{particle}} = V/V_{\text{unitcell}} \times 4 \quad (4.9)$$

$$\text{atoms}_{\text{surf}} = A \times d_{\text{surf}} \quad (4.10)$$

where  $V_{\text{unitcell}}$  is the volume of the Cu unit cell, 4 is the number of atoms in the unit cell and  $d_{\text{surf}}$  is the surface density of Cu atoms ( $1.47 \text{ Cu atoms/m}^2$  [115]). Finally the dispersion as a function of par-

ticle radius can be written as the fraction between surface atoms and total number of atoms. After some rearrangement this is:

$$\frac{\text{atoms}_{\text{surf}}}{\text{atoms}_{\text{particle}}} = \frac{3 d_{\text{surf}} \times V_{\text{unitcell}}}{4 r} \quad (4.11)$$

The dispersion as a function of particle diameter is plotted in Figure 4.20 along with the Zn content in the two groups of particles (orange lines). At the diameters where the orange and black lines intersect, the amount of Zn corresponds to one monolayer. Recalling that XPS showed that reduced Zn corresponds to 0.5-1 monolayer, it is expected that for particles containing 9% Zn, most Zn should be reduced and alloyed in the Cu surface for particles smaller than ca 8 nm. For 30% Zn this is the case for particles smaller than ca 4 nm.

In order to image the morphology and Cu-ZnO synergy as a function of size and Zn content, 4 samples were prepared for TEM: 9%/4 nm, 9%/8 nm, 25%/4 nm and 25%/8 nm.

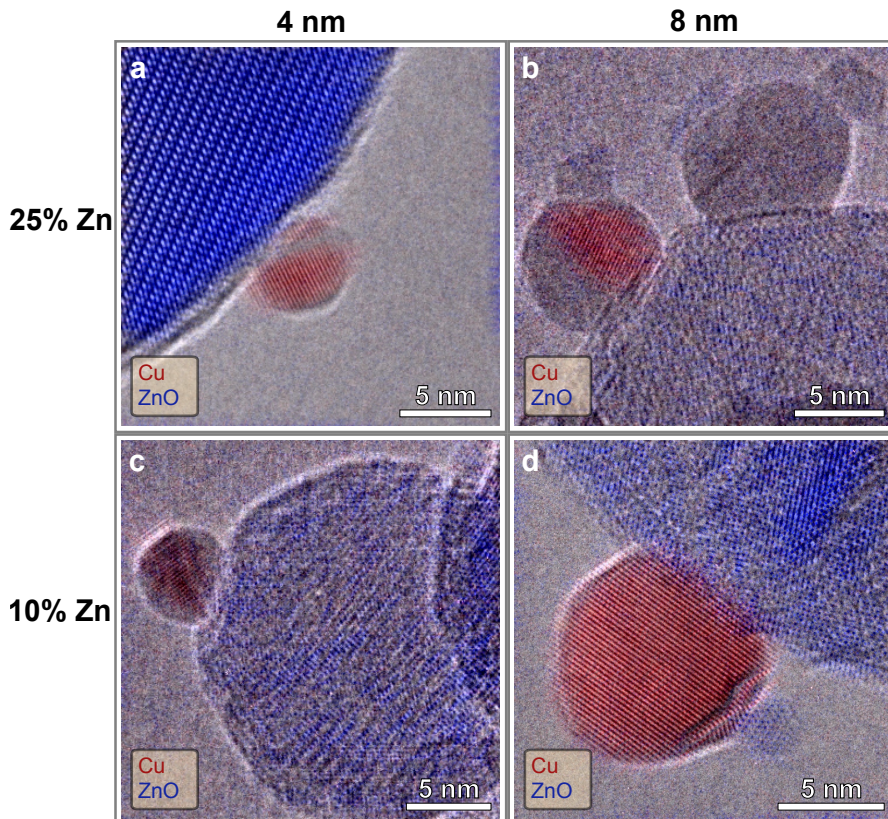


Figure 4.21: TEM images of four Cu/ZnO particles supported on  $\text{Al}_2\text{O}_3$  recorded *in situ* in 1 mbar  $\text{H}_2$  at 300 °C.

(a) 4 nm, 25% Zn. Very little or no ZnO on Cu.  $\text{Al}_2\text{O}_3$  is colored blue due to spacings shared with ZnO. (b) 8 nm, 25% Zn. Significant ZnO crystallites on the Cu surface. (c) 4 nm, 9% Zn. No ZnO seen in this case. (d) 8 nm, 9%. Small ZnO crystallites on the surface of Cu particles.

TEM images of the four samples are shown in Figure 4.21. All images were acquired in 1 mbar  $H_2$  at 300 °C. Coloring was according to lattice spacings of Cu and ZnO, assuming no oxidized Cu. Note that the  $Al_2O_3$  support may be colored blue due to overlapping lattice spacings with ZnO.

The size and Zn content of the imaged nanoparticles is marked by red circles in the plot of the calculated dispersion in Figure 4.20. Figure 4.21a shows a 4 nm particle with 25% Zn. Very little to no amounts of ZnO was seen on these particles by TEM. The Zn content corresponds to ca 1 monolayer, so this suggests that most of the ZnO is reduced to Zn in this case. Figure 4.21b shows 8 nm particles with 25% Zn. The size and composition of these was identical to previous particles shown on carbon support. In this case, ZnO crystals of significant size is seen on the surface of the Cu. Considering the calculated dispersion, 25% Zn corresponds to approximately 2 monolayers, which would leave significant amounts of residual ZnO, even if metallic Zn is present in quantities up to one monolayer. At the lowest Zn content of 10%, some residual Zn is seen in 8 nm particles whereas no ZnO was seen in the small 4 nm particles. This is also in line with the calculated dispersion and the assumption that metallic Zn can take up up to one monolayer in the Cu surface, according to Figure 4.20.

The activity data presented in this section is still inconclusive and further measurements are needed. It is interesting that a high Zn content has a detrimental effect on the catalyst activity. Considering the HRTEM images in Figure 4.21, ZnO positioned on the Cu surface may block active sites. This is however inconsistent with the size dependent activity of Figure 4.18, that shows no effect of size on the activity for particles of the same Zn content. Considering the calculated dispersion and the HRTEM images in Figure 4.21, the smallest particles with 25% Zn have a similar amount of ZnO on the surface as the 8 nm particles with 10%, yet the activity is much lower. Similarly, there is no clear detrimental effect of increased size and thereby increased surface ZnO for the particles with 10% Zn. The activity at 8 nm (Figure 4.18) is very low, but it is high at 10 nm, so this explanation seems insufficient.

More analysis is needed to explain the observations, first of all XPS of reduced particles of various sizes and compositions, to complement the HRTEM images. Furthermore, it should be investigated how low the Zn content can go before the activity decreases.

#### 4.5 CHAPTER CONCLUSION

In this chapter we have seen the advanced physical synthesis of a model catalyst system. By producing CuZn nanoparticles of prede-

finer size and composition, we were able to create single entities of Cu in close proximity to small crystallites of ZnO. These were investigated during oxidation and reduction by XPS and TEM. XPS provides sample averaged data for the surface composition, whereas TEM provides local information of particle structure. The use of these complementary techniques, showed Cu particles decorated with small ZnO crystallites under reducing conditions. Oxidation resulted in an encapsulation of ZnO by CuO, which was seen directly in the *in situ* TEM images and as a dramatic decrease in the Zn signal as measured by XPS, indicating a Cu enrichment in the surface. XPS furthermore showed a small amount of metallic Zn after reduction, indicating a Cu-Zn surface alloy formation.

The combined use of XPS and TEM on the same catalyst particles turned out to be highly beneficial. Due to the low dose rate, *in situ* TEM lacks analytical capabilities, which is provided by XPS. Furthermore, this technique is very sensitive to the oxidation state of the probed elements as well as the surface composition, which was vital information in the present case. Finally, the XPS signal is averaged over the entire sample, contrary to the TEM, where only a very small area is probed. The TEM on the other hand provides the unique capability of directly imaging the nanostructures with atomic resolution. In the present case, this was necessary in order to understand the dynamics between Cu and Zn during oxidation and reduction. Without the TEM images, the encapsulation/decapsulation mechanism would not have been directly seen, and the XPS data would not have been convincingly explained.



Aging of Cu nanoparticles deposited on thin film samples was studied as a simplified model for the complex methanol synthesis (MeOH) catalyst. This approach was inspired by the work of Simonsen et al.[52, 64, 77].

Sintering of Cu catalysts is an interesting problem, and my initial investigations showed that these could be interesting experiments, but the results were inconclusive due to inconsistencies in sample preparation and a low rate of sintering at the applied conditions. This chapter describes some key literature, methods and results from this work.

### 5.1 DEACTIVATION OF CU CATALYSTS

This section will describe some of the important literature on the subject of thermal sintering and long term stability of Cu catalysts with special emphasis on Cu/ZnO systems used for the synthesis of methanol and the low temperature water gas shift reaction. Sintering in this context refers to the increase in average size of nanoparticles in a heterogeneous catalyst over time.

Given the interest in reaction mechanisms on Cu/ZnO/Al<sub>2</sub>O<sub>3</sub>, the literature regarding sintering is somewhat sparse. Sintering and stability are of great concern in the development of commercial catalysts, but it has failed to attract the same attention in the literature as the discussions on reaction mechanisms. Perhaps this is due to the inherent trouble of researching slow phenomena like thermal sintering, especially in an academic setting. Also the lack of access to the right formulations and production methods used by the industry could play a role in how attractive the research field is, and in the quality of the published research. Recently, recipes have been published which match commercial systems in activity, e. g. Baltes et al.[72], but still with a lower stability. We could therefore divide the literature into two categories. First, publications from catalyst manufacturers or publications including studies on commercial catalyst where results and catalyst structure are only superficially described, such as Campbell[116], Young[117] (ICI), Ladebeck [118] (Süd-Chemie) and to some extent Twigg [119, 120] (Johnson Matthey) and Hansen and Nielsen in Handbook of Heterogeneous Catalysis [70] (Haldor Topsøe). Many academic papers use, or makes references to, a 'commercial catalyst', for example the MeOH steam reforming papers [121, 122] or the comparison done in the Baltes paper [72]. The second category is studies

from academia where the catalyst synthesis is very well described, but where it is done differently by different groups and where we don't know how these compare to commercial systems. This makes the interpretation and comparison of data difficult, because we know that the synthesis and formulation is extremely important for activity and stability.

#### 5.1.1 *Routes to deactivation of Cu/ZnO/Al<sub>2</sub>O<sub>3</sub>*

Cu catalysts deactivate by three main routes; chloride poisoning, sulfur poisoning and thermal sintering [119]. Chloride induces severe sintering in Cu-Zn systems because the halides of Cu and Zn have very low melting points. Even trace amount of chlorine will cause severe sintering [119]. Sulfur poisons Cu by adsorbing on the surface, blocking active sites. This is the reason low temperature shift and methanol synthesis on Cu catalysts was long unfeasible, until a change was made from coal to natural gas as feedstock[119]. I will not address those two deactivation mechanisms here, since they can more or less be eliminated in practical operation, and it turns out thermal sintering is what sets the ultimate lifetime of a methanol or low temperature shift catalyst[70].

#### 5.1.2 *Correlation between surface area and activity*

The direct effect of thermal sintering is a decrease in active surface area leading to a decrease in activity. The proportionality between surface area and activity is called the specific activity and in the case where this is constant, there will be a linear relationship between loss of surface area and loss of activity. Sintering may however also cause changes in particle morphology due to increased particle size or changes in the interaction between Cu and ZnO which could further reduce the activity. The specific activity of Cu/ZnO/Al<sub>2</sub>O<sub>3</sub> is a subject of debate, closely interlinked with the discussion on active site and reaction mechanism. It seems established though that ZnO has a promoting effect for methanol synthesis but not for the water gas shift reaction [116].

#### 5.1.3 *Stability of Cu/ZnO/Al<sub>2</sub>O<sub>3</sub>*

As mentioned the main cause of deactivation for a modern methanol synthesis catalyst is thermal sintering. Figure 5.1a from [70] shows the deactivation measured as a decrease in activity for two methanol plants. The activity is seen to drop steeply during the first time of operation, reaching about half of the initial activity after 200 days. After this first region of exponential decrease, the catalyst enters a regime of linear decrease in activity which continues until 800 days where

the activity is roughly a third of the initial value. From the academic world, we have a similar result shown in figure 5.1b[86]. The graph shows the activity of co-precipitated Cu/ZnO/Al<sub>2</sub>O<sub>3</sub> measured at 1 bar in a mixed syngas at 200°C. Interestingly, for this 1 bar experiment the deactivation qualitatively follows the same pattern as for the high pressure plant data shown in Figure 5.1a, which justifies this kind of low pressure testing. A difference to be noted is a shorter region of exponential decay; the catalyst enters the linear regime already after around 50 days and at this point the activity has only dropped by around 35%. Both the testing conditions and catalyst formulation could explain this difference.

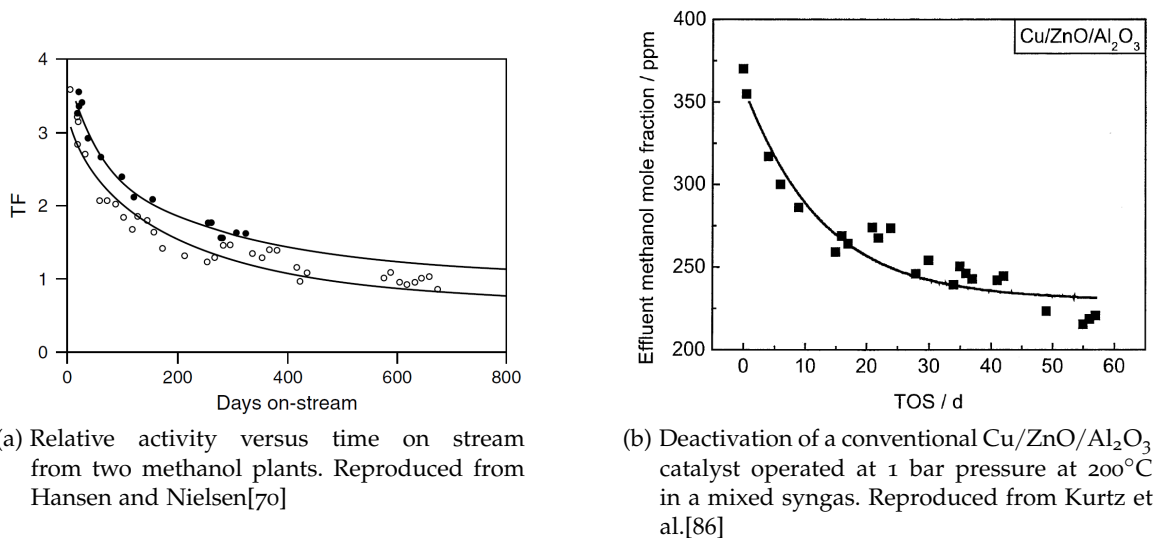


Figure 5.1: Deactivation of Cu/ZnO/Al<sub>2</sub>O<sub>3</sub> catalysts under methanol synthesis conditions.

This overall trend in deactivation is driven by the thermal sintering of Cu particles decreasing the active surface area of Cu and possibly inducing changes in morphology that could lower specific activity. In a 1992 review H. Kung refers to laboratory experiments that show an initial deactivation of up to 60% within 1-20 hours whereafter the catalyst stabilizes[123]. The original source of this is [124] and the experiment was done at 17 bar pressure and 225 °C in a mixed syngas. The catalyst was Cu/ZnO (Al free) prepared by dropwise addition of NaCO<sub>3</sub> to the nitrate solution, an approach that we now know does not yield an optimum result [72]. Kung ascribes this deactivation to Cu sintering, but also mentions a slow approach to steady state surface coverages as a possible explanation for the transient. Such a fast deactivation is not seen in the previously mentioned long term experiments (Figure 5.1a and Figure 5.1b) which is likely due to lack of alumina and bad preparation giving a faster deactivation. This shows why Al<sub>2</sub>O<sub>3</sub> is an important stabilizer in the MeOH synthesis catalyst.

#### 5.1.4 *Effect of the gas environment*

There is much evidence in the literature that the sintering of Cu/ZnO catalysts is not just a simple thermal sintering but is also affected by the gas environment. There are two somewhat contradictory trends in the literature, saying that sintering is enhanced by i) A CO rich gas feed[91, 98, 125, 126], or ii) a CO<sub>2</sub> or H<sub>2</sub>O rich gas feed[98, 118, 127]. In the following I will describe these papers in chronological order.

The first paper that mentions excessive sintering in the absence of CO<sub>2</sub> is a 1979 paper by Herman[91]. The main focus of the paper was to test a range of compositions of binary catalysts, and to report on the finding of Cu<sup>+1</sup> as the active site for the synthesis of methanol. As a side remark a test of one catalyst in H<sub>2</sub>/CO results in a very fast deactivation, which is the interesting part for the present review. The catalysts were prepared by co-precipitation at varying pH by dropwise addition of NaCO<sub>3</sub> to the solution of nitrates, again a procedure that is not optimal[72]. After the standard test in H<sub>2</sub>/CO/CO<sub>2</sub> 70/24/6 at 250 °C, a specific Cu/ZnO/Al<sub>2</sub>O<sub>3</sub> of composition 60/30/10 was tested in H<sub>2</sub>/CO/CO<sub>2</sub> 76/24/0 at the same temperature. During 8 hours the yield dropped from 0.95 kg/(liter hr) to 0.02. Oddly, the authors do not consider that the absence of CO<sub>2</sub> could be the cause of the lower rate, since it is the belief that the methanol is synthesized from CO only. Given later insight, this would presumably be the main reason why the yield drops so significantly when switching to H<sub>2</sub>/CO. There is an interesting bit of information, namely that this catalyst has a red color when removed, contrary to others which are black after test. Because of the authors' belief that Cu<sup>+1</sup> is the active site, they associate the deactivation and change of color with an 'overreduction' of the catalyst. However, this change could also be the result of increased size of Cu particles.

In a later publication from the same group [125], the catalyst deactivation is addressed in greater detail. The intention of that paper is to describe the effect of CO<sub>2</sub> and here they acknowledge the strong effect CO<sub>2</sub> has on the rate of reaction. Their belief is still that methanol is synthesized from CO, and so the role of CO<sub>2</sub> is to keep the catalyst in the right state and avoid 'overreduction'. Later studies have shown that methanol is in fact synthesized from CO<sub>2</sub> [128], at least with a much higher rate than from CO. Even if Klier et al. maintains a picture of the catalyst and reaction mechanism that is less supported today, their results are still interesting. They find that a catalyst subjected to the CO<sub>2</sub>-free syngas for 12 hours loses around 20 percent activity when comparing before and after results in a CO<sub>2</sub> containing gas. After each test the particle size was measured by XRD and the surface area was measured by BET. The results of this are collected in Table 5.1, sorted by the gas composition of the experiment. What I have done is to calculate a geometrical surface area from the Cu

Gas composition CO <sub>2</sub> /CO/H <sub>2</sub>	XRD surface area (m <sup>2</sup> /g)			BET surface (m <sup>2</sup> /g)	Ratio XRD/BET
	Cu	ZnO	Total		
0/30/70	30	66	97	40.9	2.36
2/28/70	32	56	88	37.8	2.32
4/26/70	33	53	86	40.4	2.14
6/24/70	36	66	102	42.1	2.42
8/22/70	34	53	87	37.7	2.31
10/20/70	33	52	85	36.8	2.31
30/0/70	30	41	71	33.0	2.14

Table 5.1: Surface areas from XRD data (calculated by the present author) and BET measurements. [125]

and ZnO particle sizes as measured by XRD, in order to compare this with the BET area which is also included in Table 5.1. The calculated surface areas are consistently higher than what is measured by BET, which is likely because the structure of the catalyst does not expose the entire surface, i.e. the particles are touching. The only significant change in the numbers in Table 5.1 is for the more CO<sub>2</sub> rich gasses where BET surface and calculated ZnO surface starts to shrink. In the paper they explain the drop in BET surface as a filling of micropores with CO<sub>2</sub> and claim that the original surface area can be recovered, but it is unclear if they have actually done this with their own catalyst. Taking a look at the ratio between the surface area calculated from XRD and the BET surface, this is seen to be more or less constant, so sintering of ZnO in the CO<sub>2</sub> (and H<sub>2</sub>O) rich atmosphere could be a plausible explanation for the loss of surface area. For the CO rich gases where the authors see a 20% decrease in activity, severe sintering of Cu is not observed, although the Cu surface for the 0/30/70 composition is the lowest recorded at 30 m<sup>2</sup>/g together with the CO free gas, where sintering of ZnO could also cause Cu sintering due to a break down of the supporting matrix formed by ZnO.

In a 1993 paper C. Kuechen and U. Hoffmann investigate the kinetics of methanol synthesis on a commercial Cu/ZnO catalyst in a 'Berty type' internal recycling reactor at different gas compositions[126]. They find that their catalysts deactivate strongly, especially in gases with little CO<sub>2</sub> content. Figure 5.2 shows the reaction rate over time displaying clear deactivation behavior. The effect is strongest for the tests in the most CO-rich feed gas where the deactivation is very strong, whereas in CO-free syngas there is hardly any deactivation in this setup. It is interesting that the authors find the deactivation to be so strong, which is likely due to a combination of an alumina free catalyst as well as a very long test time.

With respect to activity, they find by far the highest rates for a CO<sub>2</sub> content of 2-4% when testing a fresh catalyst. At higher CO<sub>2</sub> contents

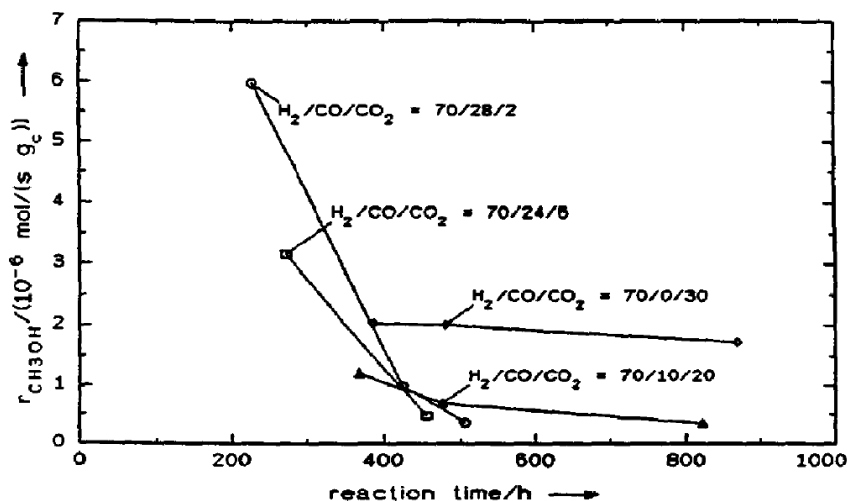


Figure 5.2: Catalyst deactivation. The plot shows methanol rate over time for various gas compositions. Catalyst is commercial Cu/ZnO,  $p = 5$  bar,  $T = 513$  K. Kuechen and Hoffmann 1993[126]

the rate drops again before starting a monotonic increase towards the maximum CO<sub>2</sub> content of 30%. For the deactivated catalyst, there is no peak in the activity as a function of CO<sub>2</sub> content, here activity just steadily increases with increasing CO<sub>2</sub> content.

Another contribution considering the effect of syngas composition is a 1993 paper from J. Ladebeck of Süd-Chemie[118]. It describes a newly developed catalyst which is more resistant to deactivation in a CO<sub>2</sub>-rich syngas. The underlying premise here is that a high CO<sub>2</sub> content increases the deactivation rate of a traditional catalyst, "by almost an order of magnitude between 3 and 12 vol% CO<sub>2</sub>". They looked further into this and found, in an electron microscopy study, that the copper crystallite growth doubles in a CO<sub>2</sub>-rich gas. By exposing the catalyst to steam at high pressure and 300°C they found a crystallite growth rate increase of 2.5 compared to thermal treatment alone. It is stated that the copper starts to migrate, but not if it is particles or atomic species, forming large agglomerates. In addition, water is found to damage the matrix material (ZnO) but it is unclear in what way this happens. The conclusion of this is that the product water has a detrimental effect on the catalyst in CO<sub>2</sub>-rich feed gases. Based on these findings, "a method was found to obtain high dispersion and fix isolated copper clusters on the support by applying a new precipitation procedure along with major changes in subsequent production steps". This is a good example of literature from a commercial setting, that cannot reveal anything substantial about otherwise impressive results.

Many of the papers described above have mainly focused on MeOH synthesis activity, and results on deactivation have been a 'side effect'. One of the first well described and thorough academic investigations

specifically targeted on Cu sintering is the 1999 paper by Sun, Metcalfe, and Sahibzada "Deactivation of Cu/ZnO/Al<sub>2</sub>O<sub>3</sub> Methanol Synthesis Catalysts by Sintering"[98]. Here the authors study short time sintering behavior under differential and finite conversion for various CO/CO<sub>2</sub> ratios at a constant hydrogen content of 80%. The syngas pressure was 45 bar and the activity tests were performed at 250 °C. The catalyst was a ternary Cu/ZnO/Al<sub>2</sub>O<sub>3</sub> system prepared by a two step precipitation from metal nitrates. During and after testing the Cu surface area was measured by N<sub>2</sub>O titration[88–90].

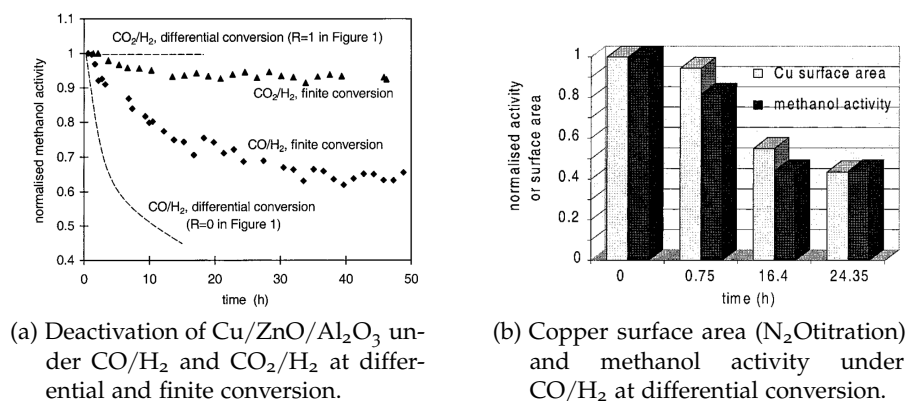


Figure 5.3: Deactivation of Cu/ZnO/Al<sub>2</sub>O<sub>3</sub>. Figures reproduced from Sun, Metcalfe, and Sahibzada[98]

For the test at differential conversion, the rate of methanol formation was found to be an order of magnitude higher for CO<sub>2</sub>/H<sub>2</sub> than for CO/H<sub>2</sub> pointing to the higher intrinsic rate of CO<sub>2</sub> hydrogenation also described elsewhere. At finite conversion however, the rates of the two reactions were found to be similar, with CO/H<sub>2</sub> unchanged and CO<sub>2</sub>/H<sub>2</sub> lowered a lot, which is thought to be caused by product water from conversion of CO<sub>2</sub>, as the authors have also previously shown[129].

The deactivation behavior for the two extreme cases, CO and CO<sub>2</sub>-free syngas, at finite and differential conversion is shown in Figure 5.3a. At differential conversion, there is no deactivation in the case of CO<sub>2</sub>/H<sub>2</sub>, whereas there is a strong effect for CO/H<sub>2</sub>. This clearly shows that the presence of CO accelerates the deactivation, in line with previously quoted results[91, 126]. In the case of finite conversion where methanol is present in the stream, the deactivation slows down in the case of CO/H<sub>2</sub>, but accelerates for CO<sub>2</sub>/H<sub>2</sub>. This could indicate that sintering is caused by presence of CO from the reverse water gas shift reaction, or that it is due to the presence of water also shown to accelerate sintering[118].

Figure 5.3b shows the activity together with the normalized Cu surface measured during the aging experiment. It is interesting to note here that the surface area seems to closely follow the activity, which points to sintering of Cu as the main deactivation mechanism. This

also means that the sintering leads to no change in specific activity, meaning the concentration of step sites per surface area is constant assuming the reaction is structure sensitive as claimed in [16].

The role of different gas components in the deactivation of Cu catalysts has been evaluated by varying the gas compositions, both to directly investigate sintering[98, 118] or indirectly in studies of kinetics and reaction mechanism[91, 125, 126]. Several of these show a tendency towards strongly increased sintering in a pure CO/H<sub>2</sub> syngas, which has been interpreted as an overreduction. Those results also fall in line with theoretical calculations, showing that the predominant Cu transport species on ZnO is CuCO[130].

### 5.1.5 Sintering mechanisms

The thermodynamic driver for sintering is the high surface energy of the small particles, and this energy is lowered as the particles grow[131]. For the sintering of supported metallic nanoparticles, we distinguish between two modes based on how material transport from small to larger particles is mediated[132, 133]. The first mode is migration and coalescence, which is the random movement of small nanoparticles that eventually meet and coalesce into larger particles (Figure 5.4a). The second mode is transport of atomic or similar entities that detach and migrate, where the net transport is from smaller to larger particles. This is referred to as Ostwald ripening (Figure 5.4b).

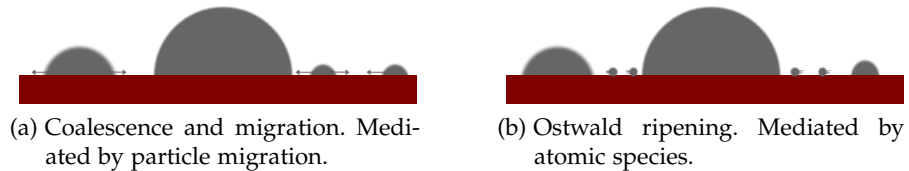


Figure 5.4: Sintering mechanisms. Particle growth may either proceed via (a) migration and coalescence of small particles, or (b) by detachment, diffusion and attachment of single atoms.

In my study of Cu on SiO<sub>x</sub>, I have only observed Ostwald ripening, so I will introduce this in more detail.

The concentration of atomic species at the edge of a particle is governed by the Gibbs-Thomson relation, which describe the relation between concentration and particle radius of curvature R[77, 132]:

$$c_p = c_p^\infty \exp\left(\frac{2\gamma\Omega}{kTR}\right) \quad (5.1)$$

where  $c_p^\infty$  is the concentration at the edge of an infinitely large particle,  $\gamma$  is the particle surface energy,  $\Omega$  is the atomic volume,  $k$  the Boltzmann constant and  $T$  the temperature. Equation 5.1 shows that

the surface concentration of atomic species increases for decreasing radius, such that the concentration around small particles will be higher than around large particles. If the atomic species are able to migrate on the support, the net effect of this will be that mass is transferred from small to large particles. Furthermore, Equation 5.1 implies that there must be a critical radius of curvature  $R^*$ , for which particles neither grow nor shrink. This can be approximated by the arithmetic mean of the particle ensemble[77, 134, 135].

A common approach to the description of Ostwald ripening of particles on a support is a mean field description of the concentration of atomic species on the support. Here it is assumed that the concentration is the same everywhere beyond a certain screening distance from the particles[77]. The effect of this is that the particle positions do not matter, i. e. there is no dependency on interparticle distances. There is however experimental evidence that the position does matter, both in planar[64] and three dimensional catalysts[136], but the mean field approximation is still a good description for ensemble averaged sintering behavior[64].

In the treatment of data obtained in the present experiment, I will utilize a model for the change of the radius of individual particles,  $\frac{dR}{dt}$ . This was developed by Wynblatt and Gjostein[132] and is excellently explained by Simonsen[77]. The expression for  $\frac{dR}{dt}$  depends on the limiting factor for the growth. The two possible cases are limitation by interface processes (detachment of atoms from the particles), or diffusion on the substrate. For the interface controlled ripening,  $\frac{dR}{dt}$  is governed by:

$$\frac{dR}{dt} = \alpha_i \frac{\alpha'_i}{R^2} \left[ \frac{R}{R^*} - 1 \right] \quad (5.2)$$

where  $\alpha'_i$  is a constant with unit  $\text{nm}^{-1}\text{min}^{-1}$  and  $\alpha_i$  is a function of the contact angle  $\theta$  between particle and support:

$$\alpha_i = \frac{\sin(\theta)}{(1/2 - 3/4 \times \cos(\theta) + \cos^3(\theta))} \quad (5.3)$$

I will only present results using the interface controlled model, since both the interface controlled and the diffusion controlled model give equally good descriptions of the experimentally observed ripening behavior as also reported by Simonsen et al.[64].

## 5.2 SINTERING OF CU NANOPARTICLES IN THE TEM

Studying the mechanism of sintering in a three-dimensional catalyst presents some challenges. Sintering, be it by Ostwald ripening or particle migration, proceeds via transport of the active element on the catalyst support surface. In a three dimensional system, this support

surface is neither well defined, nor homogenous, so there may be strong local effects which make it difficult to do a quantitative study. On the other hand, two-dimensional model systems have successfully been applied to study sintering *in situ* in the TEM[52]. These have several advantages: First, it is much simpler to track the movements and size evolution of individual particles on a flat surface. Second, it turns out that the the resulting particle size distribution (PSD) obtained after Ostwald ripening on a flat support[52] match better with the LSW distribution expected from Ostwald ripening[137]. Similar experiments on three-dimensional supports have not been able to produce the LSW-distribution, but have always led to log-normal size distributions[138].

I have performed experiments similarly to Simonsen et al.[52] with Cu on SiO<sub>x</sub> films. The intention was to investigate the effect of the gas atmosphere on the sintering behavior, by performing aging experiments in H<sub>2</sub>, H<sub>2</sub> + CO and H<sub>2</sub> + H<sub>2</sub>O. Sintering is an inherently slow process and therefore it is necessary to develop a scheme for accelerated aging. Industrial MeOH synthesis runs at pressures of 50-100 bar and temperatures of 200 - 300 °C. In the TEM, the pressure is restricted to a few mbar. This is a potential problem, as the sintering kinetics may very well depend on gas pressure[139]. The sintering process can be accelerated by increasing the temperature, and the experiments described here were all run at an increased temperature of 350 °C. Another way to increase the sintering is by starting with smaller particles[52] or a broader size distribution[136]. The effect of the initial PSD was not pursued in the present study.

### 5.2.1 *Wet impregnation of Cu*

The following experiments were the first *in situ* TEM experiments of my PhD and a first attempt at visualizing the sintering of Cu nanoparticles. They were to some extent the 'quick and dirty' approach, using the material at hand and the experimental approach could have been more systematic. I have chosen to report the data from wet impregnation here because they show a high degree of sintering, contrary to the later experiments, and because they naturally lead to the more systematic studies reported later in this thesis.

Samples were prepared on stainless steel TEM grids with a thin SiO<sub>x</sub> film. The Si/O stoichiometry was not available from the manufacturer and they refer to the material as SiO<sub>x</sub>. x is assumed to be between 1 and 2. Grids were supplied by SPI<sup>1</sup>. Cu on silica is the simplest starting point for these experiments. Aging of three dimensional Cu/SiO<sub>2</sub> has been studied as a model for MeOH catalysts[114, 136].

The first sample preparation was a wet impregnation of Cu. This method of sample preparation was later described by Damsgaard et

---

<sup>1</sup> <http://www.2spi.com/>

al.[140]. The TEM grid was placed on a piece of lens paper. A drop of  $\text{Cu}(\text{NO}_3)_2$  solution was placed on the grid in a way that completely wetted grid and paper, such that only a thin film of solution would dry out on the grid. After drying, the grid was placed in the Gatan heating holder (Section 2.2.1) and inserted into the microscope. After reduction this preparation resulted in patches of Cu particles in sizes ranging from 1 to 20 nm (an example of this can be seen in e. g. Figure 5.6, page 100).

### 5.2.2 Experimental procedure

Experiments will be shown for three gas compositions;  $\text{H}_2 + \text{CO}$ ,  $\text{H}_2 + \text{CO}_2$  and  $\text{H}_2 + \text{H}_2\text{O}$ . The experimental procedure for each sample was similar. First 1 mbar  $\text{H}_2$  gas was introduced in the e-cell and then the sample was heated to 30 °C with a heating rate of 350 °C/min. The sample was then held for approximately 4 hours in 1 mbar  $\text{H}_2$  before introducing the second gas. A total pressure of 2 mbar was aimed for, i. e. a 1:1 composition of the two gas components.

TEM images were acquired in one area with high frequency. This is referred to as the *in situ* area. Another area was only imaged a few times, this is referred to as the reference area. This was done to control for effects of electron illumination. Imaging in the *in situ* area occurred primarily during the time period with a two component gas.

After measurement, particle radii were measured manually in ImageJ<sup>2</sup>. From the measured radii in a given area, three parameters were compared over time. These were mean radius, number of particles and total volume, calculated as the sum of volumes of all measured particles, assuming a spherical shape. Due to the inhomogeneous Cu particle sizes between different regions, these parameters can only be used to follow a specific area over time.

### 5.2.3 Varying gas environment

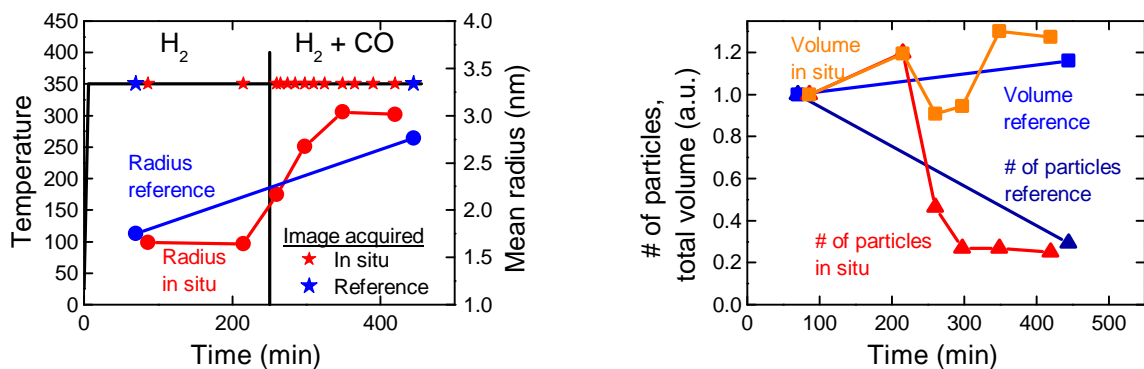
#### 5.2.3.1 $\text{H}_2 + \text{CO}$

The first experiment was sintering in a mixture of  $\text{H}_2$  and CO. The progress of the experiment is outlined in Figure 5.5a together with the development of the mean radius for *in situ* and reference areas. Development of total volume and number of particles is shown in Figure 5.5b. Corresponding TEM images are shown in Figure 5.6 (*in situ* area) and Figure 5.7 (reference area).

In this experiment the *in situ* area was imaged after 86 min and 215 min in 1 mbar  $\text{H}_2$  in order to evaluate the sample aging in pure

---

<sup>2</sup> <http://imagej.nih.gov/ij/>



(a) Temperature, time of image acquisition and mean particle radius as a function of time.

(b) Number of particles and total volume as a function of time in *in situ* and reference region.

Figure 5.5: Wet impregnated Cu/SiO<sub>x</sub> in H<sub>2</sub> + CO.

(a) 0-250 min: 1.04 mbar H<sub>2</sub>, 250-455 min 1.04 mbar H<sub>2</sub> + 0.92 mbar CO. Temperature 350 °C. ★ indicate times for image acquisition in *in situ* region. ☆ indicate times for image acquisition in reference region. Mean particle radius for *in situ* and reference region as measured in the TEM images shown in Figure 5.6 (*in situ*) and Figure 5.7 (reference). (b) Number of particles and total volume (spherical approximation) for *in situ* and reference areas. Normalized to first measurement in respective area.

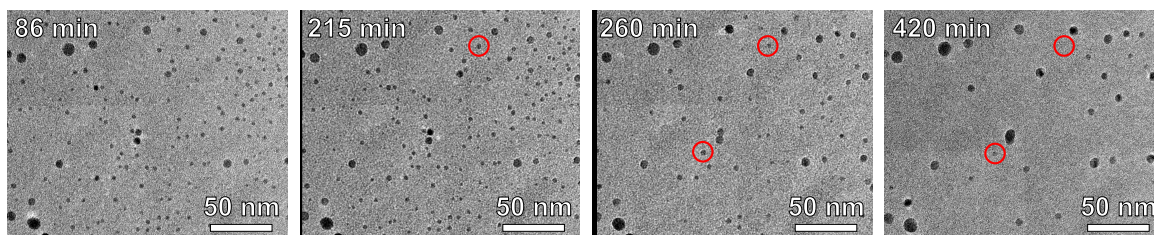


Figure 5.6: TEM images from *in situ* area acquired at 86 min (1.04 mbar H<sub>2</sub>), 215 min (1.04 mbar H<sub>2</sub>), 260 min (1.96 mbar H<sub>2</sub> + CO) and 420 min (1.96 mbar H<sub>2</sub> + CO). Red circles mark particles shrinking between consecutive frames. Temperature 350 °C for all.

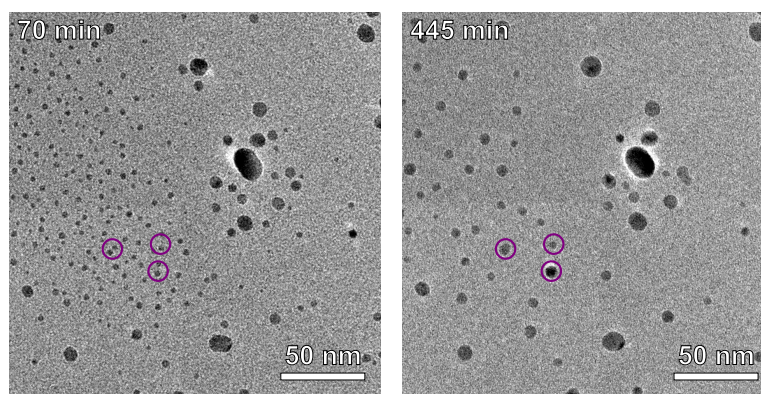


Figure 5.7: TEM images from reference area acquired at 70 min (1.04 mbar H<sub>2</sub>) and 445 min (1.96 mbar H<sub>2</sub> + CO). Purple circles mark positions of particles that grow larger. Temperature 350 °C for all.

H<sub>2</sub>. No significant change in mean radius was seen between the two measurements. The number of particles increased, which is assigned

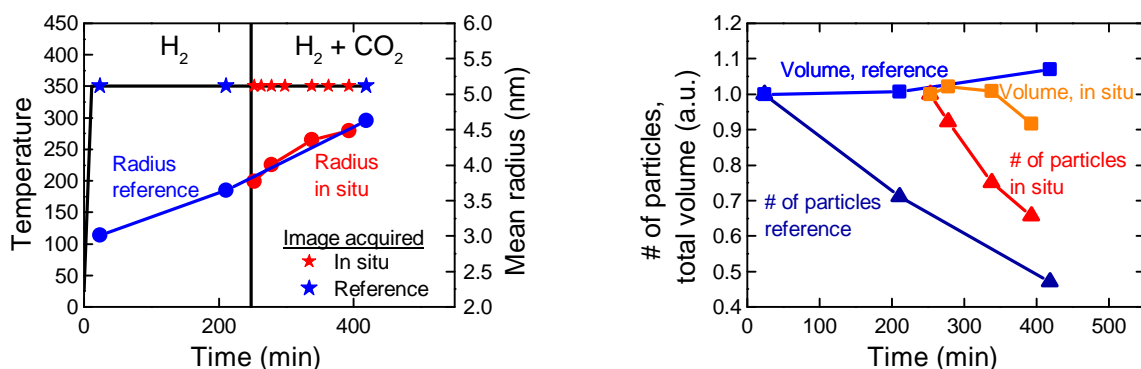
to different focus settings in the two images. This means that some of the smaller particles may only be seen in the image acquired after 215 min (Figure 5.6). This underlines the importance of strict image settings in this type of experiment.

After introduction of CO, the particle size increases steadily and the number of particles accordingly goes down sharply to 25% of the original value. The calculation of geometrical volume (Figure 5.5b) suggests that there is mass conservation, even if the points are somewhat scattered due to uncertainty of the measured radii. A more detailed analysis of the uncertainty on the measurements were not pursued for the results presented here. The absolute number of particles in the *in situ* area was 168 and 42 after 86 and 420 min respectively. In the reference area initial and final numbers were 239 and 70 after 70 min and 445 min respectively. This significant lowering of the number of particles is clearly seen in the images in Figure 5.6 and Figure 5.7.

The result presented here demonstrates that the addition of CO boosts the sintering of Cu nanoparticles on  $\text{SiO}_x$ . As expected, the smallest Cu particles clearly sinter the most, and the small particles grow fewer and larger. The purple circles in Figure 5.7 mark the position of three surviving particles after 445 min. The same positions in the image acquired after 70 min shows that particles were already present in these positions, and so these grew larger. From the *in situ* area, red circles in Figure 5.6 mark examples of shrinking particles between consecutive images. One is shrinking from 215 min to 260 min and is completely gone after 420 min. Another is shrinking in size from 260 min to 420 min. Shrinkage of the smallest particles of the ensemble is clear evidence of Ostwald ripening.

5.2.3.2 H<sub>2</sub> + CO<sub>2</sub>

The second experiment was sintering in a mixture of H<sub>2</sub> and CO<sub>2</sub>. The progress of the experiment is outlined in Figure 5.8a together with the development of the mean radius for *in situ* and reference areas. Development of total volume and number of particles is shown in Figure 5.8b. Corresponding TEM images are shown in Figure 5.9 (*in situ* area) and Figure 5.10 (reference area).



(a) Temperature, time of image acquisition and mean particle radius as a function of time

(b) Number of particles and total volume as a function of time in *in situ* and reference region.

Figure 5.8: Wet impregnated Cu/SiO<sub>x</sub> in H<sub>2</sub> + CO<sub>2</sub>.

(a) 0-248 min: 1.05 mbar H<sub>2</sub>, 248-418 min 1.05 mbar H<sub>2</sub> + 0.85 mbar CO<sub>2</sub>. Temperature 350 °C. \* indicate times for image acquisition in *in situ* region. \* indicate times for image acquisition in reference region. Mean particle radius for *in situ* and reference region as measured in the TEM images shown in Figure 5.9 (*in situ*) and Figure 5.10 (reference). (b) Number of particles and total volume (spherical approximation) for *in situ* and reference areas. Normalized to first measurement in respective area.

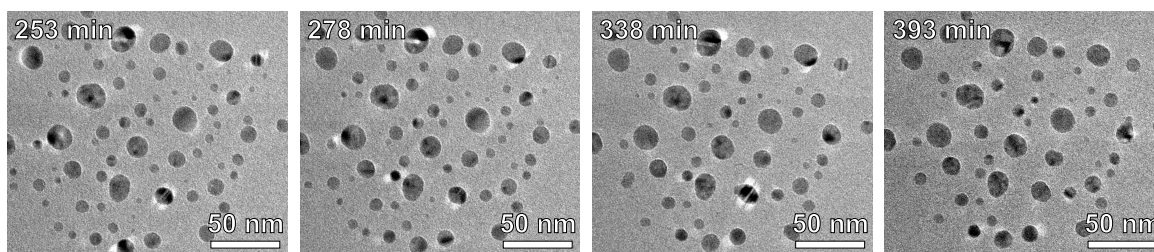


Figure 5.9: TEM images from *in situ* area acquired at 253 min, 278 min, 338 min and 393 min. 1.05 mbar H<sub>2</sub> + 0.85 mbar CO<sub>2</sub> and temperature 350 °C for all.

Starting in the time interval 0-248 min with only H<sub>2</sub> gas, we see that there is an increase in particle size and increase in number of particles in the reference area, imaged at 24 min and 211 min (Figure 5.10). This clearly shows sintering in pure H<sub>2</sub> gas contrary to the previous experiment. After introduction of CO<sub>2</sub> the rate of sintering in the reference region continues at a similar rate as seen in the image acquired

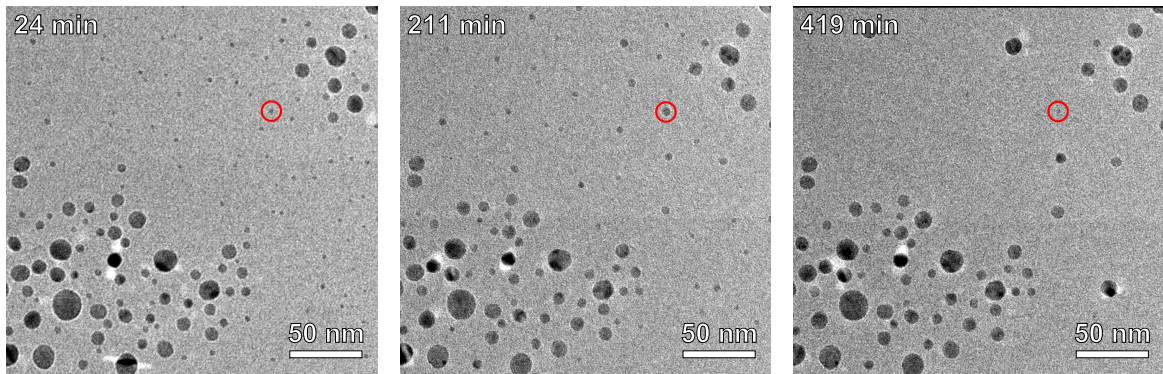


Figure 5.10: TEM images from reference area acquired at 24 min (1.05 mbar  $H_2$ ), 211 min (1.05 mbar  $H_2$ ) and 419 min (1.90 mbar  $H_2 + CO_2$ ). Temperature 350 °C for all. Red circle marks a particle that grows from 24 min to 211 and then shrinks from 211 min to 419 min.

after 419 min. The *in situ* area was only imaged after introduction of  $CO_2$ . Here, a steady decrease in particle number is also seen and a corresponding increase in mean radius.

There are two notable differences here as compared to experiment in  $H_2 + CO$ . First, that sintering occurs now in pure  $H_2$ . This may be due to variations in the initial sizes and distribution of particles or it may be due to a difference in the local temperature for the two areas. Second that  $CO_2$  does not increase the sintering rate as much as  $CO$ .

Looking at the particle positions and development in the same area, it is again indicative of Ostwald ripening. The red circles in Figure 5.10 mark a particle that first grows when it is surrounded by smaller particles (from 24 to 211 min) and then shrinks as it suddenly finds itself to be only surrounded by larger particles (211 to 419 min).

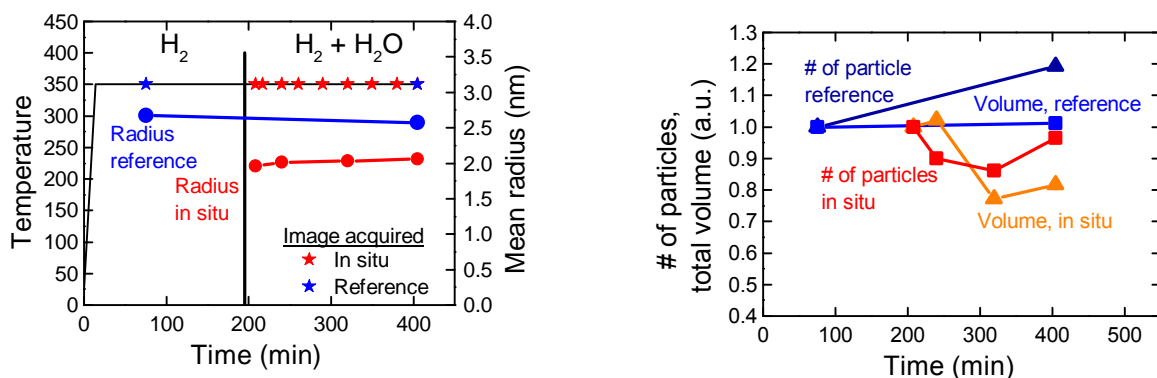
### 5.2.3.3 $H_2 + H_2O$

The third experiment was sintering in a mixture of  $H_2$  and  $H_2O$ . The progress of the experiment is outlined in Figure 5.11a together with the development of the mean radius for *in situ* and reference areas. Development of total volume and number of particles is shown in Figure 5.11b. Corresponding TEM images area are shown in Figure 5.12 (*in situ* area) and Figure 5.13 (reference area).

The result of this was remarkably different from the previous experiments in that no signs of sintering was observed. The results from the reference area recorded after 75 min in  $H_2$  and then an additional 120 min in  $H_2$  followed by 210 min in  $H_2 + H_2O$  indicates no sintering (Figure 5.11a and Figure 5.13). The total volume in the *in situ* area indicates a loss of mass, which could be a beam effect[52]. A different explanation would be a decreased wetting of the Cu particles, i. e. a higher contact angle, which falls in line with the results from Hansen et al.[22] for Cu on ZnO. A higher contact angle could mean a reduc-

tion in projected area leading to a decrease in volume for the same amount of particles as it is the case for the *in situ* area after 405 min.

Compared to the other gas mixtures, no sintering was observed for  $H_2 + H_2O$ . This may suggest that the presence of  $H_2O$  has a slowing effect on sintering. For the first two experiments, TEM images indicated that sintering proceeded via Ostwald ripening. A possible explanation for the retarding effect of water, could therefore be hydroxylation of  $SiO_x$  [141] which may slow down or prevent transport of Cu species on the surface[142].



(a) Temperature, time of image acquisition and mean particle radius as a function of time.

(b) Number of particles and total volume as a function of time in *in situ* and reference region.

Figure 5.11: Wet impregnated  $Cu/SiO_x$  in  $H_2 + H_2O$ .

(a) 0-195 min: 1.06 mbar  $H_2$ , 195-405 min 1.06 mbar  $H_2 + 0.82$  mbar  $H_2O$ . Temperature 350 °C. ★ indicate times for image acquisition in *in situ* region. ★ indicate times for image acquisition in reference region. Mean particle radius for *in situ* and reference region as measured in the TEM images shown in Figure 5.12 (*in situ*) and Figure 5.13 (reference). (b) Number of particles and total volume (spherical approximation) for *in situ* and reference areas. Normalized to first measurement in respective area.

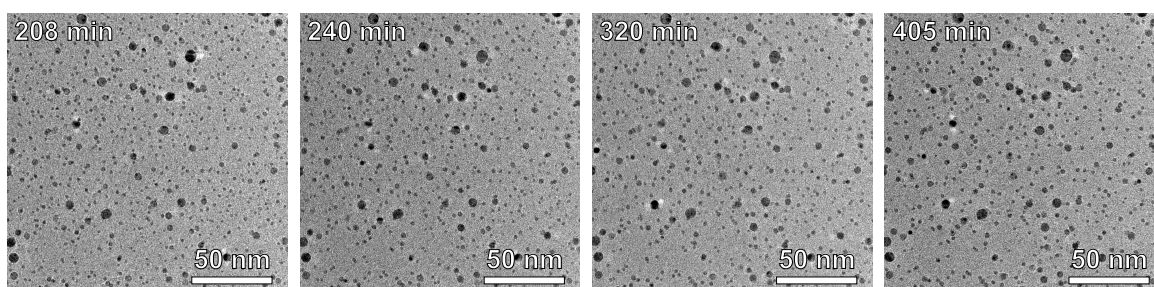


Figure 5.12: TEM images from *in situ* area acquired at 208 min, 240 min, 320 min and 405 min. 1.06 mbar  $H_2 + 0.82$  mbar  $H_2O$  and temperature 350 °C for all.

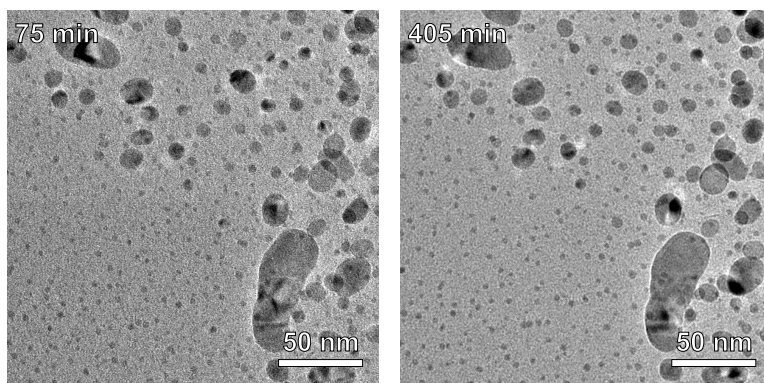


Figure 5.13: TEM images from reference area acquired at 75 min (1.06 mbar  $\text{H}_2$ ) and 405 min (1.88 mbar  $\text{H}_2 + \text{H}_2\text{O}$ ). Temperature 350 °C for all.

#### 5.2.4 Conclusions from wet impregnated samples

Cu nanoparticles were prepared on a  $\text{SiO}_x$  film by wet deposition of  $\text{Cu}(\text{NO}_3)_2$ . The samples were exposed to gases at mbar pressures and a temperature of 350 °C. Specific areas were followed over time and the size, number and location of Cu nanoparticles were tracked. Results obtained in an atmosphere of 1 mbar  $\text{H}_2$  was inconclusive, as sintering was only seen in one experiment. An atmosphere of 1.9 mbar  $\text{H}_2 + \text{CO}$  significantly increased the rate of sintering. Sintering was also observed in an atmosphere of 1.9 mbar  $\text{H}_2 + \text{CO}_2$ , at a rate similar to what was observed in pure  $\text{H}_2$  for the same sample. No sintering was observed in an atmosphere of  $\text{H}_2 + \text{H}_2\text{O}$ , which could suggest a retarding effect of water vapor on the migration of Cu species.

For all experiments where sintering was observed, no particle movement was not seen and shrinkage of small particles was observed. Both indicate an Ostwald ripening mechanism.

With respect to sintering rates, one should note that the samples shown here were highly inhomogeneous. It is therefore difficult to quantitatively compare the rate of sintering between different areas and different samples. Also, there is no control over the starting PSD, which is typically broad for these samples. This makes modeling of the sintering[52, 64] difficult or impossible.

### 5.3 DEPOSITION BY CLUSTER SOURCE

To get a more homogeneous starting point for the experiments, samples were prepared by cluster deposition. The cluster source is a physical nanoparticle synthesis based on sputtering, agglomeration and mass filtering. In this way, it is possible to create nanoparticles with a very narrow size distribution[99, 100]. This technique was also used to produce CuZn nanoparticles, and was described in Chapter 4. In the present case, a pure Cu target was used.

For a quantitative study of sintering it is preferable with a well controlled particle size and density, and a reproducible sample preparation. This is necessary in order to compare rates across different samples, in order to investigate e. g. the effect of gas atmosphere.

### 5.3.1 Sample preparation

A TEM grid was inserted in the deposition chamber, and size selected clusters were deposited. Different samples were prepared with Cu particle diameters of 3-5 nm and coverages of 10%, calculated as the projected area of the nanoparticles divided by the total sample area. During deposition, the total current is measured, as well as a deposition time. Since each particle is expected to carry 1 elementary charge, this results in a direct measure of the number of particles.

Here I will introduce the relevant numbers for deposition. In one experiment (images shown in Figure 5.14), the mass filter was adjusted to allow Cu particles of diameter  $d_{Cu} = 3.5\text{nm}$ . The deposition current was  $I_{depo} = 4.5\text{ pA}$ , and the deposition time was 45 min, or  $t_{depo} = 2700\text{ s}$ . The total number of particles  $N_{depo}$  can be calculated as:

$$N_{depo} = I_{depo} \times \frac{t_{depo}}{e} \quad (5.4)$$

$$N_{depo} = 4.5 \times 10^{-12} \frac{\text{C}}{\text{s}} \times \frac{2700\text{s}}{1.6 \times 10^{-19}\text{C}} \quad (5.5)$$

$$N_{depo} = 7.59 \times 10^{10} \quad (5.6)$$

During deposition, the TEM grid was masked by a circular hole of diameter 2 mm. This means that the measured number of particles was distributed over an area  $A_{depo} = \pi\text{ mm}^2 = \pi \times 10^{12}\text{ nm}^2$ . Using that the projected area of one particle is  $A_{particle} = \pi \times \left(\frac{3.5}{2}\right)^2\text{ nm}^2$  we can calculate coverage (unit of %) and particle density  $\rho$  (unit of  $\text{nm}^{-2}$ ).

$$\begin{aligned} \text{coverage} &= \frac{N_{depo} \times A_{particle}}{A_{depo}} \times 100\% \\ \text{coverage} &= \frac{7.59 \times 10^{10} \times \left(\frac{3.5}{2}\right)^2\text{ nm}^2}{10^{12}\text{ nm}^2} \times 100\% = 23\% \end{aligned} \quad (5.7)$$

$$\begin{aligned} \rho &= N_{depo}/A_{depo} \\ \rho &= \frac{7.59 \times 10^{10}}{\pi^{12}\text{ nm}^2} = 0.024\text{ nm}^{-2} \end{aligned} \quad (5.8)$$

Typically we have designed the deposition to arrive at a predefined coverage. After deposition, the sample was exposed to air and transported to the TEM. Alternatively samples were stored in a glovebox

until used. The Cu particles are expected to oxidize during transfer, so samples were always reduced in the microscope. Figure 5.14a shows a sample area after reduction and Figure 5.15a shows the PSD after reduction. The target diameter was 3.5 nm, and the deposition density was  $0.024 \text{ nm}^{-2}$  (23% coverage).

The measured coverage was  $0.004 \text{ nm}^{-2}$ , significantly lower than the target and the measured mean size was 3.77 nm with a standard deviation of 0.92 nm. This PSD is broader than expected from the deposition technique, Nielsen et al.[100] report e.g.  $2.8 \pm 0.5 \text{ nm}$  for nanoparticles of Ru. The broader PSD we measure for Cu is likely not due to the initial size distributions, but rather due to particles merging. This can happen at high coverage when particles land close to other particles, and during transfer when the sample is oxidized, leading to an increase in maximum particle size, which may cause particles to merge.

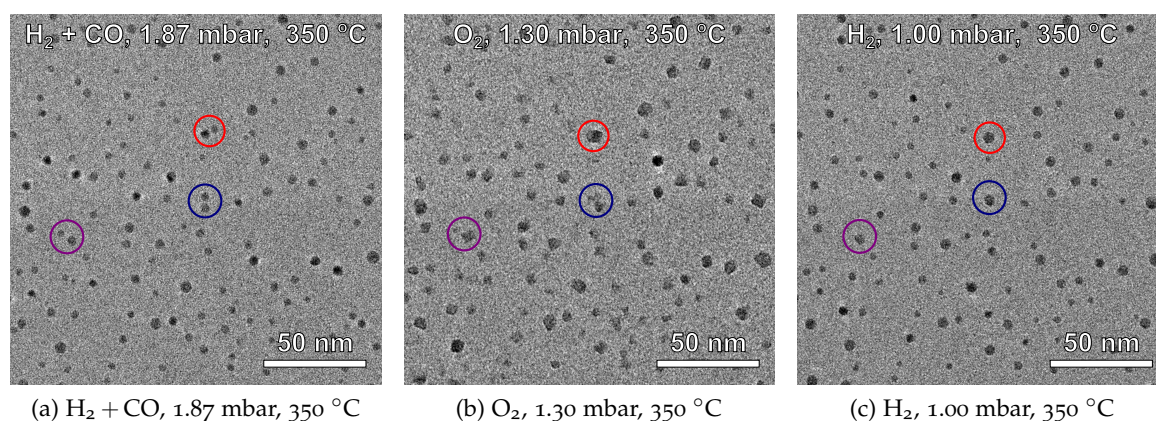


Figure 5.14: Size selected Cu nanoparticles, reduction, oxidation, reduction. 3.5 nm,  $0.024 \text{ particles/nm}^2$  (15% coverage). (a) Reduced, 1.00 mbar  $\text{H}_2 + 0.87 \text{ mbar CO}$ , 350 °C. Image acquired after 5 hours at these conditions. (b) Oxidation, 1.30 mbar  $\text{O}_2$ . Image acquired after 1 hour at these conditions. (c) Re-reduction, 1.00 mbar  $\text{H}_2$ , 350 °C. Image acquired after 2 hours at these conditions. Some particles merged after oxidation (red circle). Possible redispersion after oxidation (blue circle). Some particle merged after re-reduction (purple circle).

To illustrate this, Figure 5.14b shows the same area as Figure 5.14a in 1 mbar  $\text{O}_2$  at 350 °C. Clearly the particles have grown in size, and it is evident that several particles have merged (red circle indicate an example of this). Figure 5.15b shows the PSD after oxidation, and the broadening is evident. A significant number of larger particles ( $>5 \text{ nm}$ ) were measured in these images. Small particles ( $<3 \text{ nm}$ ) get more frequent, which may be due to redispersion upon oxidation. One possible redispersion event was seen in the *in situ* area images in Figure 5.14 (blue circle). Note that these two particles merge again after reduction. Finally, the same sample was reduced again in  $\text{H}_2$ , which caused the particles to shrink and the PSD to narrow again as seen in the TEM image (Figure 5.14c) and PSD (Figure 5.15c).

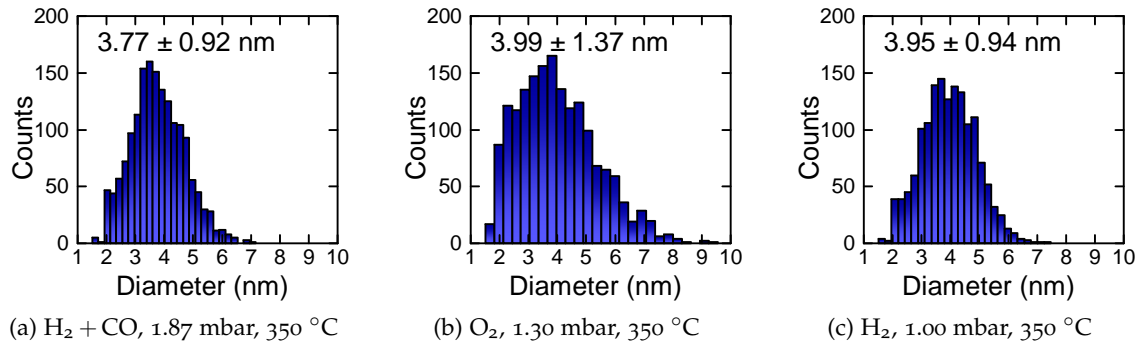


Figure 5.15: Histograms measured from random areas at the same time as the images in Figure 5.14. 8 images used for each measurement.

(a) Reduced particles. (b) Oxidized particles, broader PSD. (c) Re-reduced particles PSD narrowing again.

The above is not sufficient to explain the discrepancy between target density ( $0.024 \text{ nm}^{-2}$ ) and measured density ( $0.004 \text{ nm}^{-2}$ ). This must be due to a problem in the deposition. Later depositions matched the target density better (Section 5.3.4).

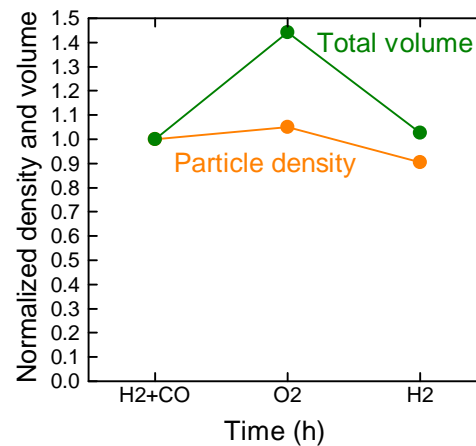


Figure 5.16: Particle density and total volume (normalized) for the three conditions shown in Figure 5.14 and Figure 5.15

Figure 5.16 compares particle density and total volume in the PSDs from Figure 5.15. It is evident that the oxidation leads to a significant increase in total volume, stemming from the increased volume and thereby projected area upon oxidation. This is similar to what was shown in Chapter 4 for Cu/ZnO nanoparticles. Particle density increases slightly on oxidation and is reduced by ca 15 % upon re-reduction.

These results demonstrate the negative effect of Cu oxidation in terms of maintaining a narrow size distribution in the pristine sample. A vacuum or protected atmosphere transfer[143] was discussed, but it was deemed beyond the scope of the current project.

### 5.3.2 *Measurement procedure*

Having a more homogeneous size distribution over the sample allowed the acquisition of broader statistics by measuring many particles in previously unilluminated areas as well as *in situ* areas that were tracked over time. This was done according to the procedure devised by Simonsen et al.[64].

The samples were subjected to an accelerated aging scheme: After inserting the sample in the microscope, 1 mbar  $H_2$  was introduced to the e-cell and the temperature was raised to 350 °C. After reaching a stable temperature, a second gas component could be introduced and the total pressure raised to ca. 1.9 mbar. The sample was held at this condition for 6 hours and imaged during the course of the experiment. One *in situ* area was followed over time, and an image acquired every 30 minutes. At each time after imaging the *in situ* area, the stage was moved to a previously unilluminated area where 8 images were acquired. Between each of these 8 acquisitions, the stage was moved a length of at least the diameter of the electron beam. This is to ensure that there had been no previous illumination. A typical beam radius was 2  $\mu\text{m}$ . A dose rate of  $100 e^-/(\text{\AA}^2\text{s})$  was used with an exposure time of 3 s. Images were acquired using the full resolution of the CCD of 2048 by 2048 pixels<sup>2</sup> and with a pixel size of 0.11 nm. This yields around 250 incident electrons per pixel on the ccd per image recorded. The measured SNR in Figure 5.14a is 25 as calculated by Equation 2.14. The choice of pixel size in an experiment like this, is a compromise between resolving the smallest particles, and maintaining a large field of view to image a sufficient number of particles per frame. With a pixel size of 0.11 nm it should be possible to resolve sub-nm particles. Such small entities were however not possible to distinguish from the  $\text{SiO}_x$  background. The field of view was 225 by 225, or 50625 nm<sup>2</sup>. With an expected particle density of 0.014 particles/nm<sup>2</sup> (3 nm particles, 10% coverage), this should result in ca 700 particles per image.

### 5.3.3 *Automated particle measurement*

Due to the large number of particles that must be measured it is crucial to develop a method to automatically measure particle diameters. The procedure of determining what are objects and what is background is known as segmentation in image processing. All treatment of images was done in Matlab and the specific procedure is described in Appendix B.

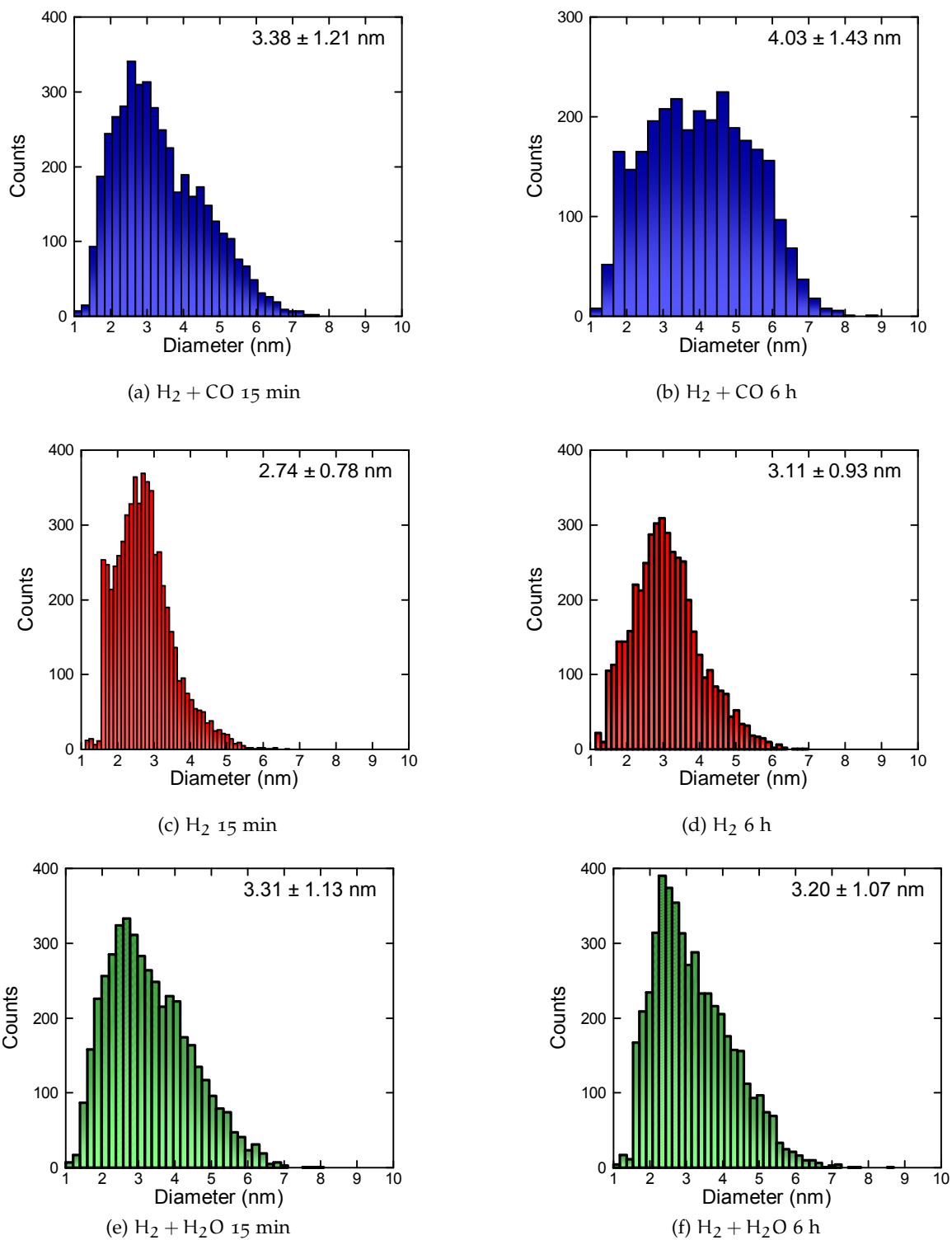


Figure 5.17: Accelerated aging scheme in 1.0 mbar  $\text{H}_2 + 0.9$  mbar  $\text{CO}$ , 1.0 mbar  $\text{H}_2$  and 1.0 mbar  $\text{H}_2 + 0.9$  mbar  $\text{H}_2\text{O}$ . 6 hours at 350 °C. Initial (15 min) and final (6 hour) PSD.

#### 5.3.4 Varying gas environment

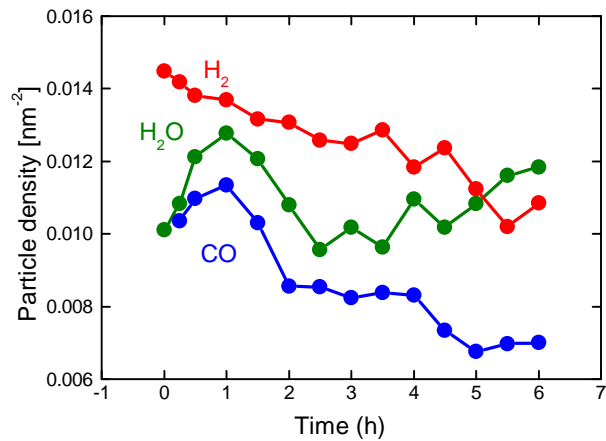
Three samples were subjected to the accelerated aging scheme. These were aged in  $\text{H}_2 + \text{CO}$ ,  $\text{H}_2$  and  $\text{H}_2 + \text{H}_2\text{O}$ . These gases were selected based on the experiments on the wet impregnated samples, and based on the interest in the literature on the effect of  $\text{CO}$  and  $\text{H}_2\text{O}$ . All three samples were produced with a target particle diameter of 3.0 nm and a target density of  $0.0155 \text{ nm}^{-2}$  (11% coverage).

Figure 5.17 shows initial and final PSDs for the three samples. The first sample was aged in 1 mbar  $\text{H}_2 + 0.9$  mbar  $\text{CO}$  (Figure 5.17a and Figure 5.17b). The PSD clearly shifts towards larger particles, with a change in mean diameter from 3.38 nm to 4.03 nm. A high number of small particles are maintained, indicative of Ostwald ripening. The second sample was aged in 1.0 mbar  $\text{H}_2$  (Figure 5.17c and Figure 5.17d). Again, there is a clear development towards larger particles, while still maintaining small particles less than 2 nm. The third sample was aged in 1.0 mbar  $\text{H}_2 + 0.9$  mbar  $\text{H}_2\text{O}$  (Figure 5.17c and Figure 5.17d). In this case, little or no change was seen in the PSD.

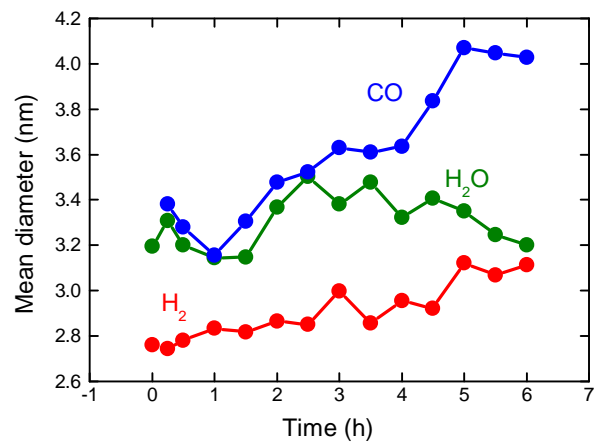
Figure 5.18 compares particle density (Figure 5.18a) and mean diameter (Figure 5.18b) for the three samples, as measured with 30 minute intervals in previously unilluminated areas. We see that the starting point for the three samples is not identical. The sample aged in  $\text{H}_2$  (red) initially has a density of  $0.014 \text{ nm}^{-2}$  and mean diameter of 2.8 nm, where the samples aged in  $\text{H}_2 + \text{H}_2\text{O}$  (green) and  $\text{H}_2 + \text{CO}$  (blue) shares a starting point of  $0.01 \text{ nm}^{-2}$  and ca 3.3 nm. From the initial and final PSD, we saw that the samples aged in  $\text{H}_2$  and  $\text{H}_2 + \text{CO}$  showed sintering, and from Figure 5.18 it is clear how these two show a steady development towards fewer and larger particles. The sample aged in  $\text{H}_2 + \text{H}_2\text{O}$  is very scattered, particle density in particular. This is ascribed to sample inhomogeneity. This makes it difficult to say whether sintering is observed, however, looking at the final data points in Figure 5.18, the initial and final PSDs as well as recalling the results from the Cu prepared by wet deposition, it is likely that there is no sintering in the case of aging in a gas of  $\text{H}_2 + \text{H}_2\text{O}$ .

#### 5.3.5 Sintering mechanism

The statistical results from the unilluminated areas presented above already alluded at an Ostwald ripening mechanism, even if the sintering didn't proceed to develop the LSW-PSD expected for Ostwald ripening[137] in the time given for the experiment. A beneficial complement to the unilluminated areas, would consider the same area tracked over time, in order to follow the development of individual particles. Here we shall consider the *in situ* area of the sample aged in  $\text{H}_2 + \text{CO}$  (Figure 5.19).



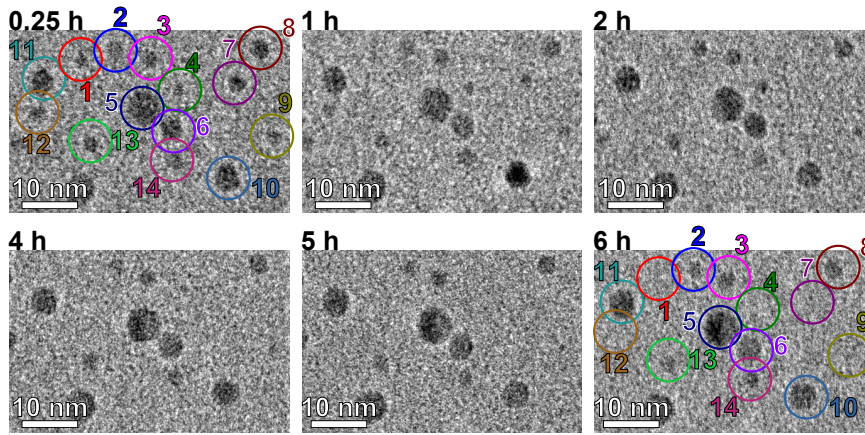
(a) Development particle density.



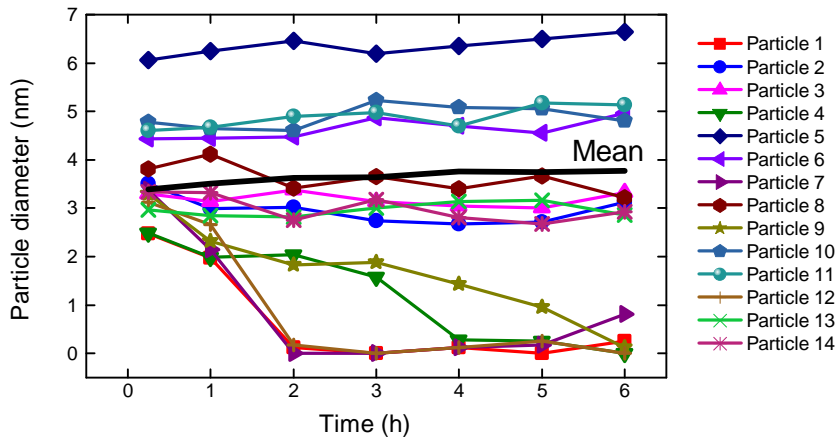
(b) Development in particle diameter.

Figure 5.18: Accelerated aging scheme in 1.0 mbar H<sub>2</sub> + 0.9 mbar CO, 1.0 mbar H<sub>2</sub> and 1.0 mbar H<sub>2</sub> + 0.9 mbar H<sub>2</sub>O. 6 hours at 350 °C. (a) Particle density and (b) mean diameter measured every 30 min over 6 h in previously unilluminated areas.

Figure 5.19a show a  $32 \times 50$  nm section of the *in situ* area tracked over 6 h. Here 14 particles were tracked over time, by manually measuring their size at time steps 0.25-1-2-3-4-5-6 hours. The measured diameters are plotted in Figure 5.19b as a function of time. First, we note that all particles are stationary. This is also the case for the full view of the *in situ* area. Second, we see that particles 1, 4, 7 and 9 shrink and eventually disappear. Particle growth is harder to track for the modest sintering in this experiment, simply because the extra mass from the 4 small particles increase the diameter only slightly for the remaining larger particles. Measurable growth is however observed for the largest particle in the frame, number 5. According to the mean field description of Ostwald ripening, particles with diameter lower than the mean should shrink, whereas particles larger than the mean should grow. The observations from the *in situ* area are



(a) Time lapsed TEM images from *in situ* area.



(b) Development in diameter for the 14 particles encircled in (a).

Figure 5.19: Accelerated aging in 1.0 mbar H<sub>2</sub> + 0.9 mbar CO, 350 °C. The size development of 14 particles was tracked over time. Particles 1, 4, 7, 9 shrank and disappeared.

to some degree consistent with this, at 1 hour, the four particles that eventually disappear are the four smallest in the ensemble. There may also be local effects, such that the mean field approximation does not hold true for the development of individual particles[64].

### 5.3.6 Sintering simulation

To extract quantitative information about the rate of sintering, I have implemented a numerical simulation of Ostwald ripening, similarly to the description by Simonsen et al.[64, 77]. For the interface controlled Ostwald ripening, the development of a particle with radius R is governed by the differential equation in Equation 5.2. What we have is an initial value problem that can be solved using a simple Euler approach to extrapolate from the initial value. The discretized

version of Equation 5.2 then describes the evolution of radii from time step  $n$  to  $n + 1$  as:

$$\frac{R[n + 1] - R[n]}{t_\delta} = \alpha_i \frac{\alpha'_i}{R[n]^2} \left[ \frac{R[n]}{R^*} - 1 \right] \quad (5.9)$$

where  $t_\delta$  denotes the size of the time step. By isolating  $R[n + 1]$  we get an expression for the radius of each particle in the ensemble as a function of its size in the previous time step  $R[n]$  and the mean radius of the ensemble  $R^*[n]$ :

$$R[n + 1] = R[n] + \alpha_i \frac{\alpha'_i}{R[n]^2} \left[ \frac{R[n]}{R^*[n]} - 1 \right] \times t_\delta \quad (5.10)$$

The initial value can be any ensemble of particle radii and from this, and with  $\alpha_i$  and  $\alpha'_i$  defined, the radii of the individual particles is extrapolated over time.

The Euler solver was implemented in Matlab, solved with a time step of 1 min.  $\alpha_i$  is a function of the contact angle  $\theta$  (Equation 5.3). Here  $\theta$  was set to  $90^\circ$ , which leaves  $\alpha'_i$  as the only free parameter. In the present case, the role of the simulations is i) to confirm that the sintering can be described by Ostwald ripening theory, and ii) to extract a value for  $\alpha'_i$ . The magnitude of  $\alpha'_i$  is a measure of the rate of sintering for the given system and allow us to compare the rate between experiments.

To find the best value for  $\alpha'_i$ , the simulation takes the list of particles at 15 min and extrapolates it to 6 hours. Here, the mean and standard deviation is compared to the mean and standard deviation of the measured PSD.  $\alpha'_i$  was adjusted such that the error for these values was minimized. No fitting was done to the PSDs at intermediate times.

Figure 5.20 shows measured and simulated data for the experiment in  $H_2 + CO$ . The TEM images in Figure 5.20a, c, e and h are from the previously unilluminated areas and the PSDs in b, d, f and g are measured in these images and others acquired at the same time (8 in total). By definition, the measured and simulated PSD are identical at time 0.25 h. At times 2 h and 4 h, the simulation displays a reminiscence of the peak in the initial PSD, that is not observed in the measured data. It may be that the sample has been sufficiently inhomogeneous such that there has been area-to area differences in the initial PSD. The other possible explanation is that the model does not capture the sintering in this intermediate regime. For the final PSD (Figure 5.20a) the simulation and the measured data agree very well. The value of  $\alpha'_i$  was  $0.00354 \text{ nm}^{-1} \text{ min}^{-1}$ .

Figure 5.21 show similar data for the experiment in  $H_2$ . In this case there is a less obvious change in the PSD over time, but we do however see that the model captures the development well, both in the final as well as the intermediate PSDs. The value of  $\alpha'_i$  was  $0.00220 \text{ nm}^{-1} \text{ min}^{-1}$ .

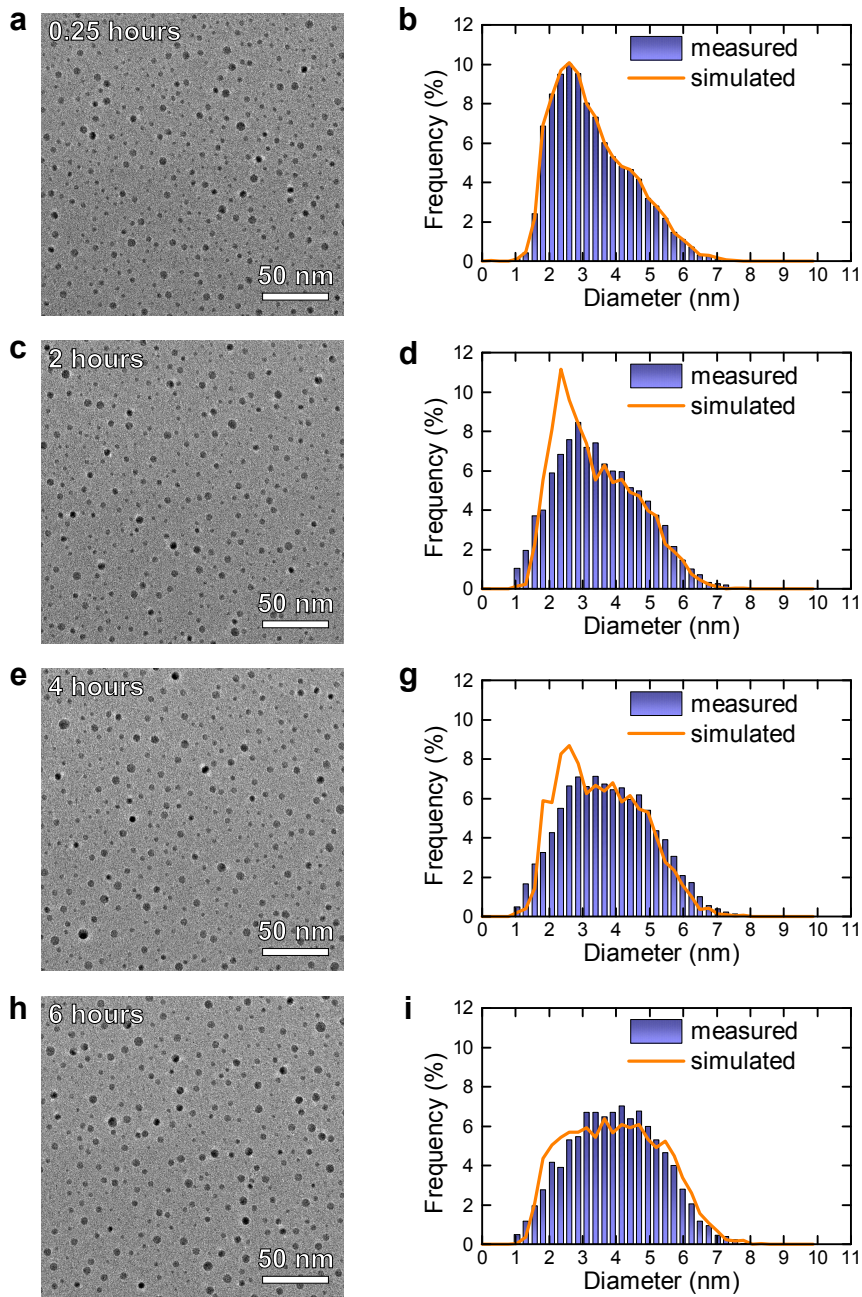


Figure 5.20: Measured and simulated PSD. 1.0 mbar  $H_2$  + 0.9 mbar  $CO$ , 350 °C. Particle sizes were extrapolated from the initial measurement, according to Equation 5.10 with  $\alpha'_i = 0.00354 \text{ nm}^{-1}\text{min}^{-1}$ .

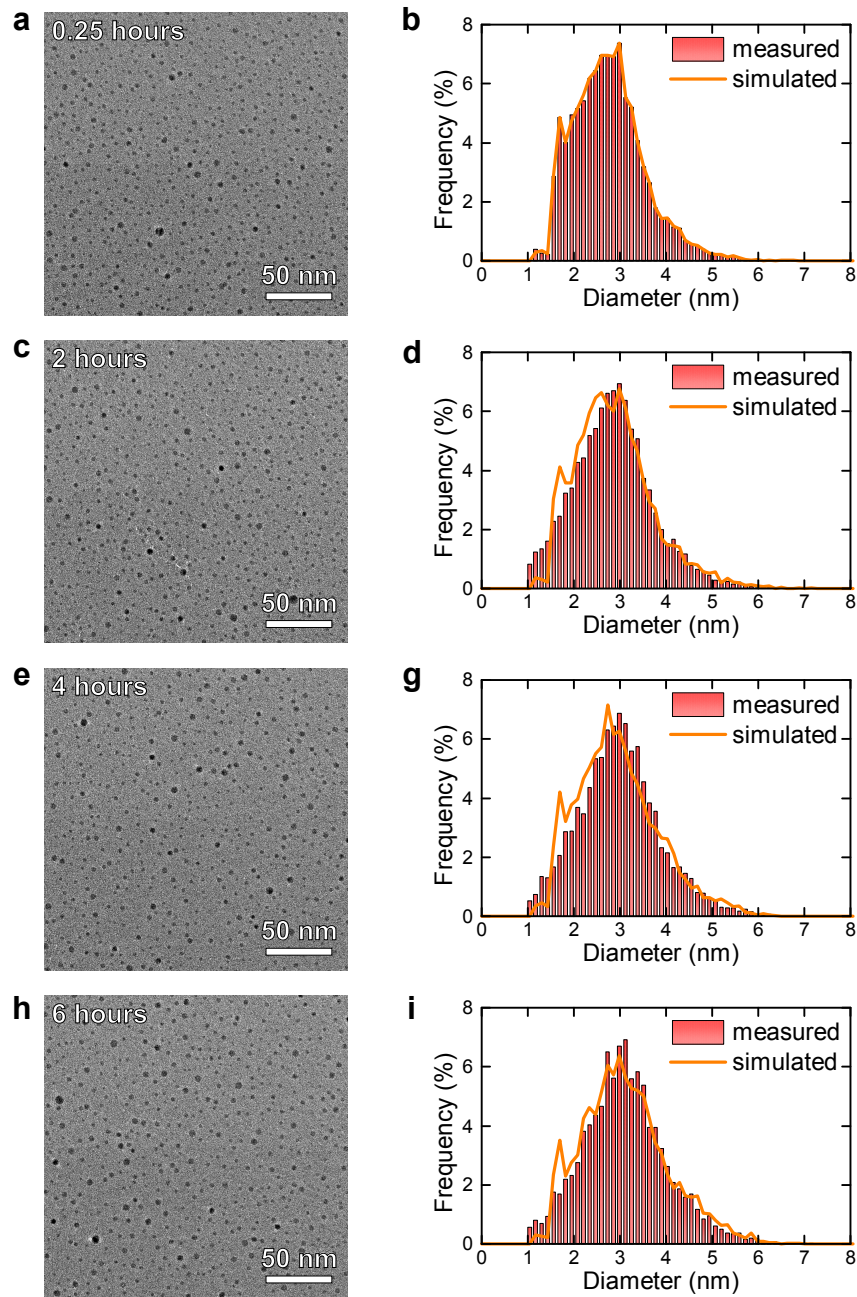
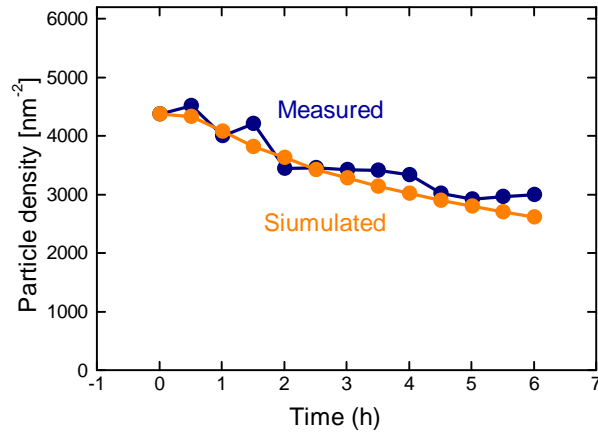


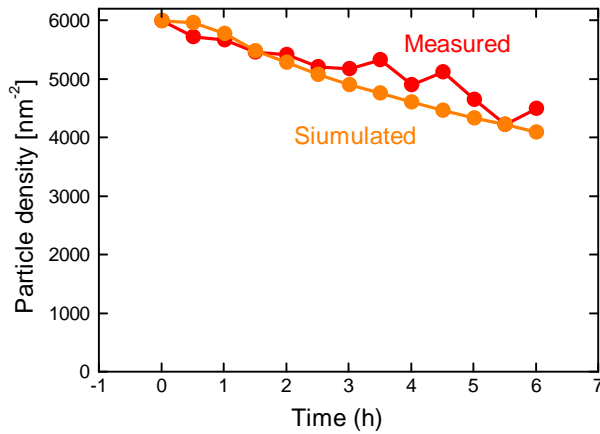
Figure 5.21: Measured and simulated PSD. 1.0 mbar  $\text{H}_2$ , 350 °C. Particle sizes were extrapolated from the initial measurement, according to Equation 5.10 with  $\alpha'_i = 0.00220 \text{ nm}^{-1} \text{ min}^{-1}$ .

Figure 5.22 validates the simulation by comparing the number of particles as measured over the course of the experiment with the simulated value. They agree very well for both  $\text{H}_2 + \text{CO}$  (Figure 5.22a) and  $\text{H}_2$  (Figure 5.22b).

The values of  $\alpha'_i$  directly show that the Ostwald ripening proceeds faster in a gas of  $\text{H}_2 + \text{CO}$  than in  $\text{H}_2$  only. Simonsen et al. reports a value for  $\alpha'_i$  of  $0.035 \text{ nm}^{-1} \text{ min}^{-1}$  for Ostwald ripening of Pt on  $\text{SiO}_2$  in 10 mbar air at 650 °C. The fastest measured rate in the present case



(a) 1.0 mbar  $\text{H}_2$  + 0.9 mbar  $\text{CO}$ , 350 °C.  $\alpha'_i = 0.00354 \text{ nm}^{-1}\text{min}^{-1}$ .



(b) 1.0 mbar  $\text{H}_2$ , 350 °C.  $\alpha'_i = 0.00220 \text{ nm}^{-1}\text{min}^{-1}$ .

Figure 5.22: Development in particle density, measurement and simulation. Same data as PSDs presented in Figure 5.20 and Figure 5.21

is thus 10 times lower. This is not saying that these numbers should have anything in common, it merely shows that our accelerated aging scheme results in a sintering rate that is on the low side for a one day *in situ* experiment. One could have considered raising the temperature, which would however distance the conditions further from actual  $\text{MeOH}$  synthesis. This is a delicate balance and shows the difficulty in studying sintering over short time scales.

### 5.3.7 Effect of electron beam

The effect of the electron beam in relation to these experiments has not been discussed yet. We have mainly focused on the previously unilluminated areas, where this is not relevant, but for the credibility of the measurements in the *in situ* areas, this must be considered.

The effect of the electron beam was investigated in two types of experiments. First, the effect of the gas composition was investigated, by continuously illuminating a sample region for 30 min and recording an image every minute for  $\text{H}_2$ ,  $\text{H}_2 + \text{CO}$  and  $\text{H}_2 + \text{H}_2\text{O}$  at  $350^\circ\text{C}$ . This was done only for a dose rate of  $100\text{ e}^-/(\text{\AA}^2\text{s})$ . Second, the effect of dose rate was investigated in  $\text{H}_2$  at  $350^\circ\text{C}$  by continuously illuminating the sample for 30 min while acquiring an image every minute. This was done for dose rates 25, 50, 100 and  $500\text{ e}^-/(\text{\AA}^2\text{s})$ . For the time-lapsed experiments reported above, the *in situ* area was typically illuminated and imaged 13 times (0.25, 0.5 h, then every 0.5 h for 6 h) with each image requiring up to 2 minutes of illumination. The total illumination time was thus up to 26 min and is captured by the beam effect experiments described here.

Figure 5.23 show collected data for the beam effect experiments. Figures 5.23a, 5.23b and 5.23c show the development in number of particles, mean diameter and total volume, for the three gas compositions. For  $\text{H}_2 + \text{CO}$  and  $\text{H}_2 + \text{H}_2\text{O}$ , the number of particles is more or less constant over the course of the experiment. For  $\text{H}_2$  only, there is a drastic decrease in number of particles at this dose rate. Since the mean diameter does not change, this is not sintering, but rather mass loss, which is also evident from the loss in total volume (Figure 5.23c). This can be due to evaporation of Cu or due to a reaction with the support forming a Cu-silicide or silicate (assuming that this phase would not be seen by TEM). Figure 5.23d clearly shows that this is an effect of the electron beam, since the rate of mass loss is dependent on the incident dose rate. For the experiments reported in the previous section, a dose rate of  $100\text{ e}^-/(\text{\AA}^2\text{s})$  was used. According to Figure 5.23d, a dose rate of  $25\text{ e}^-/(\text{\AA}^2\text{s})$  does not induce any significant loss of particles, so an *in situ* area could have been safely followed with this dose rate. Turning back to the effect of gas composition, we note that the electron beam induces a steep increase in projected diameter for the experiment in  $\text{H}_2 + \text{H}_2\text{O}$ . Comparing with the previously unilluminated areas in Figure 5.18b, where no size increase is seen, it is evident that this is an effect of the electron beam. The experiment in  $\text{H}_2 + \text{CO}$  shows a similar increase in projected mean diameter. In these two cases, an increase in projected diameter and a constant number of particles results in an apparent volume increase (Figure 5.23c). This can certainly also be due to reactions with the support, if Si is incorporated in the Cu nanoparticles. An alternative

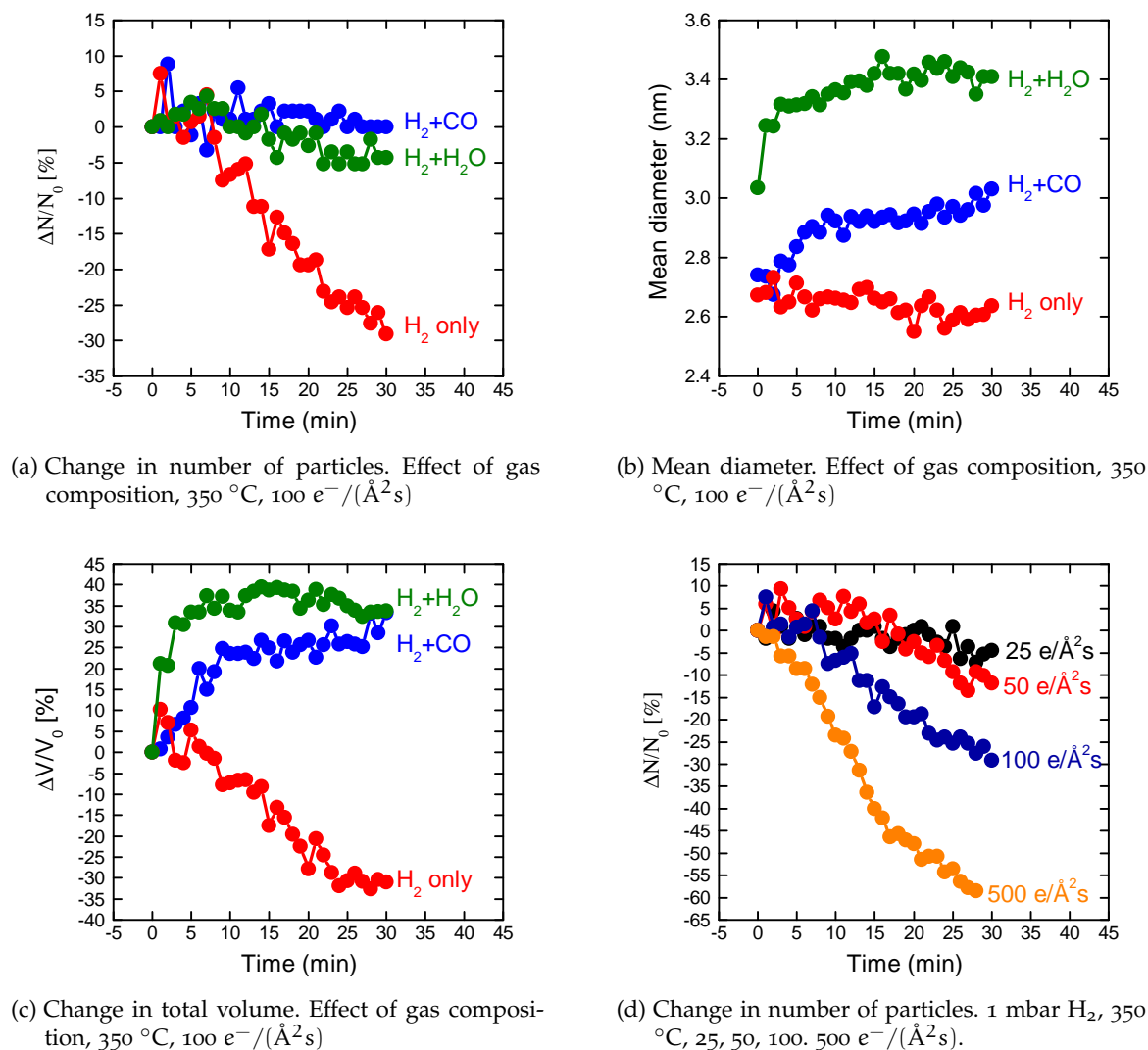


Figure 5.23: The effect of electron illumination for the accelerated aging experiment. **(a, b, c)** Effect of gas composition. **1 mbar H<sub>2</sub>**, **1 mbar H<sub>2</sub> + 0.9 mbar CO**, **1 mbar H<sub>2</sub> + 0.9 mbar H<sub>2</sub>O**. The area was continuously illuminated for 30 min for each gas composition. **(d)** The effect of dose rate measured as the number of particles. The area was continuously illuminated for 30 min at each dose rate.

explanation is increased wetting of the support, which would result in increased projected diameter.

Figure 5.24 shows an image region at the edge of the illuminated area for a dose rate of 100 e<sup>-</sup>/(Å<sup>2</sup>s) in H<sub>2</sub>. Here the difference between the two areas is quite clear. The support has changed; it appears more smooth and has lost some of the disordered contrast present in the unilluminated area. The loss of particle density shown in Figure 5.23d should also be visually apparent from the image.

The study of beam effects show that there are pronounced and diverse effects of the electron beam in this system, depending on the gas and dose rate. For a more detailed study of the sintering effects,

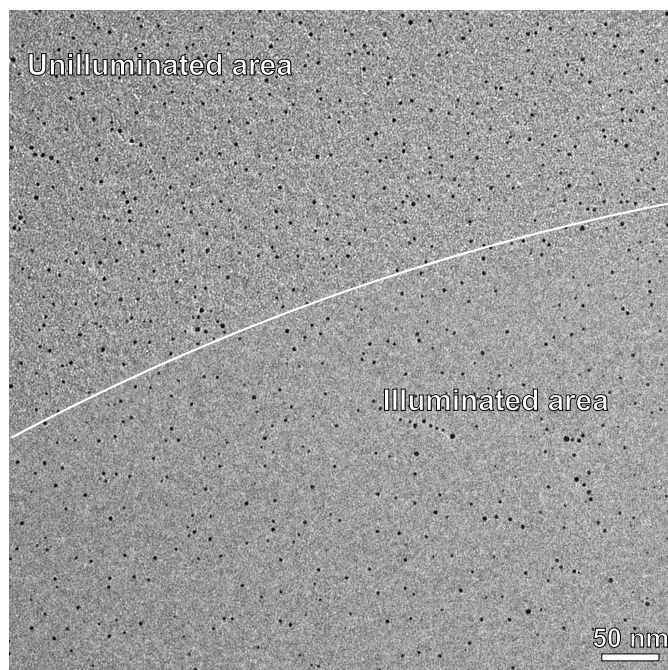


Figure 5.24: Image of an illuminated and an unilluminated region. There is a clear change to the support structure and a decrease in particle density for the illuminated area. The sample was continuously illuminated for 30 min with  $100 \text{ e}^-/(\text{\AA}^2\text{s})$ , 1 mbar  $\text{H}_2$ ,  $350 \text{ }^\circ\text{C}$ .

it would be necessary to further investigate exactly what is going on, and explore the possibility of significantly decreasing the dose rate from the  $100 \text{ e}^-/(\text{\AA}^2\text{s})$  in the *in situ* areas.

#### 5.4 CHAPTER CONCLUSION

More experiments were performed for this system than what was shown here. It was however with varying success, since in some cases the rate of sintering was even lower than what I have reported here. Furthermore, the sample production was not very reproducible, as it was already seen here with the differences in initial PSD from e.g. Figure 5.17. The apparent rate of sintering was higher for the sample prepared by wet impregnation, so one could have explored this track further with more advanced deposition[140]. Another option would have been sputter deposition which can also produce particles with a well defined PSD[52, 64]. Finally I used a rather poorly defined support of  $\text{SiO}_x$ . Here it should also be explored to use higher quality oxide supports of  $\text{SiO}_2$ ,  $\text{Al}_2\text{O}_3$  or  $\text{ZnO}$ .

The experiments presented here directly revealed a significantly different sintering rate for Cu on silica depending on the composition of the surrounding gas. The idea of these experiments was to split up the gases normally present during methanol synthesis, in order to isolate the effect of the individual gases. In  $\text{H}_2$  only, an intermediate rate of

sintering was seen. The water vapor present in the experiments with  $\text{H}_2 + \text{H}_2\text{O}$  apparently hindered sintering of Cu, perhaps due to hydroxylation of the silica surface. CO was found to significantly speed up the rate as seen in experiments with a gas of  $\text{H}_2\text{O} + \text{CO}$ . This is consistent with theory, albeit on ZnO, that finds the most probable transport species to be  $\text{CuCO}$ [130]. A close examination of the *in situ* areas that were followed over time, revealed Ostwald ripening to be the mode of sintering for this system, as seen by stationary particles and visible growth and shrinkage. A numerical solution of the differential equation governing Ostwald ripening was found to consistently describe the development from the initial to the final PSD in the sintering experiments with  $\text{H}_2$  and  $\text{H}_2 + \text{CO}$ .

The experiments presented here is a good illustration of how dynamic effects can be followed over time in order to extract quantitative information about the system. It is however also a good illustration of the need for good sample preparation and experimental design. These experiments were not continued and my attention turned to the projects described elsewhere in this thesis. Given available resources, the sintering of Cu would certainly still be interesting to study by *in situ* TEM.



## CO OXIDATION AND HIGH PRESSURE OPERANDO TEM

---

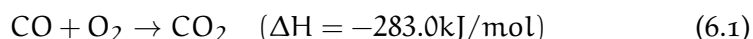
This chapter presents our work on closed gas cell systems. With this system, called the nanoreactor, it is possible to perform *in situ* TEM at gas pressures of 1 bar or higher[45, 46]. Furthermore, the gas exiting the nanoreactor is analyzed in order to measure catalytic activity. Using the combined possibilities of TEM and activity measurements have allowed us to directly couple structure and activity for the oxidation of CO on a Pt catalyst during reaction oscillations, and thereby provide important input on a widely studied reaction. Results presented in this chapter were published in [33].

### 6.1 HIGH PRESSURE *in situ* TEM AND CO OXIDATION

The differentially pumped TEM [29] offers many exciting possibilities, as I have hopefully been able to show in the previous chapters. For some experiments, it is however necessary to go to higher pressures than the few mbar offered by the differentially pumped TEM. This can be realized with closed gas cells, where the gas is confined to a very small volume around the sample [45, 144–146]. The basic principle is the same as in the e-cell of the differentially pumped microscope, but for the closed cell, the gas path has shrunk to 5–40  $\mu\text{m}$  depending on the implementation, which is a 100–1000 fold decrease compared to the e-cell. Keeping in mind that the amount of gas, and the scattering of electrons in the gas, limits the resolution of *in situ* TEM, it is evident that a decrease of the gas path can be translated into a higher maximum pressure, and 1 bar is attainable without compromising resolution[45].

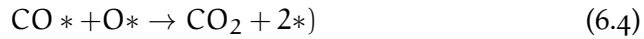
### 6.2 THE CO OXIDATION REACTION

The use of closed gas cell technology has enabled us to study the CO oxidation reaction on Pt nanoparticles under high pressure. CO oxidation is relevant in automotive catalysis for the conversion of toxic CO to CO<sub>2</sub> and in purification of hydrogen streams in the petrochemical industry.



CO oxidation is widely studied and considered a prototype reaction in surface science and heterogeneous catalysis[147]. CO oxidation

proceeds on many noble metal catalysts, those studied the most include Pt, Pd and Ru. The reaction proceeds via Langmuir-Hinshelwood kinetics on metals[147, 148], i. e. a reaction between adsorbed species on the catalyst surface. The CO oxidation may be described by the following kinetically effective steps[147]:



where \* denotes a surface site on the catalyst. Despite its apparent simplicity, CO oxidation on noble metals has stirred up some debate, particularly in the discussion of the nature of the reacting catalyst surface and whether it is metallic or oxidized during reaction[149–152]. This is especially true for reactions at high or ambient pressures, and the controversy may, in the opinion of Freund et al.[147], stem from a different definition of the term oxide, which can be anything from a chemisorbed oxygen layer to a separate phase. In the opinion of the present author, different test conditions such as gas pressure and composition, reactor design and conversion level, may also influence the result and make a comparison difficult.

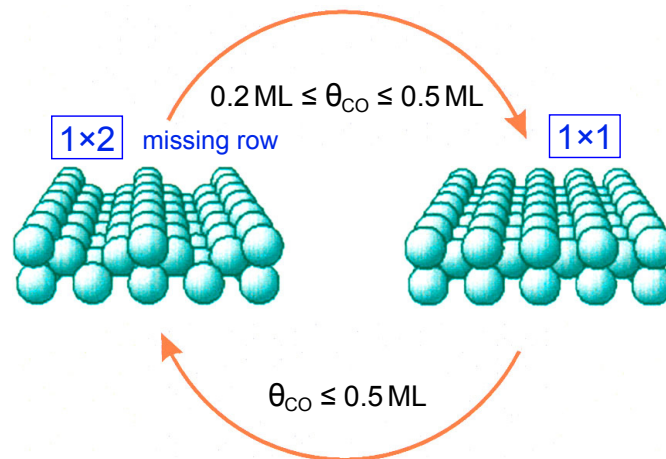


Figure 6.1: Structure of the Pt(110) surface during reaction oscillations at low pressure. The clean surface reconstructs to the 1x2 missing row structure (left). At higher CO coverage ( $> 0.2$  monolayer) the surface changes to the 1x1 termination. Reproduced from Ertl[153].

A particularly interesting aspect of CO oxidation is reaction oscillations at fixed external conditions[154]. This has been widely studied at low pressure conditions on single crystals of Pt and Pd, work that was in particular pioneered by Gerhard Ertl, who received the 2007 Nobel prize in chemistry[153]. At low pressure, reaction oscillations are caused by adsorbate-induced surface restructuring. Figure 6.1 shows the structural changes of the Pt(110) surface during reaction

oscillations at low pressure. The  $1 \times 2$  missing row reconstruction has a low sticking probability for oxygen, implying that the rate of CO conversion will be low and adsorbed CO will build up on the surface. CO has a higher adsorption energy on the  $1 \times 1$  termination and therefore the surface will transform to this structure when the CO coverage exceeds 0.2 monolayer (ML). Oxygen has a higher sticking probability on the  $1 \times 1$  surface causing an increase in reaction rate. This removes CO, such that the surface eventually changes back to the  $1 \times 2$  structure and the cycle repeats[153]. This example shows how reaction oscillations may be governed at low pressure conditions by a change in intrinsic rate due to surface reconstructions.

It has been suggested that reaction oscillations at ambient pressure conditions on Pt and Pd (110) single crystal surfaces are due to a switching between a metal and an oxide surface. Here it is assumed that the oxide surface has a significantly higher intrinsic activity than the metal [155, 156]. These studies never considered mass transport in the reactor in the description of the results, even if it is known that a bistable reaction can be directly caused by the coupling between reaction and diffusion[157, 158].

Reaction oscillations have also been demonstrated on Pt nanoparticles at ambient pressure, but with a lack of experimental characterization of surface and nanoparticle structure[112, 159]. Carlsson, Zhdanov, and Skoglundh used IR spectroscopy to show that the surface was covered by CO during the low conversion regime, whereas the surface was mostly free during high conversion[159].

In the study of nanoparticles, it would be highly beneficial to be able to directly observe the particles responsible for the catalysis during rate oscillations. With the TEM the shape and surface structure of nanoparticles have been imaged *in situ* at conditions relevant for CO oxidation [25] and even with catalytic conversion in the TEM as evidenced by electron energy loss spectroscopy (EELS)[160]. In order to study reaction oscillations, it is however necessary with simultaneous information about structure and rate, something that has hitherto been impossible to realize. Now, with state of the art closed gas cells this opportunity has opened. This will be the subject of the rest of this chapter.

### 6.3 THE NANOREACTOR SYSTEM

The implementation of closed gas cell technology used in the present work is the Nanoreactor, developed in a collaboration between TU Delft, FEI company and Haldor Topsøe A/S, beginning in 2003 and later continuing within the NIMIC consortium [161]. The general concept was presented by Creemer et al. in 2008[45], the design of the current generation was presented in [162] and our use of it was described in [33].

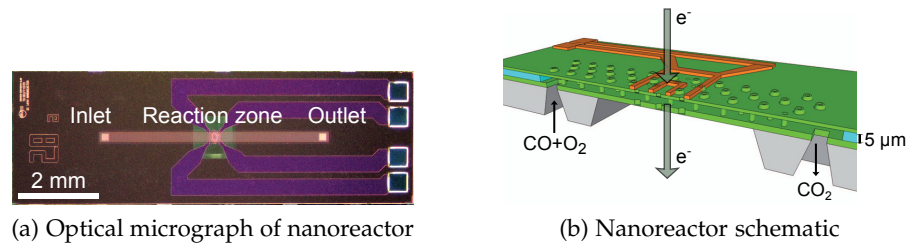


Figure 6.2: **(a)** Top view of the nanoreactor. The gas channel is placed on top of the reactor, with inlet and outlet on the backside. The channel is 5 mm long, 280 μm wide and 5 μm high. The center contains the reaction zone with heater and electron transparent windows (close view in Figure 6.4). **(b)** Schematic drawing of the nanoreactor profile (adapted from [162]).

The nanoreactor, as seen from the top in Figure 6.2a is a microelectromechanical systems (MEMS) device, made using standard clean room fabrication techniques. The present generation[162] is made on a single wafer, where the gas channel is placed on top of the reactor. The backside contains inlet and outlet that connect to a gas feed and analysis system (Section 6.3.3) via a dedicated holder (Figure 6.3).

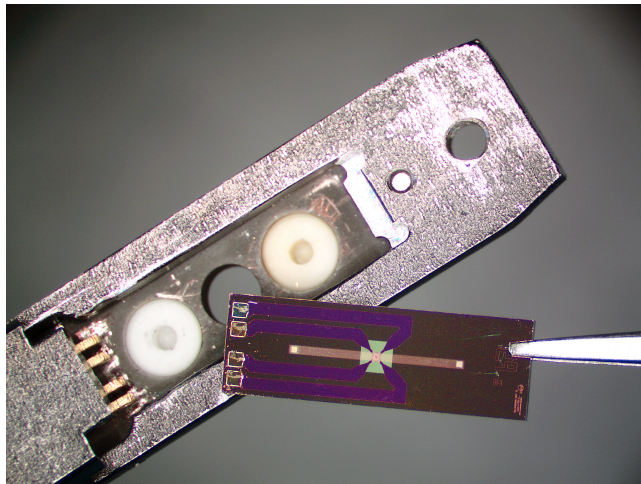


Figure 6.3: The nanoreactor shown together with the tip of the dedicated holder. The two recessions in the holder tip house o-rings which seal the gas inlet and outlet from the vacuum of the microscope when the nanoreactor is mounted in the holder. Four needles connect to the electrodes of the nanoreactor allowing temperature measurement and control.

The center of the nanoreactor, called the reaction zone, is shown in Figure 6.4. The reaction zone contains three main features: the central part of the gas channel, the spiral heater and the electron transparent windows. The gas channel contains stationary or flowing gas, depending on the pressures at inlet and outlet. The diameter of the heater is 320 μm, and the size of the reaction zone is then 320 μm by 280 μm,

as determined by the width of heater and gas channel. Because the reaction zone is so small compared to the length of the gas channel (6.4% of the 5 mm long channel), it is regarded isobaric. Furthermore, due to the symmetrical design, the pressure in the reaction is half of the pressure difference between inlet and outlet[33]. A typical mode of operation would be 2 bar at the inlet and vacuum at the outlet, for a reaction zone pressure of 1 bar.

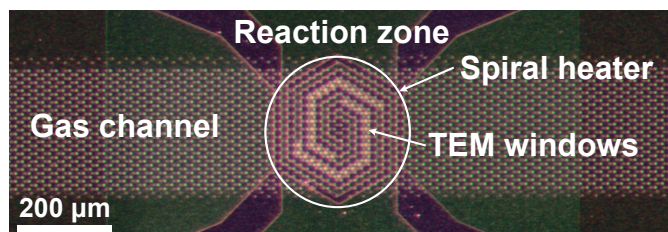


Figure 6.4: Nanoreactor reaction zone with gas channel, spiral heater and electron transparent windows.

The reaction zone contains 41 electron transparent windows made from silicon nitride ( $\text{SiN}_x$ ). The windows are 15-20 nm thick and 1-5  $\mu\text{m}$  in diameter depending on the specific design. A number of pillars connect the two membranes forming the gas channel (see Figure 6.2b and Figure 6.4). This means that there is no bulging when the reactor is pressurized, i.e. the window spacing is independent of pressure. This is unlike previous designs where the opposing membranes were not connected leading to a significant increase in the gap between windows when pressurizing the reactor[45, 163].

### 6.3.1 Nanoreactor loading

The only access to the reaction zone is via the inlet and outlet, so catalyst material must be introduced through these. Other designs for closed gas cells are produced in two separate pieces that must be assembled by the user. This offers the possibility to load by drop casting or sputter deposition directly on the windows[144].

Catalyst material for the nanoreactor can be either synthesized outside and loaded as a slurry, or nanoparticles can be synthesized directly on the windows from a salt solution. When loading a slurry, the catalyst must be ground to a fine powder, suspended in EtOH or  $\text{H}_2\text{O}$  and loaded into the reactor. Loading a liquid is typically done by placing a drop on either inlet or outlet, and then letting the capillary force fill the channel.

For the work presented in this chapter, Pt nanoparticles were synthesized directly on the TEM windows from a solution of tetraammineplatinum(II)nitrate in water. A typical procedure for loading is as follows:

- Heat the reactor on a hotplate to 250 °C for 10 min.

- Drop cast clean EtOH on the inlet. Confirm with an optical microscope that the liquid fills the reactor channel.
- Dry the reactor on hotplate.
- Drop cast tetraammineplatinum(II)nitrate solution on inlet. Reduce the drop size as much as possible to avoid excess salt on nanoreactor surface.
- Dry the reactor at room temperature or on 50-70 °C hotplate.
- Heat the reactor on a hotplate to 250-350 °C to decompose salt and remove all water.

After this, the nanoreactor is mounted in the holder and inserted in the microscope, where the catalyst is first calcined to break down the salt in the reaction zone. This is done in 0.2-1 bar of O<sub>2</sub> at temperatures of up to 773 K. This leaves PtO, which is reduced in a flow of H<sub>2</sub> at 573 K. For the CO oxidation experiment, it is crucial to get a large amount of Pt into the reactor in order to get sufficient catalytic activity. On the other hand, too much Pt may also be a problem because it can induce mechanical stress on the window material to a point where windows break, or simply because it may completely block the view through the windows. Figure 6.5 shows an example of such an overloaded reactor and what may happen. First of all, the amount of Pt means that it is not really nanoparticles forming, and second, the window has broken, as seen by the bright contrast in one area.

A more ideal case is seen in Figure 6.6 where the window integrity is maintained, and only a small area is covered with Pt nanoparticles. From Figure 6.6 (middle) we see that this method of nanoparticle synthesis results in a broad distribution of particle sizes, with Pt particles in the range of 3-50 nm. Catalysis synthesis by impregnation is normally performed on porous supports, which restricts the size and leads to smaller particles and a narrower size distribution[114].

### 6.3.2 Nanoreactor temperature

The reaction zone is resistively heated by a Mo thin-film, placed in a spiral pattern around the electron transparent windows (Figure 6.4). The heater is connected to four electrodes, which allows for simultaneous and independent temperature sensing and heating. The temperature measurement was calibrated using oven experiments [45, 164]. The temperature is automatically managed by a very fast PI-control working on a ms time scale. Due to the tiny thermal mass, temperature changes are more or less instant when applied.

In general a reactor used for catalyst testing should be isothermal, something the nanoreactor does not live up to. On the contrary there

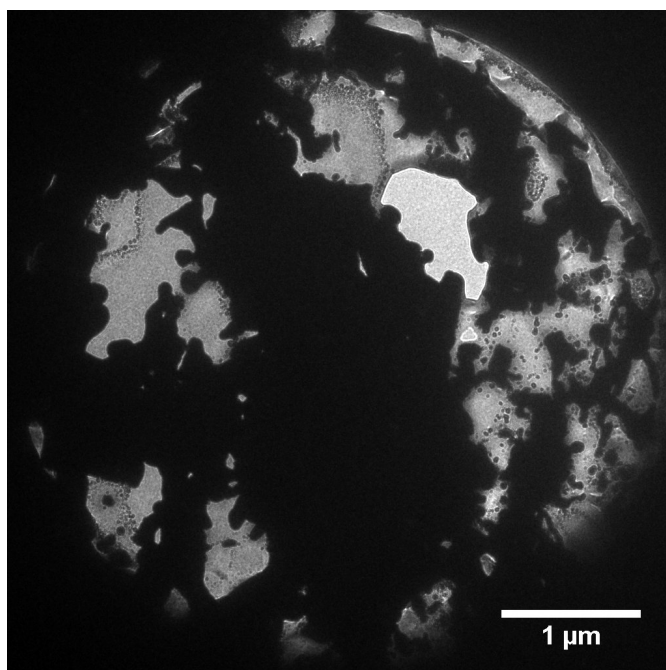


Figure 6.5: TEM micrograph of excessively loaded nanoreactor. The circular outline of the window is only just visible, while the Pt form large dark patches and not the desired nanoparticles. The large amount of Pt has induced stress on the window, breaking it in one place, as seen by the bright contrast.

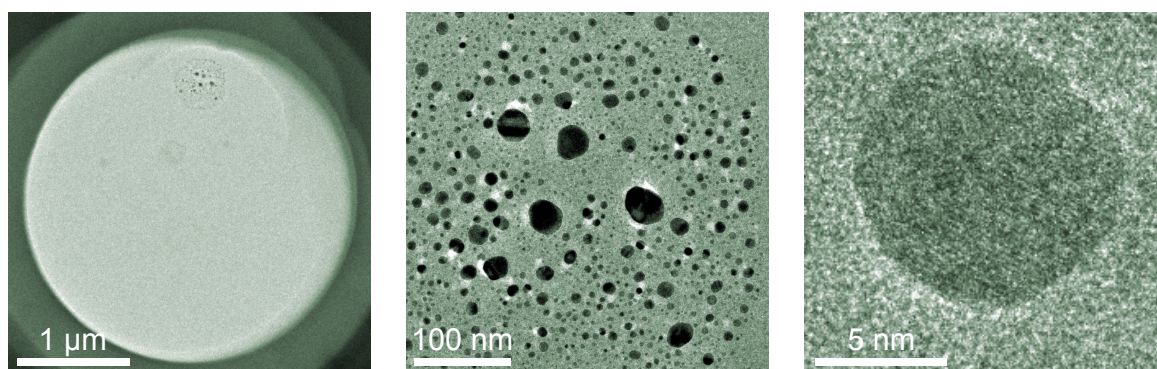


Figure 6.6: TEM images of Pt particles on an electron transparent window at three levels of magnification.

is a large temperature gradient across the reaction zone. The electrical temperature measurement on the heater gives a measure for the average temperature on the heated membrane, but gives no information about local differences. A temperature gradient across the reaction zone is a logical consequence of the miniaturized design, where the only heat transport away from the heater is laterally through the membrane material. Since the spiral heater distributes the heat uniformly over the reaction zone, there is bound to be a higher temperature in the center. This was beautifully shown by Vendelbo et al.[163], where the local temperature was measured using EELS with  $H_2$  gas in

*The history of the nanoreactor is a long one, and I only joined 'recently'. This work is from before I worked with this equipment.*

the reactor. The authors measured the local temperature in the reactor center and on the edge, showing a temperature difference of up to 99 °C between center and edge of the reaction zone (Figure 6.7), measured with 1.2 bar H<sub>2</sub> in the reactor and at a heater temperature of 575 °C. Vendelbo et al.[163] also present an analytical model for the heat transport that matches the measured values very well.

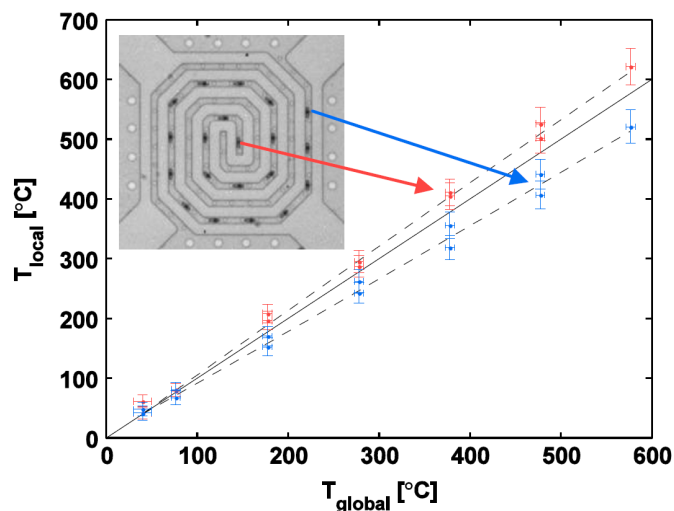


Figure 6.7: Temperature based on EELS measurement of H<sub>2</sub> gas in the nanoreactor. Local temperature is measured in the center window (red) and edge window (blue) and shown as a function of the global temperature measured by the heater. The dashed lines show the expected temperature based on an analytical model. Figure reproduced from [163]

For the work presented in this thesis and in [33] we have expanded on the description and created a full numerical model of the nanoreactor membrane and reaction zone. The main motivation for this was to get an accurate temperature input for modeling of the catalytic conversion inside the reactor. This modeling is presented later (Section 6.6), here I will just note that the numerical model is in line with the experimental results and analytical model in [163] and that the relationship between input heater power and reactor temperature is captured very well by the model.

### 6.3.3 Associated equipment

So far we have mainly discussed the design of the nanoreactor device itself, but it also takes a lot of other equipment to run such an experiment, mainly in terms of gas handling and data management.

For the gas handling, the system is naturally divided into two; i) the inlet, where gas is mixed and fed to the reactor, and ii) the outlet where gas exiting the nanoreactor is analyzed by mass spectrometry (MS). The entire system is depicted in Figure 6.8 and in the following I will go through both the gas inlet side and the gas analysis side.

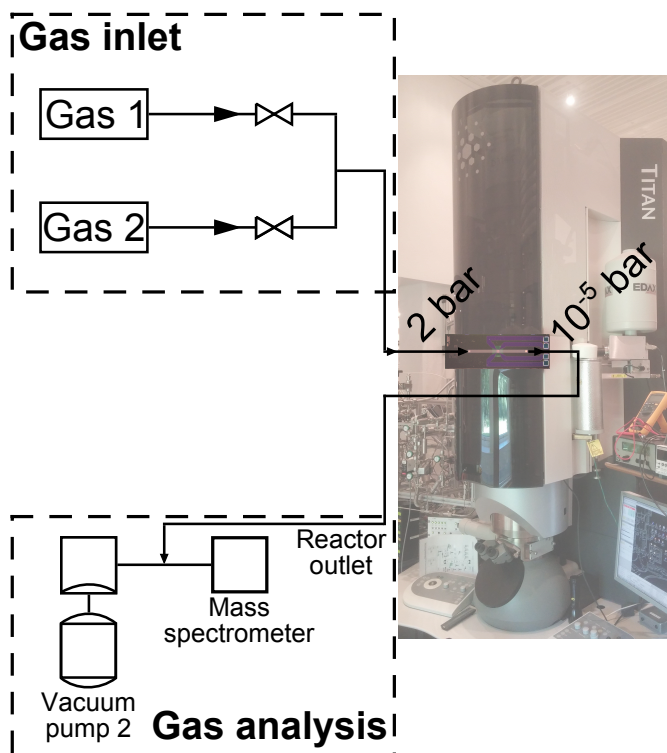


Figure 6.8: Nanoreactor gas feed (inlet) and gas analysis (outlet).

On the inlet side, a stationary gas was fed directly to the nanoreactor inlet. We used a premixed gas of composition  $\text{CO} : \text{O}_2 : \text{He} = 4.2:21:74.8$ , bought specifically for this purpose. It was possible to mix this with another gas before allowing the mixed gas to flow to the reactor inlet. This was done with pure  $\text{O}_2$  in order to increase the ratio of  $\text{O}_2$  to  $\text{CO}$ . An issue with the stationary gas approach is that all gas must flow through the nanoreactor (flow rate ca  $0.1 \text{ ml}_n/\text{min}$ ) which means that it is impossible to use mass flow controllers to control the flow and gas composition, simply because the flow rate is too low. Even assuming a scenario using extremely low flow rate controllers, it would still be impossible to dynamically change the gas composition, because the volume of the gas inlet system after the 'mixing point' is relatively large (on the order of  $10 \text{ ml}$ ) compared to the flow rate. A second challenge with the stationary approach, something that we were not initially aware of, is fractioning of gas through the nanoreactor. Because the flow rate of the different gases is not identical through the narrow nanoreactor channel, the gas concentration at the inlet changes over time. This situation made quantifying MS signals slightly more elaborate than usually.

#### 6.4 TREATMENT OF DATA

Because of the low thermal mass of the heater and the fast electronic control it is possible to use it to directly measure the heat of reaction

by calorimetry. This means we can combine global reactivity data obtained by MS and calorimetry with local information obtained by HRTEM. Figure 6.9 shows the combined data from these three sources for an experiment with oscillating CO oxidation. Treating the different data involves several steps, particularly in terms of synchronization and quantification. In this section, I will go through the synchronization of heater, MS and TEM data, as well as quantification of MS and calorimetry data. These are all the initial steps that are necessary for the following presentation and interpretation of data.

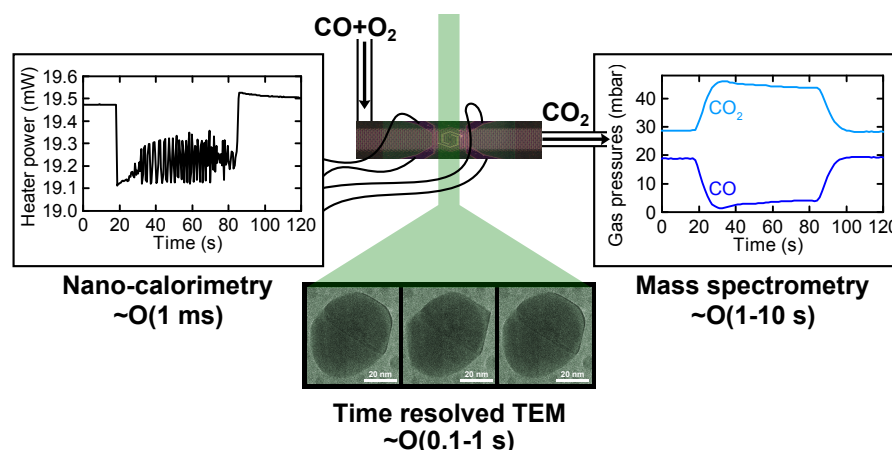


Figure 6.9: The nanoreactor system combines information from MS, calorimetry and TEM. All three provide different information and work on different time scales as indicated in the figure.

#### 6.4.1 Data synchronization

The text in this section is adapted from the supplementary information of my own publication "Visualization of oscillatory behaviour of Pt nanoparticles catalysing CO oxidation." [33].

The MS, TEM and heater power data were all recorded on separate computers. Although a clock synchronization of the computers was done prior to the experiment, the fast oscillations we observed called for a time precision of 1 s or better. A post-synchronization of all the data was therefore conducted. The heater responded to power changes on the millisecond time-scale, which is faster than any other detector in the system. The variations in the heater power were therefore chosen as a basis to link the different data sets. The synchronization was done by first aligning the MS data to heater power data and then aligning the TEM image series to heater power data.

To synchronize the MS and heater power data, it is important to determine the delay and space-time broadening that a gas mixture experiences upon traveling in the gas tubes from the nanoreactor to the MS. The delay can be addressed by exploiting the fact that a temperature increase results in a slight decrease in the gas flow rate

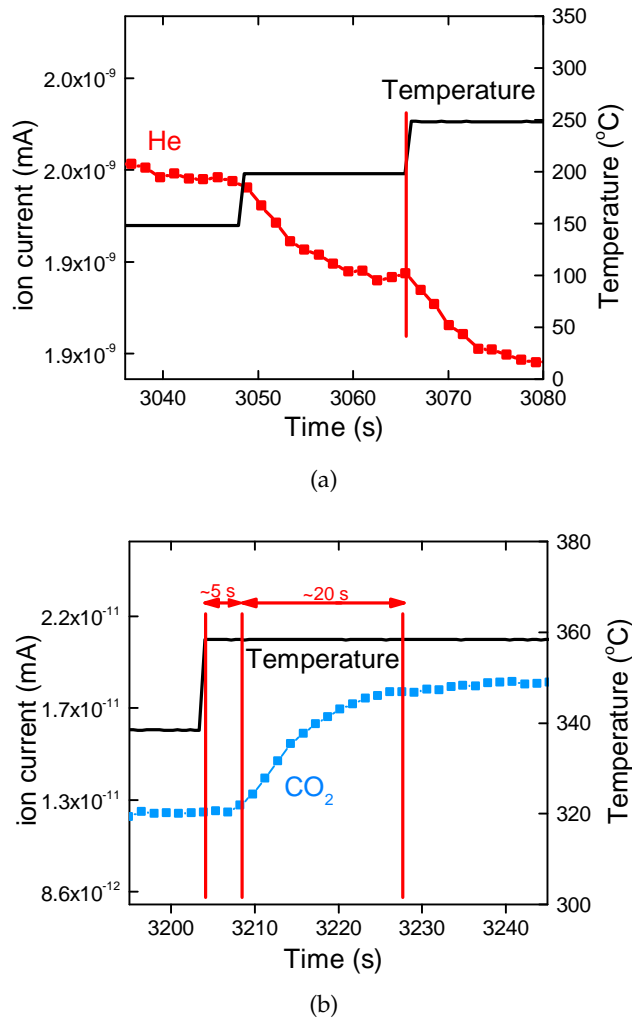


Figure 6.10: **(a)** Alignment of MS and heater data according to a drop in the He signal following a temperature increase. **(b)** Increase in  $\text{CO}_2$  production upon an increase in temperature. MS signal is delayed about 5 s, and associated with a time delay of ca 20 s before fully breaking through.  $\text{CO} : \text{O}_2 : \text{He} = 4.2 : 21 : 72.8$

through the nanoreactor (Figure 6.10a). This is due to a corresponding increase in mean molecular velocity and viscosity, lowering the flow conductance of the reactor. As a reduced flow rate lowers the downstream pressure and pressure variations travel with the speed of sound through the system, an abrupt temperature change will result in an immediate signal change in the MS data, because the gas lines separating the nanoreactor and mass spectrometer are just a few meters long. Figure 6.10a shows the heater power and MS He signal synchronized in this way at a temperature increase of 50 K, at time 3056 s (red bar). Also, Figure 6.10a shows that the synchronization holds for two such power changes. Having synchronized the MS ion current and heater power in this way, the delay by which a gas front moves through the gas line from the nanoreactor to the MS

can then be determined by inducing a sudden variation in the gas composition. A sudden change in the gas composition is seen when a Pt-loaded nanoreactor is heated stepwise resulting in an increased  $\text{CO}_2$  level. Figure 6.10b shows that the  $\text{CO}_2$  ion current starts increasing with a 5 s delay and that the  $\text{CO}_2$  increase is broadened over a 20 s period before a constant level is obtained. Based on this result, the MS and heater power data presented in the following were synchronized by subtracting 5 seconds from the MS PC clock time in order for the MS data to display the gas composition at the time it exits the nanoreactor and not as it enters the MS. Furthermore, the broadening of the MS signal through the present gas tube system implies that small-amplitude variations, such as oscillations in the CO oxidation reaction rate, shorter than 5 seconds will be damped, and eventually fall below the detection limit of the mass spectrometer, and that the front in the gas composition will be smeared out accordingly.

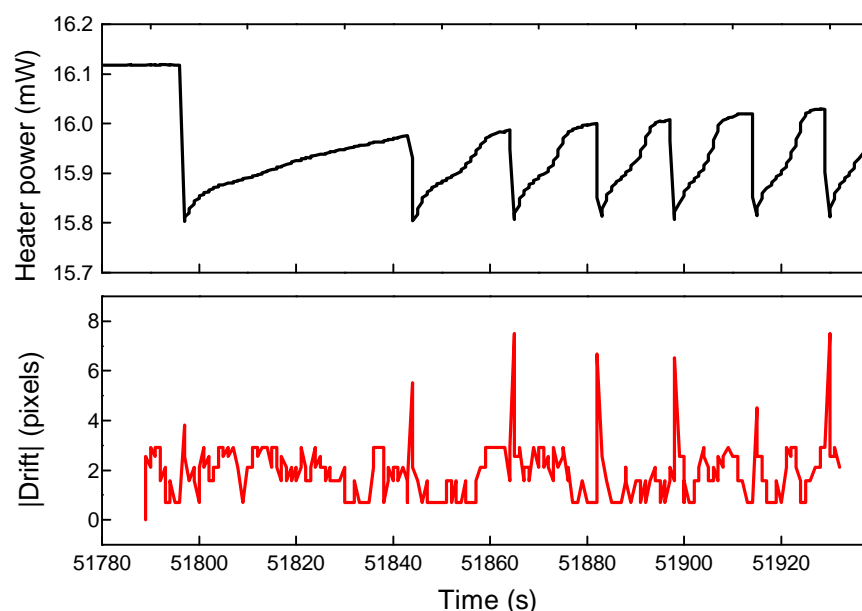


Figure 6.11: TEM images and heater data were aligned by measuring image drift (bottom) upon reactivity changes and correlate it with changes in measured heater power (top)  $\text{CO} : \text{O}_2 : \text{He} = 3 : 42 : 55$ ,  $T = 659$  K, pixel size 0.12 nm.

The synchronization of the TEM and heater power data employed information about the sample drift. Upon a change in the excitation of the heater, either by adjustments of the temperature setting or changes in the CO oxidation reaction rate, lateral drift of the sample (Pt nanoparticles) will be observed in the TEM image series. Figure 6.11 illustrates the effect for the correlated data on the heater power and frame-to-frame drift observed during oscillatory CO oxidation. The frame-to-frame drift was determined using phase correlation of successive images. The comparison of the heater data, Figure 6.11(top), and drift data, Figure 6.11(bottom), shows that each

marked drop in the heater power, caused by reaction oscillations in the constant temperature mode, is accompanied by a distinct displacement of the specimen.

#### 6.4.2 *Mass spectrometry quantification*

Although the nanoreactor was exposed to a gas of a fixed nominal composition, a quantification of the partial pressures is complicated by the fact that the actual gas composition entering the nanoreactor may vary in the course of the experiment. Such change is due to fractioning, which results from the different flow rates of different molecules through the narrow gas channel (He moves through at a faster rate than the heavier CO and O<sub>2</sub>), and to the stagnant gas volume in the tubes at the nanoreactor inlet, which gradually changes composition over an extended experimental period. Moreover, the total gas flow rate through the nanoreactor changes as a function of temperature (i.e. a lower gas flow rate at higher temperature) whereas the total pressure remains at 1000 mbar at all temperatures and flow rates, as the symmetric nanoreactor design is retained. The quantification of gas composition entering the reaction zone of the nanoreactor (referred to as inlet gas composition) taking these conditions into account, is explained in Appendix C.

#### 6.4.3 *Reaction heat and flow rate measurement*

The text in this section is adapted from the supplementary information of my own publication "Visualization of oscillatory behaviour of Pt nanoparticles catalysing CO oxidation." [33].

The heat released in the oxidation of CO can in principle be measured in two ways: i) as changes in heater power during oscillatory reaction conditions at constant average temperature and ii) by means of using the CO<sub>2</sub> pressure from the MS. However, both methods have limitations. For i), the power offset required to maintain a constant average reactor temperature must be known. For ii), the flow rate through the reactor must be known. A way to circumvent the limitations and to obtain an accurate calculation of the power off-set and gas flow-rate is to match pressure and heater power datasets for a period with reaction oscillations. Figure 6.12 shows an example of the combined data for a specific oscillation sequence.

The reaction power measured by the heater,  $P_{\text{Heater}}^{\text{Reaction}}$ , is given by:

$$P_{\text{Heater}}^{\text{Reaction}} = -(P - P_{\text{Offset}}) \quad (6.5)$$

where  $P$  is the measured heater power and  $P_{\text{Offset}}$  is the offset required to maintain a constant temperature with no reaction. The mi-

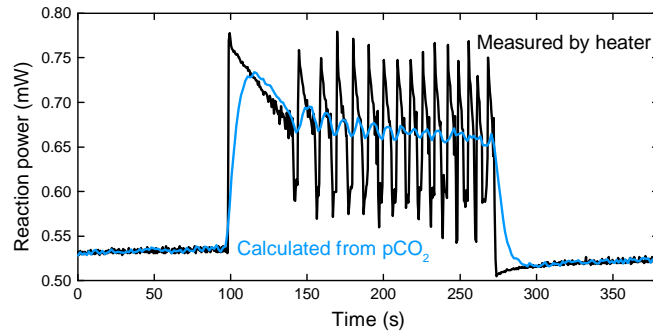


Figure 6.12: Reaction heat flow as measured by heater power and MS. Gas composition CO : O<sub>2</sub> : He = 4.2 : 21 : 72.8, T = 700.5 /C

nus reflects that the exothermic reaction is compensated by the heater power under the constant average temperature conditions.

The reaction power  $P_{MS}^{Reaction}$  (in units of mW) calculated from the CO<sub>2</sub> pressure is given by:

$$p_{MS}^{Reaction} = \frac{pCO_2}{1000 \text{ mbar}} * \frac{Q}{24800 \frac{\text{ml}}{\text{mol}} * 60 \frac{\text{s}}{\text{min}}} * 283 * 10^6 \frac{\text{mJ}}{\text{mol}} \quad (6.6)$$

where 24800 ml/mol is the molar volume of an ideal gas at standard conditions and Q is the total gas flow rate in ml<sub>n</sub>/min.

$P_{Offset}$  and Q were estimated by matching the area under the two curves in Figure 6.12 in the full interval (t = 22700-22900 s) and the power value in the non-oscillating interval (t = 22600-22680 s). For this example,  $P_{Offset} = 18.8$  mW and Q = 0.092 ml<sub>n</sub>/min for which the corresponding curves are shown in Figure 6.12. A flow rate of 0.092 ml<sub>n</sub>/min corresponds to a space velocity of 4500 s<sup>-1</sup> for the 0.34 nl reactor volume (heated area).

## 6.5 OSCILLATIONS IN CO OXIDATION

### 6.5.1 Mass spectrometry and calorimetry, global information

Upon an increase in temperature, CO and O<sub>2</sub> start reacting, as seen by an increase in the CO<sub>2</sub> exiting the nanoreactor (Arrhenius plot of activity data is shown in Figure 6.19, page 146). Furthermore, in a certain temperature interval, depending on the specific reactor and inlet gas composition, spontaneous oscillations in CO conversion were seen. Generally, the reaction enters an 'oscillating' regime, with rapid changes in conversion as seen by MS and calorimetry. Such an oscillating regime starts spontaneously or by a small increase in temperature (0.5 - 1 K). The exact shape and type of oscillation turned out to be highly dependent on both the specific reactor and gas composition. The dependency on the reactor was ascribed to the exact size and

distribution of the Pt particles. It is not possible to control these parameters with the current method of loading.

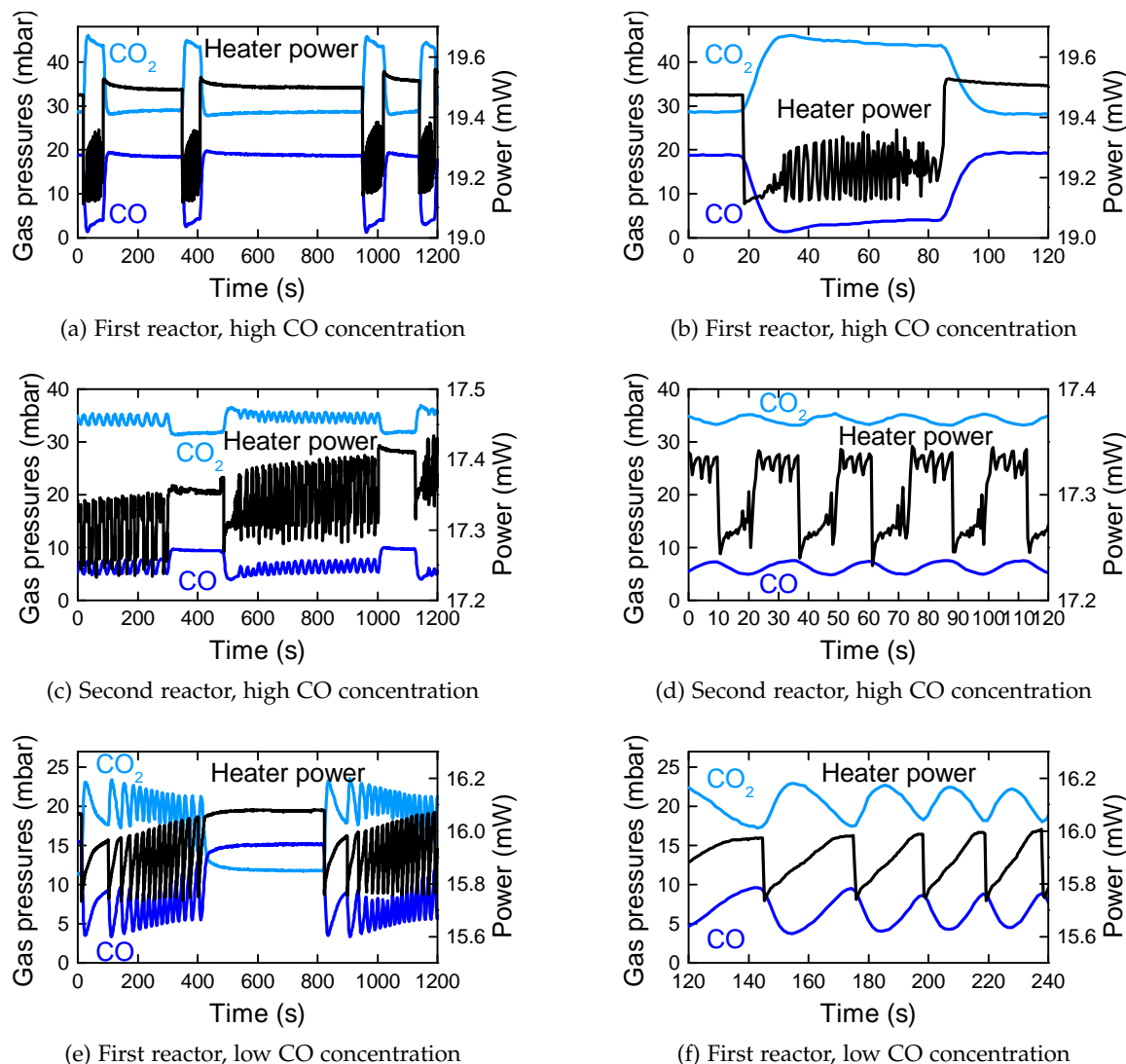


Figure 6.13: Time-resolved partial pressures and heater power data during the oscillatory oxidation of CO from two different nanoreactors.

(a, b) The first nanoreactor with the reaction zone exposed to 1.0 bar of  $\text{CO} : \text{O}_2 : \text{He} = 4.2 : 21.0 : 74.8$  at 727 K. At  $t = 19$  s and 951 s, the temperature was increased by 0.5 K to induce an oscillatory sequence. The last sequences starting at 342 s and 1142 s initiated spontaneously.

(c, d) The second nanoreactor with the reaction zone exposed to the same gas conditions as (a, b) at 683 K. At  $t = 487$  s and 746 s, the temperature was increased by 0.5 K. At  $t = 1126$  s, the temperature was increased by 1 K.

(e, f) Same nanoreactor as for (a, b) with the reaction zone exposed to 1.0 bar of  $\text{CO} : \text{O}_2 : \text{He} = 3 : 42 : 55$  at 659 K. At  $t = 12$  s and 822 s, the temperature was increased by 0.5 K.

Figure 6.13 shows three different instances of oscillations obtained from two different reactors. Figure 6.13a shows data obtained with the first reactor at high inlet CO concentration (4.2%). Figure 6.13b shows the same data at a shorter time interval. These oscillations are very fast, and only captured as fluctuations in the heater power. MS data only shows an overall increase in CO conversion during this oscillating regime. Figure 6.13c and Figure 6.13d show oscillations for the second reactor, also with high inlet CO concentration. Here the fingerprint of the oscillating regime is distinctly different, which is ascribed to a different reactor loading. Finally, Figure 6.13e and Figure 6.13f show oscillations from the first reactor, but with a lower CO concentration (3%). The trend is still the same, with oscillating and static regimes, but the individual oscillations are significantly slower than for the same reactor at higher inlet CO pressure. The slower oscillations also allow the heater to resolve finer detail, and we see in this case that the oscillations take on a saw tooth pattern with rapid increases in conversion (drop in heater power) and slower decreases (increase in heater power).

Reaction oscillations are thus seen in the global signals from heater power and MS. It is very valuable to have both global methods; MS is sensitive at low levels of conversions and allows us to extract an apparent activation energy (Figure 6.19). During oscillations, the access to both values allowed for a calculation of flow rate and off-set heater power, making it possible to transform the signal from the heater into a direct colorimetric measure of reaction power.

### 6.5.2 TEM during oscillations, local information

Simultaneously with oscillations in global reaction rate, Pt nanoparticles inside the reactor were imaged with TEM. First, results are presented from the experiment that was referred to as 'First reactor, high CO concentration' (Figure 6.13b). As seen here, the reaction oscillations are very fast, with a period of 3-4 seconds. To capture the Pt particles at different time stages of such a period thus requires a frame rate that is significantly faster. Following the Nyquist theorem at least 1 frame per second (fps) would be needed and in reality a faster sampling would be preferable. For the experiment at hand, the problem is slightly more complicated due to sample drift induced by the oscillations. Upon a rapid change in conversion and a following heater adjustment, the image rapidly shifts, leading to image drift in phase with the oscillations. This was actively used for image alignment (Figure 6.11), but also sets an upper limit on the exposure time, in order to capture the particle without drift.

For the present experiment, an exposure time of down to 0.15 s was necessary. The camera fitted to our microscope needs around 0.6 s to process the image, so that the movies were recorded with

0.76 s per image (1.4 fps) for an exposure time of 0.15 s which was sufficient to resolve reaction oscillations with a period of down to 2 s and to avoid image drift. 0.15 s is a short exposure time, and this has some implication on the other imaging parameters. To maximize the signal to noise ratio, the amount of electrons per pixel per acquisition must be as high as possible. This number is determined by pixel size, electron dose rate and exposure time, as described in Section 2.3.1. Since the exposure time is very low in this case, dose rate and/or pixel size would have to be increased, although these parameters also come with restrictions. To minimize beam damage to the sample, the electron dose rate was limited to  $300 \text{ e}^-/(\text{\AA}^2\text{s})$ . At increasing dose rates, some sintering of Pt particles was observed[33]. Finally pixel size had to be increased, but only to a value where the lattice fringes of Pt are still resolvable. For the present work, the minimum pixel size was 0.0517 nm, sufficient to resolve Pt(220) at 1.4 Å, and plenty to resolve Pt(200) and Pt(111) at 2.0 and 2.3 Å. An image acquired with these parameters, thus receives  $0.15 \times 300 \times 0.0517^2 \text{ e}^- = 12 \text{ e}^-$  per pixel. This is a very low number, and shows how these *in situ* experiments often will have to rely on very weak signals, and how important it is to balance the parameters to arrive at the best imaging conditions.

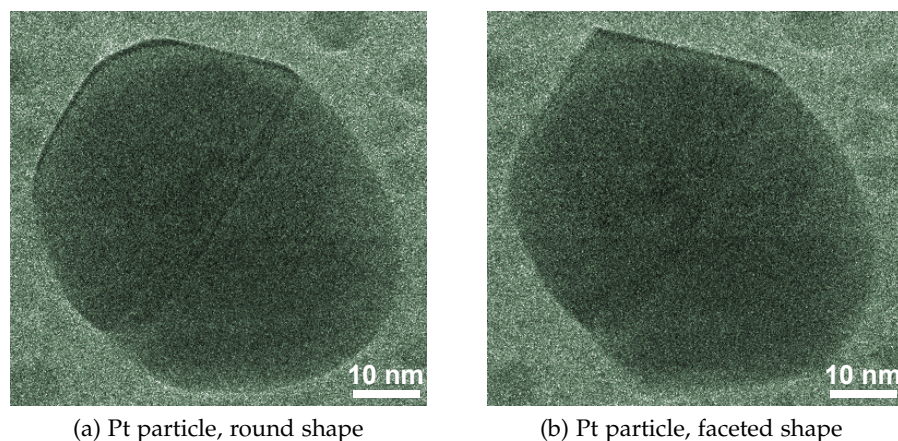


Figure 6.14: Pt particle shape changes between round (a) and faceted (b) during oscillatory CO oxidation (Figure 6.13a). Reaction zone conditions: 1.0 bar of CO : O<sub>2</sub> : He = 4.2 : 21.0 : 74.8 at 727 K.

With the proper acquisition parameters, it was possible to capture reversible shape changes of the Pt nanoparticles in phase with changes in global conversion. An example of this is shown in Figure 6.14. During the oscillatory CO conversion, this Pt particle changed between a round (Figure 6.14a) and more faceted shape (Figure 6.14b). During the regimes of steady conversion (as seen in Figure 6.13a), the particle maintained the round shape.

To investigate the relation between local shape changes and oscillations in global conversion, the correlated data is examined. Fig-

Figure 6.15 shows correlated gas pressures (a), reaction power (b) and TEM (c, d) for the oscillatory CO oxidation. TEM is presented as four frames (acquisition times marked by circles in Figure 6.15c). The shape factor plotted in Figure 6.15c, was inspired by Yoshida et al.[25]. The number was calculated by overlaying an ellipsoid on the images in Figure 6.15d and comparing the Pt outline to the elliptical shape. The higher the deviation, the higher the number. In this case, the faceted shape corresponds to a shape factor of 1, whereas the round shape is 0.

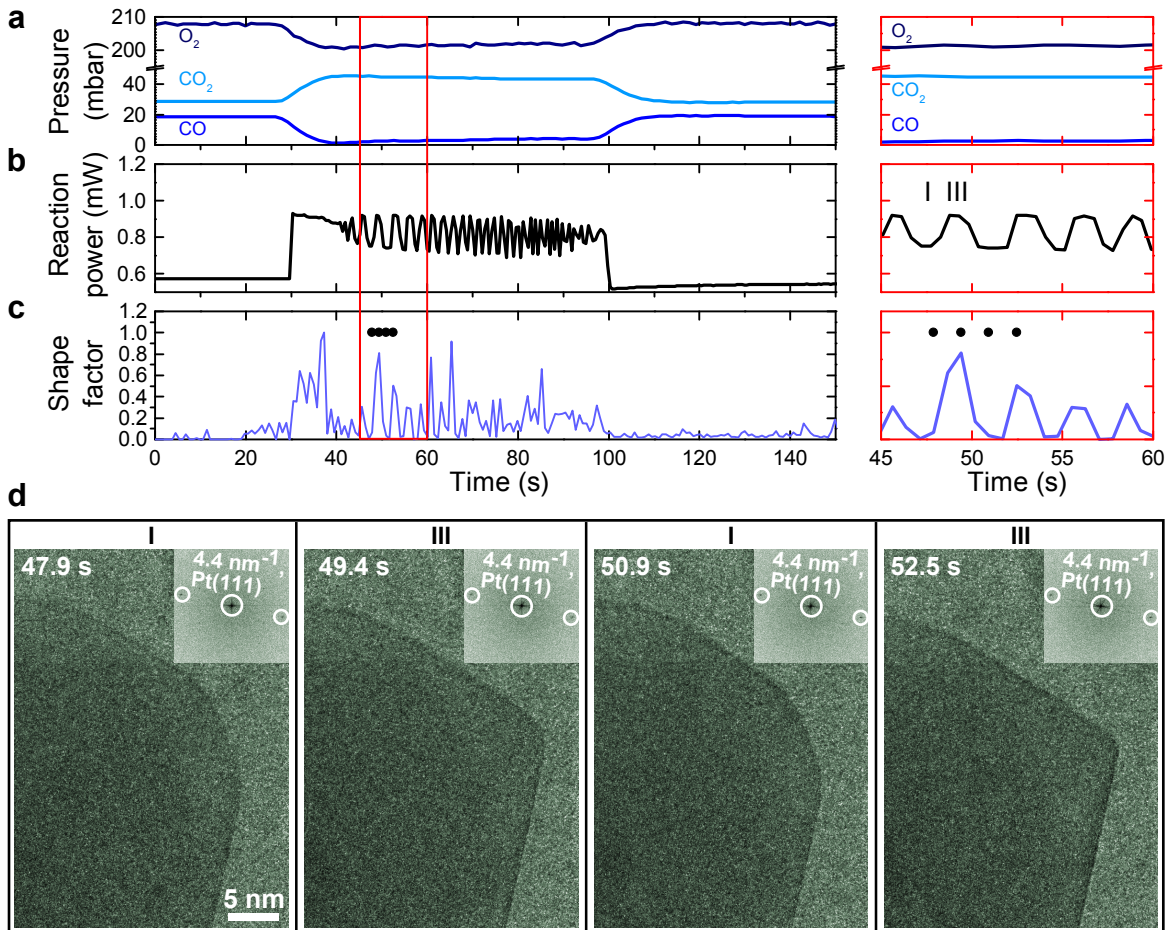
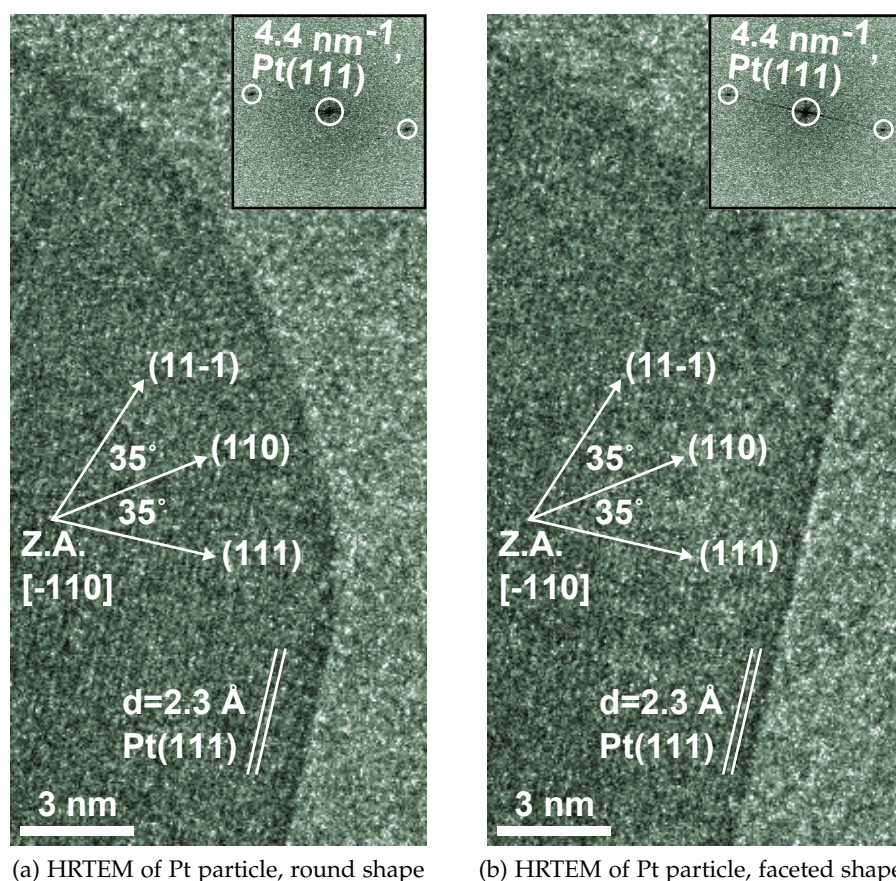


Figure 6.15: High-resolution TEM, MS and reaction power data during the oscillatory CO oxidation. The reaction zone conditions: 1.0 bar of CO : O<sub>2</sub> : He = 4.2 : 21.0 : 74.8 at 727 K. **(a)** Mass spectrometer traces resolve the envelope of the reaction oscillation. **(b)** Reaction power resolves the oscillatory state. **(c)** Shape factor of the Pt nanoparticle shown in (d). **(d)** Additional high-resolution TEM images (acquisition times marked with a circle (●) in (c)). The comparison of (c) and (d) reveals the synchronization between the changes in the Pt nanoparticle shape and reaction power data. The faceted shape (morphology factor > 0) corresponds to the high reaction rate, and the round shape (morphology factor = 0) corresponds to the low reaction rate. A movie from this experiment can be found online as supplementary information to [33].

Figure 6.15 reveals the temporal correlation between particle size and conversion; a comparison of reaction power and shape factor shows that the round shape (I) is seen when the conversion is low, and that the faceted shape (III) is seen when the conversion is high.

The TEM images in Figure 6.15d are atomically resolved and show a lattice spacing corresponding to the (111) plane of Pt. Figure 6.16 shows a zoom in on the nanoparticle edge shown in Figure 6.15d for the round and faceted shape. From Figure 6.16a it is seen that the Pt(111) is resolved only in one direction. By measuring the angle to the two other surfaces, it is suggested that these correspond to a (110) surface at  $35^\circ$  and a (-111) at  $70^\circ$  with respect to the resolved (111) direction. By comparing the round shape in Figure 6.16a to the faceted shape in Figure 6.16b it is evident that the faceting corresponds to an extension of the close packed (111) surface.



(a) HRTEM of Pt particle, round shape (b) HRTEM of Pt particle, faceted shape

Figure 6.16: HRTEM of the two different particle shapes. Reaction zone conditions: 1.0 bar of CO : O<sub>2</sub> : He = 4.2 : 21.0 : 74.8 at 727 K.

(a) Round shape observed at low global conversion (b) Faceted shape, corresponding to an extension of the close-packed Pt(111) surface.

The HRTEM images acquired in 1.0 bar of CO : O<sub>2</sub> : He = 4.2 : 21.0 : 74.8 at 727 K, show the atomic fringes corresponding to metallic Pt extending all the way towards the edge. There is no visible signs of a surface oxide. The observations made here suggest that oxides do not play a role in the mechanism behind the reaction oscillations under these conditions. Particle shape however changes in phase with the reaction oscillations, and may be a possible feedback mechanism, which is discussed in the following sections.

The oscillations presented in Figure 6.15 were very fast, with a period of 3-4 s. Given that TEM images were acquired at 0.76 s per frame and heater data at 0.5 s per point, the rate of acquisition was on the order of 4-5 images per period, which is enough to resolve the oscillation, but any finer details are lost. An important question is, whether the particle changes shape before the change in global rate, or if it is the other way around. Due to the readout time of the camera, it is not possible to acquire much faster than the 0.15 s of Figure 6.15/ Figure 6.16. The heater readout is also restricted by design to 0.5 s per data point. Instead the gas atmosphere was changed to slow down the oscillations.

Figure 6.17 shows a similar picture to Figure 6.15, but the time period of the oscillations is much longer. The data in Figure 6.17 was acquired in the same reactor as Figure 6.15, but with CO : O<sub>2</sub> : He = 3 : 42 : 55 compared to CO : O<sub>2</sub> : He = 4.2 : 21.0 : 74.8. The lower CO pressure and higher O<sub>2</sub>/CO ratio, resulted in a lower temperature for the oscillating regime (659 K compared to 727 K). The result of this was slower oscillations and a better temporal resolution in the reaction power (Figure 6.17b).

One oscillation in Figure 6.17 can be described in four steps: At the end of a period, the reaction power is low and the particle shape is round (I). After a rapid increase in CO conversion (II), the particle starts changing towards the more faceted shape. Within approximately 3 s, the fully faceted shape is evolved (III). The CO conversion start climbing down slowly, and eventually the shape of the observed particle reverts to its original round configuration (IV). The decrease in conversion continues, until the next rapid increase.

The pronounced shape changes observed here, for such large particles involve substantial transport of mass on the Pt surface. It is expected that the time for the shape to evolve (in this case 3 s) is determined by the time it takes to move the Pt atoms. This is in line with the observation that the shape change proceeds slower when the temperature is lowered as seen by comparing Figure 6.17 to Figure 6.15.

Finally it should be noted that the particle shape changes were found to be independent of the applied electron dose rate. This was shown in two experiment where the dose rate was varied from 5 to 200 e<sup>-</sup>/(Å<sup>2</sup>s) during reactor oscillations[33]. The magnitude of the particle shape changes was in this case found to be independent of the

applied dose rate which is strong evidence that the observed shape changes are an intrinsic phenomena and not caused or amplified by electron illumination. Particle mobility was observed in some cases during electron illumination and limited the usable dose rate to  $300 \text{ e}^-/(\text{\AA}^2\text{s})$  [33].

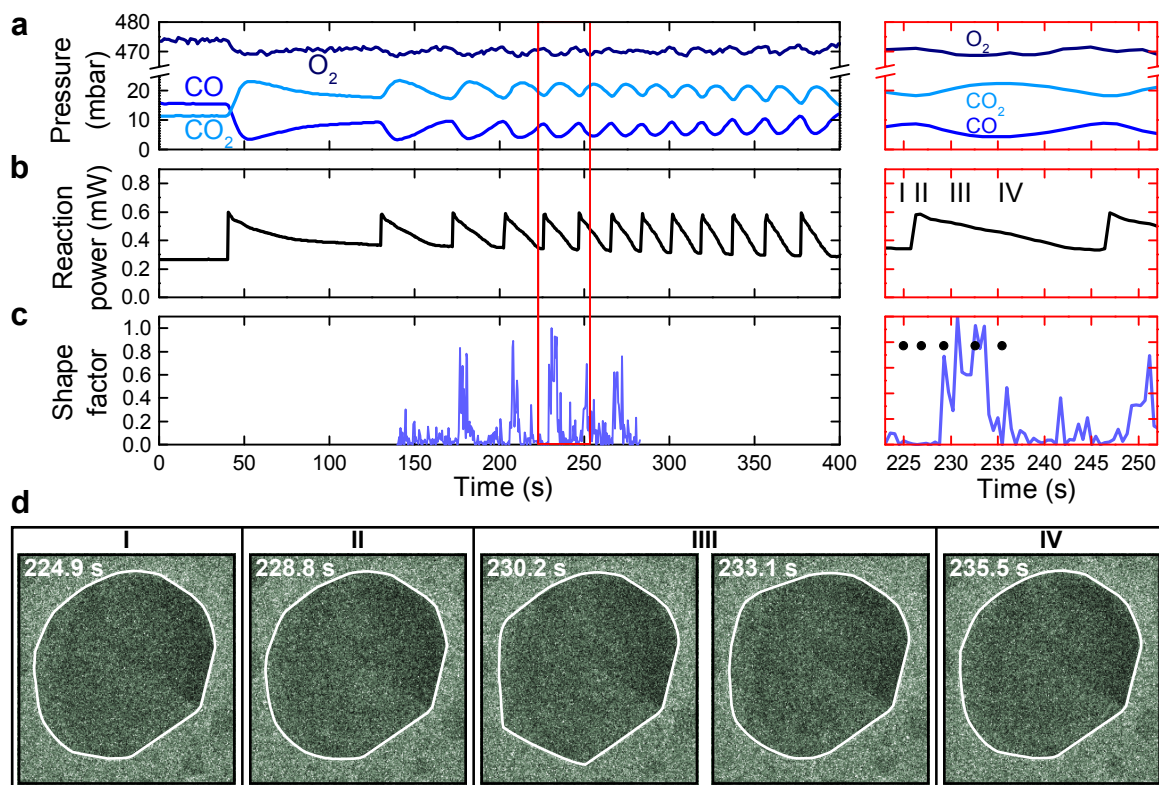


Figure 6.17: Correlation of oscillatory CO oxidation reaction data with the projected morphology of a Pt nanoparticle. The gas entering the reaction zone is 1.0 bar of CO : O<sub>2</sub> : He = 3 : 42 : 55 and nanoreactor temperature is 659 K.

(a) Mass spectrometry of the CO, O<sub>2</sub> and CO<sub>2</sub> pressures, (b) reaction power and (c) shape factor for the Pt nanoparticle in (d) as a function of time. The shape factor corresponds to the relative difference in area from the best elliptical fit in I, (d)[25]. The shape factor is zero for the more spherical shape and increases for more faceted particles. One period of the reaction oscillation data is highlighted by the red box. (d) Time-resolved TEM images of a Pt nanoparticle at the exit of the reaction zone. A movie from this experiment can be found online as supplementary information to [33].

## 6.6 REACTOR MODELING

All observations described here were made at the windows closest to the exit of the reaction zone. At the inlet these oscillations in shape were not observed. Assuming that the particle shape reacts to changes in gas atmosphere[25], this observation suggests that there is a gradient in the gas composition along the flow direction of the nanoreactor.

To understand this, a two dimensional steady model of the nanoreactor was constructed. In order to describe the correlation between shape and global reaction rate, a one dimensional time-dependent reactor model was also set up, based on shape dependent activities calculated by DFT. The modeling was primarily done by Søren Vendelbo with DFT results from Hanne Falsig[33]. Here I will present a short review on the methods, and then mainly focus on the results and their implications. For modeling details see [33] supporting information.

### 6.6.1 Steady state reactor model

As already discussed, the reaction zone is far from isothermal and a significant temperature gradient is expected and has been measured[163]. In this work we have simulated the temperature of the nanoreactor by setting up a model of the reaction zone, including the correct geometry and materials[33]. The temperature gradient was modeled using the heat equation:

$$-k_i \nabla^2 T = Q \quad (6.7)$$

where  $T$  is the temperature,  $Q$  is the heat deposited by the thin film heater and  $k$  is the thermal conductance, which depends on the materials. The equation was solved for the reaction zone, using Matlab's PDE module and the finite element method.

The temperature in the reaction zone is shown in Figure 6.18 for an input power of 18.8 mW. This results in an average temperature of 710 K. In the experiment, off-set power (power required to maintain a certain temperature without reaction) was shown to be 700 K for an input power of 18.9 mW (Section 6.4.3), demonstrating good agreement between simulation and experiment.

The local CO concentration in the reactor was simulated, taking into account flow, diffusion and CO conversion on Pt. The following transport equation was solved:

$$D \nabla^2 c_{CO} - v \frac{dc_{CO}}{dx} - r(T, c_{CO}) = 0 \quad (6.8)$$

where  $D$  is the CO diffusion constant and  $c_{CO}$  is the normalized CO pressure. The flow field is assumed constant with average velocity  $v$ .  $r(T, c_{CO})$  denotes the rate of CO conversion, which depends on temperature and local CO pressure. The rate was described by a simplified Langmuir Hinselwood expression:

$$r(T, c_{CO}) = \frac{k_1 \exp\left(-\frac{E_a}{k_B T}\right) c_{CO}}{(1 + k_2 c_{CO})^2} \quad (6.9)$$

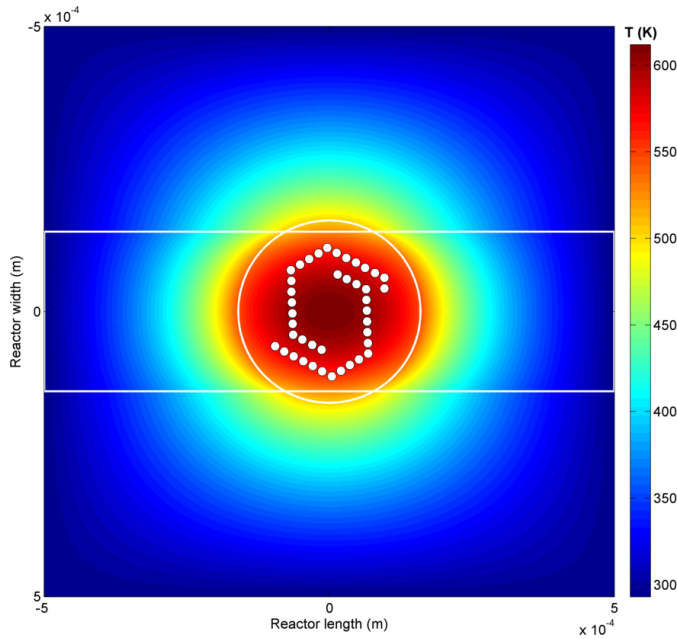


Figure 6.18: Temperature distribution across the reaction zone, based on Equation 6.7 and a full geometrical model of the nanoreactor center. The input power was 18.9 mW and resulted in an average temperature of the reaction zone of 710 K. In the experiment, 18.8 mW was required to maintain a temperature of 700 K without CO conversion (Section 6.4.3), demonstrating a good agreement between model and experiment. At this average temperature, the temperature across the reaction zone varies from 613 K to 777 K. The temperature difference from the hottest to the coldest electron transparent window was 72 K.

where  $E_a$  is the apparent activation energy of the reaction,  $k_1$  and  $k_2$  are prefactors,  $k_B$  is the Boltzmann constant,  $c_{CO}$  is the local CO concentration and  $T$  is the local temperature, where the simulated reaction zone temperature is used.  $E_a$  was determined from an Arrhenius plot of the reaction (Figure 6.19) and  $k_1$  and  $k_2$  were determined by matching the result of the simulation with experimentally determined global conversion over the entire temperature interval.

Figure 6.19 shows an Arrhenius plot of the CO conversion measured by MS as a function of temperature. The model simulates the local conversion and CO pressure in the entire reaction zone. The gas measured by MS was then compared to the simulated gas composition at the outlet of the reaction zone.

The result shows a good agreement between measurement and conversion, and even captures the steep increase in CO conversion seen at around 710 K. The model shows a bistable regime for temperatures between 706 K and 712 K. This means that there are two possible levels of conversion at the same temperature. The direction in which the bistable temperature is approached, determines if the conversion

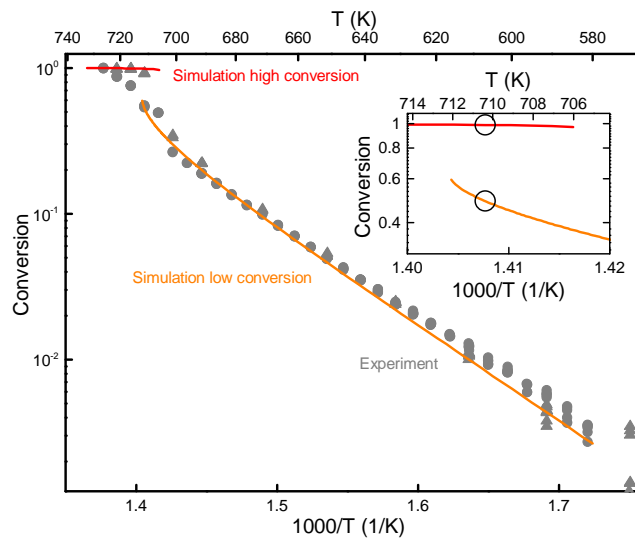


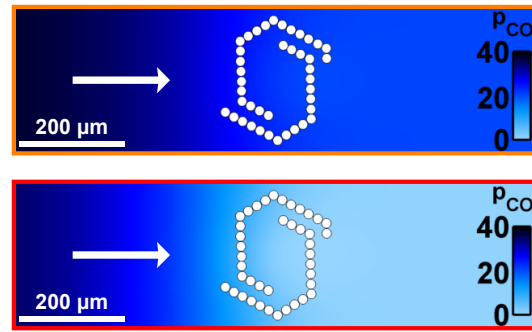
Figure 6.19: Comparison of measured and simulated CO conversion as a function of temperature. Inset: simulations show a bistable regime in the temperature interval 706 K–712 K.

will be in the high or low conversion regime. This is equivalent to experiment, where such hysteresis is seen for CO conversion[155].

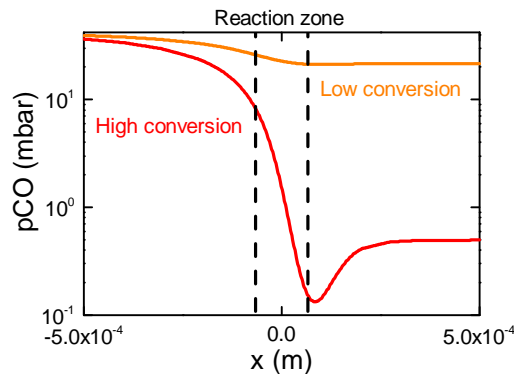
The bistability is a consequence of the form of the Langmuir Hinshelwood expression (Equation 6.9), which has a negative reaction order in CO, depending on the value of  $k_2$  and the exact geometry and flow characteristics of the nanoreactor.

The presence of bistability is interesting in relation to the observed reaction oscillations, where the switch between high and low conversion is viewed as jumping between the two possible conversion levels. The exact temperature where this is observed depends on the reactor loading. The temperature interval where bistability is seen in this experiment is therefore not necessarily the same interval where oscillations (and bistability) are seen in later experiments after aging of the reactor. At steady state, there is no possibility of switching, so the observed oscillations imply some form of dynamic changes to the catalyst structure and reactivity. This has previously been suggested to originate from a change between oxide and metal surface[156]. Here we have observed dynamic shape changes for the nanoparticles coupled to changes in global CO conversion. In order to further investigate this, we set up a time-dependent model to couple reactivity and shape changes.

Now we have only considered the global conversion, the gas composition at the reactor outlet, but the solution to the model provides local CO pressure in the entire nanoreactor. Figure 6.20a shows a map of the CO concentration for the low conversion and high conversion branches at 710.4 K. At low conversion the local CO pressure



(a) Local CO pressure through the reaction zone at low (upper) and high (lower) CO conversion.  $T = 710.4$  K



(b) Local pressure in reaction zone center along flow direction.

Figure 6.20: Local CO pressure for low and high conversion branches at 710.4 K.

(a) The full solution to the steady state model is a local CO pressure in the entire reaction zone. The white dots mark the positions of the electron transparent windows. (b) Local CO pressure along the center line of the reaction zone. Dashed lines mark the position of the electron transparent windows.

varies over the reaction zone from 25 to 21 mbar. At high conversion the local CO pressure varies significantly from 8.4 to 0.2 mbar. The change in CO concentration along the flow direction is illustrated in Figure 6.20b as line profiles. The difference in CO partial pressure between inlet and outlet at high conversion, suggests why shape oscillations were only seen at the outlet, assuming that the shape changes are coupled to local atmosphere. It is also clear from this that the particles located at the reactor exit will experience a significant change in local atmosphere and CO pressure upon a switch between low and high conversion. The result of the simulation also emphasizes the importance of taking into account gradients in both temperature and gas pressure when investigating catalytic reactions at high levels of conversion.

## 6.7 TIME-DEPENDENT REACTOR MODEL

In order to unravel the relationship between shape changes and global CO conversion, a time dependent model was constructed. It is likely that the shape of Pt particles will respond to changes in the gas composition[25, 165]. The question is however, if the observed shape changes are merely a response to the changing gas composition, and that something else is driving the oscillations, or if the shape changes themselves will feed back to the activity and drive reaction oscillations. The point here is that there is no easy answer to this question. Simplified models for similar problems, such as in the work by Hendriksen et al.[156], will have to assume a significant change in the intrinsic rate in the switch between two structures, which in that case are oxide and metal surface. In the following, a full theoretical treatment of the problem is presented. This takes into account flow and diffusion (mass transport) and uses rates based on DFT-calculated energies and microkinetic modeling[33].

Shape changes between round and more faceted geometries were observed by TEM. It comes naturally to assume that shape changes may have an influence on the intrinsic rate, since CO oxidation on Pt is site-dependent[166]. To model this, we have created a simple two-site model, where the average particle shape at any point in the reactor can be described as a linear combination of a flat close-packed Pt(111) surface and a stepped Pt(211) surface, for the faceted and round geometry respectively. The (211) step is a simplified description of the observation, but generally captures trends in reactivity for open and lower coordinated surfaces[167]. If the intrinsic rates of the two surfaces are denoted  $r_{111}$  and  $r_{211}$ , the overall rate  $r$  can be described as:

$$r = \alpha r_{111} + (1 - \alpha)r_{211} \quad (6.10)$$

where  $\alpha$  is a shape factor denoting the fraction of (111) surface.

Intrinsic rates and surface coverages as a function of CO pressure were determined by micro-kinetic modeling based on adsorption and transition state energies calculated by DFT[33, 148]. The result of this is shown in Figure 6.21 for  $T = 793$  K. The  $O_2$  pressure was constant at 210 mbar and only the effect of CO pressure was considered. Due to the excess  $O_2$  in the experiment, this will only change slightly as a function of CO conversion (see e. g. Figure 6.17 on Figure 6.17).

From Figure 6.21a, we see that the stepped surface will be almost fully covered by CO at high CO pressures ( $>1$  mbar). The (111) facet will only have a very low coverage of CO at similar conditions. This difference will stabilize the step compared to the facet, because CO is adsorbed more strongly on the step[148, 168, 169]. This favors a round particle shape with more steps exposed. At low CO pressure ( $<1$  mbar), the O coverage is similar for the two surface types. Be-

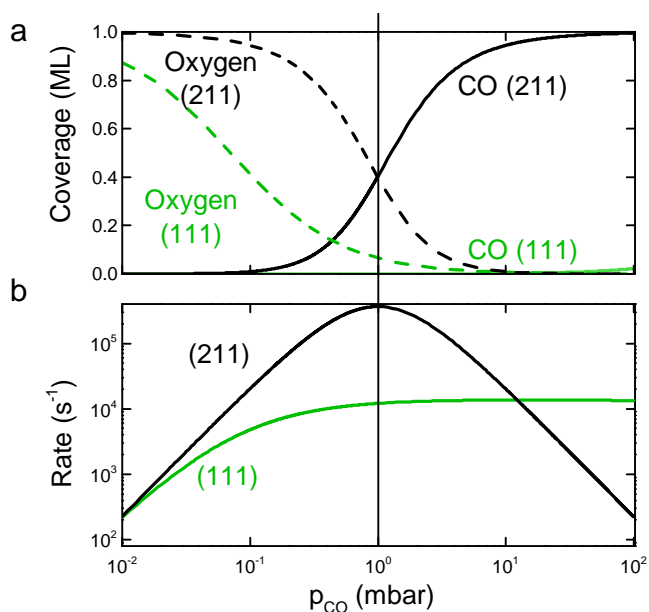


Figure 6.21: Micro-kinetic modeling of reaction rates and surface coverages as a function of CO pressure for Pt(111) and Pt(211) surfaces.  $p_{O_2} = 210$  mbar,  $T = 793$  K.

cause O binds with similar strength to the step and the facet, the facet will be favored due to the lower intrinsic surface energy of the close packed surface. The faceted shape is thus favored at low CO pressure. In this way, a consideration of surface coverages, explains why the Pt particle shape may depend directly on the CO pressure.

Next, the intrinsic rate of the two surfaces is considered. There is a marked difference between the rate as a function of CO pressure as seen from Figure 6.21b. For the step, there is a negative reaction order in CO for pressures above 1 mbar, whereas the rate on the facet is almost independent of CO. The effect of this is a regime where the step is the most active ( $p_{CO} < 10$  mbar) and a regime where the facet is the most active ( $p_{CO} > 10$  mbar). This underlines the importance of considering the conditions when the subject is the structure sensitivity of the CO oxidation reaction. The reason for the declining rate on the step is poisoning or site blocking by CO as the pressure increases.

The parameter  $\alpha$  denotes the fraction of faceted surface in the rate expression for the two-site model (Equation 6.10). It is assumed that at any CO pressure, there is an equilibrium shape, described by  $\alpha_{eq}$ . Because there is a steep change in the coverages of CO and O at a critical value  $p_{CO} = 1$  mbar in Figure 6.21, two equilibrium shapes

are defined such that  $\alpha_{eq} = \alpha_{round}$  for  $pCO > 1$  mbar and  $\alpha_{eq} = \alpha_{faceted}$  for  $pCO < 1$  mbar:

$$\alpha_{eq} = \begin{cases} \alpha_{round}, & \text{for } pCO > 1 \text{ mbar} \\ \alpha_{faceted}, & \text{for } pCO < 1 \text{ mbar} \end{cases} \quad (6.11)$$

The rate of change of  $\alpha$  is assumed to be proportional to the deviation from the equilibrium value such that:

$$k \frac{d\alpha}{dt} = \alpha_{eq}(pCO) - \alpha \quad (6.12)$$

where  $k$  is a scalar determining the rate of change.

The TEM images, such as Figure 6.16 on page 141, show a round shape consisting of both faceted and stepped surfaces, and a faceted shape that corresponds to an increase in the amount of faceted surface. To qualitatively account for this, the equilibrium values for  $\alpha$  were set to 0.7 for the round shape and 1 for the faceted shape.

The time-dependent model is a one dimensional reactor with flow and pressure characteristics identical to the nanoreactor[33]. A time-dependent solution for the full two dimensional description of the nanoreactor is computationally very heavy and was not possible to pursue within the current project.

The result of the time-dependent model is shown in Figure 6.22 as CO pressure at the outlet of the reaction zone (a) and shape factor  $\alpha$  along the reaction zone (b). The result exhibits oscillations in both gas pressures and particle shape and as such captures the observations well. At the inlet to the reaction zone the particle shape is round at all times ( $\alpha = 0.7$ ), because the local CO pressure never reaches the critical value. Further down the reaction zone, the shape oscillates in phase with the CO pressure at the outlet. The shape is faceted ( $\alpha = 1$ ) when the conversion is high, and round ( $\alpha = 0.7$ ), when the conversion is low.

The simulation proves that rate oscillations in the time-dependent model originate from the shape changes and site-specific rates coupled with the mass transport properties of the reactor. Figure 6.22 however does not necessarily answer why shape changes can induce reaction oscillations. To go more in depth with this, we will consider just one period and investigate the reactor properties at different times during an oscillation.

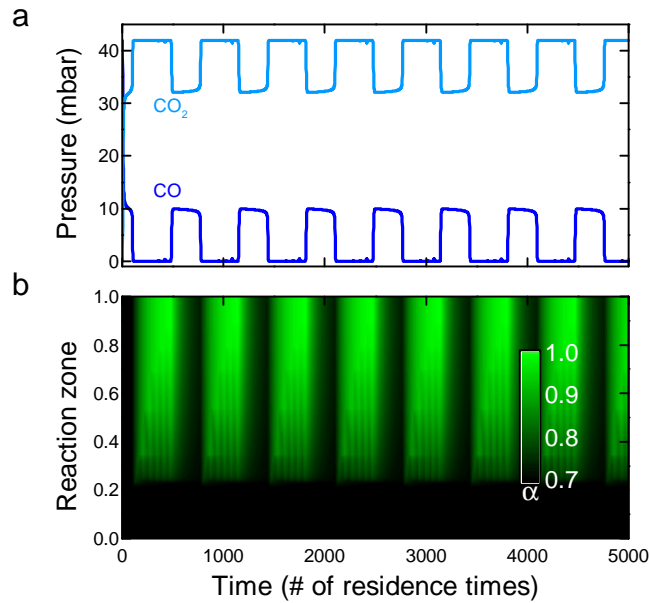


Figure 6.22: Time-dependent reactor model with dynamical shape changes. **(a)** CO and  $\text{CO}_2$  pressure at the exit of the reaction zone as a function of time. **(b)** Shape factor  $\alpha$  along the length of the reaction zone as a function of time. At the inlet to the reaction zone, the shape is always round. Further towards the exit of the reaction zone, the shape oscillates between round and faceted in phase with oscillations in CO pressure (a). The reaction zone is  $320 \mu\text{m}$ , time step is  $2.69^{-4} \text{ s}$ , inlet pressures are  $p_{\text{CO}} = 42 \text{ mbar}$  and  $p_{\text{O}_2} = 210 \text{ mbar}$ . Temperature is  $793 \text{ K}$ .

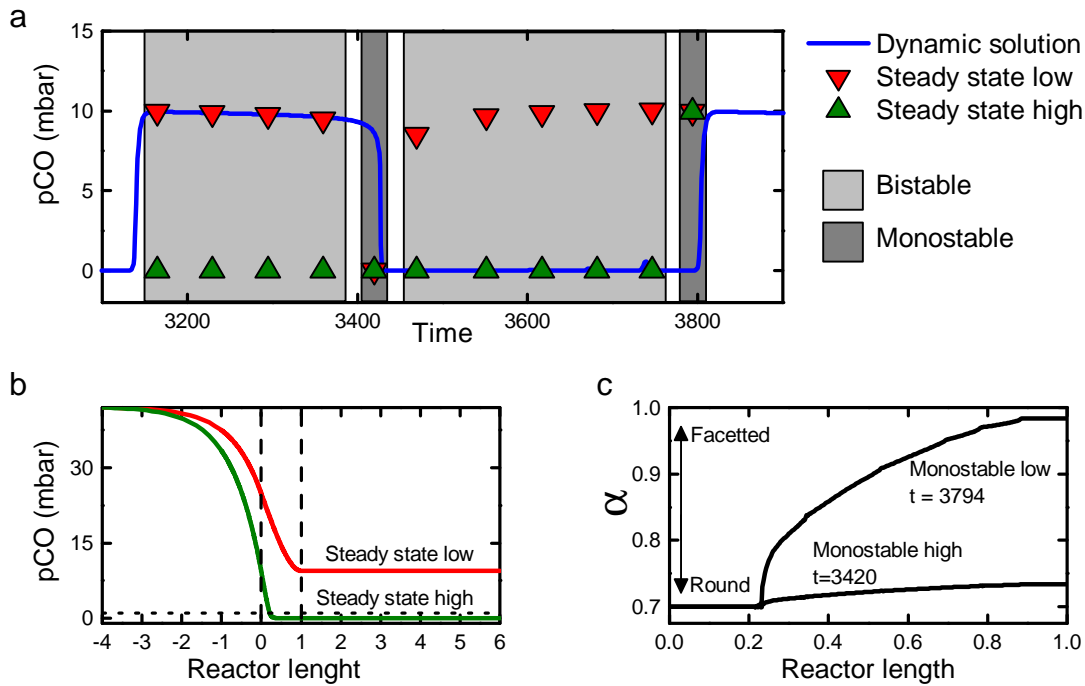


Figure 6.23: Detailed analysis of a single oscillation period in the time dependent model. **(a)** The reactor is bistable at most times. Monostability occurs at the end of a high or low conversion sequence and forces the reactor to switch level. **(b)** CO pressure along the reaction zone at high and low conversion. When the CO pressure is below the critical value of 1 mbar (dashed line) the shape factor  $\alpha$  increases, indicating a more faceted shape. **(c)**  $\alpha$ -distribution along the reaction zone for the two monostable conditions. At the switch to high conversion ( $t=3420$ ) the particles are mostly round. At the switch to low conversion ( $t=3794$ ) the particles are faceted towards the exit of the reaction zone.

Figure 6.23a shows the CO pressure at the reactor outlet during one oscillation period from Figure 6.22. At specific times, the  $\alpha$ -distribution was frozen, and the CO pressure in the reactor was solved at steady state. This was done with two initial conditions; full conversion and no conversion. This corresponds to approaching from high and low temperature, equivalent to the procedure for the two dimensional model at steady state (Section 6.6.1). This steady state solution will reveal if the reactor is bistable, that is, if two solutions, high and low conversion, exist at the same temperature. If there is only one solution, high or low conversion, the reactor is said to be monostable. It is the specific  $\alpha$ -distribution, and according rates, that determine whether the reactor is bi- or monostable. Since the  $\alpha$ -distribution changes over time, the result will depend on the specific point in time. Figure 6.23b shows the CO pressure along the length of the reaction zone for a high and low conversion solution at the same  $\alpha$ -distribution. Red triangles in Figure 6.23a mark a low conversion solution, and green triangles mark a high conversion solution. From time ca 3150 to 3400, the reactor is in the low conversion regime in

the time-dependent solution, as seen from the 10 mbar CO pressure at the outlet (Figure 6.23a). For the first four steady state solutions, the reactor is found to be bistable. This means, that the intrinsic rate of the reactor, given by the  $\alpha$ -distribution, could facilitate both a high and a low global conversion level. There is however no mechanism to switch to the high conversion level, and the reactor will be stuck at low conversion. This changes at time 3420. The steady state solution now has only a single solution; the reactor has become monostable. In this case, the only possible solution is a high level of conversion ( $p_{\text{CO}_{\text{outlet}}} = 0$ ) and the reactor will instantly switch. Figure 6.23c shows the specific  $\alpha$ -distribution at this point in time, and we see that the particle shape is round in almost the entire reactor. As soon as the global conversion changes,  $\alpha$  will start to change again to approach the new equilibrium value, which will be the faceted shape in most of the reactor (critical CO pressure shown as dotted line in Figure 6.23b). The result of this is that the  $\alpha$ -distribution again allows two solutions and the reactor has become bistable at time 3470. During the period of high conversion, the values of  $\alpha$  will thus gradually change, until at time 3793, suddenly only one solution is allowed, this time the low conversion level and the global conversion will immediately change. The  $\alpha$ -distribution at this point is shown in Figure 6.23c.

The take home message here is the following: Two global conversion levels exist for the same  $\alpha$ -distribution and thereby intrinsic rates. It only takes an incremental change in the  $\alpha$ -distribution in order to push the reactor from bistable to monostable which is reflected in a dramatic change in the global conversion. This is an effect of the self-poisoning/negative reaction order of CO-oxidation coupled to flow and diffusion in the specific reactor design.

## 6.8 CHAPTER CONCLUSION

This chapter has demonstrated the use of nanoreactor technology to investigate the oscillatory oxidation of CO on a Pt catalyst. The experiment was performed at 1 bar total pressure and with a partial pressure of CO of 30-42 mbar.

1 bar experiments require some auxiliary functions in terms of gas feed system and gas analysis. This however allows us to obtain simultaneous TEM images and reaction rate data in the form of outlet gas analysis and calorimetry. The calorimetry benefits from the very fast thermal response of the miniaturized nanoreactor and has allowed us to resolve reaction oscillations with periods down to a few seconds. Simultaneous TEM captured images at a similar rate and was able to reveal shape changes of the Pt particles in phase with global oscillations in reaction power. By a careful alignment and analysis of the different data sources, we were able to see that the particle shape changed after the change in global reaction rate.

In order to quantify our observations and to test the hypothesis that the shape changes were the drivers behind the oscillations, it was necessary to set up a full two-dimensional steady-state model of the nanoreactor as well as a simplified one-dimensional but time-dependent model. By using site specific reaction rates for a flat and a stepped Pt surface, as calculated by density functional theory and micro-kinetic modeling, it was possible to reveal that the shape changes could indeed be the driver behind the rate oscillations. This does not rule out other phenomena such as e.g. oxidation/reduction or restructuring of the Pt surface, but our data shows that shape changes is a sufficient description.

The results presented here has revealed a hitherto unknown mechanism for rate oscillations in CO oxidation on Pt. It is improbable that this finding could have been made with other experimental techniques, and so this is a strong demonstration of the benefit and value of *Operando* TEM and nanoreactor technology in heterogeneous catalysis.

## SUMMARY AND CONCLUSION

---

This thesis has presented results on four different catalyst systems, each with their own set of challenging questions requiring a careful investigation and answer. In all cases, dynamics have been investigated by the extensive use of *in situ* TEM imaging. Following the processes live as they happen allow us to directly see phenomena where we would otherwise have to rely on indirect measurements and assumptions. In this thesis, we have followed individual particles live as they nucleated and grew from a solid precursor, we have followed particles during sintering and we have seen particles respond to changes in atmosphere; Pt particles that change shape during reaction oscillations and Cu/ZnO particle oxidizing and reducing. In the following I will sum up the main scientific conclusions from these observations.

### CATALYST ACTIVATION. REDUCTION OF CU PHYLLOSILICATE

Cu phyllosilicate was reduced to Cu on silica inside the TEM while the process was imaged *in situ*. The data obtained established the foundation for modeling work which revealed that the reduction proceeded by an autocatalytic route. Here, the initial nucleation of Cu is slow and the subsequent growth in size is fast because the Cu particles themselves catalyze further reduction.

### CATALYST STRUCTURE AND ACTIVITY

Size selected particles of a CuZn alloy was used to create Cu/ZnO particles. This is a simplified model of the complex high surface area Cu/ZnO/Al<sub>2</sub>O<sub>3</sub> catalyst used for the synthesis of methanol. This tool allows us to tune the size and composition of such particles in order to investigate the interplay between Cu and ZnO and the effect of ZnO as a promoter for catalytic activity. By following this approach and studying these particles by XPS and TEM, it was revealed that the surface of the reduced catalyst consists of Cu decorated with well defined ZnO particles. Furthermore, it was shown that a fraction of the ZnO is reduced simultaneously with the Cu under H<sub>2</sub> atmosphere, presumably forming a surface alloy with the Cu.

### CATALYST DEACTIVATION

Sintering of Cu nanoparticles was investigated for size-selected Cu particles deposited on a flat SiO<sub>x</sub> surface. Sintering is the main deactivation mechanism for the methanol synthesis catalyst so this topic is of great interest to the development of better catalysts. By following

individual particles over time with *in situ* TEM, it was revealed that the sintering proceeded via Ostwald ripening. The presence of CO increased the rate of sintering significantly and the presence of H<sub>2</sub>O slowed it down.

#### A DYNAMIC STRUCTURE-ACTIVITY RELATIONSHIP

Pt nanoparticles were imaged *in situ* by TEM during CO oxidation. Specifically, we studied temporal rate oscillations under fixed conditions. Nanoreactor technology was employed, such that it was possible to simultaneously acquire TEM images and measure catalytic activity. This is referred to as an *Operando* experiment. The work presented here is the first published demonstration of such simultaneous TEM and activity measurement. It was revealed that the shape of the Pt nanoparticles change in phase with changes in global reaction rate. By the use of reactor modeling it was shown that the oscillations are possible because the reactor is bistable, which is an effect of the self-poisoning nature of the CO oxidation reaction on Pt coupled with gas flow and diffusion in the reactor. Our work showed that shape changes were sufficient to drive global rate oscillations.

*In situ* TEM has by far been the dominant experimental technique in this work and the technical implementation and use of the microscope has therefore been important throughout. In order to realize the experimental goals and reach the conclusions listed above, it has been necessary to constantly evaluate and develop the experimental approach. Important subjects have been sample preparation, reference experiments, control of beam effects, gas feed and gas analysis, data synchronization and image analysis. These practical and technical challenges can sometimes outshine the scientific perspective, either because they are very challenging and require dedication and perseverance or because we get lost in experimental detail out of pure and genuine interest! The development of the experimental techniques is certainly very important but it is of course also important to keep in mind the scientific goals and the implications of our findings. Maintaining this balance has been an important challenge during my PhD, and I feel privileged to have worked with new techniques and high end equipment and applied it to interesting scientific issues. I hope my research and the results presented in this thesis are of interest to the scientific community and that I have helped advance the fields of catalysis and *in situ* transmission electron microscopy.

Thank you for taking the time to read my thesis, I hope you have enjoyed it.

## APPENDIX



## COLORING OF TEM IMAGES

CRYSTAL PHASE	(HKL)	d(Å)	COLOR
CuO	(-202)	1.87	Green
CuO	(-112)	1.96	Green
CuO	(111) & (200)	2.31	Green
Cu <sub>2</sub> O	(011)	3.02	Purple
Cu	(200)	1.81	Red
Cu	(111)	2.08	Red
ZnO	(002)	2.60	Blue
ZnO	(010)	2.81	Blue
CuO	(-1-11)	2.52	Green
Cu <sub>2</sub> O	(111)	2.46	Purple
ZnO	(011)	2.48	Blue

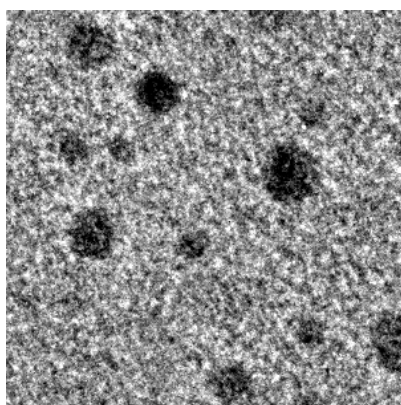
Table A.1: Lattice spacings used in phase identification of Cu, CuO, Cu<sub>2</sub>O and ZnO. The spacings in the top eight rows are unique to the associated phase. The three bottom rows show the spacing at ca 2.5 Å shared by the three relevant oxides.



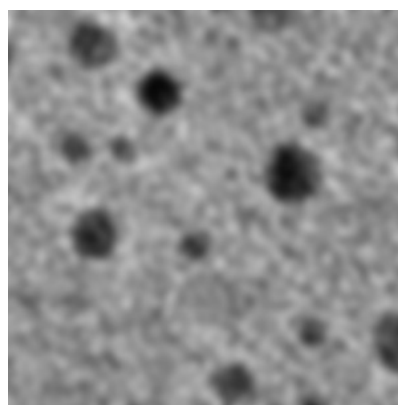
## AUTOMATIC PARTICLE SIZE MEASUREMENT

Here the procedure for measuring the size of particles used in connection with Chapter 5 is explained.

The procedure can be divided into two main steps; noise removal and thresholding. Due to contrast variations in the amorphous background material, filtering of noise is crucial in order to perform correct thresholding. A crop of a TEM image is shown in Figure B.1a. It is recorded with a beam current of  $100 e^-/(\text{\AA}^2\text{s})$  and an exposure time of 3 seconds.



(a) Original TEM image of Cu particles on  $\text{SiO}_x$  film, pixel size 0.11 nm, 3 s exposure.



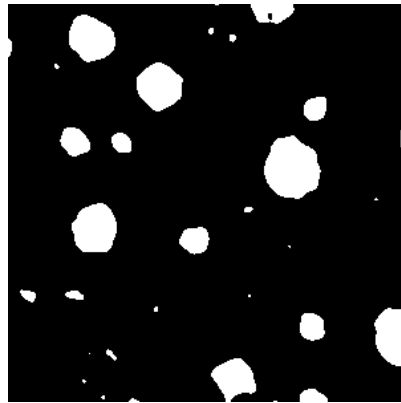
(b) Smoothed image using a gaussian blur filter with 17 by 17 pixel kernel and  $\sigma = 3.7$

Figure B.1: Automatic particle size measurement 1

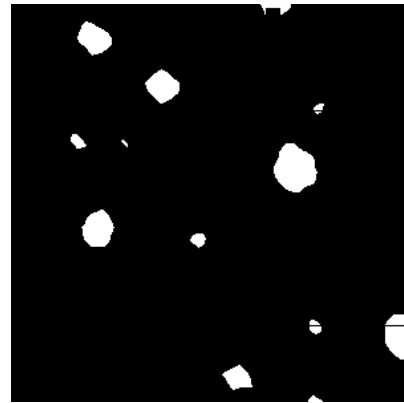
Removal of noise is done by smoothing the image with an averaging algorithm, which acts as a low pass filter removing all high frequency detail in the image. This works by setting the value of a pixel to a weighted average of itself and its neighboring pixels. This weighting can be done in various ways depending on how strong a noise removal is required and how much detail loss is acceptable. For the treatment of the images in this work I have averaged with a Gaussian kernel, which means the weighting is performed with a rotationally symmetric gaussian filter with a defined standard deviation ( $\sigma$ ). Figure B.1b shows the selected image smoothed with a gaussian blur filter with  $\sigma = 3.7$  and a kernel size of 17 by 17 pixels. Detail is clearly lost and the image appears blurred, also around the edge of the particles, but we can still recognize all particles and the blurring has certainly removed the high frequency noise.

The next step is to separate pixels into either particles or background, a process called segmentation. Here the interesting objects,

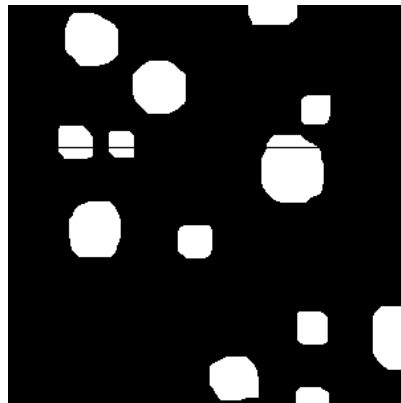
the particles, are dark, i.e. have a lower pixel value than the background, so the segmentation is done by finding a threshold pixel value and regarding everything brighter as belonging to the background. Matlab has a built in thresholding function using Otsu's method [170]. This was however not very effective for the images recorded here. Instead the method of maximum entropy[171] worked very well and was implemented in Matlab based on the description by Kapur, Sahoo, and Wong[171].



(a) Thresholded image using the Kapur, Sahoo, and Wong Method[171].



(b) Thresholded image after 4 consecutive erosion operations with a 3 by 3 pixel kernel. This will remove all objects with a shortest length less than 9 pixels, corresponding to 1 nm.



(c) Eroded image (Figure B.2b) after 6 dilation operations with a 3 by 3 pixel kernel.



(d) Logical OR between (a) and (c).

Figure B.2: Automatic particle size measurement 2

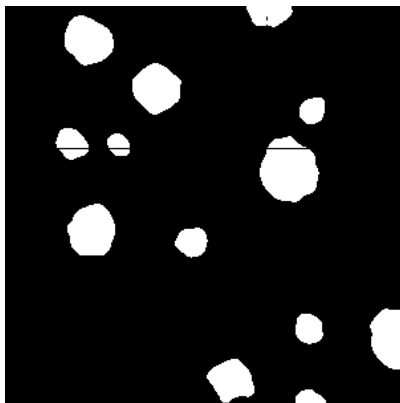
Figure B.2a shows the filtered image after thresholding, now represented as a binary image. In the segmented image, some noise is still present which needs to be removed. This is done by a simple three-step procedure that includes the following three operations:

- 4 consecutive erosion operations (Figure B.2b)

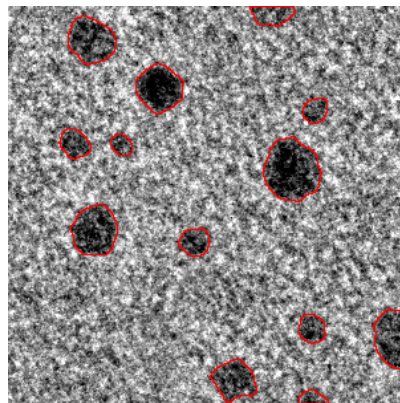
- 6 consecutive dilation operations on eroded image (Figure B.2c)
- Logic AND of dilated image and original threshold image (Figure B.2d)

An erosion with a 3 by 3 kernel sets a pixel's value to zero if any of its 8 neighbors have the value zero. This shrinks all objects in the image as can be seen from Figure B.2b. A dilation is the opposite operation which sets a pixel's value to 1 if any of its neighbors have the value 1, which expands all objects in the image as seen from Figure B.2c. The erosion is repeated 4 times, which means that any object with a length or width less than 9 pixels will disappear. This sets a lower limit for the size of particle that is measured of 1 nm. The dilation is performed 6 times to make sure all particles are larger than the original.

The final logic AND between the dilated image and the original thresholded image serves to recreate all particle of 1 nm or more with the correct shape as seen in Figure B.2d. The last operation is a dilation, again with a 3 by 3 pixel kernel which simply expands the size of all particles to better match the size measured by hand. Figure B.3a shows the area after two dilation operations. Finally Figure B.3b shows the original image with boundaries corresponding to the result of the automatic measurement.



(a) Final dilation to slightly increase particle size to match hand measured. Two times dilation with a 3 by 3 pixel kernel.



(b) Original image with outlines showing automatically determined particle areas.

Figure B.3: Automatic particle size measurement 3

The automatic routine finds the areas of the particles and as seen from Figure B.3b these are not necessarily circular. For this work it has been decided to represent particle size as the diameter of a circle with the same area as the irregular shape, similarly to [52].



## QUANTIFICATION OF MS SIGNALS FOR NANOREACTOR EXPERIMENTS

Here, the quantification of MS data is explained, taking gas fractioning into account, i. e. a changing inlet gas composition over the course of the experiment.

First, a nanoreactor was held at room temperature at the beginning and at the end of the experiment, to ensure that the total gas flow rate is the same and CO conversion is absent. Under these conditions, mass spectrometry data was acquired, corresponding to regions 1 and 3 in Figure C.1a.

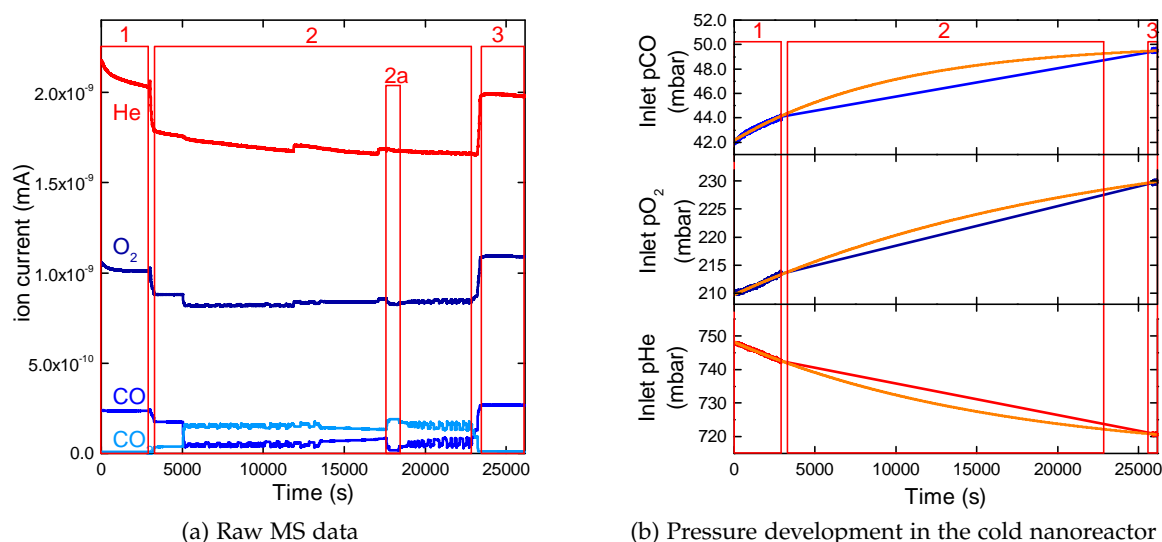


Figure C.1: **(a)** Ion currents recorded for an experiment. Region 1 denotes the beginning time interval in which the nanoreactor was at room temperature. In region 2, CO oxidation was induced by temperature variations to allow for observations of reaction oscillations by HRTEM and MS. Region 2a denotes a time interval in which full CO conversion is obtained. Region 3 denotes the end interval of the experiment in which the nanoreactor was again kept at room temperature. **(b)** Partial pressures of He, CO and  $O_2$  entering the reaction zone as obtained from the ion currents in (a). Blue and red points denote the partial pressures in regions 1 and 3 as obtained from ion current and the nominal initial partial pressures. The orange curves denote the exponential extrapolation of the inlet partial pressures during the entire experiment.

At time 0 s, when the gas starts entering the nanoreactor, it must have the nominal composition. This assessment allows a sensitivity coefficient for each gas component to be obtained. That is, the sensitivity coefficient  $\alpha_x$  for a gas  $x$  (where  $x$  is He, CO or  $O_2$ ) was

calculated from the ion current  $ic_x^{initial}$  and known partial pressure  $p_x^{initial}$  as:

$$a_x = p_x^{initial} / ic_x^{initial} \quad (C.1)$$

These sensitivity coefficients allow the partial pressures of He, CO and O<sub>2</sub> to be calculated throughout the initial and final interval at room temperature and with no conversion, corresponding to regions 1 and 3 (Figure C.1a):

$$P_x(t) = a_x * ic_x(t), \quad x = \text{He, CO, O}_2 \quad (C.2)$$

However, in the course of the experiment, the conditioning of the mass spectrometer resulted in a slight decrease in the total ion current. The effect of this conditioning is compensated for by multiplying all partial pressures in regions 1 and 3 by a scaling factor  $s(t)$  :

$$s(t) = \frac{1000}{p_{\text{He}}(t) + p_{\text{CO}}(t) + p_{\text{O}_2}(t)} \quad (C.3)$$

For the experiment, Figure C.1a,  $s$  was 1.06 at time 26000 s, which demonstrates that the correction is indeed minor. Thus, the partial pressures entering the reaction zone at the beginning and at the end of an experiment, corresponding to regions 1 and 3 (Figure C.1a), was therefore:

$$P_x(t) = a_x * ic_x(t) * s(t) \quad (C.4)$$

The partial pressures entering the reaction zone during the period with the actual experiments, corresponding to region 2 in Figure C.1a, were estimated by interpolating the pressures obtained at the beginning and at the end of the experiment (regions 1 and 3) using an exponential decay function of the form  $y(x) = A \times \exp(-x/t) + y_0$ . The exponential form was used as it describes the pressure decay through an orifice from a closed container. For each partial pressure, the exponential form was fitted to the inlet pressures at the beginning and end period, as demonstrated by the orange lines in Figure C.1b. The partial pressures described by the exponential fit over the entire time interval of the experiment are referred to as  $P_{\text{He}}^{in}(t)$ ,  $P_{\text{CO}}^{in}(t)$ ,  $P_{\text{O}_2}^{in}(t)$  in the following.

To quantify the CO, CO<sub>2</sub> and O<sub>2</sub> pressures during the actual CO oxidation experiment, the ion currents were first normalized based on the He signal to eliminate the effect of temperature-induced changes in the gas flow rate. Subsequently, to convert the He-normalized ion

currents to partial pressures for each of the three gases a multiplication factor was calculated:

$$k_x = p_x / \left( \frac{ic_x}{ic_{He}} - \left[ \frac{ic_x^{background}}{ic_{He}^{background}} \right] \right), \quad x = CO, CO_2, O_2 \quad (C.5)$$

To estimate  $k_{CO}$ , the CO background pressure is first considered. It corresponds to the CO pressure under conditions for full CO conversion. Such conditions can be identified when the CO<sub>2</sub> signal remains stable upon further temperature increase (Figure C.1a region 2a and Figure C.2a). Moreover, under such conditions, the ratio of CO to CO<sub>2</sub> ion current, which is 9.4% in Figure C.2a, agrees with the expected cracking ratio of CO and CO<sub>2</sub> of 11.4% in the mass spectrometer (Pfeiffer MS spectra library). Thus, these findings indicate that the CO ion current at the conversion conditions as in Figure C.2a stems from the background signal due to cracking of CO<sub>2</sub> in the mass spectrometer and is not due to unconverted CO, i.e. demonstrating that the system is not mass transfer limited under these conditions. Thus, under full conversion conditions, the background CO ion current  $ic_{CO}^{background}$  is directly obtained and normalized to the He ion current at that point.

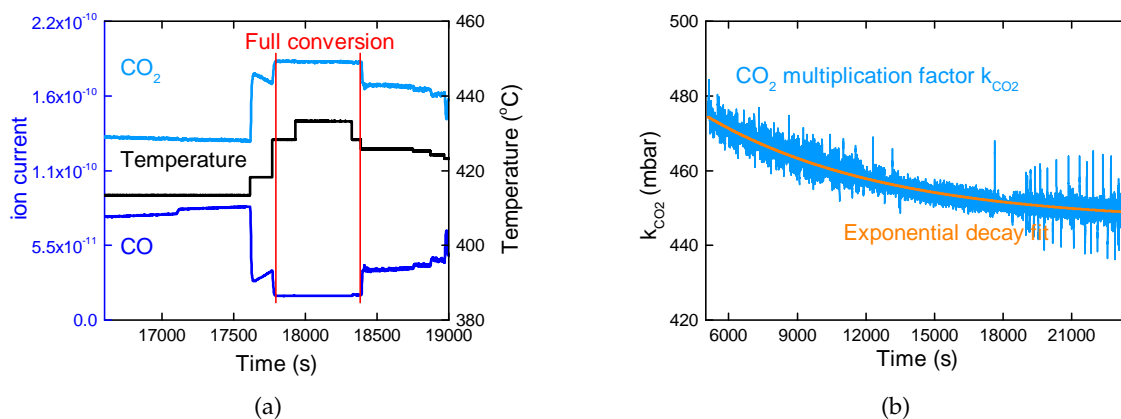


Figure C.2: **(a)** A close-up region 2a in Figure C.1a showing CO and CO<sub>2</sub> ion currents as a function of time during heating through a full conversion (corresponding to time interval marked by red vertical bars). **(b)** The CO<sub>2</sub> multiplication factor  $k_{CO_2}$  is calculated from the difference between CO inlet pressure (Figure C.1b) and measured CO partial pressure during the experimental time interval. An exponential decay function fitted to the data (orange) is shown as well.

Next,  $k_{CO}$  will change during the course of the experiment due to the variations in gas composition entering the reaction zone and the conditioning of the MS. To take such variations into account, the exponentially extrapolated inlet pressures  $P_{He}^{in}(t)$ ,  $P_{CO}^{in}(t)$ ,  $P_{O_2}^{in}(t)$  (Figure C.1b) are combined with equation Equation C.4 to yield the cor-

rected ion current (where  $x$  is He, CO or O<sub>2</sub>) used to calculate  $k_{CO}$  as a function of time:

$$ic_x = \frac{p_x^{in}(t)}{a_x * s(t)} \quad (C.6)$$

where  $p_x^{in}(t)$  and  $s(t)$  are estimated as described above and  $a_x$  is constant. Using the corrected ion current in combination with equation Equation C.5, allows  $k_{CO}$  to be expressed as:

$$k_{CO}(t) = p_{CO}^{in}(t) / \left( \frac{p_{CO}^{in}(t) * a_{He}}{p_{He}^{in}(t) * a_{He}} - \left[ \frac{ic_{CO}^{background}}{ic_{He}^{background}} \right] \right) \quad (C.7)$$

Following from this expression, the CO pressure exiting the reaction zone is at any time  $t$  during the experimental period given as:

$$p_{CO} = k_{CO}(t) \left( \frac{ic_{CO}(t)}{ic_{He}(t)} - \left[ \frac{ic_{CO}^{background}}{ic_{He}^{background}} \right] \right) \quad (C.8)$$

Using the same approach, the partial pressure of O<sub>2</sub> entering into the reaction zone, can be calculated from the He-normalized O<sub>2</sub> ion current. The only difference is that background subtraction is omitted because the O<sub>2</sub> ion current remains an order of magnitude higher than other signals and is thus almost unaffected by the reaction. To calculate any CO<sub>2</sub> partial pressure from the ion currents, a different approach had to be used because the inlet gas does not contain any CO<sub>2</sub> that could act as an internal gas calibration standard. However, the experiment allows for a CO<sub>2</sub> multiplication factor to be derived using other information. First, at the beginning and end of the experiment, corresponding to regions 1 and 3 (Figure C.1), no CO oxidation occurs implying that the CO<sub>2</sub> ion current corresponds to the background level of the mass spectrometer. Second, during the experimental period, corresponding to region 2 (Figure C.1), the CO<sub>2</sub> partial pressure was estimated as the difference between inlet CO and measured CO partial pressures as:

$$p_{CO_2}^{calibration}(t) = p_{CO}^{in}(t) - p_{CO} \quad (C.9)$$

Thus, the multiplication factor for the experimental time interval (Figure C.1, region 2) was then calculated as:

$$k_{CO_2}^{calibration}(t) = p_{CO_2}^{calibration}(t) / \left( \frac{ic_{CO_2}(t)}{ic_{He}(t)} - \left[ \frac{ic_{CO_2}^{background}}{ic_{He}^{background}} \right] \right) \quad (C.10)$$

Just as for CO and O<sub>2</sub>,  $k_{CO_2}$  decays over the experimental period (Figure C.2b). To describe this long-term development caused by the changes in CO and He inlet pressures (Figure C.1a, region 2),  $k_{CO_2}$  was described by an exponential decay function (Figure C.2b), since

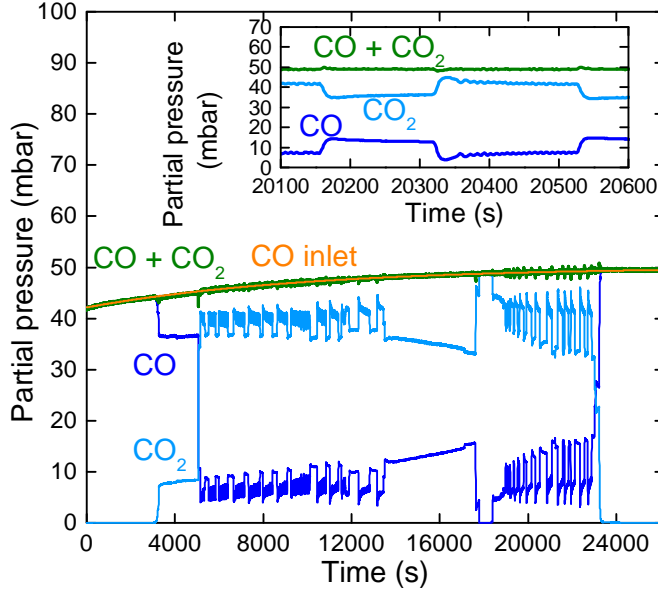


Figure C.3: Comparison of the sum of CO and CO<sub>2</sub> partial pressures with the inlet CO partial pressure. Also the individual partial pressures of CO and CO<sub>2</sub> are shown. The inset shows how abrupt changes lead to deviations in the summed signal due to a slight delay of the CO<sub>2</sub> signal compared to CO.

this corresponds well to the changing inlet pressures. Using the fitted function, the partial pressure of CO<sub>2</sub> during the experiment is described as:

$$p_{\text{CO}_2}(t) = k_{\text{CO}_2}(t) \frac{i_{\text{CO}_2}(t)}{i_{\text{He}}(t)} - \left[ \frac{i_{\text{CO}_2}^{\text{Background}}}{i_{\text{He}}^{\text{Background}}} \right] \quad (\text{C.11})$$

To confirm this pressure calibration, the sum of the CO and CO<sub>2</sub> partial pressures  $p_{\text{CO}}(t) + p_{\text{CO}_2}$  is compared with the CO inlet pressure  $p_{\text{CO inlet}}^i(t)$  (Figure C.3) and shows a good agreement, because the summed partial pressures remain a continuous function, resembling the inlet CO pressure, during the reaction-induced changes in CO and CO<sub>2</sub> pressures. Minor deviations in the summed partial pressures are however observed (Figure C.3, insert). These deviations appear in the rapid cross-over from the low to the high conversion level in the oscillatory regimes. The comparison with the individual CO and CO<sub>2</sub> partial pressures indicates that the deviations are caused by a delay of the CO<sub>2</sub> signal compared to CO. Thus, the deviations are attributed to a space-time broadening effect during these fast changes in the gas composition.



## BIBLIOGRAPHY

---

- [1] I. Chorkendorff and J. W. Niemantsverdriet. *Concepts of Modern Catalysis and Kinetics*. 2nd. Weinheim, FRG: Wiley-VCH Verlag GmbH & Co. KGaA, 2003, p. 477. ISBN: 9783527602650. DOI: 10.1002/3527602658.
- [2] B. Hammer and J.K. Nørskov. "Electronic factors determining the reactivity of metal surfaces." In: *Surface Science* 343.3 (1995), pp. 211–220. DOI: 10.1016/0039-6028(96)80007-0.
- [3] B. Hammer and J. K. Nørskov. *Why gold is the noblest of all the metals*. 1995. DOI: 10.1038/376238a0.
- [4] B. Hammer and J.K. Nørskov. "Theoretical Surface Science and Catalysis - Calculations and Concepts." In: *Advances in Catalysis* 45 (2000), pp. 71–129. DOI: 10.1016/S0360-0564(02)45013-4.
- [5] P. W. Anderson. "Localized Magnetic States in Metals." In: *Phys. Rev.* 124.1 (1961), p. 41. DOI: 10.1103/PhysRev.124.41.
- [6] D. M. Newns. "Self-consistent model of hydrogen chemisorption." In: *Physical Review* 178.3 (1969), pp. 1123–1135. DOI: 10.1103/PhysRev.178.1123.
- [7] A Ozaki and K Aika. *Catalysis: science and technology, Volume 1*. Springer-Verlag, 1981.
- [8] T. Bligaard, J.K. Nørskov, S. Dahl, J. Matthiesen, C.H. Christensen, and J. Sehested. "The Brønsted–Evans–Polanyi relation and the volcano curve in heterogeneous catalysis." In: *Journal of Catalysis* 224.1 (2004), pp. 206–217. DOI: 10.1016/j.jcat.2004.02.034.
- [9] J.K. Nørskov et al. "Universality in Heterogeneous Catalysis." In: *Journal of Catalysis* 209.2 (2002), pp. 275–278. DOI: 10.1006/jcat.2002.3615.
- [10] K. Honkala, A. Hellman, I. N. Remediakis, A. Logadottir, Carlsson A., S. Dahls, C. H. Christensen, and J. K. Nørskov. "Ammonia Synthesis from First-Principles Calculations." In: *Science* 307.5709 (2005), pp. 555–558. DOI: 10.1126/science.1106435.
- [11] J. K. Nørskov, T. Bligaard, J. Rossmeisl, and C. H. Christensen. "Towards the computational design of solid catalysts." In: *Nature Chemistry* 1.1 (2009), pp. 37–46. DOI: 10.1038/nchem.121.
- [12] Samira Siahrostami et al. "Enabling direct H<sub>2</sub>O<sub>2</sub> production through rational electrocatalyst design." In: *Nature materials* 12.December (2013), pp. 1137–43. DOI: 10.1038/nmat3795.

- [13] Felix Studt, Irek Sharafutdinov, Frank Abild-Pedersen, Christian F. Elkjær, Jens S. Hummelshøj, Søren Dahl, Ib Chorkendorff, and Jens K. Nørskov. "Discovery of a Ni-Ga catalyst for carbon dioxide reduction to methanol." In: *Nature Chemistry* March (2014), pp. 1–5. DOI: 10.1038/nchem.1873.
- [14] S. Dahl, A. Logadottir, R. Egeberg, J. Larsen, I. Chorkendorff, E. Törnqvist, and J. Nørskov. "Role of Steps in N<sub>2</sub> Activation on Ru(0001)." In: *Physical Review Letters* 83.9 (1999), pp. 1814–1817. DOI: 10.1103/PhysRevLett.83.1814.
- [15] Jens K Nørskov, Thomas Bligaard, Britt Hvolbaek, Frank Abild-Pedersen, Ib Chorkendorff, and Claus H Christensen. "The nature of the active site in heterogeneous metal catalysis." en. In: *Chemical Society reviews* 37.10 (2008), pp. 2163–71. DOI: 10.1039/b800260f.
- [16] Malte Behrens et al. "The active site of methanol synthesis over Cu/ZnO/Al<sub>2</sub>O<sub>3</sub> industrial catalysts." In: *Science (New York, N.Y.)* 336.6083 (2012), pp. 893–7. DOI: 10.1126/science.1219831.
- [17] Ifan E. L. Stephens et al. "Tuning the Activity of Pt(111) for Oxygen Electroreduction by Subsurface Alloying." In: *Journal of the American Chemical Society* 133.14 (2011), pp. 5485–5491. DOI: 10.1021/ja111690g.
- [18] Søren B Vendelbo, Martin Johansson, Jane H Nielsen, and Ib Chorkendorff. "Is the methanation reaction over Ru single crystals structure dependent?" In: *Physical chemistry chemical physics : PCCP* 13.10 (2011), pp. 4486–4493. DOI: 10.1039/c0cp02371j.
- [19] F. Besenbacher. "Design of a Surface Alloy Catalyst for Steam Reforming." In: *Science* 279.5358 (1998), pp. 1913–1915. DOI: 10.1126/science.279.5358.1913.
- [20] M.P. Andersson, F. Abild-Pedersen, I.N. Remediakis, T. Bligaard, G. Jones, J. Engbæk, O. Lytken, S. Horch, J.H. Nielsen, and J. Sehested. "Structure sensitivity of the methanation reaction: H<sub>2</sub>-induced CO dissociation on nickel surfaces." In: *Journal of Catalysis* 255.1 (2008), pp. 6–19. DOI: 10.1016/j.jcat.2007.12.016.
- [21] H Topsøe. "Developments in operando studies and in situ characterization of heterogeneous catalysts." In: *Journal of Catalysis* 216.1-2 (2003), pp. 155–164. DOI: 10.1016/S0021-9517(02)00133-1.
- [22] Poul L Hansen, Jakob B Wagner, Stig Helveg, Jens R Rostrup-Nielsen, Bjerne S Clausen, and Henrik Topsøe. "Atom-resolved imaging of dynamic shape changes in supported copper nanocrystals." In: *Science (New York, N.Y.)* 295.5562 (2002), pp. 2053–5. DOI: 10.1126/science.1069325.

- [23] F. Tao, M. E. Grass, Y. Zhang, D. R. Butcher, J. R. Renzas, Z. Liu, J. Y. Chung, B. S. Mun, M. Salmeron, and G. A. Somorjai. "Reaction-Driven Restructuring of Rh-Pd and Pt-Pd Core-Shell Nanoparticles." In: *Science* 322.5903 (2008), pp. 932–934. DOI: 10.1126/science.1164170.
- [24] Mark A Newton, Carolina Belver-Coldeira, Arturo Martínez-Arias, and Marcos Fernández-García. "Dynamic in situ observation of rapid size and shape change of supported Pd nanoparticles during CO/NO cycling." In: *Nature materials* 6.7 (2007), pp. 528–532. DOI: 10.1038/nmat1924.
- [25] Hideto Yoshida, Koji Matsuura, Yasufumi Kuwauchi, Hideo Kohno, Satoshi Shimada, Masatake Haruta, and Seiji Takeda. "Temperature-dependent change in shape of platinum nanoparticles supported on CeO<sub>2</sub> during catalytic reactions." In: *Applied Physics Express* 4 (2011), p. 065001. DOI: 10.1143/APEX.4.065001.
- [26] Bjerne S. Clausen, Henrik Topsøe, and Ronald Frahm. "Application of Combined X-Ray Diffraction and Absorption Techniques for in Situ Catalyst Characterization." In: 1998, pp. 315–344. DOI: 10.1016/S0360-0564(08)60630-6.
- [27] Richard W. Joyner, M.Wyn Roberts, and Kenneth Yates. "A "high-pressure" electron spectrometer for surface studies." In: *Surface Science* 87.2 (1979), pp. 501–509. DOI: 10.1016/0039-6028(79)90544-2.
- [28] D. Frank Ogletree, Hendrik Bluhm, Gennadi Lebedev, Charles S. Fadley, Zahid Hussain, and Miquel Salmeron. "A differentially pumped electrostatic lens system for photoemission studies in the millibar range." In: *Review of Scientific Instruments* 73.11 (2002), p. 3872. DOI: 10.1063/1.1512336.
- [29] E. D. Boyes and P. L. Gai. "Environmental high resolution electron microscopy and applications to chemical science." In: *Ultramicroscopy* 67.1-4 (1997), pp. 219–232. DOI: 10.1016/S0304-3991(96)00099-X.
- [30] Stig Helveg. "An industrial perspective of the impact of Hal-dor Topsøe on (in situ) electron microscopy in catalysis." In: *Journal of Catalysis* 328 (2015), pp. 102–110. DOI: 10.1016/j.jcat.2014.12.017.
- [31] Bert M. Weckhuysen. "Determining the active site in a catalytic process: Operando spectroscopy is more than a buzzword." In: *Physical Chemistry Chemical Physics* 5.20 (2003), p. 4351. DOI: 10.1039/b309650p.

- [32] Miguel A. Bañares. "Operando methodology: Combination of in situ spectroscopy and simultaneous activity measurements under catalytic reaction conditions." In: *Catalysis Today* 100.1-2 (2005), pp. 71–77. DOI: 10.1016/j.cattod.2004.12.017.
- [33] S B Vendelbo et al. "Visualization of oscillatory behaviour of Pt nanoparticles catalysing CO oxidation." In: *Nature materials* 13.9 (2014), pp. 884–890. DOI: 10.1038/nmat4033.
- [34] Iva Ridjan, Brian Vad Mathiesen, David Connolly, and Neven Duić. "The feasibility of synthetic fuels in renewable energy systems." In: *Energy* 57 (2013), pp. 76–84. DOI: 10.1016/j.energy.2013.01.046.
- [35] George a Olah. "Beyond oil and gas: the methanol economy." In: *Angewandte Chemie (International ed. in English)* 44.18 (2005), pp. 2636–9. DOI: 10.1002/anie.200462121.
- [36] Iva Ridjan, Brian Vad Mathiesen, and David Connolly. "Synthetic fuel production costs by means of solid oxide electrolysis cells." In: *Energy* 76 (2014), pp. 104–113. DOI: 10.1016/j.energy.2014.04.002.
- [37] David B Williams and C Barry Carter. *The Transmission electron microscope*. 2009. DOI: 10.1007/978-0-387-76501-3{\\_}1.
- [38] C Kisielowski, E Principe, B Freitag, and D Hubert. "Benefits of microscopy with super resolution." In: *Physica B-Condensed Matter* 308 (2001), pp. 1090–1096. DOI: 10.1016/S0921-4526(01)00896-1.
- [39] C Kisielowski et al. "Detection of single atoms and buried defects in three dimensions by aberration-corrected electron microscope with 0.5-Å information limit." In: *Microscopy and microanalysis* 14.5 (2008), pp. 469–477. DOI: 10.1017/S1431927608080902.
- [40] Abhaya K. Datye. "Electron microscopy of catalysts: Recent achievements and future prospects." In: *Journal of Catalysis* 216 (2003), pp. 144–154. DOI: 10.1016/S0021-9517(02)00113-6.
- [41] T W Hansen, J B Wagner, P L Hansen, S Dahl, H Topsøe, and C J Jacobsen. "Atomic-resolution in situ transmission electron microscopy of a promoter of a heterogeneous catalyst." In: *Science (New York, N.Y.)* 294.5546 (2001), pp. 1508–1510. DOI: 10.1126/science.1064399.
- [42] Stig Helveg et al. "Atomic-scale imaging of carbon nanofibre growth." In: *Nature* 427.January (2004), pp. 426–9. DOI: 10.1038/nature02278.
- [43] R Sharma. "An environmental transmission electron microscope for in situ synthesis and characterization of nanomaterials." In: *Journal of Materials Research* 20.7 (2005), pp. 1695–1707. DOI: 10.1557/JMR.2005.0241.

- [44] P.L. Hansen, S. Helveg, and A.K. Datye. "Atomic-Scale Imaging of Supported Metal Nanocluster Catalysts in the Working State." In: 2006, pp. 77–95. DOI: 10.1016/S0360-0564(06)50002-1.
- [45] J. F. Creemer, S. Helveg, G. H. Hoveling, S. Ullmann, A.M. Molenbroek, P. M. Sarro, and H. W. Zandbergen. "Atomic-scale electron microscopy at ambient pressure." In: *Ultramicroscopy* 108.9 (2008), pp. 993–8. DOI: 10.1016/j.ultramic.2008.04.014.
- [46] Tadahiro Yokosawa, Tuncay Alan, Gregory Pandraud, Bernard Dam, and Henny Zandbergen. "In-situ TEM on (de)hydrogenation of Pd at 0.5-4.5 bar hydrogen pressure and 20-400°C." In: *Ultramicroscopy* 112.1 (2012), pp. 47–52. DOI: 10.1016/j.ultramic.2011.10.010.
- [47] Max Haider, Harald Rose, Stephan Uhlemann, Eugen Schwan, Bernd Kabius, and Knut Urban. "A spherical-aberration-corrected 200kV transmission electron microscope." In: *Ultramicroscopy* 75.1 (1998), pp. 53–60. DOI: 10.1016/S0304-3991(98)00048-5.
- [48] P C Tiemeijer, M Bischoff, B Freitag, and C Kisielowski. "Using a monochromator to improve the resolution in TEM to below 0.5Å. Part I: Creating highly coherent monochromated illumination." In: *Ultramicroscopy* 114 (2012), pp. 72–81. DOI: 10.1016/j.ultramic.2012.01.008.
- [49] Hideto Yoshida, Yasufumi Kuwauchi, Joerg R Jinschek, Keju Sun, Shingo Tanaka, Masanori Kohyama, Satoshi Shimada, Masatake Haruta, and Seiji Takeda. "Visualizing gas molecules interacting with supported nanoparticulate catalysts at reaction conditions." In: *Science (New York, N.Y.)* 335.6066 (2012), pp. 317–9. DOI: 10.1126/science.1213194.
- [50] J R Jinschek and S Helveg. "Image resolution and sensitivity in an environmental transmission electron microscope." In: *Micron (Oxford, England : 1993)* 43.11 (2012), pp. 1156–68. DOI: 10.1016/j.micron.2012.01.006.
- [51] Peter Mølgaard Mortensen, Thomas Willum Hansen, Jakob Birkedal Wagner, and Anker Degn Jensen. "Modeling of temperature profiles in an environmental transmission electron microscope using computational fluid dynamics." In: *Ultramicroscopy* 152 (2014), pp. 1–9. DOI: 10.1016/j.ultramic.2014.12.007.
- [52] Søren B Simonsen, Ib Chorkendorff, Søren Dahl, Magnus Skoglundh, Jens Sehested, and Stig Helveg. "Direct observations of oxygen-induced platinum nanoparticle ripening studied by in situ TEM." In: *Journal of the American Chemical Society* 132.23 (2010), pp. 7968–75. DOI: 10.1021/ja910094r.

- [53] Yasufumi Kuwauchi, Hideto Yoshida, Tomoki Akita, Masatake Haruta, and Seiji Takeda. "Intrinsic catalytic structure of gold nanoparticles supported on TiO<sub>2</sub>." In: *Angewandte Chemie (International ed. in English)* 51.31 (2012), pp. 7729–33. DOI: 10.1002/anie.201201283.
- [54] Roy van den Berg, Christian Fink Elkjaer, Cedric J. Gommès, Ib Chorkendorff, Jens Sehested, P E de Jongh, Krijn P de Jong, and Stig Helveg. "Revealing the formation of copper nanoparticles from a homogeneous precursor by electron microscopy." In: *In preparation* (2015).
- [55] R.F. Egerton, P. Li, and M. Malac. "Radiation damage in the TEM and SEM." In: *Micron* 35.6 (2004), pp. 399–409. DOI: 10.1016/j.micron.2004.02.003.
- [56] R. F. Egerton. "Control of radiation damage in the TEM." In: *Ultramicroscopy* 127 (2013), pp. 100–8. DOI: 10.1016/j.ultramic.2012.07.006.
- [57] Ludwig Reimer and Helmut Kohl. *Transmission Electron Microscopy*. 2008. ISBN: 9780387400938. DOI: 10.1007/978-0-387-34758-5.
- [58] Dirk Van Dyck, Ivan Lobato, Fu-Rong Chen, and Christian Kisielowski. "Do you believe that atoms stay in place when you observe them in HREM?" In: *Micron* 68 (2015), pp. 158–163. DOI: 10.1016/j.micron.2014.09.003.
- [59] Christian Kisielowski. "Observing Atoms at Work by Controlling Beam-Sample Interactions." In: *Advanced Materials* 27.38 (2015), pp. 5838–5844. DOI: 10.1002/adma.201500082.
- [60] Christian Kisielowski, Lin-Wang Wang, Petra Specht, Hector a. Calderon, Bastian Barton, Bin Jiang, Joo H. Kang, and Robert Cieslinski. "Real-time sub-Ångstrom imaging of reversible and irreversible conformations in rhodium catalysts and graphene." In: *Physical Review B* 88.2 (2013), p. 024305. DOI: 10.1103/PhysRevB.88.024305.
- [61] F.-R. Chen, C. Kisielowski, and D. Van Dyck. "3D reconstruction of nanocrystalline particles from a single projection." In: *Micron* 68 (2015), pp. 59–65. DOI: 10.1016/j.micron.2014.08.009.
- [62] H.-G. Liao, D. Zhrebetsky, H. Xin, C. Czarnik, P. Ercius, H. Elmlund, M. Pan, L.-W. Wang, and H. Zheng. "Facet development during platinum nanocube growth." In: *Science* 345.6199 (2014), pp. 916–919. DOI: 10.1126/science.1253149.

- [63] Christian Holse, Christian F. Elkjær, Anders Nierhoff, Jens Sehested, Ib Chorkendorff, Stig Helveg, and Jane H. Nielsen. "Dynamic Behavior of CuZn Nanoparticles under Oxidizing and Reducing Conditions." In: *The Journal of Physical Chemistry C* 119.5 (2015), pp. 2804–2812. DOI: 10.1021/jp510015v.
- [64] Søren Bredmose Simonsen, Ib Chorkendorff, Søren Dahl, Magnus Skoglundh, Jens Sehested, and Stig Helveg. "Ostwald ripening in a Pt/SiO<sub>2</sub> model catalyst studied by in situ TEM." In: *Journal of Catalysis* 281.1 (2011), pp. 147–155. DOI: 10.1016/j.jcat.2011.04.011.
- [65] Andrew T. DeLaRiva, Thomas W. Hansen, Sivakumar R. Challa, and Abhaya K. Datye. "In situ Transmission Electron Microscopy of catalyst sintering." In: *Journal of Catalysis* 308 (2013), pp. 291–305. DOI: 10.1016/j.jcat.2013.08.018.
- [66] R. J. Liu, P. a. Crozier, C. M. Smith, D. a. Hucul, J. Blackson, and G. Salaita. "Metal sintering mechanisms and regeneration of palladium/alumina hydrogenation catalysts." In: *Applied Catalysis A: General* 282.1-2 (2005), pp. 111–121. DOI: 10.1016/j.apcata.2004.12.015.
- [67] Tatiana Kozlova, Maria Rudneva, and Henny W Zandbergen. "In situ TEM and STEM studies of reversible electromigration in thin palladium–platinum bridges." In: *Nanotechnology* 24.50 (2013), p. 505708. DOI: 10.1088/0957-4484/24/50/505708.
- [68] Fiz. *Inorganic crystal structure database ICSD*. URL: <http://icsd.fiz-karlsruhe.de>.
- [69] John C. Russ. *The Image Processing Handbook, Sixth Edition*. CRC Press, 2011, p. 885. ISBN: 1439840636.
- [70] John Bøgild Hansen and Poul Erik Højlund Nielsen. *Handbook of Heterogeneous Catalysis*. Ed. by Gerhard Ertl, Helmut Knözinger, Ferdi Schüth, and Jens Weitkamp. Weinheim, Germany: Wiley-VCH Verlag GmbH & Co. KGaA, 2008, pp. 2920–2949. DOI: 10.1002/9783527610044.hetcat0148.
- [71] Malte Behrens. "Coprecipitation: An excellent tool for the synthesis of supported metal catalysts – From the understanding of the well known recipes to new materials." In: *Catalysis Today* 246 (2015), pp. 46–54. DOI: 10.1016/j.cattod.2014.07.050.
- [72] C. Balthes, S. Vukojevic, F. Schueth, and F. Schüth. "Correlations between synthesis, precursor, and catalyst structure and activity of a large set of CuO/ZnO/Al<sub>2</sub>O<sub>3</sub> catalysts for methanol synthesis." In: *Journal of Catalysis* 258.2 (2008), pp. 334–344. DOI: 10.1016/j.jcat.2008.07.004.

- [73] Joseph E. Mondloch, Ercan Bayram, and Richard G. Finke. "A review of the kinetics and mechanisms of formation of supported-nanoparticle heterogeneous catalysts." In: *Journal of Molecular Catalysis A: Chemical* 355 (2012), pp. 1–38. DOI: 10.1016/j.molcata.2011.11.011.
- [74] Irek Sharafutdinov, Christian Fink Elkjær, Hudson Wallace Pereira de Carvalho, Diego Gardini, Gian Luca Chiarello, Christian Danvad Damsgaard, Jakob Birkedal Wagner, Jan-Dierk Grunwaldt, Søren Dahl, and Ib Chorkendorff. "Intermetallic compounds of Ni and Ga as catalysts for the synthesis of methanol." In: *Journal of Catalysis* 320 (2014), pp. 77–88. DOI: 10.1016/j.jcat.2014.09.025.
- [75] Lionel Cervera Gontard, Dogan Ozkaya, and Rafal E. Dunin-Borkowski. "A simple algorithm for measuring particle size distributions on an uneven background from TEM images." In: *Ultramicroscopy* 111.2 (2011), pp. 101–6. DOI: 10.1016/j.ultramic.2010.10.011.
- [76] David Freedman and Persi Diaconis. "On the histogram as a density estimator: L<sub>2</sub> theory." In: *Zeitschrift für Wahrscheinlichkeitstheorie und Verwandte Gebiete* 57.4 (1981), pp. 453–476. DOI: 10.1007/BF01025868.
- [77] SB Simonsen. "Sintering of oxide-supported Pt and Pd nanoparticles in air studied by in situ TEM." In: *Technical University of Denmark* June (2011). URL: [http://orbit.dtu.dk/en/publications/sintering-of-oxidesupported-pt-and-pd-nanoparticles-in-air-studied-by-in-situ-tem\(bf141a9b-b94a-46cf-9e5a-7ddcdd0f27fe\).html](http://orbit.dtu.dk/en/publications/sintering-of-oxidesupported-pt-and-pd-nanoparticles-in-air-studied-by-in-situ-tem(bf141a9b-b94a-46cf-9e5a-7ddcdd0f27fe).html).
- [78] Thierry Toupance, Maggy Kermarec, Jean-François Lambert, and Catherine Louis. "Conditions of Formation of Copper Phyllosilicates in Silica-Supported Copper Catalysts Prepared by Selective Adsorption." In: *The Journal of Physical Chemistry B* 106.9 (2002), pp. 2277–2286. DOI: 10.1021/jp013153x.
- [79] C.J.G. Van Der Grift, P.A. Elberse, A. Mulder, and J.W. Geus. "Preparation of silica-supported copper catalysts by means of deposition-precipitation." In: *Applied Catalysis* 59.1 (1990), pp. 275–289. DOI: 10.1016/S0166-9834(00)82204-6.
- [80] V. LaMer and R. Dinegar. "Theory, production and mechanism of formation of monodispersed hydrosols." In: *Journal of the American Chemical Society* 72.8 (1950), pp. 4847–4854. DOI: 10.1021/ja01167a001.
- [81] Murielle a. Watzky and Richard G. Finke. "Transition metal nanocluster formation kinetic and mechanistic studies. A new mechanism when hydrogen is the reductant: Slow, continuous nucleation and fast autocatalytic surface growth." In: *Journal*

- of the American Chemical Society 119.43 (1997), pp. 10382–10400. DOI: 10.1021/ja9705102.
- [82] John D. Aiken and Richard G. Finke. “Nanocluster Formation Synthetic, Kinetic, and Mechanistic Studies. † The Detection of, and Then Methods To Avoid, Hydrogen Mass-Transfer Limitations in the Synthesis of Polyoxoanion- and Tetrabutylammonium-Stabilized, Near-Monodisperse  $40 \pm 6 \text{ \AA}$  Rh(o) Nano.” In: *Journal of the American Chemical Society* 120.37 (1998), pp. 9545–9554. DOI: 10.1021/ja9719485. URL: <http://pubs.acs.org/doi/abs/10.1021/ja9719485>.
- [83] P. H. Heitjans and J. Kärger. *Diffusion in Condensed Matter*. Springer-Verlag, 2005.
- [84] K C Waugh. “Methanol Synthesis.” In: *Catalysis Letters* 142.10 (2012), pp. 1153–1166. DOI: 10.1007/s10562-012-0905-2.
- [85] Malte Behrens. “Meso- and nano-structuring of industrial Cu/ZnO/(Al<sub>2</sub>O<sub>3</sub>) catalysts.” In: *Journal of Catalysis* 267.1 (2009), pp. 24–29. DOI: 10.1016/j.jcat.2009.07.009.
- [86] M Kurtz, H Wilmer, T Genger, O Hinrichsen, and M Muhler. “Deactivation of supported copper catalysts for methanol synthesis.” In: *Catalysis Letters* 86.1-3 (2003), pp. 77–80. DOI: 10.1023/A:1022663125977.
- [87] G. C. Chinen, K. C. Waugh, and D. A. Whan. “The activity and state of the copper surface in methanol synthesis catalysts.” In: *Applied Catalysis* 25.1-2 (1986), p. 101. DOI: 10.1016/S0166-9834(00)81226-9.
- [88] G. Chinen. “The measurement of copper surface areas by reactive frontal chromatography.” In: *Journal of Catalysis* 103.1 (1987), pp. 79–86. DOI: 10.1016/0021-9517(87)90094-7.
- [89] O. Hinrichsen, T. Genger, and M. Muhler. “Chemisorption of N<sub>2</sub>O and H<sub>2</sub> for the Surface Determination of Copper Catalysts.” In: *Chemical Engineering & Technology* 23.11 (2000), pp. 956–959. DOI: 10.1002/1521-4125(200011)23:11<956::AID-CEAT956>3.0.CO;2-L.
- [90] Sebastian Kuld, Christian Conradsen, Poul Georg Moses, Ib Chorkendorff, and Jens Sehested. “Quantification of Zinc Atoms in a Surface Alloy on Copper in an Industrial-Type Methanol Synthesis Catalyst.” In: *Angewandte Chemie (International ed. in English)* 53.23 (2014), pp. 5941–5. DOI: 10.1002/anie.201311073.
- [91] R Herman. “Catalytic synthesis of methanol from CO/H<sub>2</sub> I. Phase composition, electronic properties, and activities of the Cu/ZnO/M<sub>2</sub>O<sub>3</sub> catalysts.” In: *Journal of Catalysis* 56.3 (1979), pp. 407–429. DOI: 10.1016/0021-9517(79)90132-5.

- [92] Bjerne S. Clausen, Jakob Schiøtz, Lars Grabæk, Charlotte V. Ovesen, Karsten W. Jacobsen, Jens K. Nørskov, and Henrik Topsøe. "Wetting/ non-wetting phenomena during catalysis: Evidence from in situ on-line EXAFS studies of Cu-based catalysts." In: *Topics in Catalysis* 1.3-4 (1994), pp. 367–376. DOI: 10.1007/BF01492289.
- [93] J D Grunwaldt, A M Molenbroek, N Y Topsoe, H Topsoe, and B S Clausen. "In situ investigations of structural changes in Cu/ZnO catalysts." In: *Journal of Catalysis* 194.2 (2000), pp. 452–460. DOI: DOI10.1006/jcat.2000.2930.
- [94] CV Ovesen, BS Clausen, J Schiøtz, P. Stoltze, H. Topsøe, and J.K. Nørskov. "Kinetic Implications of Dynamical Changes in Catalyst Morphology during Methanol Synthesis over Cu/ZnO Catalysts." In: *Journal of Catalysis* 168.2 (1997), pp. 133–142. DOI: 10.1006/jcat.1997.1629.
- [95] T Fujitani and J Nakamura. "The effect of ZnO in methanol synthesis catalysts on Cu dispersion and the specific activity." In: *Catalysis Letters* 56.2-3 (1998), pp. 119–124. DOI: 10.1023/A:1019000927366.
- [96] Thomas Lunkenbein, Julia Schumann, Malte Behrens, Robert Schlögl, and Marc G Willinger. "Formation of a ZnO overlayer in industrial Cu/ZnO/Al<sub>2</sub>O<sub>3</sub> catalysts induced by strong metal-support interactions." In: *Angewandte Chemie (International ed. in English)* 54.15 (2015), pp. 4544–8. DOI: 10.1002/anie.201411581.
- [97] Jesper Nerlov and Ib Chorkendorff. "Methanol Synthesis from CO<sub>2</sub>, CO, and H<sub>2</sub> over Cu(100) and Ni/Cu(100)." In: *Journal of Catalysis* 181.2 (1999), pp. 271–279. DOI: 10.1006/jcat.1998.2301.
- [98] J T Sun, I S Metcalfe, and M Sahibzada. "Deactivation of Cu/ZnO/Al<sub>2</sub>O<sub>3</sub> methanol synthesis catalyst by sintering." In: *Industrial & Engineering Chemistry Research* 38.10 (1999), pp. 3868–3872. DOI: 10.1021/ie990078s.
- [99] Hellmut Haberland and Martin Karrais. "Thin films from energetic cluster impact: A feasibility study." In: *Journal of Vacuum Science & Technology A: Vacuum, Surfaces, and Films* 10.5 (1992), p. 3266. DOI: 10.1116/1.577853.
- [100] R. M. Nielsen, S. Murphy, C. Strebler, M. Johansson, Ib Chorkendorff, and J. H. Nielsen. "The morphology of mass selected ruthenium nanoparticles from a magnetron-sputter gas-aggregation source." In: *Journal of Nanoparticle Research* 12.4 (2009), pp. 1249–1262. DOI: 10.1007/s11051-009-9830-8.

- [101] Patricia Hernandez-Fernandez et al. "Mass-selected nanoparticles of Pt<sub>x</sub>Y as model catalysts for oxygen electroreduction." In: *Nature Chemistry* 6:July (2014), pp. 1–7. DOI: 10.1038/nchem.2001.
- [102] Christian Holse. "Studies of Catalytic Model Systems: Single Crystals and Nanoparticles." PhD thesis. 2015. URL: [http://orbit.dtu.dk/en/publications/studies-of-catalytic-model-systems\(282e9594-0247-4a0f-9714-a9b6b41b8c45\).html](http://orbit.dtu.dk/en/publications/studies-of-catalytic-model-systems(282e9594-0247-4a0f-9714-a9b6b41b8c45).html).
- [103] M.S. Spencer. "α-Brass formation in copper/zinc oxide catalysts I. Bulk equilibrium concentrations of zinc under methanol synthesis and water-gas shift reaction conditions." In: *Surface Science* 192.2-3 (1987), pp. 323–328. DOI: 10.1016/S0039-6028(87)81127-5.
- [104] Dahlang Tahir and Sven Tougaard. "Electronic and optical properties of Cu, CuO and Cu<sub>2</sub>O studied by electron spectroscopy." In: *Journal of physics. Condensed matter : an Institute of Physics journal* 24.17 (2012), p. 175002. DOI: 10.1088/0953-8984/24/17/175002.
- [105] R. Nakamura, D. Tokozakura, H. Nakajima, J.-G. Lee, and H. Mori. "Hollow oxide formation by oxidation of Al and Cu nanoparticles." In: *Journal of Applied Physics* 101.7 (2007), p. 074303. DOI: 10.1063/1.2711383.
- [106] S Helveg, Jv Lauritsen, E. Lægsgaard, I Stensgaard, J. Nørskov, Bs Clausen, H. Topsøe, and F Besenbacher. "Atomic-Scale Structure of Single-Layer MoS<sub>2</sub> Nanoclusters." In: *Physical Review Letters* 84.5 (2000), pp. 951–954. DOI: 10.1103/PhysRevLett.84.951.
- [107] H. A. Michelsen and D. J. Auerbach. "A critical examination of data on the dissociative adsorption and associative desorption of hydrogen at copper surfaces." In: *The Journal of Chemical Physics* 94.11 (1991), p. 7502. DOI: 10.1063/1.460182.
- [108] Peter C.K. Vesborg, Ib Chorkendorff, Ida Knudsen, Olivier Balmes, Jesper Nerlov, Alfons M. Molenbroek, Bjerne S. Clausen, and Stig Helveg. "Transient behavior of Cu/ZnO-based methanol synthesis catalysts." In: *Journal of Catalysis* 262.1 (2009), pp. 65–72. DOI: 10.1016/j.jcat.2008.11.028.
- [109] M.S. Spencer. "The role of zinc oxide in Cu/ZnO catalysts for methanol synthesis and the water-gas shift reaction." en. In: *Topics in Catalysis* 8.3-4 (1999), pp. 259–266. DOI: 10.1023/A:1019181715731.

- [110] M.S. Spencer. "α-BRASS FORMATION IN COPPER/ZINC OXIDE CATALYSTS II. Diffusion of zinc in copper and α-brass under reaction conditions." In: *Surface Science* 192.2-3 (1987), pp. 329–335. DOI: 10.1016/S0039-6028(87)81128-7.
- [111] Toke R Henriksen, Jakob L Olsen, Peter Vesborg, Ib Chorkendorff, and Ole Hansen. "Highly sensitive silicon microreactor for catalyst testing." In: *Review of Scientific Instruments* 80.12 (2009), p. 124101. DOI: 10.1063/1.3270191.
- [112] Robert Jensen, Thomas Andersen, Anders Nierhoff, Thomas Pedersen, Ole Hansen, Søren Dahl, and Ib Chorkendorff. "Self-sustained carbon monoxide oxidation oscillations on size-selected platinum nanoparticles at atmospheric pressure." In: *Physical chemistry chemical physics : PCCP* 15.8 (2013), pp. 2698–702. DOI: 10.1039/c2cp43684a.
- [113] Anders Nierhoff. "Surface Modification of Catalytic Materials." PhD thesis. 2015.
- [114] Gonzalo Prieto, Mozaffar Shakeri, Krijn P. de Jong, and Petra E. de Jongh. "Quantitative Relationship between Support Porosity and the Stability of Pore-Confined Metal Nanoparticles Studied on CuZnO/SiO<sub>2</sub> Methanol Synthesis Catalysts." In: *ACS Nano* 8.3 (2014), pp. 2522–2531. DOI: 10.1021/nn406119j.
- [115] H Wilmer and O Hinrichsen. "Dynamical changes in Cu/ZnO/Al<sub>2</sub>O<sub>3</sub> catalysts." In: *Catalysis Letters* 82.1/2 (2002), pp. 117–122. DOI: 10.1023/A:1020560628950.
- [116] John S. Campbell. "Influences of Catalyst Formulation and Poisoning on the Activity and Die-Off of Low Temperature Shift Catalysts." In: *Industrial & Engineering Chemistry Process Design and Development* 9.4 (1970), pp. 588–595. DOI: 10.1021/i260036a016.
- [117] P W Young and Clark C B. "Why Shift Catalysts De-activate." In: *Chemical Engineering Progress* 69.5 (1973), pp. 69–74.
- [118] J Ladebeck. "Improve methanol synthesis." In: *Hydrocarbon Processing* 72.3 (1993), pp. 89–91.
- [119] M V Twigg and M S Spencer. "Deactivation of supported copper metal catalysts for hydrogenation reactions." In: *Applied Catalysis A-General* 212.1-2 (2001), pp. 161–174. DOI: 10.1016/S0926-860X(00)00854-1.
- [120] Michael S. Spencer and Martyn V. Twigg. "Metal Catalyst Design and Preparation in Control of Deactivation." In: *Annual Review of Materials Research* 35.1 (2005), pp. 427–464. DOI: 10.1146/annurev.matsci.35.100303.120733.

- [121] Yasuyuki Matsumura and Hideomi Ishibe. "Effect of zirconium oxide added to Cu/ZnO catalyst for steam reforming of methanol to hydrogen." In: *Journal of Molecular Catalysis A: Chemical* 345.1-2 (2011), pp. 44–53. DOI: 10.1016/j.molcata.2011.05.017.
- [122] D G Loffler, S D Mcdermott, and C N Renn. "Activity and durability of water-gas shift catalysts used for the steam reforming of methanol." In: 114 (2003), pp. 1–6.
- [123] Harold H. Kung. "Deactivation of methanol synthesis catalysts - a review." In: *Catalysis Today* 11.4 (1992), pp. 443–453. DOI: 10.1016/0920-5861(92)80037-N.
- [124] G Liu, D Willcox, M Garland, and HH Kung. "The role of CO<sub>2</sub> in methanol synthesis on Cu<sub>2</sub>Sb/Zn oxide: An isotope labeling study." In: *Journal of Catalysis* 96.1 (1985), pp. 251–260. DOI: 10.1016/0021-9517(85)90378-1.
- [125] K Klier, V Chatikavanij, R G Herman, and G W Simmons. "Catalytic Synthesis of Methanol from CO / H<sub>2</sub> IV. The Effect of Carbon Dioxide." In: *Journal of Catalysis* 360 (1982), pp. 343–360.
- [126] C. Kuechen and U. Hoffmann. "Investigation of simultaneous reaction of carbon monoxide and carbon dioxide with hydrogen on a commercial copper/zinc oxide catalyst." In: *Chemical Engineering Science* 48.22 (1993), pp. 3767–3776. DOI: 10.1016/0009-2509(93)80219-G.
- [127] J G Wu, M Saito, M Takeuchi, and T Watanabe. "The stability of Cu/ZnO-based catalysts in methanol synthesis from a CO<sub>2</sub>-rich feed and from a CO-rich feed." In: *Applied Catalysis A-General* 218.1-2 (2001), pp. 235–240. DOI: 10.1016/S0926-860X(01)00650-0.
- [128] G. C. Chinchin, P. J. Denny, D. G. Parker, M. S. Spencer, and D. A. Whan. "Mechanism of methanol synthesis from CO<sub>2</sub>/CO/H<sub>2</sub> mixtures over copper/zinc oxide/alumina catalysts: use of <sup>14</sup>C-labelled reactants." In: *Applied Catalysis* 30 (1987), pp. 333–338. DOI: 10.1016/S0166-9834(00)84123-8.
- [129] M Sahibzada, I S Metcalfe, and D Chadwick. "Methanol synthesis from CO/CO<sub>2</sub>/H<sub>2</sub> over Cu/ZnO/Al<sub>2</sub>O<sub>3</sub> at differential and finite conversions." In: *Journal of Catalysis* 174.2 (1998), pp. 111–118. DOI: 10.1006/jcat.1998.1964.
- [130] Dominik Bjørn Bjorn Rasmussen, Ton V.W. W Janssens, Burcin Temel, Thomas Bligaard, Berit Hinnemann, Stig Helveg, and Jens Sehested. "The energies of formation and mobilities of Cu surface species on Cu and ZnO in methanol and water gas shift atmospheres studied by DFT." In: *Journal of Catalysis* 293 (2012), pp. 205–214. DOI: 10.1016/j.jcat.2012.07.001.

- [131] Sieghard E Wanke and Peter C Flynn. "The Sintering of Supported Metal Catalysts." In: *Catalysis Reviews* 12.1 (1975), pp. 93–135. DOI: 10.1080/01614947508067523.
- [132] P. Wynblatt and N.a. Gjostein. "Supported metal crystallites." In: *Progress in Solid State Chemistry* 9 (1975), pp. 21–58. DOI: 10.1016/0079-6786(75)90013-8.
- [133] Thomas W. Hansen, Andrew T. Delariva, Sivakumar R. Challa, and Abhaya K. Datye. "Sintering of catalytic nanoparticles: Particle migration or ostwald ripening?" In: *Accounts of Chemical Research* 46.8 (2013), pp. 1720–1730. DOI: 10.1021/ar3002427.
- [134] Robert Finsky. "On the critical radius in Ostwald ripening." In: *Langmuir* 20.7 (2004), pp. 2975–2976. DOI: 10.1021/la035966d.
- [135] Levi R Houk, Sivakumar R Challa, Benjamin Grayson, Paul Fanson, and Abhaya K Datye. "The definition of "critical radius" for a collection of nanoparticles undergoing Ostwald ripening." In: *Langmuir : the ACS journal of surfaces and colloids* 25.19 (2009), pp. 11225–7. DOI: 10.1021/la902263s.
- [136] Gonzalo Prieto, Jovana Zečević, Heiner Friedrich, Krijn P. de Jong, and Petra E. de Jongh. "Towards stable catalysts by controlling collective properties of supported metal nanoparticles." In: *Nature Materials* 12.1 (2012), pp. 34–39. DOI: 10.1038/nmat3471.
- [137] I.M. Lifshitz and V.V. Slyozov. "The kinetics of precipitation from supersaturated solid solutions." In: *Journal of Physics and Chemistry of Solids* 19.1-2 (1961), pp. 35–50. DOI: 10.1016/0022-3697(61)90054-3. arXiv: arXiv:1011.1669v3.
- [138] Abhaya K. Datye, Qing Xu, Karl C. Kharas, and Jon M. McCarty. "Particle size distributions in heterogeneous catalysts: What do they tell us about the sintering mechanism?" In: *Catalysis Today* 111.1-2 (2006), pp. 59–67. DOI: 10.1016/j.cattod.2005.10.013.
- [139] J Sehested, J A P Gelten, I N Remediakis, H Bengaard, and J K Norskov. "Sintering of nickel steam-reforming catalysts: effects of temperature and steam and hydrogen pressures." In: *Journal of Catalysis* 223.2 (2004), pp. 432–443. DOI: 10.1016/j.jcat.2004.01.026.
- [140] C. D. Damsgaard, L. D. L. Duchstein, I. Sharafutdinov, M. G. Nielsen, I. Chorkendorff, and J. B. Wagner. "In situ ETEM synthesis of NiGa alloy nanoparticles from nitrate salt solution." In: *Microscopy* 63.5 (2014), pp. 397–401. DOI: 10.1093/jmicro/dfu025.
- [141] L.T. Zhuravlev. "The surface chemistry of amorphous silica. Zhuravlev model." In: *Colloids and Surfaces A: Physicochemical and Engineering Aspects* 173.1-3 (2000), pp. 1–38. DOI: 10.1016/S0927-7757(00)00556-2.

- [142] Roy van den Berg, Tanja E. Parmentier, Christian F. Elkjær, Cedric J. Gommès, Jens Sehested, Stig Helveg, Petra E. de Jongh, and Krijn P. de Jong. "Support Functionalization to Retard Ostwald Ripening in Copper Methanol Synthesis Catalysts." In: *ACS Catalysis* 5.7 (2015), pp. 4439–4448. DOI: 10.1021/acscatal.5b00833.
- [143] Christian D. Damsgaard, Henny Zandbergen, Thomas W. Hansen, Ib Chorkendorff, and Jakob B. Wagner. "Controlled Environment Specimen Transfer." In: *Microscopy and Microanalysis* 20.04 (2014), pp. 1038–1045. DOI: 10.1017/S1431927614000853.
- [144] Lawrence F. Allard, Wilbur C. Bigelow, Miguel Jose-Yacaman, David P. Nackashi, John Damiano, and Stephen E. Mick. "A new MEMS-based system for ultra-high-resolution imaging at elevated temperatures." In: *Microscopy Research and Technique* 72.3 (2009), pp. 208–215. DOI: 10.1002/jemt.20673.
- [145] Lawrence F. Allard, Steven H. Overbury, Wilbur C. Bigelow, Michael B. Katz, David P. Nackashi, and John Damiano. "Novel MEMS-Based Gas-Cell/Heating Specimen Holder Provides Advanced Imaging Capabilities for In Situ Reaction Studies." In: *Microscopy and Microanalysis* 18.04 (2012), pp. 656–666. DOI: 10.1017/S1431927612001249. URL: [http://www.journals.cambridge.org/abstract{\\\_}S1431927612001249](http://www.journals.cambridge.org/abstract{\_}S1431927612001249).
- [146] Huolin L. Xin, Kaiyang Niu, Daan Hein Alsem, and Haimei Zheng. "In Situ TEM Study of Catalytic Nanoparticle Reactions in Atmospheric Pressure Gas Environment." In: *Microscopy and Microanalysis* 19.06 (2013), pp. 1558–1568. DOI: 10.1017/S1431927613013433.
- [147] Hans-Joachim Freund, Gerard Meijer, Matthias Scheffler, Robert Schlögl, and Martin Wolf. "CO oxidation as a prototypical reaction for heterogeneous processes." In: *Angewandte Chemie (International ed. in English)* 50.43 (2011), pp. 10064–94. DOI: 10.1002/anie.201101378.
- [148] T. Jiang, D. J. Mowbray, S. Dobrin, H. Falsig, B. Hvolbæk, T. Bligaard, and J. K. Nørskov. "Trends in CO oxidation rates for metal nanoparticles and close-packed, stepped, and kinked surfaces." In: *Journal of Physical Chemistry C* 113.24 (2009), pp. 10548–10553. DOI: 10.1021/jp811185g.
- [149] F. Gao, Y. Wang, Y. Cai, and D. W. Goodman. "CO Oxidation on Pt-Group Metals from Ultrahigh Vacuum to Near Atmospheric Pressures. 2. Palladium and Platinum." In: *The Journal of Physical Chemistry C* 113.1 (2009), pp. 174–181. DOI: 10.1021/jp8077985.

- [150] Feng Gao, Sean McClure, Mingshu Chen, and D. Wayne Goodman. "Comment on "Catalytic Activity of the Rh Surface Oxide: CO Oxidation over Rh(111) under Realistic Conditions"." In: *The Journal of Physical Chemistry C* 114.50 (2010), pp. 22369–22371. DOI: 10.1021/jp106796e.
- [151] J. Gustafson, Westerström R., O. Balmes, A. Resta, R. van Rijn, X. Torrelles, C. T. Herbschleb, J. W M Frenken, and E. Lundgren. "Reply to "Comment on 'Catalytic Activity of the Rh Surface Oxide: CO Oxidation over Rh(111) under Realistic Conditions'"." In: *The Journal of Physical Chemistry C* 114.50 (2010), pp. 22372–22373. DOI: 10.1021/jp108816j.
- [152] J. Gustafson, R. Westerström, O. Balmes, A. Resta, R. van Rijn, X. Torrelles, C. T. Herbschleb, J. W M Frenken, and E. Lundgren. "Catalytic Activity of the Rh Surface Oxide: CO Oxidation over Rh(111) under Realistic Conditions." In: *The Journal of Physical Chemistry C* 114.10 (2010), pp. 4580–4583. DOI: 10.1021/jp910988b.
- [153] Gerhard Ertl. "Reactions at Surfaces: From Atoms to Complexity (Nobel Lecture)." In: *Angewandte Chemie International Edition* 47.19 (2008), pp. 3524–3535. DOI: 10.1002/anie.200800480.
- [154] Ronald. Imbihl and Gerhard. Ertl. "Oscillatory Kinetics in Heterogeneous Catalysis." In: *Chemical Reviews* 95.3 (1995), pp. 697–733. DOI: 10.1021/cr00035a012.
- [155] B Hendriksen, S Bobaru, and J Frenken. "Bistability and oscillations in CO oxidation studied with scanning tunnelling microscopy inside a reactor." In: *Catalysis Today* 105.2 (2005), pp. 234–243. DOI: 10.1016/j.cattod.2005.02.041.
- [156] Bas L M Hendriksen et al. "The role of steps in surface catalysis and reaction oscillations." In: *Nature chemistry* 2.9 (2010), pp. 730–4. DOI: 10.1038/nchem.728.
- [157] Sebastian Matera and Karsten Reuter. "Transport limitations and bistability for in situ CO oxidation at RuO<sub>2</sub> (110): First-principles based multiscale modeling." In: 2.110 (2010), pp. 1–13. DOI: 10.1103/PhysRevB.82.085446.
- [158] M. A. Liauw, P. J. Plath, and N. I. Jaeger. "Complex oscillations and global coupling during the catalytic oxidation of CO." In: *The Journal of Chemical Physics* 104.16 (1996), p. 6375. DOI: 10.1063/1.471299.
- [159] P. A. Carlsson, V. P. Zhdanov, and Magnus Skoglundh. "Self-sustained kinetic oscillations in CO oxidation over silica-supported Pt." In: ... *Chemistry Chemical Physics* 8.23 (2006), pp. 2703–2706. DOI: 10.1039/b602958b.

- [160] Santhosh Chenna and Peter A. Crozier. "Operando Transmission Electron Microscopy: A Technique for Detection of Catalysis Using Electron Energy-Loss Spectroscopy in the Transmission Electron Microscope." In: *ACS Catalysis* 2.11 (2012), pp. 2395–2402. DOI: 10.1021/cs3004853.
- [161] Nimic. *NIMIC consortium*. URL: <http://nimic.physics.leidenuniv.nl/>.
- [162] J. F. Creemer, F. Santagata, B. Morana, L. Mele, T. Alan, E. Iervolino, G. Pandraud, and P. M. Sarro. "An all-in-one nanoreactor for high-resolution microscopy on nanomaterials at high pressures." In: *2011 IEEE 24th International Conference on Micro Electro Mechanical Systems* (2011), pp. 1103–1106. DOI: 10.1109/ MEMSYS.2011.5734622.
- [163] S B Vendelbo, P J Kooyman, J F Creemer, B Morana, L Mele, P Dona, B J Nelissen, and S Helveg. "Method for local temperature measurement in a nanoreactor for in situ high-resolution electron microscopy." In: *Ultramicroscopy* 133C (2013), pp. 72–79. ISSN: 1879-2723. DOI: 10.1016/j.ultramic.2013.04.004.
- [164] D. Briand, A. Krauss, B. Van Der Schoot, U. Weimar, N. Barsan, W. Göpel, and N. F. De Rooij. "Design and fabrication of high-temperature micro-hotplates for drop-coated gas sensors." In: *Sensors and Actuators, B: Chemical* 68.1 (2000), pp. 223–233. DOI: 10.1016/S0925-4005(00)00433-0.
- [165] D. N. McCarthy, C. E. Strelbel, T. P. Johansson, A. den Dunnen, A. Nierhoff, J. H. Nielsen, and Ib Chorkendorff. "Structural Modification of Platinum Model Systems under High Pressure CO Annealing." In: *The Journal of Physical Chemistry C* 116.29 (2012), pp. 15353–15360. DOI: 10.1021/jp302379x.
- [166] Diana Vogel, Christian Spiel, Yuri Suchorski, Adriana Trincherro, Robert Schlögl, Henrik Grönbeck, and Günther Rupprechter. "Local catalytic ignition during CO oxidation on low-index Pt and Pd surfaces: A combined PEEM, MS, and DFT study." In: *Angewandte Chemie - International Edition* 51.40 (2012), pp. 10041–10044. DOI: 10.1002/anie.201204031.
- [167] Hanne Falsig, Juan Shen, Tuhin Suvra Khan, Wei Guo, Glenn Jones, Søren Dahl, and Thomas Bligaard. "On the structure sensitivity of direct NO decomposition over low-index transition metal facets." In: *Topics in Catalysis* 57.1-4 (2014), pp. 80–88. DOI: 10.1007/s11244-013-0164-5.
- [168] P. Thostrup, E. Christoffersen, H. T. Lorensen, K. W. Jacobsen, F. Besenbacher, and J. K. Nørskov. "Adsorption-Induced Step Formation." In: *Physical Review Letters* 87.12 (2001), p. 126102. DOI: 10.1103/PhysRevLett.87.126102.

- [169] Feng Tao, Sefa Dag, Lin-Wang Wang, Zhi Liu, Derek R Butcher, Hendrik Bluhm, Miquel Salmeron, and Gabor a Somorjai. "Break-up of stepped platinum catalyst surfaces by high CO coverage." In: *Science (New York, N.Y.)* 327.5967 (2010), pp. 850–3. DOI: 10.1126/science.1182122.
- [170] N Otsu. "A Threshold Selection Method from Gray-Level Histograms." In: *IEEE Transactions on Systems, Man, and Cybernetics* 9.1 (1979), pp. 62–66. DOI: 10.1109/TSMC.1979.4310076.
- [171] J. N. Kapur, P. K. Sahoo, and A. K. C. Wong. *A New Method for Gray-Level Picture Thresholding Using the Entropy of the Histogram*. 1985. DOI: 10.1016/0734-189X(85)90125-2.

#### COLOPHON

This document was typeset using the typographical look-and-feel classicthesis developed by André Miede. The style was inspired by Robert Bringhurst's seminal book on typography "*The Elements of Typographic Style*". classicthesis is available for both L<sup>A</sup>T<sub>E</sub>X and L<sup>Y</sup>X:

<https://bitbucket.org/amiede/classicthesis/>

Happy users of classicthesis usually send a real postcard to the author, a collection of postcards received so far is featured here:

<http://postcards.miede.de/>



## PAPERS



## Visualization of oscillatory behaviour of Pt nanoparticles catalysing CO oxidation

Søren Vendelbo, Christian F. Elkjær, Hanne Falsig, Indra Puspitasari, P. Dona, Luigi Mele, Bart J. Nelissen, Richard van Rijn, Patricia J. Kooyman and Stig Helveg.

*Nature Materials* **13**, 884-890 (2014).

DOI:10.1038/nmat4033

Supplementary information and supplementary movies can be found on the journal homepage.

# Visualization of oscillatory behaviour of Pt nanoparticles catalysing CO oxidation

S. B. Vendelbo<sup>1</sup>, C. F. Elkjær<sup>2</sup>, H. Falsig<sup>2</sup>, I. Puspitasari<sup>1</sup>, P. Dona<sup>3</sup>, L. Mele<sup>3</sup>, B. Morana<sup>4</sup>, B. J. Nelissen<sup>5</sup>, R. van Rijn<sup>6</sup>, J. F. Cremer<sup>4</sup>, P. J. Kooyman<sup>1\*</sup> and S. Helveg<sup>2\*</sup>

**Many catalytic reactions under fixed conditions exhibit oscillatory behaviour. The oscillations are often attributed to dynamic changes in the catalyst surface. So far, however, such relationships were difficult to determine for catalysts consisting of supported nanoparticles. Here, we employ a nanoreactor to study the oscillatory CO oxidation catalysed by Pt nanoparticles using time-resolved high-resolution transmission electron microscopy, mass spectrometry and calorimetry. The observations reveal that periodic changes in the CO oxidation are synchronous with a periodic refacetting of the Pt nanoparticles. The oscillatory reaction is modelled using density functional theory and mass transport calculations, considering the CO adsorption energy and the oxidation rate as site-dependent. We find that to successfully explain the oscillations, the model must contain the phenomenon of refacetting. The nanoreactor approach can thus provide atomic-scale information that is specific to surface sites. This will improve the understanding of dynamic properties in catalysis and related fields.**

Understanding how nanometre-sized particles catalyse chemical reactions is important for the development of efficient catalytic materials for a wide range of energy and environmental technologies. These nanoparticles generally expose different surface sites simultaneously, each with distinct reactivity for the turnover of reactants<sup>1</sup>. A detailed characterization of the nanoparticle surface and the site-specific reactivity is therefore required to describe the catalytic performance of nanoparticles. However, nanoparticles often respond dynamically to changes in the surrounding environment, because changes in the gas composition affect the free energy of the exposed surfaces<sup>2–5</sup>. The surface structure and reactivity are therefore coupled to the reaction conditions, emphasizing the need for identification of active sites and their properties *in situ*, during catalysis. Although many *in situ* and *operando* techniques are available<sup>6–10</sup>, it remains a challenge to simultaneously obtain atomic-scale information about the surface structure and reactivity of nanoparticles under relevant reaction conditions.

Here, we focus on the role of Pt nanoparticle surfaces in the catalytic oxidation of carbon monoxide. This reaction is considered as a prototype reaction for understanding fundamental concepts in heterogeneous catalysis and is relevant for automotive emission control<sup>11</sup>. Intriguingly, under fixed reaction parameters (flow, pressure, temperature), the Pt-catalysed CO oxidation can proceed at conversions that spontaneously oscillate as a function of time<sup>12</sup>. This oscillatory behaviour is commonly perceived as a periodic transformation between the two different conversion levels of a bistable reaction. The bistable reaction is caused by nonlinear kinetics<sup>12</sup>, possibly in conjunction with mass transport<sup>13,14</sup>. The periodic transformation has been attributed to dynamic changes in the catalyst surface<sup>12</sup>. So far, the more detailed information has been obtained from studies of extended, single-crystal Pt surfaces. Those studies have proposed that the oscillatory reaction is caused

by an adsorbate-induced restructuring at low pressures (below 10<sup>−4</sup> mbar; ref. 12) and is related to switching between a metallic and an oxidic state at higher pressures (above 1 mbar; refs 15,16). In contrast, direct observations of Pt nanoparticles during oscillatory CO oxidation are lacking. Therefore, the role of the Pt nanoparticle surface structure still remains unresolved.

A direct visualization of the shape and surface structure of nanoparticles can be obtained by means of transmission electron microscopy (TEM), which can provide two-dimensional projected images of nanoparticles with a resolution and sensitivity at the atomic level<sup>17–19</sup>. Such images can even be acquired during the exposure of the nanoparticles to reactive gas atmospheres, confined to the vicinity of the nanoparticles using a differential pumping system<sup>4–6</sup> or a closed, electron-transparent cell<sup>20–23</sup>. Although the *in situ* TEM capability has provided unprecedented time-resolved observations of gas-induced processes on nanoparticles<sup>4–6,24,25</sup>, high-resolution TEM studies have so far been limited to pressures of a few millibars (which is well below the atmospheric pressure levels used in heterogeneous catalysis) and to a complex gas-flow geometry (which hampers structural information being uniquely correlated with concurrent activity measurements<sup>26</sup>).

In the present study, we employ a recently developed nanoreactor<sup>21,22</sup> to study Pt nanoparticles during the oscillatory CO oxidation. The nanoreactor is a microelectromechanical system<sup>21–23,27</sup> and includes a unidirectional gas-flow channel with a reaction zone at 1 bar pressure and elevated temperatures, representative for automotive exhaust catalysis. The nanoreactor is functionalized for simultaneous high-resolution TEM observations of the Pt nanoparticles, quantitative mass spectrometry of gas exiting the nanoreactor, and reaction calorimetry. From such time-resolved observations, the oscillatory CO oxidation reaction is shown to be synchronized with a periodic refacetting of the Pt nanoparticles in such a way that higher conversion is associated

<sup>1</sup>ChemE, Delft University of Technology, Julianalaan 136, 2628 BL Delft, The Netherlands, <sup>2</sup>Haldor Topsøe A/S, Nymøllevej 55, DK-2800 Kgs. Lyngby, Denmark, <sup>3</sup>FEI Company, Achtseweg Noord 5, 5651 GG Eindhoven, The Netherlands, <sup>4</sup>DIMES-ECTM, Delft University of Technology, PO Box 5053, 2600 GB Delft, The Netherlands, <sup>5</sup>Albemarle Catalyst Company BV, PO Box 37650, 1030 BE Amsterdam, The Netherlands, <sup>6</sup>Leiden Probe Microscopy BV, Niels Bohrweg 2, 2333 CA Leiden, The Netherlands. \*e-mail: [p.j.kooyman@tudelft.nl](mailto:p.j.kooyman@tudelft.nl); [sth@topsoe.dk](mailto:sth@topsoe.dk)

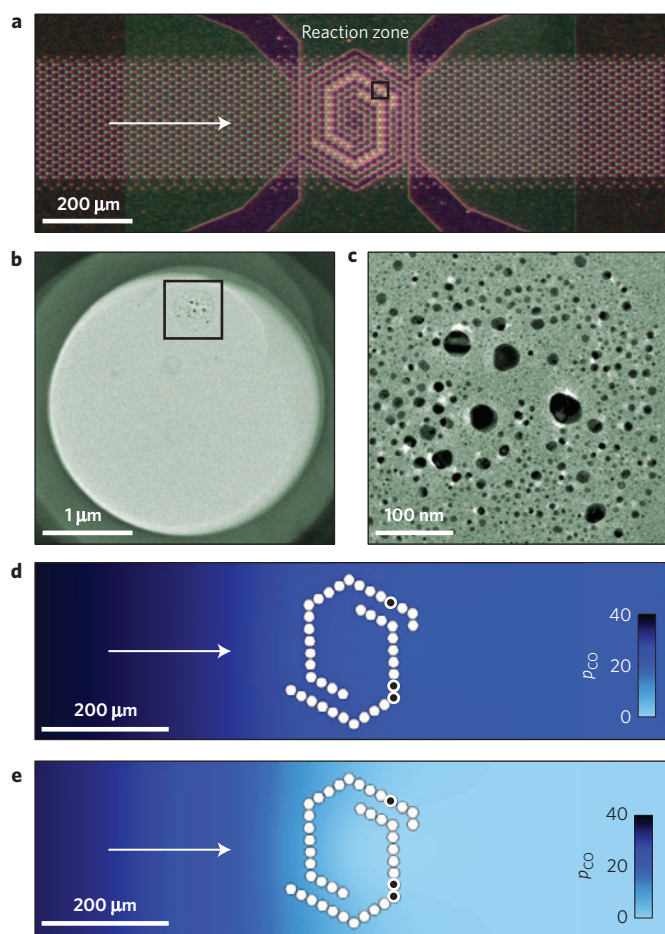


**Figure 1 | A nanoreactor loaded with Pt nanoparticles catalysing CO oxidation.** **a**, Light optical micrograph of the nanoreactor with the gas channel and the reaction zone including the heater spiral and electron-transparent windows. **b**, An electron micrograph of the framed window in **a** showing that Pt nanoparticles (dark contrast) are dispersed heterogeneously on the electron-transparent windows (uniform, bright contrast). **c**, An electron micrograph showing a close-up of the as-prepared Pt nanoparticles framed in **b**. **d, e**, Steady-state simulation of the CO concentration profile ( $[p_{\text{CO}}]$ : mbar) in the nanoreactor for the low conversion branch of the bistable regime at 710 K (**d**) and the high conversion branch of the bistable regime at 710 K (**e**) (Supplementary Information 1 and Supplementary Fig. 4). The arrow in **a, d** and **e** indicates the gas flow direction. White discs superimposed on **d** and **e** indicate the positions of the electron transparent windows. Black discs mark windows corresponding to the TEM image series in Figs 2 and 3 and Supplementary Fig. 9. For the simulations, the gas entering the reaction zone is 1.0 bar of CO/O<sub>2</sub>/He at 4.2%:21.0%:74.8% and all parameters are based on the actual nanoreactor geometry (Supplementary Tables 1 and 2).

with a transformation towards more extended close-packed facet terminations of the Pt nanoparticles and lower conversion is associated with a transformation towards more higher-index stepped terminations of the Pt nanoparticles, respectively. A comparison with density functional theory (DFT) and mass transport calculations suggests that the refaceting is due to site-dependency of the CO adsorption energy and oxidation rate and represents a mechanism for oscillatory shifts between the conversion levels. A significant implication of this study is therefore that dynamic structure–functionality relationships in heterogeneous catalysis can now be directly determined at the atomic level under relevant reaction conditions.

## Results and discussion

Figure 1a shows an optical micrograph of a nanoreactor. It includes a 280- $\mu\text{m}$ -wide and 4.5- $\mu\text{m}$ -high unidirectional gas-flow channel, enclosed between two 1- $\mu\text{m}$ -thick SiN<sub>x</sub> membranes. The channel is interfaced to a gas supply at the inlet and a mass spectrometer at the outlet. At the nanoreactor centre, a Mo thin-film resistor enables heating and temperature measurement of a reaction zone of 0.34 nl at 1 bar pressure, and 18-nm-thick electron-transparent windows facilitate TEM. The catalyst was prepared by impregnation of a nanoreactor with an aqueous solution of tetraammineplatinum(II)nitrate followed by calcination in air at 573 K. This procedure results in 3–30-nm-diameter Pt nanoparticles dispersed heterogeneously across the reaction zone (Fig. 1b,c).

To initialize the CO oxidation reaction, a unidirectional gas flow was established in the reaction zone, consisting of about 0.09 ml<sub>n</sub> min<sup>-1</sup> of CO, O<sub>2</sub> and He at a total pressure of 1.0 bar. By heating the zone above 573 K, an increasing amount of CO<sub>2</sub> is detected in the outlet gas by mass spectrometry, indicating the onset of CO oxidation (Supplementary Fig. 1). The unidirectional gas flow combined with the nanolitre volume of the reaction zone enables activity measurements by gas detection<sup>26</sup>. The relatively high onset temperature is attributed to the short gas residence time in the reaction zone of 0.2 ms (Supplementary Fig. 2). The CO oxidation is unambiguously assigned to the catalytic effect of the Pt nanoparticles, because the gas composition remained constant for an unloaded nanoreactor under the same reaction conditions. With increasing temperature, the CO conversion follows Arrhenius behaviour with an apparent activation energy of 1.3 eV, until the CO conversion abruptly exceeds Arrhenius behaviour and approaches full conversion (Supplementary Fig. 1). To interpret the CO conversion, the intrinsic reaction rate, temperature distribution and mass-transport through the nanoreactor must be considered. The CO oxidation reaction in the nanoreactor is therefore simulated using a two-dimensional convection–diffusion equation including Langmuir–Hinshelwood kinetics and an assumed homogeneous dispersion of Pt over the reaction zone (Supplementary Information 1 and Supplementary Figs 3 and 4). The match of the simulated and measured conversion of CO suggests that the model is sufficient to capture the overall conditions in the nanoreactor (Supplementary Fig. 4). The simulations of the model reveal the coexistence of two stable steady-state conversions of CO in a narrow temperature interval for the present reaction conditions and nanoreactor geometry, consistent with refs 13,14. Transitions between these two CO conversion levels (Fig. 1d,e and Supplementary Fig. 12) establish oscillatory behaviour when a feedback mechanism dynamically alters the intrinsic reaction rate of the catalyst surface.

Indeed, mass spectrometry demonstrates periodic oscillations in O<sub>2</sub> and CO pressures, which are in anti-phase with similar variations in the CO<sub>2</sub> pressure (Fig. 2a). These oscillations appeared spontaneously, or by a minor temperature change of 0.5–1.0 K, and were observed at temperatures in the range 659–729 K (Supplementary Fig. 5). The broad temperature range reported for the present experiments can be attributed to the loading and distribution of nanoparticles as well as reaction conditions and ageing times. During the oscillating reaction, the average nanoreactor temperature was kept constant by compensating the exothermic reaction heat with a reduction in the heater power. The heater equilibrated within a few milliseconds, which is at least 3 orders of magnitude faster than the timescale of the observed reaction oscillations. Therefore, the reaction oscillations occurred under constant temperature conditions<sup>28</sup> and the heater power measures the reaction power (Fig. 2b and Supplementary Fig. 2). The reaction power oscillates asymmetrically, showing a fast rise in CO conversion and a subsequent slower decay (Fig. 2a,b). The reaction power peaks at the maximum global reaction rate

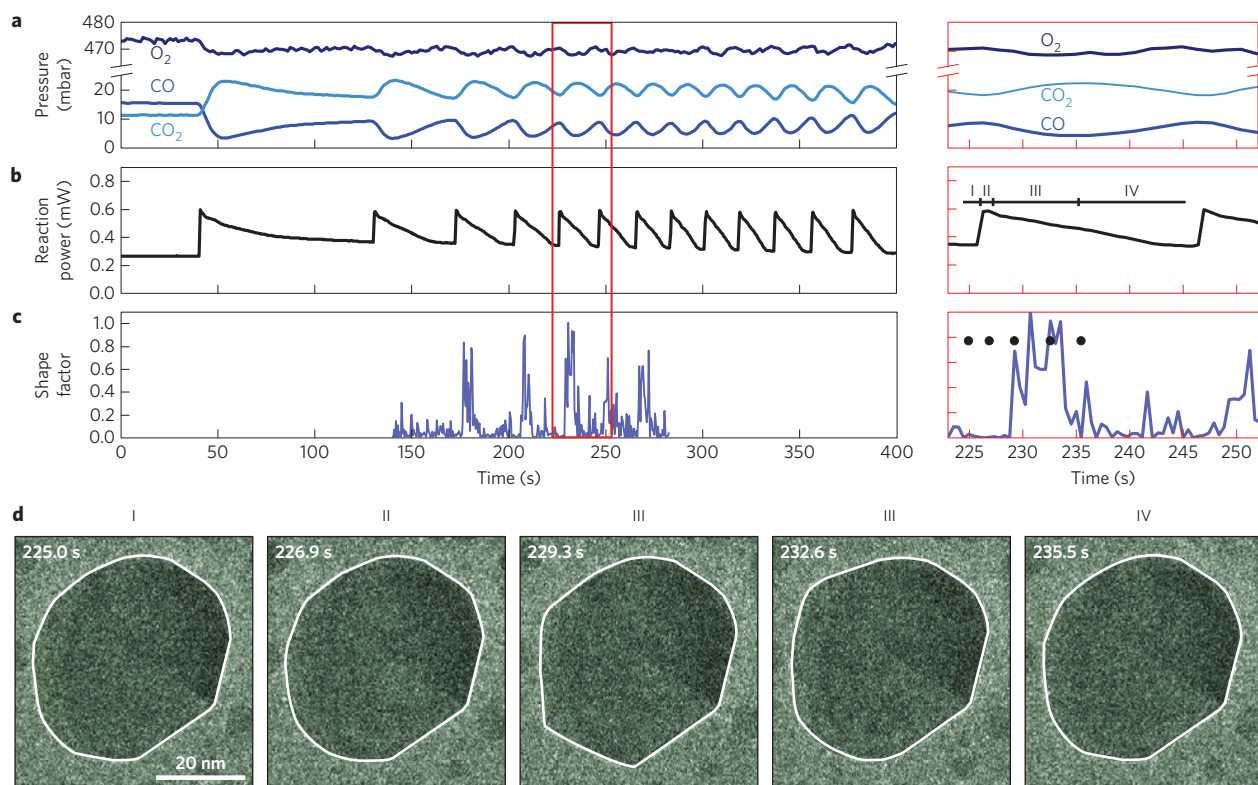


**Figure 2 | Correlation of oscillatory CO oxidation reaction data with the projected morphology of a Pt nanoparticle.** (Supplementary Movie 1.) The gas entering the reaction zone is 1.0 bar of CO:O<sub>2</sub>:He at 3%:42%:55% and nanoreactor temperature is 659 K. **a–c**, Mass spectrometry of the CO, O<sub>2</sub> and CO<sub>2</sub> pressures (**a**), reaction power (**b**) and shape factor (**c**) for the Pt nanoparticle in **d** as a function of time. The shape factor corresponds to the relative difference in area from the best elliptical fit in image I in **d** (ref. 4). The morphology factor is zero for the more spherical shape and deviates for more faceted particles. Part of the reaction oscillation data is highlighted by the red rectangle. **d**, Time-resolved TEM images of a Pt nanoparticle at the gas exit of the reaction zone.

where the CO pressure is maximal. However, the minimum CO pressure observed is delayed by space-time broadening of the gas in the tubing from the nanoreactor to the mass spectrometer (Supplementary Fig. 6), and the time-resolved CO pressure is smeared out in mass spectrometry as compared with the reaction power (heater readout time, 0.5 s). Thus, the reaction power provides a more distinct fingerprint of the oscillatory reaction.

During the oscillatory reaction, the Pt nanoparticles were monitored by time-resolved TEM. The gas composition will inevitably vary across the reaction zone as reflected by the simulated CO profiles (Fig. 1d,e). At the low CO conversion branch (Fig. 1d), the local CO pressure is 25 and 21 mbar at the windows at the entrance and exit of the reaction zone, respectively. At the high conversion branch (Fig. 1e), the local CO pressure varies significantly over the reaction zone from 8.4 to 0.2 mbar (Supplementary Fig. 4). TEM image series of the Pt nanoparticles were therefore acquired at windows both at the entrance and exit of the reaction zone, at a rate (1–2 frames per second) faster than the rate of the reaction oscillations, to directly visualize the nanoparticles on this timescale. The TEM images were acquired at electron dose rates sufficiently low to avoid electron-beam-induced artefacts (Supplementary Information 2 and Supplementary Figs 7 and 8). Near the reaction zone entrance, the nanoparticles had a stationary and more spherical morphology during the oscillating reaction. In contrast, near the reaction zone exit, the Pt nanoparticles switched between a more spherical and a more faceted morphology (Fig. 2c,d and Supplementary Movie 1). The shape changes varied in extent between different particle sizes and locations in the nanoreactor (Supplementary Fig. 9), which is probably due to the spatial variation in the gas composition and the heterogeneous distribution of

nanoparticles (Fig. 1). Specifically, as the CO conversion increases rapidly, Pt nanoparticles immediately start a gradual transformation from the more spherical shape towards a more faceted shape. The fully faceted shape is reached within 3 s after the CO peak conversion (III, Fig. 2b–d). The time associated with the shape transformation probably reflects both the Pt mass transport and the nanoparticle size and orientation, as the transformation appeared faster for nanoparticles at higher temperatures (Fig. 3 and Supplementary Fig. 11). On decrease in the CO conversion, the nanoparticle transforms back to the more spherical shape (IV, Fig. 2b–d) and retains that shape until the CO conversion rises steeply again. Thus, the individual nanoparticles near the exit from the reaction zone can undergo oscillatory and reversible shape changes with a temporal frequency matching the oscillations in reaction power, indicating that the oscillatory CO conversion and the dynamic shape change of the Pt nanoparticles are coupled.

To address the mechanism governing the oscillatory reaction, the state of the Pt nanoparticles is examined at the atomic scale. High-resolution TEM images of the Pt nanoparticles acquired *in situ* during CO conversion, such as Fig. 3c–e, show crystalline lattice fringes with spacings corresponding to metallic Pt. The uniform contrast across the projected image of the nanoparticles is also consistent with a metallic state. The presence of a surface oxide confined to the outermost surface layer cannot be excluded<sup>29</sup>, owing to the speckled contrast from electron scattering on the amorphous window material and the low electron dose. However, DFT calculations show consistently that even the close-packed facet of  $\alpha$ -PtO<sub>2</sub>(0001) is unstable under the present reaction conditions ( $T = 693$  K,  $p_{\text{O}_2} = 0.21$  bar, corresponding to a maximum oxygen chemical potential of  $\Delta\mu(\text{O}) = -0.83$  eV; ref. 30). Thus, the

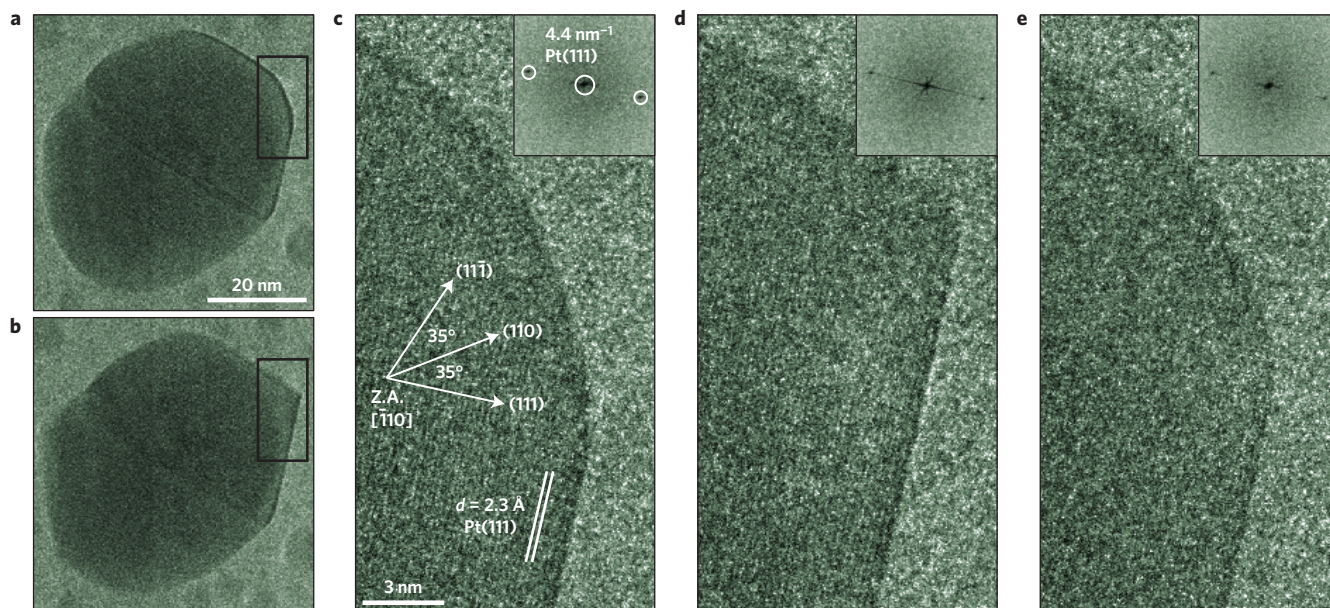


**Figure 3 | Atomic-scale visualization of the dynamic refacetting of a Pt nanoparticle during the oscillatory CO oxidation.** (Supplementary Movie 2.) Time-resolved, high-resolution TEM images of a Pt nanoparticle at the gas exit of the reaction zone. The gas entering the reaction zone is 1.0 bar of CO:O<sub>2</sub>:He at 4.2%:21.0%:74.8% and nanoreactor temperature is 727 K. **a–e**, The TEM images show the more spherical shape (**a,c,e**) and the more faceted shape (**b,d**), during the oscillatory reaction. Fast Fourier transforms included as insets in **c–e** reveal a lattice spacing corresponding to the Pt(111) lattice planes. The orientation of the observed Pt(111) lattice fringes is consistent with the superimposed crystal lattice vectors and zone axis (Z.A.). Simultaneous mass spectrometry data and reaction power are shown in Supplementary Fig. 11.

combined high-resolution TEM and DFT analyses indicate that the Pt surfaces remain in the metallic state under the present conditions. A Pt oxide becomes stable at lower temperatures and higher O<sub>2</sub> pressures<sup>29</sup>. At higher  $\Delta\mu(O) = -0.62$  eV (in 1.0 bar O<sub>2</sub> at 573 K) than encountered in the present experiments, a similar analysis shows that Pt still remains in the metallic state (Supplementary Fig. 10). Time-resolved series of high-resolution TEM images acquired during the reversible shape transformation (Fig. 3 and Supplementary Fig. 11) show that, in the more spherical state, the Pt nanoparticles are terminated by close-packed (111) planes, more open (110) planes and step sites (Fig. 3a,c,e), whereas, for the more faceted state, the nanoparticles are terminated by extended (111) planes and a reduced abundance of higher index terminations and steps (Fig. 3b,d).

The way Pt nanoparticles respond to the CO–O<sub>2</sub> gas mixture can be explained using a simple microkinetic model based on DFT calculations of adsorption and transition state energies from ref. 31 and on a thermochemical extrapolation<sup>31</sup> (Supplementary Information 4). The observed faceted surface terminations are modelled by a Pt(111) facet and the observed rounded surface terminations are modelled by a Pt(211) facet, which captures the main trends in the reactivity of more open surfaces and low-coordinated surface sites<sup>32</sup>. For each surface, the model describes the CO and O coverage (Fig. 4a) as well as the reaction rate (Fig. 4b). The dependency on CO pressure is emphasized, because O<sub>2</sub> is in excess in the gas phase and the CO pressure changes markedly across the reaction zone (Fig. 1d,e)<sup>33</sup>. At high CO pressures ( $p_{\text{CO}} > 1$  mbar), the model shows that the step is almost fully covered by CO, whereas the facet is only sparsely covered (Fig. 4a). The surface sites are practically depleted in O. The step is therefore stabilized compared with the facet, because CO adsorption is stronger on the step than at the facet<sup>31,34,35</sup>, and a more spherical shape of the Pt nanoparticles is thus expected at high CO pressure. At lower CO pressures ( $p_{\text{CO}} < 1$  mbar), the facet and step sites obtain a significant O coverage. As O binds more equally to both sites, the facet is stabilized compared with the step, so a more faceted shape

is expected. Thus, in agreement with ref. 4, the shape change of the Pt nanoparticles is attributed to the CO pressure variation under the present reaction conditions.

The gas-dependent shape of the Pt nanoparticles affects the CO conversion, because the CO oxidation rate is site-dependent<sup>36</sup>, and will depend on the position of the nanoparticle in the reaction zone due to the CO oxidation along the gas flow. Thus, a simple time-dependent model is established based on the two-site first-principles microkinetic model and a description of mass-transport (gas-phase communication between the nanoparticles) in the nanoreactor. The model makes it possible to address whether the dynamic shape of the Pt nanoparticles represents a sufficient explanation for the reaction oscillations. In the present two-site microkinetic model, Fig. 4b reveals that the step site is more active at lower CO pressures and is poisoned at higher CO pressures, whereas the facet site remains more constant in activity over the CO pressure range in the experiment. The overall CO conversion can be estimated by approximating the local reaction rate by a linear combination of both site-specific reaction rates ( $r_{hkl}$ ) weighted by the site distribution (that is,  $r = \alpha r_{111} + (1 - \alpha)r_{211}$ , with  $\alpha$  denoting the fraction of (111) sites). The estimate explicitly neglects the effect of particle size<sup>37</sup> and facet communication<sup>38</sup> to solely address the effect of the nanoparticle shape. Moreover, the gas-dependent nanoparticle shape is modelled using an equilibrium form, which is assumed to be faceted ( $\alpha = 1$ ) for CO < 1 mbar and round ( $\alpha = 0.7$ ) for CO > 1 mbar, and using a rate of morphological change ( $d\alpha/dt$ ), which is proportional to the deviation from the equilibrium shape (Supplementary Information 5). Combining this two-site model for the Pt morphology and reaction rate with a convection–diffusion equation, which approximates the nanoreactor by a one-dimensional environment (Supplementary Information 5), allows for a time-dependent simulation of the partial pressures and shape descriptor ( $\alpha$ ) throughout the nanoreactor under conditions similar to Fig. 3.

Insight into the relation between the dynamic nanoparticle shape and oscillatory reaction is obtained from the simple time-dependent model. Figure 4c shows that the simulated CO and

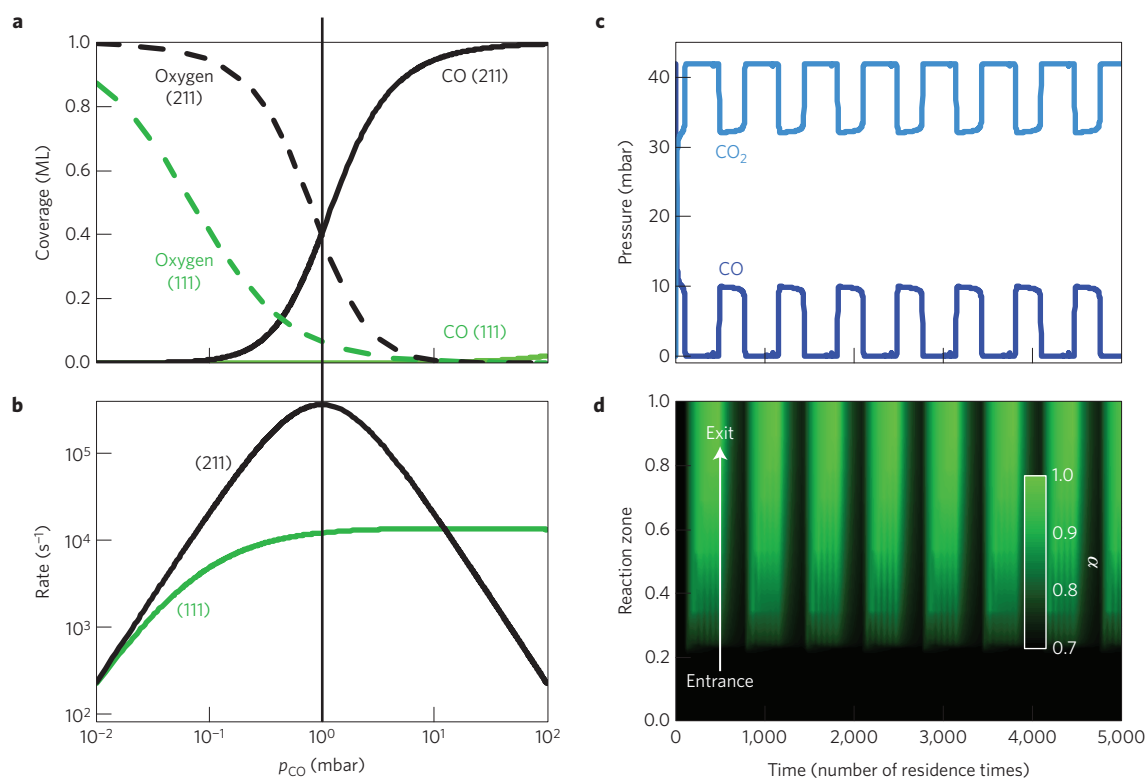


**Figure 4 | Microkinetic modelling of CO and O coverage as well as CO oxidation reaction rate on Pt surfaces.** **a**, CO and O coverage versus CO pressure at Pt(111) and Pt(211), respectively. **b**, CO oxidation rate versus CO pressure at Pt(111) and Pt(211), respectively.  $T = 793$  K,  $p_{\text{O}_2} = 210$  mbar. **c**, Time-dependent CO and CO<sub>2</sub> pressures at the reaction zone exit. **d**, The time-dependent shape factor along the entire reaction zone, simulated using the one-dimensional convection-diffusion equation for the nanoreactor and the reaction rates from **b**. The reaction zone length  $L = 320$   $\mu\text{m}$  and the residence time  $\tau = 2.69 \times 10^{-4}$  s. The inlet pressure  $p_{\text{CO}} = 42$  mbar and  $p_{\text{O}_2} = 210$  mbar and average temperature  $T = 793$  K. In the simulations, the equilibrium shape factor  $\alpha = 1$  (faceted particle) for  $p_{\text{CO}} < 1$  mbar and  $\alpha = 0.7$  (round particle) for  $p_{\text{CO}} > 1$  mbar. Further details are provided in Supplementary Information 4 and 5 and Supplementary Fig. 12. The temperature (793 K) in the isothermal model represents the local temperature in the hotter part of the nanoreactor in the experiment in Fig. 3 (Supplementary Fig. 3).

CO<sub>2</sub> pressures at the nanoreactor outlet exhibit a periodic variation in time. Specifically, the changes in partial pressures correspond to transitions between the high and low conversion states of the nanoreactor (Supplementary Fig. 12). Moreover, Fig. 4d shows that the shape descriptor remains constant in time at the reaction zone entrance (CO pressure  $> 1$  mbar), and that the nanoparticle adopts a spherical shape. Towards the exit of the reaction zone, the shape descriptor gradually adopts a temporal variation between a more faceted and a rounded shape, and the temporal variation in the shape descriptor matches the variation in CO pressure. The simulations therefore match the observations of the nanoparticle shape at the entrance and exit of the reaction zone during the oscillatory reaction. In similar simulations with fixed nanoparticle shape, the result is either a single high or low steady-state conversion and no transitions between these states occur (Supplementary Fig. 12). Furthermore, the oscillating CO pressure exhibits a saw-tooth shape in the experiment (Fig. 2a,b), whereas a more hat-shaped oscillation results from the time-dependent model (Fig. 4c and Supplementary Fig. 12). As different nanoreactors and experiments exhibited oscillations with different shapes in the CO pressure profiles (Supplementary Fig. 5), the exact change-over between high and low conversion states is probably affected by the spatial and size distribution of nanoparticles.

In conclusion, the time-dependent model captures the observations of the Pt nanoparticles during the oscillatory reaction at the reaction zone entrance and exit and demonstrates that a dynamic and reversible refaceting of Pt nanoparticles represents a mechanism that causes periodic transitions in the CO conversion

in a bistable reaction. Thus, the present findings demonstrate that nanoparticle shape dynamics should be taken into account for a complete description of oscillating catalytic reactions. The reaction oscillations may be associated with additional complexity under some reaction conditions. For example, in-plane restructuring<sup>12</sup> or oxide formation<sup>15,29</sup> could contribute to the oscillatory CO conversion as well. Although such in-plane dynamical effects remain unresolved in the present high-resolution TEM images, they are not required to obtain a consistent explanation of the observed reaction oscillations. Moreover, the nanoreactor approach is a beneficial complement to the multitude of *in situ* and *operando* techniques<sup>6–10</sup> used for uncovering gas-surface phenomena under meaningful conditions in heterogeneous catalysis and nanoparticle research, because it helps to extend the description of dynamic properties and functions with information specific to the exposed surface sites.

## Methods

**The nanoreactor system.** The employed nanoreactors are silicon-based microelectromechanical systems described in ref. 22. The nanoreactor was mounted in a custom-made holder<sup>21</sup> for insertion into the electron microscope. The holder was connected to a gas system supplying the holder inlet with a CO, O<sub>2</sub> and He mixture at a constant pressure of 2.0 bar. The holder outlet was connected to a mass spectrometer maintained at about  $10^{-5}$  mbar. The lowest gas flow conductivity in the set-up is the nanoreactor, so it is assumed that the pressure drop across the gas tubes is negligible and the pressures measured at the holder inlet and outlet equal those at the nanoreactor inlet and outlet. Owing to the symmetric design of the nanoreactor, the pressure in the centre of the nanoreactor, corresponding to the reaction zone<sup>21</sup>, is the average of the pressures at the nanoreactor inlet and outlet<sup>39</sup>.

The temperature of the reaction zone was increased by resistively heating the Mo thin film. The electrical resistance of the Mo heater was used to measure the average temperature of the nanoreactor<sup>40</sup>. The nanoreactor temperature was regulated by a proportional-integral loop, in a custom-made controller<sup>21</sup>, with about 1 ms response time. Owing to the low thermal mass of the reaction zone, temperature changes settled within a few milliseconds. The controller was steered by a LabView script with 0.5 s readout time. The maximum heat released by the CO oxidation was 0.8 mW, which is at least one order of magnitude less than the electrical power required by the Mo heater to maintain a constant temperature (Supplementary Fig. 2). At constant-temperature operation, this heat exchange led to small but perceptible changes in the electrical power consumed by the Mo heater, which enabled calorimetric information about the chemical reaction to be obtained.

Two different gas mixtures were used: a premixed gas with CO/O<sub>2</sub>/He of 4.2%:21.0%:74.8% (nominal purity 99.999% for O<sub>2</sub> and He and 99.97% for CO); and the premixed gas mixed with pure O<sub>2</sub> (nominal purity 99.999%) resulting in CO/O<sub>2</sub>/He of 3%:42%:55%. Both gas compositions passed through an active carbon filter to remove Ni-carbonyl before inlet into the nanoreactor.

Mass spectrometry was done using a Pfeiffer Prisma QME200 quadrupole mass spectrometer. During the experiments, the spectrometer continuously monitored the ion currents at 4, 28, 32 and 44 AMU, corresponding to signals from He, CO, O<sub>2</sub> and CO<sub>2</sub>, respectively. The four ion currents were sampled with 0.1 s dwell time per mass and 1.8 s total spectrum acquisition time. Ion currents were quantified as partial pressures using the known composition of the gas mixtures and correcting for mass fractioning of the inlet gas mixture during the experiment.

**TEM.** The experiments were performed using a FEI Titan 80-300 environmental transmission electron microscope<sup>41</sup>. During the experiments, the pressure around the nanoreactor was kept below  $1 \times 10^{-5}$  mbar. The microscope was operated using primary electron energy of 300 keV. Before an experiment, the aberration corrector was tuned using a Au/C cross-grating (Agar S106). The spherical aberration coefficient was in the range  $-16$  to  $-23$   $\mu\text{m}$  and flat information transfer was established at electron scattering angles up to at least 11 mrad.

High-resolution TEM images were acquired with electron dose rates of  $5\text{--}300 \text{ e}^- \text{ \AA}^{-2} \text{ s}^{-1}$ . The dose rate measured through vacuum with the nanoreactor retracted from the electron beam path was within 1% of the value measured through the nanoreactor containing 1 bar of reaction gas. As the gas and windows of the nanoreactor add on the order of 30 atoms  $\text{ \AA}^{-2}$  to the electron beam path<sup>21</sup>, the inherent microscope resolution is not substantially altered under the present electron illumination conditions<sup>41</sup> as also substantiated by the presented atomic lattice fringes resolved in the images of the Pt nanoparticles. The TEM images were acquired at 0.1–0.5 s exposure time using a CCD (charge-coupled device) camera either without or with zero-loss peak filtering by a 15 eV energy slit. Moreover, the TEM images were acquired at different magnifications corresponding to a pixel size extending down to 0.05 nm. This detection limit is sufficient for resolving the Pt(111) and Pt(200) lattice planes having lattice spacing of 0.23 nm and 0.20 nm, respectively. The imaging strategy was adopted to optimize the image signal and reduce beam-induced artefacts. The electron microscopy images are shown as a linear representation of the CCD pixel currents in a monochromatic green colour. In addition, contrast and brightness were linearly adjusted.

The high-resolution TEM, mass spectrometry and heater power data were recorded on separate computers. A clock synchronization of the computers was done before the experiment. Furthermore, the data were post-synchronized to achieve a precision of 1 s in the temporal synchronization. The heater controller responded to power changes on the millisecond timescale, which was faster than the readout of the CCD camera and mass spectrometer. The post-synchronization was therefore done by first relating mass spectrometry data to heater power data (Supplementary Fig. 6). Subsequent alignment of TEM data to heater power data was done by exploiting the small detectable specimen drift that occurs on changes of the heater power.

Received 16 October 2013; accepted 15 May 2014;  
published online 20 July 2014

## References

- Nørskov, J. K., Bligaard, T., Rossmeisl, J. & Christensen, C. H. Towards the computational design of solid catalysts. *Nature Chem.* **1**, 37–46 (2009).
- Newton, M. A., Belver-Coldeira, C., Martínez-Arias, A. & Fernandez-Garcia, M. Dynamic *in situ* observation of rapid size and shape change of supported Pd nanoparticles during CO/NO cycling. *Nature Mater.* **6**, 528–532 (2007).
- Tao, F. *et al.* Reaction-driven restructuring of Rh–Pd and Pt–Pd core-shell nanoparticles. *Science* **322**, 932–934 (2008).
- Yoshida, H. *et al.* Temperature-dependent change in shape of platinum nanoparticles supported on CeO<sub>2</sub> during catalytic reactions. *Appl. Phys. Exp.* **4**, 065001 (2011).
- Hansen, P. L. *et al.* Atom-resolved imaging of dynamic shape changes in supported copper nanocrystals. *Science* **295**, 2053–2055 (2002).
- Boyes, E. D. & Gai, P. L. Environmental high resolution electron microscopy and applications to chemical science. *Ultramicroscopy* **67**, 219–232 (1997).
- Thomas, J. M. & Somorjai, G. A. (eds) *Top. Catal.* **8** (special issue), 1–140 (1999).
- Campbell, C. T. Catalysts under pressure. *Science* **294**, 1471–1472 (2001).
- Buurmans, I. L. C. & Weckhuysen, B. M. Heterogeneities of individual catalyst particles in space and time as monitored by spectroscopy. *Nature Chem.* **4**, 873–886 (2012).
- Topsøe, H. Developments in operando studies and in situ characterization of heterogeneous catalysts. *J. Catalys.* **216**, 155–164 (2003).
- Freund, H. J., Meijer, G., Scheffler, M., Schlögl, R. & Wolf, M. CO oxidation as a prototypical reaction for heterogeneous processes. *Angew. Chem. Int. Ed.* **50**, 10064–10094 (2011).
- Imbihl, R. & Ertl, G. Oscillatory kinetics in heterogeneous catalysis. *Chem. Rev.* **95**, 697–733 (1995).
- Liau, M. A., Plath, P. J. & Jaeger, N. I. Complex oscillations and global coupling during the catalytic oxidation of CO. *J. Chem. Phys.* **104**, 6375–6386 (1996).
- Matera, S. & Reuter, K. Transport limitations and bistability for in situ CO oxidation at RuO<sub>2</sub> (110): First-principles based multiscale modeling. *Phys. Rev. B* **82**, 085446 (2010).
- Turner, J. E., Sales, B. C. & Maple, M. B. Oscillatory oxidation of CO over a Pt catalyst. *Surf. Sci.* **103**, 54–74 (1981).
- Hendriksen, B. L. M., Bobaru, S. C. & Frenken, J. W. M. Bistability and oscillations in CO oxidation studied with scanning tunneling microscopy inside a reactor. *Catal. Today* **105**, 234–243 (2005).
- Harris, P. J. F. Sulphur-induced faceting of platinum catalyst particles. *Nature* **323**, 792–794 (1986).
- Contard, L. C. *et al.* Aberration-corrected imaging of active sites on industrial catalyst nanoparticles. *Angew. Chem. Int. Ed.* **46**, 3683–3685 (2007).
- Hansen, L. P. *et al.* Atomic-scale edge structures on industrial-style MoS<sub>2</sub> nanocatalysts. *Angew. Chem. Int. Ed.* **50**, 10153–10156 (2011).
- Giorgio, S. *et al.* Environmental electron microscopy (EEM) for catalysts with a closed e-cell with carbon windows. *Ultramicroscopy* **106**, 503–507 (2006).
- Creemer, J. F. *et al.* Atomic-scale electron microscopy at ambient pressure. *Ultramicroscopy* **337**, 209–212 (2008).
- Creemer, J. F. *et al.* Proc. 2011 IEEE 24th Int. Conf. MEMS 1103–1106 (IEEE, 2011).
- Allard, L. F. *et al.* Novel MEMS-based gas-cell/heating specimen holder provides advanced imaging capabilities for in situ reaction studies. *Microsc. Microanal.* **18**, 656–666 (2012).
- Baker, R. T. K. In situ electron microscopy studies of catalyst particle behavior. *Catal. Rev. Sci. Eng.* **19**, 161–209 (1979).
- Sharma, R. & Crozier, P. in *Handbook of Microscopy for Nanotechnology* Vol. 531 (eds Yao, N. & Wang, Z. L.) (Kluwer Academic Publishers, 2005).
- Chenna, S. & Crozier, P. A. Operando transmission electron microscopy: A technique for detection of catalysis using electron energy-loss spectroscopy in the transmission electron microscope. *ACS Catal.* **2**, 2395–2402 (2012).
- Williamson, M. J., Tromp, R. M., Vereecken, P. M., Hull, R. & Ross, F. M. Dynamic microscopy of nanoscale cluster growth at the solid–liquid interface. *Nature Mater.* **2**, 532–536 (2003).
- Jensen, R. *et al.* Self-sustained carbon monoxide oxidation oscillations on size-selected platinum nanoparticles at atmospheric pressure. *Phys. Chem. Chem. Phys.* **15**, 2698–2702 (2013).
- Ackermann, M. D. *et al.* Structure and reactivity of surface oxides on Pt(110) during catalytic CO oxidation. *Phys. Rev. Lett.* **95**, 255505 (2005).
- Li, W. X. *et al.* Oxidation of Pt(110). *Phys. Rev. Lett.* **30**, 146104 (2004).
- Jiang, T. *et al.* Trends in CO oxidation rates for metal nanoparticles and close-packed, stepped, and kinked surfaces. *J. Phys. Chem. C* **113**, 10548–10553 (2009).
- Falsig, H. *et al.* On the structure sensitivity of direct NO decomposition over low-index transition metals facets. *Top. Catal.* **57**, 80–88 (2014).
- Carlsson, P. A., Zhdanov, V. P. & Skoglundh, M. Self-sustained kinetic oscillations in CO oxidation over silica-supported Pt. *Phys. Chem. Chem. Phys.* **8**, 2703–2706 (2006).
- Thosttrup, P. *et al.* Adsorption-induced step formation. *Phys. Rev. Lett.* **87**, 126102 (2001).
- Tao, F. *et al.* Break-up of stepped platinum catalyst surfaces by high CO coverage. *Science* **327**, 850–853 (2010).
- Vogel, D. *et al.* Local catalytic ignition during CO oxidation on low-index Pt and Pd surfaces: A combined PEEM, MS, and DFT study. *Angew. Chem. Int. Ed.* **51**, 10041–10044 (2012).

37. Johánek, V. *et al.* Fluctuations and bistabilities on catalyst nanoparticles. *Science* **304**, 1639–1644 (2004).
38. Gorodetskii, V. *et al.* Coupling between adjacent crystal planes in heterogeneous catalysis by propagating reaction–diffusion waves. *Nature* **370**, 276–279 (1994).
39. Robertson, J. K. & Wise, K. D. Modeling a microfluidic system using Knudsen's empirical equation for flow in the transition regime. *J. Vac. Sci. Technol. A* **19**, 358–364 (2001).
40. Vendelbo, S. B. *et al.* Method for local temperature measurement in a nanoreactor for in situ high-resolution electron microscopy. *Ultramicroscopy* **133**, 72–79 (2013).
41. Jinchek, J. R. & Helveg, S. Image resolution and sensitivity in an environmental transmission electron microscope. *Micron* **11**, 1156–1168 (2012).

### Acknowledgements

This work was performed in the framework of NIMIC (Nano IMaging under Industrial Conditions), a SmartMix project of the Dutch Ministry of Economic Affairs. The authors acknowledge support from J.C. Wolff and J. van Wingerden (DIMES Technology Centre), G.J.C. van Baarle (Leiden Probe Microscopy BV), and M. Thorhauge and S. Ullmann (Haldor Topsøe A/S). The authors acknowledge Ib Chorkendorff (Technical University of

Denmark) for fruitful discussions. Haldor Topsøe A/S is acknowledged for access to its electron microscopy facility. The work is dedicated to the legacy of H. Topsøe and his 100 years of dedication to catalysis and fundamental science.

### Author contributions

J.F.C., B.M. and L.M. developed and produced the nanoreactors. S.B.V. and P.D. designed and built the specimen holder. S.B.V. and I.P. prepared samples. S.B.V., C.F.E., P.J.K. and S.H. performed the experiments. S.B.V., C.F.E. and S.H. analysed the data. H.F. performed microkinetic modelling. S.B.V. performed reactor simulations. S.H., S.B.V., C.F.E. and H.F. composed the manuscript and it was critically discussed and revised together with J.F.C., P.J.K., B.J.N. and R.R. The project was supervised by S.H.

### Additional information

Supplementary information is available in the [online version of the paper](#). Reprints and permissions information is available online at [www.nature.com/reprints](http://www.nature.com/reprints).

Correspondence and requests for materials should be addressed to P.J.K. or S.H.

### Competing financial interests

The authors declare no competing financial interests.

## The dynamic behavior of CuZn nanoparticles under oxidizing and reducing conditions

Christian Holse, Christian F. Elkjær, Anders Nierhoff, Jens Sehested, Ib Chorkendorff, Stig Helveg, Jane H. Nielsen.

*The Journal of Physical Chemistry C* **119**, 2804-2812 (2015)

DOI:10.1021/jp510015v

Supplementary information can be found on the journal homepage.

# Dynamic Behavior of CuZn Nanoparticles under Oxidizing and Reducing Conditions

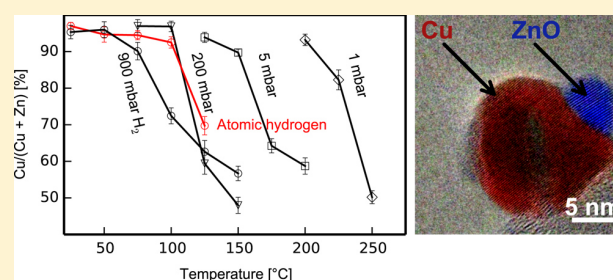
Christian Holse,<sup>†</sup> Christian F. Elkjær,<sup>†,‡</sup> Anders Nierhoff,<sup>†</sup> Jens Sehested,<sup>‡</sup> Ib Chorkendorff,<sup>†</sup> Stig Helveg,<sup>\*,‡</sup> and Jane H. Nielsen<sup>\*,†</sup>

<sup>†</sup>Center for Individual Nanoparticle Functionality, Department of Physics, Technical University of Denmark, DK-2800 Kongens Lyngby, Denmark

<sup>‡</sup>Haldor Topsoe A/S, Nymøllevvej 55, DK-2800 Kongens Lyngby, Denmark

## Supporting Information

**ABSTRACT:** The oxidation and reduction of CuZn nanoparticles was studied using X-ray photoelectron spectroscopy (XPS) and in situ transmission electron microscopy (TEM). CuZn nanoparticles with a narrow size distribution were produced with a gas-aggregation cluster source in conjunction with mass-filtration. A direct comparison between the spatially averaged XPS information and the local TEM observations was thus made possible. Upon oxidation in O<sub>2</sub>, the as-deposited metal clusters transform into a polycrystalline cluster consisting of separate CuO and ZnO nanocrystals. Specifically, the CuO is observed to segregate to the cluster surface and partially cover the ZnO nanocrystals. Upon subsequent reduction in H<sub>2</sub> the CuO converts into metallic Cu with ZnO nanocrystal covering their surface. In addition, a small amount of metallic Zn is detected suggesting that ZnO is reduced. It is likely that Zn species can migrate to the Cu surface forming a Cu–Zn surface alloy. The oxidation and reduction dynamics of the CuZn nanoparticles is of great importance to industrial methanol synthesis for which the direct interaction of Cu and ZnO nanocrystals synergistically boosts the catalytic activity. Thus, the present results demonstrate a new model approach that should be generally applicable to address metal–support interactions in coprecipitated catalysts and multicomponent nanomaterials.



## INTRODUCTION

Nanometer-sized particles of metals and metal oxides can have unique catalytic, magnetic, and electronic properties that are often strongly dependent on their structural and chemical state. In catalytic reactions, for example, the activity for molecular turnovers, is well-known to depend on the type and abundance of surface sites on the nanoparticles.<sup>1–3</sup> Procedures for the synthesis of nanoparticles with well-defined shapes and surfaces are in principle available to address such structure-dependent properties.<sup>4–7</sup> However, during catalysis, the stability of nanoparticle morphology is not guaranteed.<sup>8–10</sup> Solid surfaces tend to restructure upon exposure to gas environments and nanoparticles therefore tend to dynamically adapt a shape and structure that is coupled to the reaction conditions. Hereby, new surface sites might be exposed and the catalytic functionality of the nanoparticle change.

Here we focus on the binary Cu/ZnO nanoparticle system which is relevant for the industrial synthesis of methanol<sup>11</sup> and has become a prototypical system for studying complex gas-dependent nanoparticle dynamics. Whereas Cu alone is active, the methanol production is significantly enhanced by the intimate contact with ZnO. The role of the Cu–ZnO interaction and the nature of the catalytic active surface site has been the subject of much research. Possible explanations for the Cu–ZnO synergy include gas-dependent morphology of

Cu<sup>12–16</sup> on ZnO, Zn-species segregation onto Cu,<sup>17</sup> Cu–Zn alloy formation,<sup>18–21</sup> and support-induced strain.<sup>22,23</sup> The relative importance of these different effects is still a subject of debate and could reflect the effect of the catalyst preparation and reaction conditions.<sup>20</sup>

Much information about the gas-dependent structure of Cu/ZnO-based methanol synthesis catalysts have been obtained using bulk X-ray or neutron characterization techniques.<sup>8,18</sup> In addition, adsorption techniques have been used to correlate the Cu surface area and methanol synthesis activity.<sup>24,25</sup> Despite these efforts there is still limited insight into the surface dynamics of the Cu/ZnO nanoparticle catalyst. For instance, recent studies of an industrial catalyst showed that under reducing conditions the copper area probed by reactive nitrous oxide frontal chromatography (N<sub>2</sub>O-RFC) is overestimated and that the overestimation originates from the presence of either metallic Zn in a CuZn surface alloy or from oxygen vacancies in ZnO.<sup>26,27</sup> Moreover, a spillover effect of hydrogen in the interface between Cu and ZnO has also been proposed to have a significant role in the synthesis of methanol.<sup>16,28</sup> Understanding such phenomena in more detail requires deeper

Received: October 3, 2014

Revised: December 8, 2014

Published: December 16, 2014

insight into the dynamic surface behavior of the Cu-ZnO nanoparticle system under reducing conditions. In order to address the dynamic surface behavior in the binary Cu and ZnO nanoparticle catalyst system, we have developed a new nanoparticle synthesis method invoking formation of mass-selected CuZn alloy nanoparticles and transformation of these into binary clusters of Cu and ZnO nanocrystals on a substrate. The binary Cu-ZnO nanoparticle clusters can be regarded as confined units of the industrial Cu/ZnO methanol catalyst,<sup>29–31</sup> and these simpler structures advantageously allow the structural and chemical state of the Cu–ZnO nanoparticle surface to be studied by complementary techniques such as X-ray photoelectron spectroscopy (XPS) and in situ transmission electron microscopy (TEM).

## RESULTS AND DISCUSSION

**Particle Synthesis.** The CuZn nanoparticles were produced in a cluster source<sup>32,33</sup> by gas aggregation of Cu and Zn sputtered off a solid target and subsequently mass selected by a quadrupole mass filter. First, the mass selected CuZn nanoclusters were deposited under ultra high vacuum (UHV) conditions ( $2 \times 10^{-10}$  mbar) onto a TiO<sub>2</sub> substrate (for XPS studies) or a carbon film supported on a Cu grid (for TEM studies). TEM images of the as-prepared particles showed an average diameter of  $7.7 \pm 1$  nm (Figure S1) for particles deposited with a mass filter setting of 6.5 nm. Next, the nanoparticles were exposed to oxygen in order to facilitate a phase separation into CuO and ZnO. Finally, an exposure to hydrogen was done in order to prepare well-defined nanoparticles of Cu and ZnO in intimate contact. The TEM samples were transferred through ambient air to the microscope and treated in situ therein, while the XPS samples were treated in a high pressure cell (HPC) attached to the UHV setup. During the oxidation treatment, the O<sub>2</sub> pressure was 1 mbar and 200 mbar for the TEM and XPS experiments, respectively. In the TEM, the temperature was 300 °C and, in the HPC, the temperature was 200 °C. The higher oxidation temperature in the TEM was necessary due to the lower obtainable O<sub>2</sub> pressure. In both cases the sample was oxidized for 1 h. During reduction, the H<sub>2</sub> pressure was 1 mbar for both experiments. In the TEM, the temperature was 300 °C, and in the HPC, the temperature was increased in steps of 1 h to a maximum of 250 °C.

For these three preparation steps (deposition, oxidation and reduction), Figure 1 shows the elemental surface composition as determined by XPS, which approximately probes the first 3–5 monolayers, depending on the electron energy. Further details on calculation of the composition are in the Materials and Methods section. In the as-deposited state, the line positions and shape of Cu L<sub>3</sub>VV and Zn L<sub>3</sub>M<sub>4,5</sub>M<sub>4,5</sub> reveal that the nanoparticles are metallic, and the 2p line intensities reveal an average composition of the nanoparticles of Cu:Zn  $\approx$  75:25. Due to the nature of the cluster source we anticipate a homogeneous mixture of Cu and Zn in the as-deposited nanoparticles. Hence the surface composition is expected to be representative for the bulk composition. Corresponding Auger spectra of Cu and Zn are shown in the following. The oxidation treatment of the nanoparticles results in a decrease of the apparent amount of Zn at the surface and the formation of CuO and ZnO with a composition of Cu:Zn  $\approx$  95:5. The satellite feature at 941 eV in the Cu 2p<sub>3/2</sub> line reveals that Cu is fully oxidized.<sup>34</sup> Moreover, the oxidation treatment results in a shift in the Zn Auger line revealing a transformation of Zn into

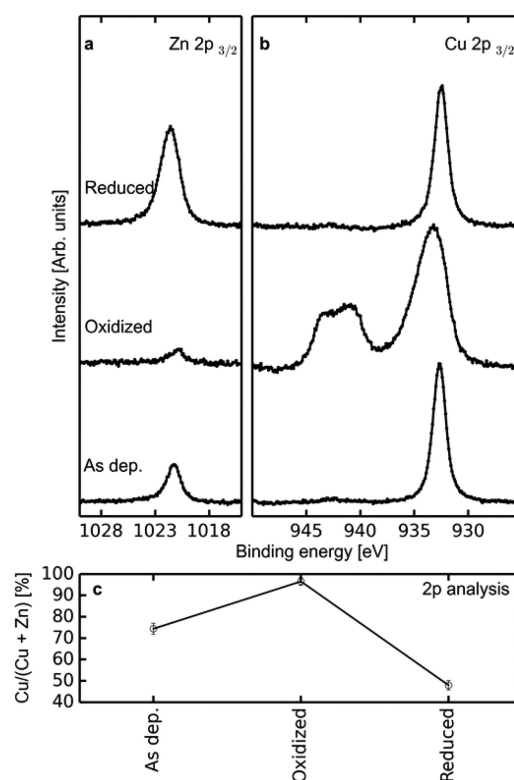


**Figure 1.** XPS Cu:Zn composition analysis. (a) Zn XPS 2p<sub>3/2</sub> in as-deposited, oxidized, and reduced condition. (b) Cu XPS 2p<sub>3/2</sub> in as-deposited, oxidized, and reduced condition. The 2p lines of Cu and Zn are background subtracted and normalized to the corresponding Cu spectrum. (c) The Cu:Zn composition taking sensitivity factors into account shown for the as-deposited, oxidized, and reduced condition, respectively.

ZnO. Finally, the reduction treatment of the oxidized nanoparticles reduces the CuO to Cu and changes the observed composition of Cu:Zn to  $\sim$ 45:55. The system thus does not revert to the as-deposited state upon reduction. The Cu/ZnO nanoparticles produced in this manner comprise our model for the methanol synthesis catalyst.

**Copper Oxidation State References.** In order to monitor the change of the oxidation state of copper in the phase separated state, the model system was exposed to reducing conditions (1 mbar H<sub>2</sub> in the HPC) at increasing temperatures, each temperature held for 1 h. After each reduction step, the sample was cooled to room temperature in the H<sub>2</sub> gas, the HPC was evacuated, and the sample was characterized by XPS under UHV conditions. Figure 2a shows normalized and background corrected XPS spectra at the Cu L<sub>3</sub>VV Auger line after each reduction treatment. In order to interpret these spectra, reference spectra were acquired of Cu, Cu<sub>2</sub>O, and CuO, with corresponding oxidation states Cu<sup>0</sup>, Cu<sup>I</sup>, and Cu<sup>II</sup>, respectively (Figure 2b). The metallic Cu reference spectrum was obtained by XPS measurement of the as-deposited nanoparticles. The copper oxide reference spectra were obtained by previously reported procedures.<sup>34</sup> To obtain the CuO reference spectrum, the as-deposited nanoparticles were fully oxidized by exposure to 200 mbar O<sub>2</sub> at 200 °C for 1 h in the HPC and subsequently measured by XPS. Finally, in order to obtain the partially oxidized Cu<sub>2</sub>O reference spectrum, the as-deposited sample was exposed to 200 mbar O<sub>2</sub> at room

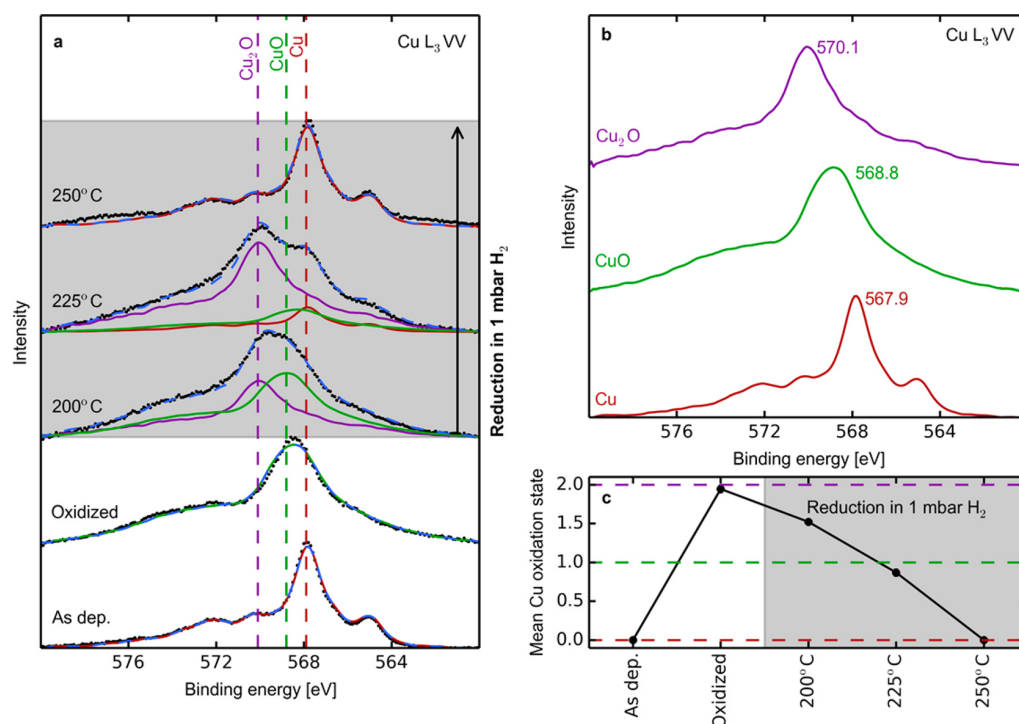


**Figure 2.** Changes to the XPS Cu L<sub>3</sub>VV features. (a) Reduction of CuZn nanoparticles in 1 mbar H<sub>2</sub>. Data points are shown as black dots while the light blue dashed lines are fits. The vertical lines indicate peak position for Cu (red), CuO (green), and Cu<sub>2</sub>O (purple). Subsequent to oxidation the nanoparticles are reduced in 1 mbar H<sub>2</sub> in steps for 1 h at increasing temperature. XPS is conducted in between each H<sub>2</sub> treatment. The change in the Cu L<sub>3</sub>VV Auger lines reveal that CuO is gradually reduced through the Cu<sub>2</sub>O state before it reaches full reduction at 250 °C. (b) The three different oxidation states of Cu. The fit in (a) is obtained by fitting a linear combination of the three Cu L<sub>3</sub>VV basis reference spectra. (c) The mean oxidation state of Cu as a function of reduction temperature. The mean oxidation state is obtained through the fits in (a).

temperature for 16 h in the HPC. For these three samples the Cu L<sub>3</sub>VV Auger lines are similar to spectra for Cu, CuO, and Cu<sub>2</sub>O as reported for copper thin films.<sup>34</sup> These spectra are therefore used as references in the following. Specifically, the different reference spectra consists of a main peak at 567.9, 568.8, and 570.1 eV for Cu, CuO, and Cu<sub>2</sub>O, respectively, corresponding, for the Al anode, to electron kinetic energies of 918.7, 918.8, and 916.5 eV.

A linear combination of the three references (Cu, CuO, and Cu<sub>2</sub>O) can be fitted to the Cu L<sub>3</sub>VV Auger lines in Figure 2a and the relative abundance of each phase is determined from the fitting parameters. The results in Figure 2a show that the as-deposited nanoparticles consist only of metallic Cu. As shown before, in the case of exposure to 200 mbar O<sub>2</sub> at 200 °C, the nanoparticles consist of copper in its fully oxidized state, i.e., CuO. During the reduction at successively higher temperatures, copper gradually transforms from fully oxidized CuO, through the Cu<sub>2</sub>O phase, to fully reduced Cu.

Furthermore, the fitting of the Cu L<sub>3</sub>VV Auger line into Cu<sup>0</sup>, Cu<sup>I</sup>, and Cu<sup>II</sup> allows for an estimation of the average copper oxidation state in the nanoparticles (Figure 2c). This procedure shows that copper in the oxidized CuZn nanoparticles is reducible under 1 mbar H<sub>2</sub> at 250 °C for 1 h. These conditions are similar to those used in the present in situ TEM experiments and consistent with previous in situ TEM studies.<sup>15,16,35</sup>

**In Situ TEM Imaging.** Next, the relationship between the oxidation state and the morphology of the nanoparticles is addressed by in situ TEM of the nanoparticles under exposure to 1 mbar of H<sub>2</sub> or O<sub>2</sub>. Figure 3a shows a frame-averaged TEM

image of a Cu/ZnO nanoparticle supported on carbon under exposure to 1 mbar H<sub>2</sub> at 300 °C. In order to interpret the TEM image, different crystal phases present in the nanoparticle are identified from the crystal lattice fringe spacings. Figure 3b shows a fast Fourier transform (FFT) revealing several different lattice spacings and directions. By masking out a given lattice spot in the FFT and inverting the FFT, the spatial location of the corresponding crystal phase is readily identified. For example, Figure 3c shows annular masks superimposed on the FFT in Figure 3b at reciprocal lattice vectors of 1/2.08 Å<sup>-1</sup> and 1/1.81 Å<sup>-1</sup>, corresponding to the (111) and (200) planes of Cu. The mask width is 1/0.03 Å<sup>-1</sup>. Figure 3d shows the corresponding inverted FFT revealing that metallic Cu comprises the large central region of the nanoparticle. Figures 3e,f show similarly an annular mask at lattice spacings of 2.81 and 2.60 Å, corresponding to the (010) and (002) planes of ZnO, and the corresponding inverted FFT of the ZnO location. This procedure was employed for the interpretation of the spatial location of the various crystalline phases depicted in the high-resolution TEM images. Specifically, the image analysis focuses on the four relevant phases of Cu, CuO, Cu<sub>2</sub>O, and ZnO which each has unique crystal plane distances as depicted by the colored annular masks superimposed in Figure 3g. Hereby, each crystal phase is characterized by its spatial domain in the TEM image and the superposition of all filtered crystal phases provides a fingerprint of the relative content and location of the different crystal phases as illustrated in Figure 3h.

**Reduction/Oxidation Cycles.** The ex situ XPS and the in situ TEM methods outlined above are used to monitor the

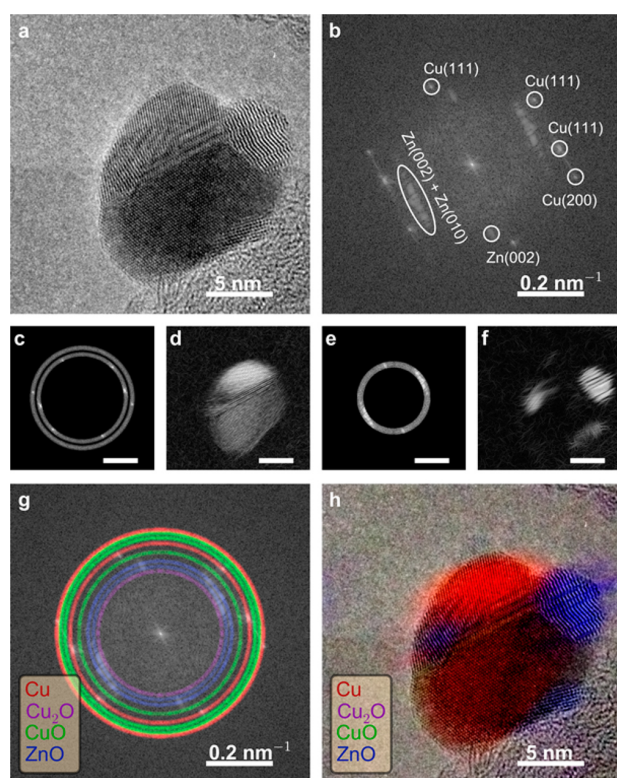


**Figure 3.** (a) TEM image of a Cu nanoparticle decorated with ZnO (1 mbar  $H_2$ , 300 °C). (b) Fast Fourier Transform (FFT) shows crystal lattice vectors. (c) Annular masks applied to the FFT at  $1/2.08$  and  $1/1.81 \text{ \AA}^{-1}$ , corresponding to (111) and (200) planes of Cu. Mask width  $1/0.03 \text{ \AA}^{-1}$ . (d) Inverse FFT (IFFT) of (c). (e) Annular masks applied at lattice spacings of  $1/2.81$  and  $1/2.60 \text{ \AA}^{-1}$ , corresponding to (010) and (002) planes of ZnO. (f) IFFT of (e). (g) Annular masks superimposed on (b) for each unique lattice spacing of Cu,  $Cu_2O$ , CuO, and ZnO (Table 1) with corresponding color code. (h) The image (a) with colored crystal phase domains superimposed.

CuZn nanoparticles during successive reduction and oxidation cycles. While XPS is a strong averaging technique providing a global picture of the surface composition and oxidation state of the entire ensemble of nanoparticles, TEM imaging is a strong local tool providing insight into the nonperiodic structural features of the nanoparticles, such as their shapes and surfaces that are needed to explain the global trends. The TEM images were acquired of as-deposited nanoparticles under high vacuum conditions and in situ during subsequent exposure to 1 mbar  $O_2$  and  $H_2$  at 300 °C, respectively (Figure 4a–d). The XPS data were acquired starting from an as-deposited sample treated first in 1 mbar  $O_2$  and  $H_2$ , as described above, and subsequently in 200 mbar  $O_2$  or  $H_2$  at 200 °C (Figure 4e). For the XPS experiments a higher gas pressure was used to ensure full reduction and oxidation (Figure 5). This pressure is, however, not possible to obtain in the applied microscope configuration. Figure 4 compiles the combination of in situ TEM and XPS data. When alternating between the oxidized state and the reduced state, the XPS analysis shows that the surface ratio between Cu and Zn changes reversibly, with the apparent amount of Cu varying from  $\sim 55\%$  to  $\sim 85\%$ . A change in surface composition of Cu and Zn has previously been reported by means of low-energy ion scattering experiments on Cu/ZnO/SiO<sub>2</sub>.<sup>36</sup>

One possible explanation for this reversible change in the surface of the nanoparticles is encapsulation and decapsulation of ZnO by CuO. Encapsulation leads to a hindrance of Zn 2p photoelectrons in reaching the analyzer, and decapsulation reestablishes the Zn signal, as observed. Figure 4a demonstrates a reduced CuZn nanoparticle consisting of separate domains of metallic Cu (red) and ZnO (blue). In Figure 4b, the nanoparticle is in the oxidized state with a CuO domain (green) extending across the entire nanoparticle and with a ZnO domain (blue) present only inside the projected image of the nanoparticle. As the TEM images represent two-dimensional projections, this observation is consistent with crystalline ZnO in the subsurface region of the nanoparticle. The finding agrees with the XPS data which shows that the Zn signal is drastically damped during these oxidizing conditions (Figure 4e). Upon rereduction, the TEM shows that the nanoparticle reverts back toward its original state. In Figure 4c, faint lattice fringes corresponding to crystalline ZnO (blue) and a core with darker contrast is observed. In the intermediate state between fully oxidized and fully reduced, shown in Figure 4c, the crystals are oriented such that no major zone axes are parallel with the incident electron beam, which results in a lack of clearly resolved atomic lattice fringes. This, in turn, has the consequence that the automatic coloring routine will not add color, and Figure 4c thus represents the original TEM image, except for the blue coloring of the faintly resolved ZnO. In Figure 4d, the darker core appears with lattice fringes and the fringe spacing corresponds to metallic Cu. Moreover, the ZnO nanocrystal reappears on the Cu surface close to the position as in the reduced state (Figure 4a). Thus, in the example shown in Figure 4d, the nanoparticle has reverted back close to its original configuration with ZnO sitting at the surface of the metallic Cu, which is also consistent with the XPS data in Figure 4e, showing that the ZnO content recovers almost reversibly upon rereduction. For Figure 4(a–d), the nanoparticle is deemed reduced or partly reduced/oxidized, based only on the observation of lattice spacings from Cu metal or from any Cu oxide. It cannot be excluded that smaller crystal domains, representing Cu oxide in the reduced state and Cu metal in the oxidized state of the nanoparticle, may be simultaneously present, because a tilted orientation of the crystal domain with respect to the electron beam direction could prevent their identification in the high-resolution TEM image. In fact, images obtained at different regions of the sample showed the presence of copper oxide after the 5 h reduction in 1 mbar  $H_2$  at 300 °C. This difference could be due to temperature variations across the TEM grid or an accelerated reduction rate under electron illumination in Figure 4, and from the discussion below the difference is attributed to the former cause. The encapsulation/decapsulation mechanism can, however, be explained by considering the crystal structure of Cu and CuO. When the sample is oxidized, the copper phase content will expand and take up more space than of metallic copper. As the oxide grows it appears to cover the ZnO. This may happen due to the different diffusion rate of Cu and O in CuO.<sup>37</sup> Because Cu diffuses faster than O in CuO, the oxide tends to grow on the surface of the existing oxide, which may create voided particles, or, as in the present case, may lead to an encapsulation of the ZnO sitting on the Cu surface. No voided particles were observed in the present study. During reduction, the CuO will consequently shrink and start to reveal ZnO. A rough estimate of the particle volume based on the projected areas reveals volume conservation between Figure 4a and d.

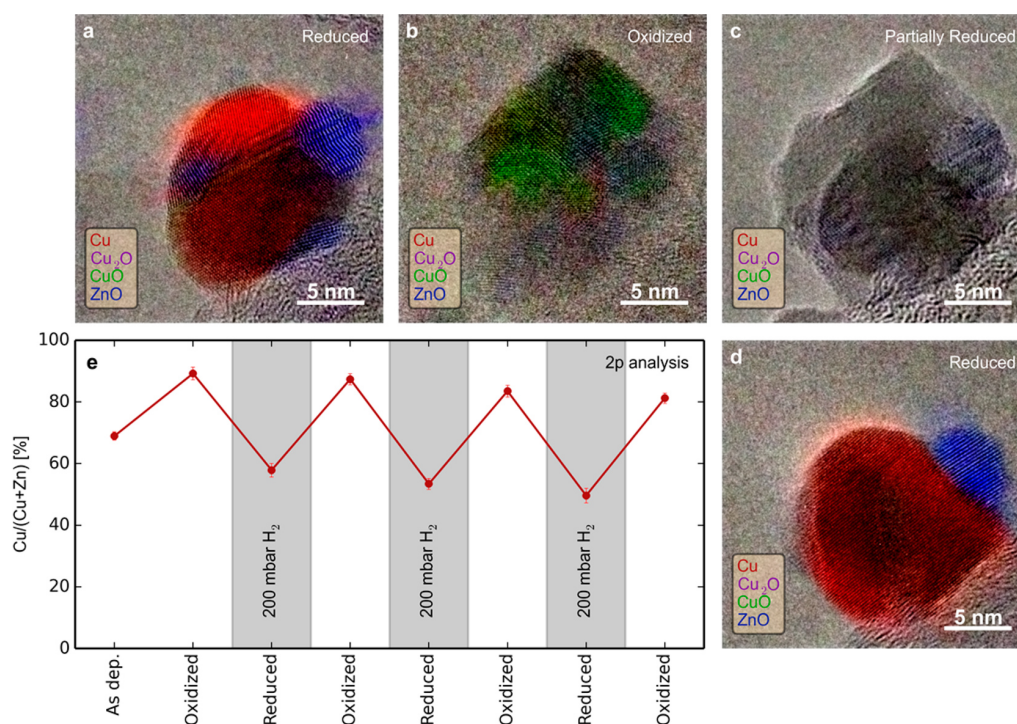


**Figure 4.** (a–d) In situ TEM images of the same CuZn nanoparticle during an oxidation/reduction cycle. (a) Reduced nanoparticle after 5 h in 1 mbar  $H_2$  at 300 °C. (b) Oxidized nanoparticle after 1 h in 1 mbar  $O_2$  at 300 °C. (c) Partly reduced nanoparticle after 0.5 h in 1 mbar  $H_2$  at 300 °C. (d) Fully reduced particle after 1.5 h in 1 mbar  $H_2$  at 300 °C. For (a–d), the nanoparticle is deemed reduced or partly reduced/oxidized based only on the observation of lattice spacings from Cu metal or from any Cu oxide. It can therefore not be excluded that small crystal domains, representing Cu oxide in the reduced state and Cu metal in the oxidized state, may be simultaneously present because a tilted orientation with respect to the electron beam could prevent their identification. (e) Ratio between the XPS signal from the Cu  $2p_{3/2}$  and Zn  $2p_{3/2}$  lines after oxidation (200 mbar  $O_2$  for 1 h at 200 °C) and reduction (200 mbar  $H_2$  for 1 h at 200 °C).

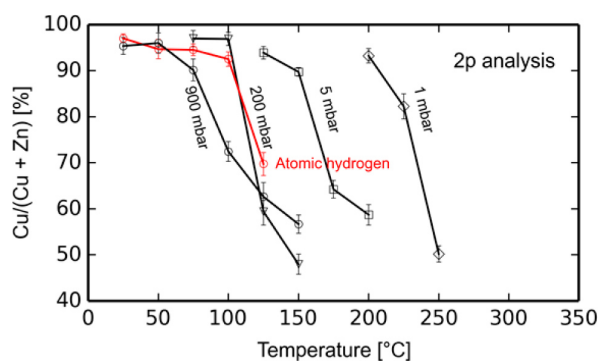


**Figure 5.** Change in ratio between the Cu  $2p_{3/2}$  and Zn  $2p_{3/2}$  XPS line as a function of increasing temperature in different pressures of hydrogen. At 1 mbar the Cu/(Cu + Zn) ratio drops when the temperature reaches 250 °C. This is the same conditions needed to fully reduce the Cu (Figure 2). The same behavior, although at lower temperature, is observed for 200 mbar  $H_2$ , 900 mbar  $H_2$  and atomic hydrogen at a pressure of  $10^{-6}$  mbar  $H_2$ . In the latter case, the ratio changes at 125 °C. At 5 mbar  $H_2$  the Cu/(Cu + Zn) ratio drops when the temperature reaches 175 °C.

The expansion from Figure 4a to b is 88%, reasonably close to the 72% increase, expected from the difference in unit cell volume between Cu and CuO. A similar analysis of 88 particles in the same area shows an average volume increase of 82% (Figure S2).

The single image series in Figure 4 reveals the transformation of the nanoparticle during the reduction–oxidation–reduction

cycle. Whereas the Cu nanocrystal and a ZnO nanocrystal apparently transforms reversibly, some smaller ZnO nanocrystals disappears and a single ZnO nanocrystal emerges on the left side of the particle. Because of the narrow size distribution of the nanoparticles and a presumably low spread of their composition, the observations in Figure 4 are likely to be representative for the deposited nanoparticles. Furthermore, the XPS data (Figure 4e) shows a slight decrease in the Cu:Zn ratio as repeated cycles are performed. This decrease in the Cu:Zn ratio for repeated cycles can be explained by migration of Cu between individual Cu/ZnO nanoparticles and is known to be a possible mechanism for Cu sintering in methanol synthesis catalysts.<sup>38</sup> In the present study sintering was observed during the reduction/oxidation cycle of the TEM sample (Figure S2). Coarsening of Cu particles lowers the Cu surface area of the sample, thus effectively also lowering the Cu:Zn ratio.

**Reduction of Cu in Different Environments.** Although the XPS and TEM experiments agree qualitatively, they differ by the gas pressure. To address this pressure gap, oxidized Cu–Zn nanoparticles are exposed to  $H_2$  at different pressures and characterized by XPS. Prior to the reduction, the nanoparticles were oxidized by 200 mbar  $O_2$ . The temperature required for reduction is presumably determined by either diffusion-limitations in the nanoparticles or limitations due to hydrogen dissociation. Thus, it is expected that the reduction temperature is lower at higher pressures because of the increased chemical potential of  $H_2$ . Figure 5 shows the Cu:Zn composition obtained from the Cu 2p and Zn 2p line intensities as a

function of reduction temperature for five different reducing conditions.

First, the reduction of oxidized CuZn nanoparticles is addressed in 1 mbar  $H_2$ . Figure 5 shows that the Cu:Zn ratio has a transition at 250 °C, which is the same temperature required to fully reduce CuO to Cu (see Figure 2). A similar sudden change in Cu:Zn ratio has been reported by Behrens et al. based on synchrotron XPS.<sup>18</sup> However, in their study the temperature for the transition occurs at a lower temperature and  $H_2$  pressure (175 °C, 0.25 mbar). This will be further discussed below. The discrepancy in reduction temperature between the 1 mbar XPS (250 °C) and 1 mbar TEM (300 °C) in our experiments is attributed to an expected lower temperature away from the TEM Cu grid upon which the temperature is measured. The temperature at the nanoparticle site for our XPS and TEM investigations is therefore assumed similar.

Next, in 5 mbar  $H_2$ , the transition occurs at 200 °C, lower than the 250 °C required for reduction in 1 mbar  $H_2$ , indicating that reduction is hindered by the reductive potential of the  $H_2$  gas. This tendency is followed upon reduction of the oxidized CuZn nanoparticles in 200 mbar  $H_2$  for which the Cu:Zn ratio transition occurs already at 125 °C. In all cases the transition coincides with CuO reduction to Cu.

Finally, at 900 mbar reducing conditions, the curve shape is slightly different but the transition to a lower Cu content is below or similar to the 200 mbar experiment at 125 °C. This may indicate that for temperatures lower than 125 °C, oxygen diffusion from bulk to the surface in the CuO nanoparticle is kinetically hindered.

Another way of increasing the chemical potential for reduction is predissociation of  $H_2$ .<sup>39</sup> The atomic hydrogen can be formed at UHV compatible pressures by ionization in a dedicated gas doser. Figure 5 shows that the predissociation is a very effective way of increasing the chemical potential of  $H_2$  because the oxide-metal transition is observed at temperatures around 125 °C (see Figure S3 for detailed XPS data), similar to the 200 mbar  $H_2$  conditions.

In the in situ TEM experiments, the reducing temperature of 300 °C was needed to fully reduce CuO in 1 mbar  $H_2$  (as determined by inspection of high-resolution TEM images). This finding indicates that atomic hydrogen is not produced by the electron beam in significant amounts in the present experiments and suggests, in turn, that the variation in the degree of reduction across the TEM grid is rather due to temperature variations. Furthermore, the effect of the beam on creating atomic hydrogen might explain the temperature discrepancy with the results obtained on synchrotron XPS.<sup>18</sup>

**Reduction of ZnO.** To address the chemical state of zinc resulting from the reduction treatment, the Zn  $L_{3M_{4,5}M_{4,5}}$  Auger line is considered in the following. Figure 6 evidently shows that the Zn in the as-deposited CuZn nanoparticles is metallic as the particles are deposited on the  $TiO_2$  substrate.<sup>40,41</sup> After oxidation in 200 mbar  $O_2$  at 200 °C, based on the comparison to literature,<sup>40</sup> Zn is present as ZnO as shown in Figure 6. Using these as-deposited and fully oxidized spectra as reference spectra for metallic and oxidized Zn, a linear combination can be fitted to the Zn  $L_{3M_{4,5}M_{4,5}}$  Auger lines obtained after reduction in 1 mbar  $H_2$  at different temperatures to determine the relative abundance of those species. At 250 °C, the Zn Auger line can best be fitted including a Zn-component resulting in the shoulder at 495 eV binding energy (991.6 eV kinetic energy). This indicates that

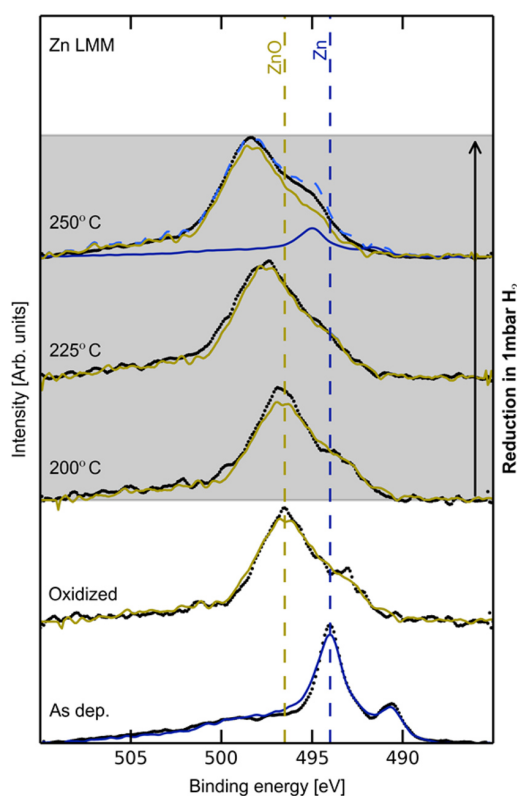


**Figure 6.** Zn  $L_{3M_{4,5}M_{4,5}}$  Auger line obtained during the 1 mbar reduction experiment. Blue lines correspond to metallic Zn while yellow lines correspond to ZnO. The dotted black line is 7 point smoothed XPS data while the dashed light blue line is the best fit of the data based on the reference spectra of Zn and ZnO.

ZnO is partially reduced at this temperature. The presence of reduced Zn after low temperature reduction in  $H_2$  has previously been reported<sup>26</sup> for a commercial catalyst. Moreover, it is observed that the Zn  $L_{3M_{4,5}M_{4,5}}$  line shifts toward higher binding energies as the reduction temperature is increased. This effect may be related to charging effects in the  $TiO_2$  substrate which is more pronounced at higher reductive potentials.<sup>42</sup> The separation between the ZnO and the Zn peak is kept fixed while performing the fitting routine.

The presence of reduced ZnO is observed at the same temperature needed to reduce CuO. The concurrent reduction for CuO and ZnO is also observed for reduction in 5 mbar  $H_2$ , 200 mbar  $H_2$ , 900 mbar  $H_2$ , and in atomic hydrogen (see Figure S4 for the atomic hydrogen experiment). It is well-known that  $H_2$  dissociates on Cu.<sup>43</sup> As ZnO is present at the surface of the nanoparticle during reduction of CuO (Figure 4), it is possible that ZnO reduction proceeds via spillover of dissociated hydrogen to sites at the ZnO surface from the reduced Cu.<sup>16,28</sup> Thus, it is likely that dissociated hydrogen can reduce ZnO to Zn at the interface between Cu and ZnO. The experiment shows that even at low pressures of hydrogen it is possible to reduce ZnO to Zn, coinciding with previous experiments made on a commercial catalyst.<sup>26</sup> However, a more pronounced Zn signal is observed in our experiments. We attribute this to the lower amount of ZnO in our model system compared to the commercial catalyst system, which increases the sensitivity for detection of metallic Zn. This stresses the advantage of using simplified model systems to investigate such complex systems.

## CONCLUSION

In order to address metal–support interactions in heterogeneous catalysis, a novel model approach is presented. It is demonstrated that size and composition selection of nanoparticles allows for generating a uniform ensemble of bimetallic nanoparticles and for combining spatial averaging and local techniques to probe gas-dependent dynamics in the nanoparticles. Specifically, the method is used to study the complex Cu–ZnO system representing the active part of industrial methanol synthesis catalysts. The as-prepared Cu–Zn particles were exposed to oxidizing and reducing atmospheres. By combining ex situ XPS and in situ TEM, it is observed that upon repeated oxidization–reduction cycles, the CuO tends to encapsulate and decapsulate the ZnO in a reversibly manner. Furthermore, the present findings reveal that the hydrogen reduction is sufficient to cause a reduction of the ZnO leaving metallic Zn in the surface. The metallic zinc is only observed as the copper is in the metallic states. On the basis of this, a spillover mechanism for the reduction of Zn has been proposed.

## MATERIALS AND METHODS

**Ultra High Vacuum Setup.** The cluster synthesis, spectroscopy experiments, and high pressure treatments were conducted in a home build multipurpose UHV chamber with a base pressure in the  $2 \times 10^{-10}$  mbar pressure range and capable of performing XPS measurements. Furthermore, it is possible to treat samples in a HPC annexed to the chamber. Finally, the UHV setup is in connection with a cluster source capable of producing metallic nanoparticles with a narrow size distribution in the range 3–10 nm, described elsewhere.<sup>33,44,45</sup> All transfers between different parts of the chamber are in UHV.

For this study, metallic CuZn nanoparticles are deposited on a TiO<sub>2</sub>(110) rutile single crystal. The nanoparticles are produced by a cluster source developed by Mantis Deposition Ltd. The mass filter of the cluster source was adjusted to select particles with a diameter of 9 nm. Based on earlier studies on the same cluster source, operated under similar conditions, the standard deviation of the size distribution of the nanoparticles is expected to be 2 nm.<sup>45</sup> The CuZn clusters are sputtered off a metal target with Cu:Zn composition of 90:10. The metal clusters are condensed in a cooled gas-aggregation zone and mass filtered by a quadrupole. After deposition of CuZn nanoparticles on the TiO<sub>2</sub>(110) substrate the nanoparticles were investigated by XPS. The Cu 2p<sub>3/2</sub> and Zn 2p<sub>3/2</sub> XPS lines reveal a 76:24 atomic composition in the surface region probed by the Al K $\alpha$  X-rays (1486.6 eV). Comparison of the Cu(L<sub>3</sub>VV) and Zn(L<sub>3</sub>M<sub>4,5</sub>M<sub>4,5</sub>) lines to literature confirms that the produced nanoparticles are metallic.<sup>34,40,41</sup> In order to bring the CuZn nanoparticles in a state similar to the commercial methanol catalyst, the sample is oxidized at 200 °C in 200 mbar O<sub>2</sub> for 1 h in the HPC by a molybdenum substrate heater. The Cu Auger and Zn Auger lines confirm that the probed region of the nanoparticle becomes fully oxidized. The ratio between the amount of Cu and Zn is determined by integrating the 2p<sub>3/2</sub> lines from each element, taking sensitivity factors into account. After phase separation of Cu and Zn, i.e., oxidation, two different set of experiments are performed; (1) a repeated cycle of reduction and oxidation at 200 °C and 200 mbar H<sub>2</sub> and O<sub>2</sub> respectively. The sample is exposed to the gas for 1 h. Between each gas treatment the sample is investigated by XPS. (2) A cumulative reduction of

the CuZn in 1 mbar H<sub>2</sub> at increasing temperatures, starting at 200 °C and ending at 250 °C, in steps of 25 °C. Each step was held for 1 h. XPS analysis of the sample is performed after each temperature step. The stepwise reduction experiment has also been conducted in 5 mbar H<sub>2</sub>, 200 mbar H<sub>2</sub>, 900 mbar H<sub>2</sub>, and in the presence of atomic hydrogen. The atomic hydrogen was produced by a hot filament with an emission current of 10 mA pointing in the direction of the sample in a background pressure of  $1 \times 10^{-6}$  mbar H<sub>2</sub>. In all XPS experiments, the presence of contaminants such as carbon has been checked for. In none of the experiments a peak at the C 1s relevant binding energy could be detected. A typical overview scan is presented in Figure S5. A Shirley background is applied to the XPS data during data treatment. Error bars are calculated by performing fits with 25 randomly chosen Shirley backgrounds. Presented data with no apparent error bar have errors smaller than the marker indicating the point.

**In Situ TEM.** In situ TEM was performed using a FEI Titan 80–300 environmental transmission electron microscope operated with primary electron energy of 300 keV.<sup>46</sup> Prior to the experiment, the image aberration corrector was tuned using a Au/C cross-grating (Ager S106) and the spherical aberration coefficient was set in the range of –10 to –20  $\mu\text{m}$ .

Samples for in situ TEM were prepared by depositing CuZn alloy particles directly onto a lacey carbon film supported on a Cu TEM grid. Nanoparticles with a diameter of 6.5 nm were selected by tuning the filter of the cluster source. Based on TEM investigations this resulted in an average projected diameter of  $7.7 \pm 1$  nm (Figure S1). The difference between the mass filter setting and the TEM measurement is ascribed to particle wetting on the support and possible surface oxidation of the CuZn particles, both effects will increase the projected diameter. The cluster deposition was carried out under UHV conditions, and subsequently the sample was transferred in air to either a glovebox (the levels of oxygen and moisture were below 0.1 ppm and 1 ppm, respectively) or directly into the electron microscope. The air exposure amounted to maximum 30 min.

For the in situ experiments, a TEM grid was placed in a Gatan furnace type heating holder (model 628). The sample was exposed to 1 mbar O<sub>2</sub> (Air Liquide, nominal purity N4.5) or 1 mbar H<sub>2</sub> (CK gas, nominal purity N6.0). The TEM is conducted using low electron dose-rate and low electron dose conditions in order to suppress beam excitations and atom displacements in the gas-sample system and to ensure structures and processes inherent to the nanoparticle catalysts are detected.<sup>46,47</sup> The low electron doses compromise the image signal-to-noise ratio, and so, to detect features in the specimens at high resolution, signal enhancement is pursued in two steps. First, the projection system and charged-coupled device camera (Gatan US1000) was operated with an effective pixel size of 0.063 nm, which is sufficient for resolving the Cu (111) and (200) lattice spacing of 0.21 and 0.18 nm, respectively. Second, frame-averaging is pursued by acquisition of 20 consecutive frames (each with a CCD exposure time of 1 s), postalignment of the frames using cross correlation<sup>48</sup> in a Matlab script and, finally, summation of the aligned frames into the final image. All displayed images represent such a frame-average. Specifically, the TEM frames were acquired at an electron dose rate of 300 e<sup>-</sup>/Å<sup>2</sup> s and an estimated total dose of 90 000 e<sup>-</sup>/Å<sup>2</sup> (ca. 5 min exposure) of a given sample area. Figure 4a–d represents images acquired of that particular particle with an accumulated electron dose of approximately 2.7

$\times 10^5$ ,  $7.2 \times 10^5$ ,  $8.1 \times 10^5$ , and  $9.0 \times 10^5$   $e^-/\text{\AA}^2$ . These imaging conditions were sufficiently low to avoid beam-induced artifacts as the comparison with the pressure-dependent XPS reduction data shows (Figure 5). Several particles were imaged under reducing conditions, and the overall configuration of the reduced particle shown in Figure 3 (reduced Cu decorated with ZnO) is representative of the particles seen with in situ TEM in reducing atmosphere. Only the particle shown in Figure 4 was imaged with high magnification under both reducing and oxidizing conditions. 88 particles in the same area were imaged with low magnification under both reducing and oxidizing conditions (Figure S2).

Domains of crystalline Cu, CuO, Cu<sub>2</sub>O, and ZnO were identified in high-resolution TEM images using for each phase the unique lattice spacings as described in Table 1. Annular

**Table 1. Crystal Structures and Corresponding Lattice Planes (*hkl*)<sup>a</sup>**

crystal phase	( <i>hkl</i> )	<i>d</i> (Å)
CuO	(-202)	1.87
	(-112)	1.96
Cu <sub>2</sub> O	(011)	3.02
Cu	(200)	1.81
	(111)	2.08
ZnO	(002)	2.60
	(010)	2.81

<sup>a</sup>Crystal structures from ICSD.<sup>49</sup>

masks in the FFT included a region of  $\pm 1/0.015$   $\text{\AA}^{-1}$  centered on the corresponding lattice vector. Masking of the FFT employed an edge smoothing. The edge smoothing used a circular averaging filter with a size of 3 pixels. Color coding was implemented in a Matlab script.

## ■ ASSOCIATED CONTENT

### Supporting Information

Overview XPS scan as well as details on reduction experiment in atomic hydrogen. This material is available free of charge via the Internet at <http://pubs.acs.org>.

## ■ AUTHOR INFORMATION

### Corresponding Authors

\*E-mail: [sth@topsoe.dk](mailto:sth@topsoe.dk).

\*E-mail: [Jane@fysik.dtu.dk](mailto:Jane@fysik.dtu.dk).

### Notes

The authors declare no competing financial interest.

## ■ ACKNOWLEDGMENTS

The authors gratefully acknowledge The Danish National Research Foundation's Center for Individual Nanoparticle Functionality, supported by the Danish National Research Foundation (DNRF54). The authors acknowledge S. B. Vendelbo for fruitful discussions regarding coloring of TEM images.

## ■ ABBREVIATIONS

UHV, ultra high vacuum; XPS, X-ray photoelectron spectroscopy; TEM, transmission electron microscopy

## ■ REFERENCES

- (1) Li, Y.; Somorjai, G. A. Nanoscale Advances in Catalysis and Energy Applications. *Nano Lett.* **2010**, *10*, 2289–2295.
- (2) Nørskov, J. K.; Bligaard, T.; Hvolbæk, B.; Abild-Pedersen, F.; Chorkendorff, I.; Christensen, C. H. The Nature of the Active Site in Heterogeneous Metal Catalysis. *Chem. Soc. Rev.* **2008**, *37*, 2163–2171.
- (3) Bell, A. T. The Impact of Nanoscience on Heterogeneous Catalysis. *Science* **2003**, *299*, 1688–1691.
- (4) Burda, C.; Chen, X.; Narayanan, R.; El-Sayed, M. A. Chemistry and Properties of Nanocrystals of Different Shapes. *Chem. Rev.* **2005**, *105*, 1025–1102.
- (5) An, K.; Somorjai, G. A. Size and Shape Control of Metal Nanoparticles for Reaction Selectivity in Catalysis. *ChemCatChem* **2012**, *4*, 1512–1524.
- (6) Xia, Y.; Xiong, Y.; Lim, B.; Skrabalak, S. E. Shape-Controlled Synthesis of Metal Nanocrystals: Simple Chemistry Meets Complex Physics? *Angew. Chem., Int. Ed.* **2009**, *48*, 60–103.
- (7) Cuenya, B. R. Synthesis and Catalytic Properties of Metal Nanoparticles: Size, Shape, Support, Composition, and Oxidation State Effects. *Thin Solid Films* **2010**, *518*, 3127–3150.
- (8) Topsøe, H. Developments in Operando Studies and in Situ Characterization of Heterogeneous Catalysts. *J. Catal.* **2003**, *216*, 155–164.
- (9) Tao, F. F.; Salmeron, M. In Situ Studies of Chemistry and Structure of Materials in Reactive Environments. *Science* **2011**, *331*, 171–174.
- (10) Porsgaard, S.; Merte, L. R.; Ono, L. K.; Beharid, F.; Matos, J.; Helveg, S.; Salmeron, M.; Roldan Cuenya, B.; Besenbacher, F. Stability of Platinum Nanoparticles Supported on SiO<sub>2</sub>/Si(111): A High-Pressure X-Ray Photoelectron Spectroscopy Study. *ACS Nano* **2012**, *6*, 10743–10749.
- (11) Hansen, J. B.; Nielsen, P. E. H. *Handbook of Heterogeneous Catalysis*; Ertl, G., Knözinger, H., Schuth, F., Weitkamp, J., Eds.; Wiley-VCH Verlag GmbH & Co. KGaA: Weinheim, Germany, 2008; pp 2920–2949.
- (12) Clausen, B. S.; Schiøtz, J.; Gråbæk, L.; Ovesen, C. V.; Jacobsen, K. W.; Nørskov, J. K.; Topsøe, H. Wetting/ Non-Wetting Phenomena during Catalysis: Evidence from in Situ on-Line EXAFS Studies of Cu-Based Catalysts. *Top. Catal.* **1994**, *1*, 367–376.
- (13) Ovesen, C. V.; Clausen, B. S.; Schiøtz, J.; Stoltze, P.; Topsøe, H.; Nørskov, J. K. Kinetic Implications of Dynamical Changes in Catalyst Morphology During Methanol Synthesis Over Cu/ZnO Catalysts. *J. Catal.* **1997**, *168*, 133–142.
- (14) Grunwaldt, J.-D. D.; Molenbroek, A. M.; Topsøe, N. Y.; Topsøe, H.; Clausen, B. S. In Situ Investigations of Structural Changes in Cu/ZnO Catalysts. *J. Catal.* **2000**, *194*, 452–460.
- (15) Hansen, P. L.; Wagner, J. B.; Helveg, S.; Rostrup-Nielsen, J. R.; Clausen, B. S.; Topsøe, H. Atom-Resolved Imaging of Dynamic Shape Changes in Supported Copper Nanocrystals. *Science* **2002**, *295*, 2053–2055.
- (16) Vesborg, P. C. K.; Chorkendorff, I.; Knudsen, I.; Balmes, O.; Nerlov, J.; Molenbroek, A. M.; Clausen, B. S.; Helveg, S. Transient Behavior of Cu/ZnO-Based Methanol Synthesis Catalysts. *J. Catal.* **2009**, *262*, 65–72.
- (17) Viitanen, M. M.; Jansen, W. P. A.; Welzenis, R. G.; Van; Brongersma, H. H.; Brands, D. S.; Poels, E. K.; Blik, A. Cu/ZnO and Cu/ZnO/SiO<sub>2</sub> Catalysts Studied by Low-Energy Ion Scattering. *J. Phys. Chem. B* **1999**, *103*, 6025–6029.
- (18) Behrens, M.; Studt, F.; Kasatkin, I.; Kühn, S.; Hävecker, M.; Abild-Pedersen, F.; Zander, S.; Girgsdies, F.; Kurr, P.; Knief, B.-L.; et al. The Active Site of Methanol Synthesis Over Cu/ZnO/Al<sub>2</sub>O<sub>3</sub> Industrial Catalysts. *Science* **2012**, *336*, 893–897.
- (19) Fujitani, T.; Nakamura, J. The Effect of ZnO in Methanol Synthesis Catalysts on Cu Dispersion and the Specific Activity. *Catal. Lett.* **1998**, *56*, 119–124.
- (20) Topsøe, N.; Topsøe, H. On the Nature of Surface Structural Changes in Cu/ZnO Methanol Synthesis Catalysts. *Top. Catal.* **1999**, *8*, 267–270.

- (21) Naumann d'Alnoncourt, R. N.; Kurtz, M.; Wilmer, H.; Löffler, E.; Hagen, V.; Shen, J.; Muhler, M. The Influence of ZnO on the Differential Heat of Adsorption of CO on Cu Catalysts: A Microcalorimetric Study. *J. Catal.* **2003**, *220*, 249–253.
- (22) Günter, M. M.; Ressler, T.; Bems, B.; Büscher, C.; Genger, T.; Hinrichsen, O.; Muhler, M.; Schlögl, R. Implication of the Microstructure of Binary Cu/ZnO Catalysts for Their Catalytic Activity in Methanol Synthesis. *Catal. Lett.* **2001**, *71*, 37–44.
- (23) Kasatkin, I.; Kurr, P.; Kniep, B.; Trunschke, A.; Schlögl, R. Role of Lattice Strain and Defects in Copper Particles on the Activity of Cu/ZnO/Al<sub>2</sub>O<sub>3</sub> Catalysts for Methanol Synthesis. *Angew. Chem.* **2007**, *119*, 7465–7468.
- (24) Chinchin, G. C.; Hay, C. M.; Vandervell, H. D.; Waugh, K. C. The Measurement of Copper Surface Areas by Reactive Frontal Chromatography. *J. Catal.* **1987**, *103*, 79–86.
- (25) Muhler, M.; Nielsen, L. P.; Törnqvist, E.; Clausen, B. S.; Topsøe, H. Temperature-Programmed Desorption of H<sub>2</sub> as a Tool to Determine Metal Surface Areas of Cu Catalysts. *Catal. Lett.* **1992**, *14*, 241–249.
- (26) Kuld, S.; Conradsen, C.; Moses, P. G.; Chorkendorff, I.; Sehested, J. Quantification of Zinc Atoms in a Surface Alloy on Copper in an Industrial-Type Methanol Synthesis Catalyst. *Angew. Chem., Int. Ed.* **2014**, *53*, 5941–5945.
- (27) Fichtl, M. B.; Schumann, J.; Kasatkin, I.; Jacobsen, N.; Behrens, M.; Schlögl, R.; Muhler, M.; Hinrichsen, O. Counting of Oxygen Defects Versus Metal Surface Sites in Methanol Synthesis Catalysts by Different Probe Molecules. *Angew. Chem., Int. Ed.* **2014**, *53*, 7043–7047.
- (28) Spencer, M. S. The Role of Zinc Oxide in Cu/ZnO Catalysts for Methanol Synthesis and the Water–gas Shift Reaction. *Top. Catal.* **1999**, *8*, 259–266.
- (29) Baltes, C.; Vukojevic, S.; Schuth, F. Correlations Between Synthesis, Precursor, and Catalyst Structure and Activity of a Large Set of CuO/ZnO/Al<sub>2</sub>O<sub>3</sub> Catalysts for Methanol Synthesis. *J. Catal.* **2008**, *258*, 334–344.
- (30) Behrens, M. Meso- and Nano-Structuring of Industrial Cu/ZnO/(Al<sub>2</sub>O<sub>3</sub>) Catalysts. *J. Catal.* **2009**, *267*, 24–29.
- (31) Sloczyński, J. Antisintering Criteria in the Metal–spacer Catalytic System. *Chem. Eng. Sci.* **1994**, *49*, 115–121.
- (32) Haberland, H.; Karrais, M.; Mall, M.; Thurner, T. Thin Films from Energetic Cluster Impact: A Feasibility Study. *J. Vac. Sci. Technol. A* **1992**, *10*, 3266.
- (33) Nielsen, R. M.; Murphy, S.; Streb, C.; Johansson, M.; Chorkendorff, I.; Nielsen, J. H. The Morphology of Mass Selected Ruthenium Nanoparticles from a Magnetron-Sputter Gas-Aggregation Source. *J. Nanoparticle Res.* **2009**, *12*, 1249–1262.
- (34) Tahir, D.; Tougaard, S. Electronic and Optical Properties of Cu, CuO and Cu<sub>2</sub>O Studied by Electron Spectroscopy. *J. Phys.: Condens. Matter* **2012**, *24*, 175002.
- (35) Wagner, J. B.; Hansen, P. L.; Molenbroek, A. M.; Topsøe, H.; Clausen, B. S.; Helveg, S. In Situ Electron Energy Loss Spectroscopy Studies of Gas-Dependent Metal–Support Interactions in Cu/ZnO Catalysts. *J. Phys. Chem. B* **2003**, *107*, 7753–7758.
- (36) Jansen, W. P. A.; Beckers, J.; Heuvel, J. C. v. d.; Gon, A. W. D. v. d.; Blik, A.; Brongersma, H. H. Dynamic Behavior of the Surface Structure of Cu/ZnO/SiO<sub>2</sub> Catalysts. *J. Catal.* **2002**, *210*, 229–236.
- (37) Nakamura, R.; Tokozakura, D.; Nakajima, H.; Lee, J.-G.; Mori, H. Hollow Oxide Formation by Oxidation of Al and Cu Nanoparticles. *J. Appl. Phys.* **2007**, *101*, 074303.
- (38) Rasmussen, D. B.; Janssens, T. V. W.; Temel, B.; Bligaard, T.; Hinnemann, B.; Helveg, S.; Sehested, J. The Energies of Formation and Mobilities of Cu Surface Species on Cu and ZnO in Methanol and Water Gas Shift Atmospheres Studied by DFT. *J. Catal.* **2012**, *293*, 205–214.
- (39) Helveg, S.; Lauritsen, J.; Lægsgaard, E.; Stensgaard, I.; Nørskov, J.; Clausen, B.; Topsøe, H.; Besenbacher, F. Atomic-Scale Structure of Single-Layer MoS<sub>2</sub> Nanoclusters. *Phys. Rev. Lett.* **2000**, *84*, 951–954.
- (40) Fu, S. S.; Somorjai, G. A. Zinc Oxide and Oxygen Overlayers on Cu(110): A Model for CuZnO Catalysts. *Appl. Surf. Sci.* **1991**, *48–49*, 93–103.
- (41) Kowalczyk, S.; Pollak, R.; McFeely, F.; Ley, L.; Shirley, D. L<sub>2,3</sub>M<sub>45</sub>M<sub>45</sub> Auger Spectra of Metallic Copper and Zinc: Theory and Experiment. *Phys. Rev. B* **1973**, *8*, 2387–2391.
- (42) Diebold, U. The Surface Science of Titanium Dioxide. *Surf. Sci. Rep.* **2003**, *48*, 53–229.
- (43) Michelsen, H. A.; Auerbach, D. J. A Critical Examination of Data on the Dissociative Adsorption and Associative Desorption of Hydrogen at Copper Surfaces. *J. Chem. Phys.* **1991**, *94*, 7502.
- (44) Nielsen, R. M.; Murphy, S.; Streb, C.; Johansson, M.; Nielsen, J. H.; Chorkendorff, I. A Comparative STM Study of Ru Nanoparticles Deposited on HOPG by Mass-Selected Gas Aggregation Versus Thermal Evaporation. *Surf. Sci.* **2009**, *603*, 3420–3430.
- (45) Murphy, S.; Nielsen, R. M.; Streb, C. E.; Johansson, M.; Nielsen, J. H. Catalytic Oxidation of Graphite by Mass-Selected Ruthenium Nanoparticles. *Carbon* **2011**, *49*, 376–385.
- (46) Jinschek, J. R.; Helveg, S. Image Resolution and Sensitivity in an Environmental Transmission Electron Microscope. *Micron* **2012**, *43*, 1156–1168.
- (47) Kisielowski, C.; Wang, L.-W.; Specht, P.; Calderon, H. A.; Barton, B.; Jiang, B.; Kang, J. H.; Cieslinski, R. Real-Time Sub-Ångstrom Imaging of Reversible and Irreversible Conformations in Rhodium Catalysts and Graphene. *Phys. Rev. B* **2013**, *88*, 024305.
- (48) Russ, J. C. *The Image Processing Handbook*, 6th ed.; CRC Press: Boca Raton, FL, 2011; p 885.
- (49) Fiz. Inorganic crystal structure database ICSD <http://icsd.fiz-karlsruhe.de>; accessed May 20, 2014.

## Revealing the formation of copper nanoparticles from a homogeneous solid precursor by electron microscopy

Roy van den Berg, Christian F. Elkjær, Cedric J. Gommès, Ib Chorkendorff, Jens Sehested, Petra E. de Jongh, Krijn P. de Jong, Stig Helveg.

*Submitted*

Supplementary information and supplementary movies will be available online once the paper is published.

# Revealing the formation of copper nanoparticles from a homogeneous solid precursor by electron microscopy

Roy van den Berg<sup>1</sup>, Christian F. Elkjaer<sup>2,3</sup>, Cedric J. Gommès<sup>4</sup>, Ib Chorkendorff<sup>3</sup>, Jens Sehested<sup>2</sup>, Petra E. de Jongh<sup>1</sup>, Krijn P. de Jong<sup>1</sup>, Stig Helveg<sup>2,\*</sup>

<sup>1</sup> Inorganic Chemistry and Catalysis, Debye Institute for Nanomaterials Science, Utrecht University, Universiteitsweg 99, Utrecht, Netherlands

<sup>2</sup> Haldor Topsoe A/S, Haldor Topsøes Allé 1, DK-2800 Kgs. Lyngby, Denmark

<sup>3</sup> Department of Physics, Technical University of Denmark, Fysikvej 312, DK-2800 Kgs. Lyngby, Denmark

<sup>4</sup> Department of Chemical Engineering, University of Liège, Allée du 6 août 3, B-4000 Liège, Belgium

*Transmission electron microscopy, in situ, copper, nanoparticles, growth mechanism, kinetic model*

---

**ABSTRACT:** The understanding of processes leading to the formation of nanometer-sized particles is important for tailoring of their size, shape and location. The growth mechanisms and kinetics of nanoparticles from solid precursors are, however, often poorly described. Here we examine the formation of copper nanoparticles on a silica support during the reduction of copper phyllosilicate by H<sub>2</sub> by means of transmission electron microscopy (TEM). Specifically, time-lapsed TEM image series acquired of the material during the reduction provide a direct visualization of the growth dynamics of an ensemble of individual nanoparticles and enable a quantitative evaluation of the nucleation and growth of the nanoparticles. This quantitative information is compared with kinetic models and found to be best described by a nucleation-and-growth scenario involving autocatalytic reduction of the copper phyllosilicate followed by diffusion-limited or reaction-limited growth of the copper nanoparticles. In this way, *in situ* observations made by electron microscopy provide mechanistic and kinetic insights into the formation of metallic nanoparticles, essential for the rational design of nanomaterials.

---

## INTRODUCTION

Nanometer-sized particles provide electronic, optical and catalytic properties that strongly depend on their size, shape and spatial arrangement. The synthesis of nanoparticles with predefined structural characteristics has therefore become an important research theme. Synthesis procedures include the aggregation of atomic species to form colloidal nanoparticles in liquid and the transformation of solid precursors by gas phase treatments to form supported nanoparticles.<sup>1</sup> In the latter case, precursors often consist of a metal salt impregnated on a support or of a co-precipitate of the metal oxide and support material. This approach is particularly beneficial for preparing nanoparticles at large scales for e.g. industrial catalytic processes.<sup>1a-c</sup> Despite the significant efforts devoted to optimize procedures for transforming solid precursors into supported nanoparticles, a fundamental understanding of the particle growth mechanisms and their relation with the growth kinetics is often limited.<sup>2</sup> As growth processes involve atom exchange at or across solid surfaces, observations made *in situ* at high-spatial resolution would be beneficial for elucidating nanoparticle growth mechanisms.

In recent years, transmission electron microscopy (TEM) has become a powerful tool for visualizing nanoparticles at atomic-resolution.<sup>3</sup> Studies of nanoparticles during exposure to gas or liquid environments are, however, hampered by the small mean free path of the electron beam in dense media. The introduction of differentially pumped vacuum systems and closed electron-transparent cells provides a means to confine gas or liquid phases to the vicinity of the sample in the transmission electron microscope.<sup>4</sup> Hereby, TEM can be used to monitor nanoparticles in reactive environments by the acquisition of time-lapsed image series. This approach has resulted in new insights into the dynamical formation of nanoparticles in the liquid phase,<sup>5</sup> and, by gas phase treatment of impregnated support materials, in the solid phase.<sup>6</sup> However, the way in which nanoparticles grow in the solid phase by gas phase treatment of co-precipitated precursors has not been addressed so far although the homogeneity of these materials offer the possibility to obtain mechanistic and kinetic information that can be translated to large scale material synthesis.

Here we use TEM to examine the growth of an ensemble of Cu nanoparticles on SiO<sub>2</sub>, which results in a material that catalyzes the hydrogenation of carbon-oxygen

bonds.<sup>7</sup> The nanoparticles and the silica support are formed in the electron microscope by reduction in H<sub>2</sub> of copper phyllosilicate, which is a precipitated solid precursor that consists of platelets with a homogeneous distribution of Cu<sup>2+</sup>.<sup>8</sup> To ensure that the TEM observations reflect processes inherent to the reduction treatment, the impact of the electron beam on the process was characterized and a beam-insensitive imaging scheme developed. By employing this optimized imaging scheme, time-resolved TEM images were acquired during the formation of the copper nanoparticles which enabled the extraction of quantitative information about the nucleation and growth of individual copper nanoparticles. This dynamic information is compared to predictions made by kinetic models which allowed deriving a mechanism for the nanoparticle formation.

## EXPERIMENTAL SECTION

### Synthesis of copper phyllosilicate

Copper phyllosilicate can be synthesized by deposition precipitation of copper nitrate using ammonia evaporation<sup>7a, 7d, 9</sup> or urea hydrolysis<sup>8b</sup> and by using selective adsorption of [Cu(NH<sub>3</sub>)<sub>4</sub>]<sup>2+</sup> on SiO<sub>2</sub>.<sup>8a</sup> However, both deposition-precipitation and selective adsorption often lead to heterogeneous materials comprising unreacted silica, copper phyllosilicate, and other copper species like copper(II) oxide.<sup>8</sup> To obtain only the copper phyllosilicate phase for our material, the homogeneous deposition-precipitation procedure of van der Grift and coworkers was followed by a hydrothermal treatment.<sup>8b</sup>

Specifically, a mass of 20.1 g LUDOX-AS 30 (Sigma-Aldrich), 16.1 g Cu(NO<sub>3</sub>)<sub>2</sub>·3H<sub>2</sub>O (Acros Organics, 99% for analysis) and 12.1 g Urea (Acros Organics, 99.5% for analysis) were added to 1.7 L of demineralized water in a 2 L reaction vessel. The pH was adjusted to 2-3 with a few drops of HNO<sub>3</sub> (Merck, 65% for analysis) to prevent premature hydrolysis of copper nitrate. The suspension was then heated to 90 °C in 1 h under stirring. At 90 °C, hydrolysis of urea led to an increase in pH resulting in the precipitation of Cu<sub>2</sub>(NO<sub>3</sub>)(OH)<sub>3</sub> and the formation of the [Cu(OH)<sub>2</sub>(H<sub>2</sub>O)<sub>4</sub>]<sup>0</sup> complex in solution. The well-stirred suspension was kept at 90 °C for 7 days to allow recrystallization of precipitated copper and silica, which resulted in the formation of copper phyllosilicate. The precipitate was obtained by hot filtration of the suspension. Thereafter, the precipitate was washed three times at room temperature with demineralized water, filtered and dried overnight at 60 °C. The yield was about 10 g, which is close to the intended dry copper phyllosilicate weight. A relatively high copper to silicon atomic ratio of 0.66 was chosen, corresponding to 41 wt% copper in the final Cu/SiO<sub>2</sub> material. Lower copper loadings resulted in partly unreacted silica and a copper loading above 45 wt% resulted in the presence of copper oxide particles.<sup>7b</sup>

### Reduction in a plug-flow reactor

A mass of 0.3 g of the as-prepared copper phyllosilicate was reduced in a plug-flow reactor (diameter 1 cm) at 250 °C (heating rate 2 °C/min) in a flow of 30 mL/min of 20% H<sub>2</sub> in Ar for 2½ h. After the reduction treatment, the reduced sample was passivated for 15 min at room tempera-

ture by slowly exposing the sample to a diluted air/N<sub>2</sub> flow by creating a small leak in the flow supply system. The sample was stored in a glove box containing an argon atmosphere.

### Characterization

X-ray diffraction was performed with a Bruker-Nonius D8 Advance X-ray diffractometer using Co-K<sub>α1,2</sub> (λ = 1.79026 Å) radiation. For the reduced sample, the specimen holder was loaded in the glovebox and subsequently sealed to prevent exposure to air. Diffractograms of the material before and after reduction were obtained at room temperature from 20° to 70° (2θ). N<sub>2</sub> physisorption measurements were performed at -196 °C, using a Micromeritics Tristar 3000 apparatus. The BET method was used to calculate the specific surface area. Energy dispersive X-ray (EDX) spectroscopy was performed using a Technai 20FEG (FEI) electron microscope equipped with a field emission gun and with an EDAX Super Ultra Thin Window EDX detector. The as-prepared copper phyllosilicate was dispersed on a carbon coated Ni TEM grid (Agar 162 200 Mesh Ni) and this sample was introduced into the microscope using a low-background sample holder (Philips) with a 0.1 mm thick Be specimen support film and a Be ring to clamp the grid. EDX spectra were acquired of 22 regions of the sample using an electron beam diameter of 100 to 500 nm and of 6 regions by scanning a 0.3 – 1.2 nm wide electron beam along a line of 100 to 500 nm in length. The EDX spectra were quantified using the Tecnai Imaging and Analysis (TIA) software by using a detector correction of 0.977 and 0.997 and a k-factor of 1.000 and 1.757 for Si and Cu, respectively, on the integrated intensities of the Si-K and Cu-K signal. Temperature programmed reduction (TPR) was performed using an Autochem II ASAP 2910 from micromeritics. The H<sub>2</sub> concentration during the experiment was measured with a thermal conductivity detector. About 0.05 g copper phyllosilicate was placed on top of a quartz wool bed in a glass reactor tube. The sample was heated to 500 °C (5 °C/min) under a flow of 5% H<sub>2</sub>/Ar. Thermal gravimetric analysis (TGA) was performed with a Perkin-Elmer Pyris 1 apparatus. About 2.5 mg of copper phyllosilicate was heated to 500 °C under a flow of 2.5 mL/min 5% H<sub>2</sub>/Ar.

### Transmission electron microscopy

*In situ* observations by TEM were made using an image-aberration corrected Titan 80-300 ETEM (FEI Company).<sup>10</sup> The microscope was operated at a primary electron energy of 300 keV. Prior to the experiment, the image-aberration corrector was tuned using a cross-grating (Agar S106) and the spherical aberration coefficient was set in the range of -10 to -20 μm. All quoted electron dose-rates were measured using the microscope's fluorescent screen. TEM grids were placed in a heating holder (Gatan model 628) for introduction into the electron microscope. TEM images were acquired with a bottom-mounted 2k × 2k charged-coupled device (CCD) camera (Gatan US1000) and with the projection system set to an effective CCD pixel size between 0.37 and 0.56 nm.

The reduced Cu/SiO<sub>2</sub> was used as reference. A sample was prepared by grinding the powder and dispersing it on a stainless steel grid. The sample was re-reduced in 1 mbar H<sub>2</sub> at 250 °C (heating rate 30 °C/min) for 45 min. Under these conditions, TEM images of the sample were acquired using an electron dose-rate of 10 e<sup>-</sup>/Å<sup>2</sup>s).

The as-prepared copper phyllosilicate was studied in three types of experiments in the electron microscope to address the effect of electron illumination and to establish conditions of negligible impact of the electron beam on the formation of copper particles. Specifically, experiment E1 addresses the effect of thermal reduction in H<sub>2</sub> without any electron beam illumination, experiment E2 addresses the effect of illuminating the sample in vacuum prior to a reduction treatment, and experiment E3 addresses the effect of the electron beam in H<sub>2</sub> with no thermally induced particle growth.

For the experiments E1-E3, samples of as-prepared copper phyllosilicate were prepared by grinding and dispersing the powder on stainless steel grids. Firstly, in experiment E1, separate samples were exposed to 1 mbar H<sub>2</sub> at 150 °C (4h), 200 °C (½ h), 250 °C (3h) and 280 °C (1 ¼ h) and subsequently imaged at the respective conditions or at base vacuum (1.9 · 10<sup>-6</sup> mbar) at room temperature. Secondly, in experiment E2, one sample was kept at base vacuum (2.3 · 10<sup>-5</sup> mbar) at room temperature and five distinct regions of copper phyllosilicate were illuminated at electron dose-rates of 1, 5, 10, 20 and 100 e<sup>-</sup>/Å<sup>2</sup>s for a total of ca. 2 min. Subsequently, the sample was exposed to 1 mbar H<sub>2</sub>, heated at 30 °C/min to 280 °C and held at that temperature for 75 min before it was heated further at 30 °C/min to 310 °C at which it was held for 30 min. Afterwards, the sample was cooled to room temperature in H<sub>2</sub> and the microscope was evacuated. Finally, the five areas were imaged in vacuum with a dose-rate of 20 e<sup>-</sup>/Å<sup>2</sup>s). In addition, ten previously unilluminated regions were imaged as reference locations. Thirdly, in experiment E3, one sample was exposed to 1 mbar H<sub>2</sub> at 150 °C. Five distinct copper phyllosilicate regions were continuously illuminated at an electron dose-rate of 1, 5, 10, 20 or 100 e<sup>-</sup>/Å<sup>2</sup>s, respectively, for 20 min while time-resolved series of TEM images were recorded. After the acquisition of these series, several distinct and previously unilluminated regions were located at 150 °C at base vacuum (1.4 · 10<sup>-6</sup> mbar) and TEM images were acquired at an electron dose-rate of 10 e<sup>-</sup>/Å<sup>2</sup>s).

The information obtained from experiments E1-E3 enables an experimental procedure for the beam-insensitive experiments to be established (Figure 1). For these experiments, two samples were prepared by grinding and dispersing the as-prepared copper phyllosilicate on gold grids. In the microscope, the samples were exposed to 1 mbar H<sub>2</sub> and heated at 30 °C/min to 200 °C. At these conditions, regions of interest were identified with an electron dose-rate of 0.05 e<sup>-</sup>/Å<sup>2</sup>s) and maximum illumination time of one minute per region. This short illumination prior to reduction had no detectable effect on the reduction process, as will be consistently shown in the Results & Discussion section. After 20 min, thermal drift of the heating holder subsided and the samples were further

heated to 280 °C (heating rate 30 °C/min). At those conditions, time-lapsed TEM images were recorded with an electron dose-rate of 1 e<sup>-</sup>/Å<sup>2</sup>s). Specifically, by operating the projection system corresponding to a CCD camera pixel size of 0.56 nm and a CCD illumination time of 1 s, the electron beam penetrating only the gas phase creates on average about 32 electrons per pixel with a standard deviation of about 8 electrons, resulting in a signal-to-noise ratio (SNR) of 4. Due to this low SNR, particles were only distinguishable in the present phyllosilicate materials at diameters larger than ca. 3.4 nm (6 pixels). In comparison the sample reduced in the plug-flow reactor was examined by TEM at illumination conditions with a corresponding SNR of about 25. It was shown that the particle size distribution for this sample is similar to the final distribution obtained in the electron microscope with a SNR of about 20 and that the lower cutoff particle size was 3 nm. Hence, the illumination conditions employed during the reduction process were sufficient to monitor the growth of all the particles.

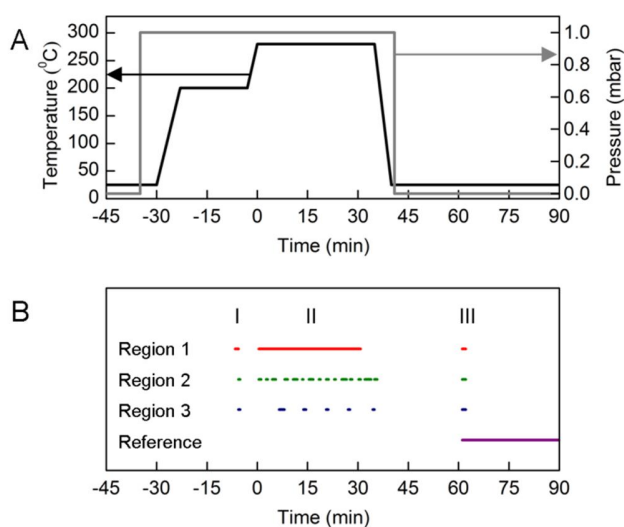


Figure 1. Procedure for TEM image acquisition during H<sub>2</sub> reduction of the copper phyllosilicate. (A) Temporal profiles of temperature and H<sub>2</sub> pressure in the experiment. Time t = 0 min corresponds to the time at which the temperature reaches 280 °C. (B) Scheme for electron illumination. The electron dose-rate: 0.05 e<sup>-</sup>/Å<sup>2</sup>s) (before reduction (I)), 1 e<sup>-</sup>/Å<sup>2</sup>s) (during reduction (II)) and 5 e<sup>-</sup>/Å<sup>2</sup>s) (after reduction (III)). During reduction, region 1 (red) was continuously illuminated and Region 2 (green) and Region 3 (blue) were intermittently illuminated at time intervals of ca. 2 min and 6 min, respectively. After reduction, TEM images were acquired of regions 1-3 and at previously unilluminated regions (purple).

The time-lapsed images were acquired as outlined in the scheme in Figure 1: In one experiment, one region (Region 1) was continuously illuminated and images acquired with a CCD illumination time of 1 s and a frame rate of 1 per 5 s. In a second experiment, two distinct regions (Region 2 and Region 3), outside of each other's illuminated areas, were illuminated at intervals of ca. 2 and 6 min, respectively. The illumination persisted for approximately 45 seconds, for locating and focusing the sample region and subsequent image acquisition (2 s CCD

illumination, see Figure 1B for the exact times each region was illuminated). In the intervening periods between successive electron illuminations, the electron beam was blanked off or moved to the other location. With this illumination scheme, the accumulated electron dose for Region 1, 2 and 3 was 1735, 620 and 230  $e^-/\text{\AA}^2$ , respectively. After 30 min at 1 mbar  $H_2$  at 280 °C the sample was cooled to room temperature and the microscope was evacuated to its base vacuum ( $1.9 \cdot 10^{-6}$  mbar). Under those conditions, TEM images were acquired of Region 1-3 as well as reference areas on the two samples at 5  $e^-/(\text{\AA}^2s)$ , which did not lead to any detectable changes to the sample.

## Image analysis

The time-resolved TEM image series provide information about the time for the first visual appearance of the copper particles and about the subsequent evolution of the copper particle size. For the different experiments, this information is evaluated by selecting 20 or 25 visually distinguishable particles in the last image of a time-series of images. The individual particles were tracked backwards in time in the earlier acquired images until the image of their first visual appearance. This tracking was possible because all of the particles remained immobile. In each image, the particle diameter (referred to as size) is determined by measuring the projected area manually with ImageJ and assuming a spherical particle shape. Particle size distributions (PSDs) were obtained to compare the size of the copper particles after the different experiments. PSDs can appear visually distinct while others can appear similar. To provide a quantitative assessment of the similarity of PSDs that considers the statistical significance of the limited number of particles in the distributions, the ANOVA method was used to determine the probability that two different PSDs had the same mean particle size.<sup>11</sup> With this method, the PSDs were considered significantly different, if the probability was lower than 2.5% ( $p_{(\text{same mean size})} < 0.025$ ). To evaluate the progress of the particle formation, the size evolution of the particles should be combined with the evolution of the particle density. A simplistic measure, the "stage of particle evolution", quantifies the size and density evolution in a combined way by considering at each time the average size of the same 20 or 25 copper particles, including the particle size of 0 nm for particles prior to their first appearance.

## RESULTS & DISCUSSION

### Copper phyllosilicate

The composition and structure of the as-prepared copper phyllosilicate was examined by several experimental techniques. X-ray diffraction shows that the as-prepared copper phyllosilicate mainly consisted of an amorphous phase (Figure 2A, blue), in agreement with earlier observations.<sup>8a</sup> Weak diffraction peaks reveal a minor crystalline phase corresponding to chrysocolla ( $Cu_2Si_2O_5(OH)_2 \cdot nH_2O$ ), which is a form of copper phyllosilicate.<sup>8</sup> Diffraction peaks characteristic for silica or other copper species were absent. The reaction between copper and silica was furthermore confirmed by the BET surface

area, which increased from 100  $m^2/g$  for colloidal silica to 550  $m^2/g$  for the as-prepared copper phyllosilicate, in agreement with a previous report.<sup>8b</sup> Moreover, TEM images as in Figure 2B reveal that the material consisted of platelets with a width and thickness in the range of 5 to 20 nm and a length of up to 100 nm. The anisotropic morphology was confirmed by a  $N_2$  physisorption profile that is typical for aggregates of platelets (Figure 2C).<sup>8b, 9</sup> The TEM images did not show any particles with a spherical morphology as the original colloidal silica spheres and therefore also indicate a complete reaction with copper. The chemical composition across the as-prepared copper phyllosilicate was addressed by EDX. Spot analysis of more than 20 regions of 100-500 nm in diameter revealed a Cu/Si atomic ratio of 0.59 with a standard deviation of 0.09, and 6 EDX line-scans of 100-500 nm in length crossing several single platelets revealed a Cu/Si ratio between 0.50 and 0.75 for all points. Thus, the copper loading was very homogeneous throughout the as-prepared copper phyllosilicate with a composition of Cu/Si that agrees with the nominal ratio of 0.66.

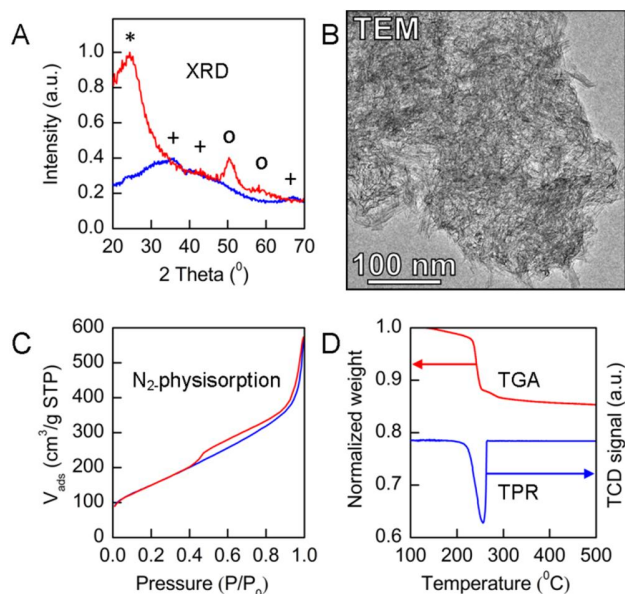


Figure 2. Characterization of the copper phyllosilicate. (A) X-ray diffractograms of the material before (blue) and after (red) reduction in the plug-flow reactor. The peak positions correspond to chrysocolla (+), silica (\*) and metallic copper (o). (B) A TEM image of the as-prepared copper phyllosilicate. (C)  $N_2$  physisorption of the as-prepared copper phyllosilicate (adsorption blue, desorption red). (D) TPR (blue) and TGA (red) of copper phyllosilicate in  $H_2/Ar$  flow.

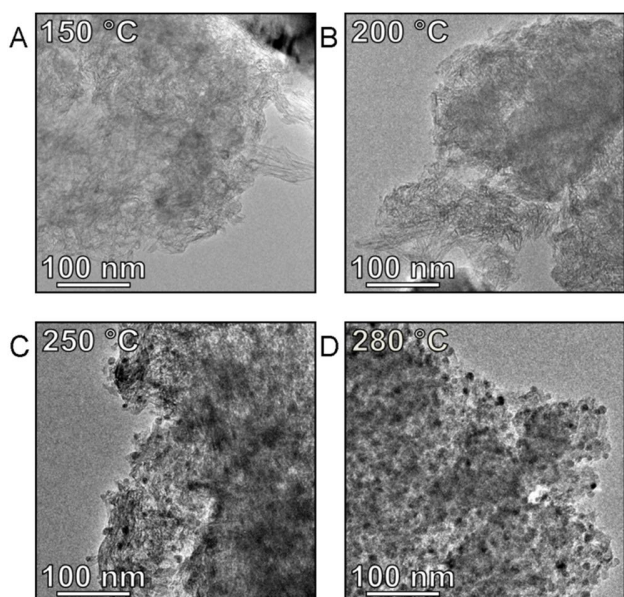


Figure 3. TEM images of copper phyllosilicate after exposure to 1 mbar  $H_2$  at different temperatures and reaction conditions in the electron microscope. Reduction conditions: (A) 150 °C, 4 hours (B) 200 °C, 30 min (C) 250 °C, 30 min and (D) 280 °C, 30 min. TEM image acquisition (A)-(B) *in situ* at 1 mbar  $H_2$  at 150 °C and (C)-(D) at vacuum at room temperature.

### Reduction of copper phyllosilicate

First, the reduction of copper phyllosilicate was addressed with TPR and TGA (Figure 2D). In TPR, the hydrogen consumption started at 220 °C, peaked at 255 °C and ceased above 270 °C. The amount of hydrogen consumed by this reduction was 140  $cm^3$  (STP)/g. The weight loss during the reduction up to 500 °C amounted to 15%, as determined by TGA. A minimum weight loss of 9% was expected based upon the loss of oxygen atoms acting as counter ions for the  $Cu^{2+}$ . The additional 6% is presumably due to crystal water in the copper phyllosilicate. Taking into account the weight loss during reduction, the amount of  $H_2$  consumed corresponded to the reduction of 40 wt%  $Cu^{2+}$  to  $Cu^0$ . Since the intended copper loading was ca. 41 wt%, it is concluded that copper phyllosilicate was fully reduced to metallic copper between 220 and 270 °C.<sup>7d, 9</sup> Consistently, XRD showed the presence of crystalline metallic Cu and silica after reduction at 250 °C in a plug-flow reactor with 20%  $H_2$  in Ar for 2.5 hours (Figure 2A, red).

Next, the reduction was examined in the electron microscope by exposing the copper phyllosilicate to 1 mbar  $H_2$  at different temperatures (experiment E1). Figure 3 shows TEM images of four different samples acquired after reduction for 4 hours at 150 °C (A), and for 30 minutes at 200 °C (B), 250 °C (C) and 280 °C (D). That is, the TEM images show sample regions that were unexposed to the electron beam prior to and during the reduction. Therefore, the images show the results of transformations of the copper phyllosilicate that were inherent to the reduction process in the electron microscope, excluding any electron-beam-induced changes. The copper phyllosili-

cate appeared unchanged after reduction at 150 and 200 °C, in line with TGA and TPR. After 30 minutes at 250 °C, nanoparticles were clearly visible and the average size of the nanoparticles was about 5 nm. Reducing the sample for up to 2 hours resulted in the appearance of more nanoparticles and a further growth of the nanoparticles to an average size of 8 nm (not shown in Figure 3). At the higher temperature of 280 °C, the nanoparticles developed with an average size of 8 nm already after half an hour of reduction (Fig 3D). Extending the reduction treatment to longer reduction times and increasing the temperature to 310 °C (75 min at 280 °C and 30 min at 310 °C) did not lead to any further changes. Thus, the copper phyllosilicate was fully reduced to  $Cu/SiO_2$  within 30 minutes at 280 °C in the electron microscope. Subsequently, the reduction in the electron microscope was compared to the reduction in a plug-flow reactor. For the two instruments, Figure 4 shows TEM images of the copper phyllosilicate after reduction and corresponding particle size distributions. The distributions, average particle size and standard deviation are similar (Table S2). Therefore, the formation of copper nanoparticles during reduction by  $H_2$  in the microscope was representative for the formation process in a standard plug-flow reactor. Moreover, the comparison demonstrates that the particle formation was insensitive to the different  $H_2$  pressure and heating rate employed in the two instruments.

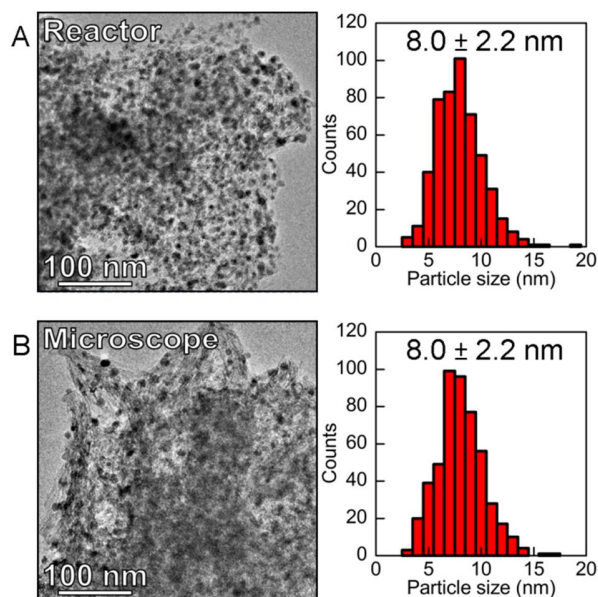


Figure 4. TEM images of copper phyllosilicate after reduction in a plug-flow reactor and in the electron microscope. (A) Copper phyllosilicate reduced in a plug-flow reactor (20%  $H_2$  in Ar, 250 °C, 150 min) and re-reduced in the electron microscope (1 mbar  $H_2$ , 250 °C, 45 min). The TEM image was acquired *in situ* at 1 mbar  $H_2$  at 250 °C. The PSD is based on such TEM images of 17 different regions of the samples. (B) Copper phyllosilicate reduced in the electron microscope (1 mbar  $H_2$ , 280 °C, 30 min). The TEM image was acquired in vacuum at room temperature. The PSD is based on such images of 17 different regions. Each PSD include the size of 500 copper nanoparticles and the number-averaged particle size and standard deviation of the distributions are included.

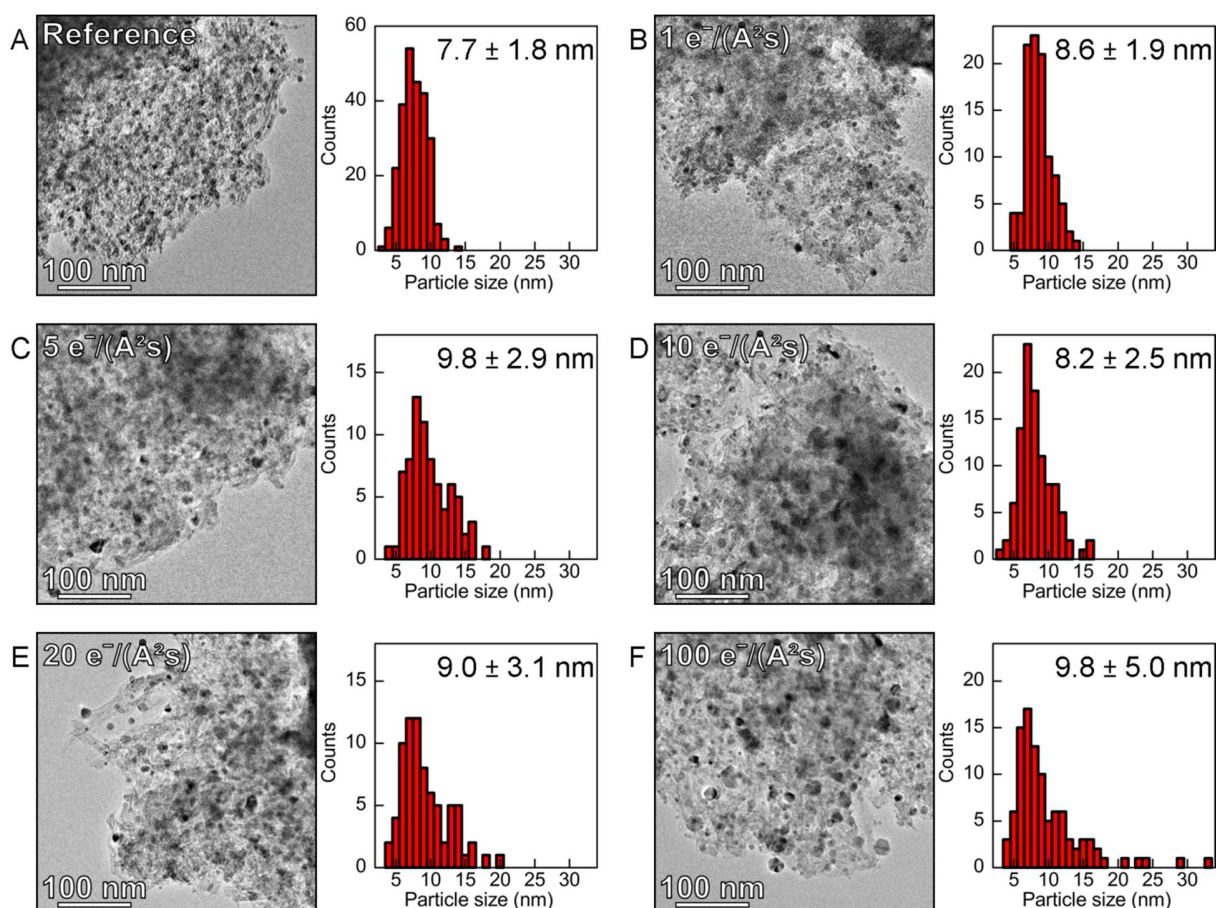


Figure 5. The effect of electron pre-illumination on the reduction of copper phyllosilicate (Experiment E2). (A) A TEM image of a reference region without pre-illumination and after reduction in 1 mbar  $H_2$  for 75 min at 280 °C and subsequently for 30 min at 310 °C. The PSD is evaluated from TEM images of 10 different reference regions (without pre-illumination and after reduction). (B-F) TEM images of copper phyllosilicate regions, which were pre-illuminated by the electron beam in base vacuum ( $2.3 \cdot 10^{-5}$  mbar) at room temperature and subsequently reduced in 1 mbar  $H_2$  for 75 min at 280 °C and 30 min at 310 °C. The pre-illumination comprised electron dose-rates of 1, 5, 10, 20 and 100  $e^-/(\text{\AA}^2s)$ , respectively, for 2 min. All TEM images were acquired at base vacuum ( $2.3 \cdot 10^{-5}$  mbar) at room temperature after reduction. The pre-illuminated regions enabled acquisition of 1-3 independent TEM images, which were used to evaluate the PSD. For each PSD, its number-averaged particle size and standard deviation are included.

### Electron beam effects

For the *in situ* experiments, it is important to minimize the influence of the electron beam on the phenomena under investigation and to distinguish the thermally activated evolution of the sample from the electron beam-induced changes.<sup>5a, 12</sup> In this case, careful examination is particularly important given the ionic complex structure and constituent light elements of the copper phyllosilicate. In fact, electron beam alterations may even occur under high vacuum conditions.<sup>13</sup> It is therefore important to consider the electron beam illumination prior to as well as during the reduction treatment.

To address the impact of such pre-illumination, experiment E2 evaluates the reduction of copper phyllosilicate that was illuminated in vacuum at room temperature prior to the reduction. Specifically, five different regions were illuminated for 2 min. by electron dose-rates of 1, 5, 10, 20 and 100  $e^-/(\text{\AA}^2s)$ , respectively. At these illumination conditions, the copper phyllosilicate remained visually

unchanged at a dose-rate of 20  $e^-/(\text{\AA}^2s)$  (Figure S1). The pre-illuminated sample was subsequently reduced in the microscope without electron illumination during reduction. After the reduction treatment, TEM images were acquired of reference sample regions, which had not been pre-illuminated, and of the five pre-illuminated regions. Figure 5 shows a TEM image representative of the reference regions, the particle size distribution (PSD) corresponding to the reference regions, and TEM images of the pre-illuminated regions with their corresponding PSDs. Compared to reference regions (Figure 5A), the PSDs tend to broaden toward larger sizes and the average copper nanoparticle size increases for the pre-illuminated regions (Figure 5B-F). Specifically, a significant number of nanoparticles larger than 14 nm formed after pre-illumination by the highest electron dose-rate of 100  $e^-/(\text{\AA}^2s)$  (Figure 5F). Even for pre-illumination with the lowest dose-rate of 1  $e^-/(\text{\AA}^2s)$ , the PSD differs with statistical significance ( $p_{\text{same mean size}} = 2.7 \cdot 10^{-5}$ , Table S3) from the PSD of the

reference regions, even though the PSDs may appear close to identical. Thus, these experiments show that although the copper phyllosilicate remained visually unchanged after electron pre-illumination, the pre-illumination had a significant effect on the evolution of the copper particle sizes upon subsequent reduction. It is therefore important to log and control the electron illumination prior to and during reduction by  $H_2$ . In the actual growth experiments, suitable sample areas were identified prior to reduction by employing a pre-illumination in 1 mbar  $H_2$  at 200 °C, using a yet lower electron dose-rate of  $0.05 e^-/(\text{\AA}^2s)$ . At this dose-rate, the image signal-to-noise ratio was just sufficient to localize regions of interest and the pre-illumination did not change the final PSD, as will be demonstrated by comparison to non-illuminated regions.

Next, the interaction of the electron beam with the combined gas-sample system is addressed in experiment E3. Specifically, different areas of copper phyllosilicate were illuminated continuously by electrons at rates of 1, 5, 10, 20 and  $100 e^-/(\text{\AA}^2s)$ , respectively, in 1 mbar  $H_2$  at 150 °C. This temperature is sufficiently low to suppress particle growth due to reduction by  $H_2$  (Figure 3A). After 7 min of continuous illumination, TEM images reveal that particles had formed for all electron dose-rates. The particle density was significantly lower for the dose-rate of  $1 e^-/(\text{\AA}^2s)$  than for higher dose-rates (Figure 6A-F). Extending the illumination at  $1 e^-/(\text{\AA}^2s)$  up to 20 min led to an increased particle density, which by visual inspection appears to be similar to the particle density in regions illuminated for 7 min at higher dose-rates (Figure 6 and S2). Moreover, visual inspection of Figure 6D, F and S3 indicates that the particle density is significantly lower in the absence of  $H_2$  at 150 °C after similar electron illumination. The particle formation is thus not directly induced by the electron beam interaction with the sample but indirectly via the electron beam interaction with  $H_2$ , presumably via pre-dissociation of  $H_2$  to form more reactive H atoms.<sup>14</sup> The stage of particle evolution was assessed quantitatively by simplistically convoluting the apparent particle density and the size of 20 or 25 particles over time (see Image analysis section). For regions illuminated at  $5 e^-/(\text{\AA}^2s)$  or higher, the majority of particles nucleated and grew larger than 5 nm within the first 10 minutes of reduction. Figure 6G shows that the stage of particle evolution developed similarly for these regions independent of applied electron dose-rate. In contrast, at an electron dose-rate of  $1 e^-/(\text{\AA}^2s)$ , the particle evolution was significantly slower and 15 minutes passed before the majority of nanoparticles had nucleated and grown larger than 5 nm. Thus, lowering the electron dose-rate and illumination time as much as possible is crucial to minimize the contribution from electron-induced reduction by  $H_2$ . In the present beam-insensitive experiments an electron dose-rate of  $1 e^-/(\text{\AA}^2s)$  was used and illumination times were limited to ensure that the formation of particles was dominated by the thermal reduction by  $H_2$ . This was demonstrated by comparing the particle formation in one region continuously illuminated to the formation in several regions illuminated intermittently during the reduction process.

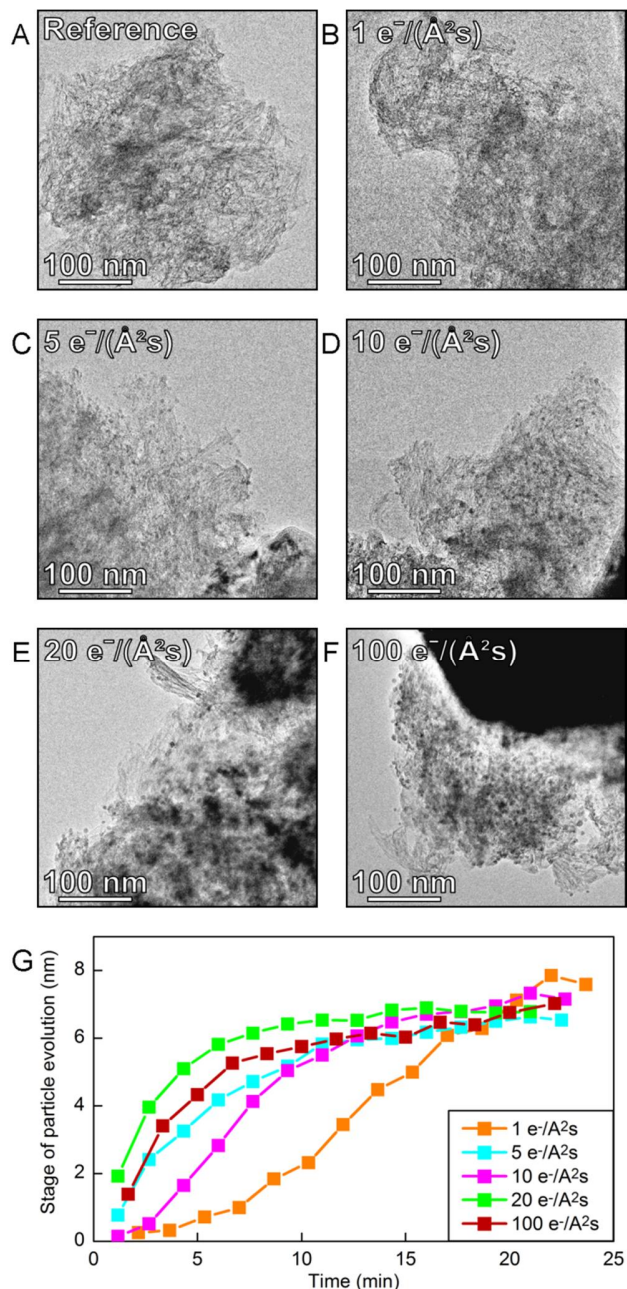


Figure 6. Formation of copper nanoparticles by reduction in 1 mbar  $H_2$  at 150 °C under different electron illumination conditions. (A) TEM image of a reference area after 250 min in 1 mbar  $H_2$  at 150 °C. (B-F) TEM images of the five different regions after 7 minutes of electron illumination at 1, 5, 10, 20 and  $100 e^-/(\text{\AA}^2s)$ , respectively. (G) The stage of particle evolution of 20 or 25 particles plotted as a function of time for regions exposed to electron dose-rates of 1 (orange), 5 (blue), 10 (pink), 20 (green) and  $100 e^-/(\text{\AA}^2s)$  (red).

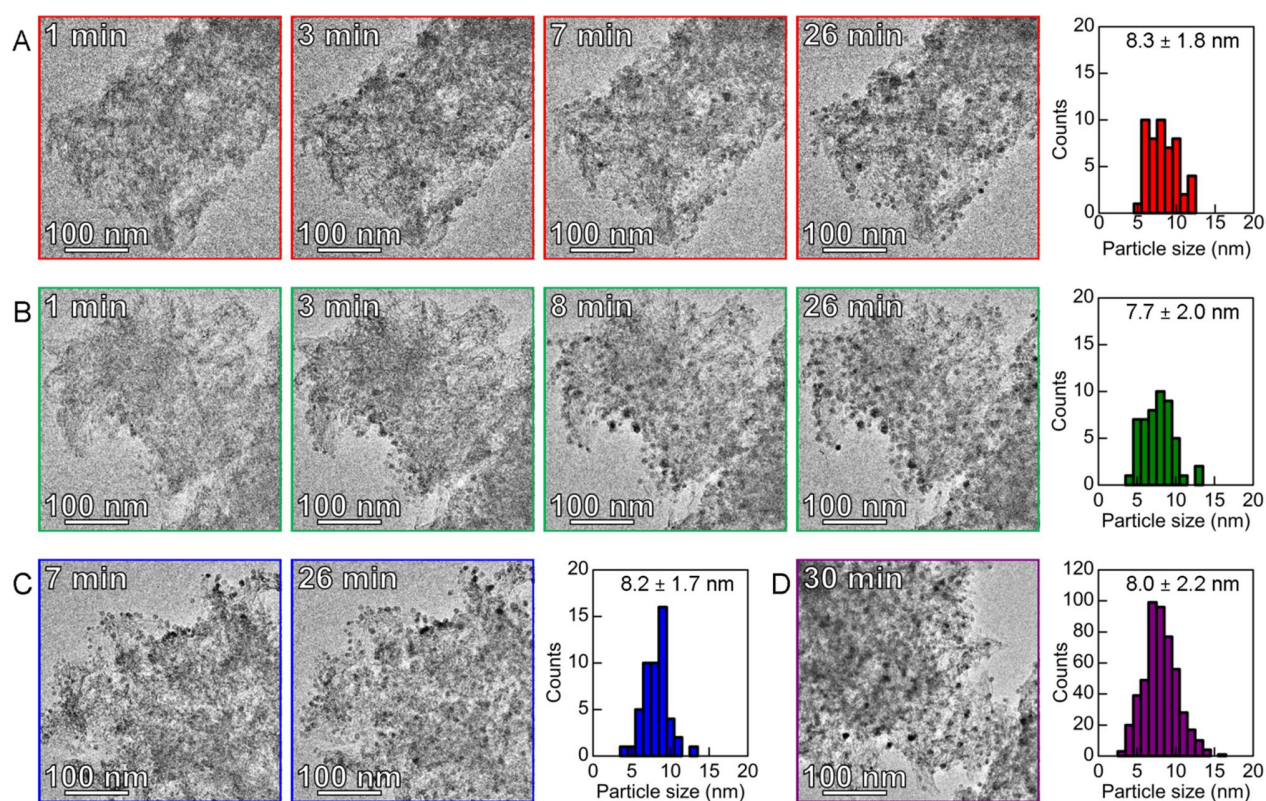


Figure 7. Time-resolved TEM images of copper phyllosilicate during exposure to 1 mbar  $H_2$  at 280 °C. (A) Region 1 observed by continuous electron illumination at an electron dose-rate of  $1 e^-/(\text{\AA}^2s)$  (Supplementary movie S1), and the corresponding PSD after reduction. (B) Region 2 observed with intermittent electron illumination at ca. 2 min intervals at an electron dose-rate of  $1 e^-/(\text{\AA}^2s)$  and the corresponding PSD after reduction. (C) Region 3 observed with intermittent electron illumination at ca. 6 min intervals at an electron dose-rate of  $1 e^-/(\text{\AA}^2s)$  and the corresponding PSD after reduction. (D) A TEM image of a reference region imaged after reduction and the PSD corresponding to 17 reference regions imaged after reduction. The PSDs include the number-averaged particle size and corresponding standard deviation.

### Monitoring nanoparticle formation by TEM

Guided by the investigation of the temperature and the electron beam-induced changes, the measurement scheme in Figure 1 was followed in monitoring the formation of copper nanoparticles. This scheme excludes electron illumination of the sample in the microscope's base vacuum prior to the reduction process, uses a low electron dose-rate, limits the total illumination time by conducting reduction at 280 °C which increases the reaction rate, and acquires time-lapsed TEM image series at different intervals to fragmentize the effect of the accumulated electron dose. Two separate experiments were conducted to monitor the formation of copper nanoparticles in three distinct regions. In the first experiment, Region 1 was continuously illuminated during reduction. In the second experiment, Region 2 and Region 3 were intermittently illuminated with different time intervals (~2 and ~6 minutes) to address the effect of electron dose accumulation on the growth of copper nanoparticles. At the timed instants (Figure 1), TEM images were recorded enabling time-lapsed image series of the three regions during the reduction process. When such image series are played back as a movie, a vivid impression of the growth scenario is obtained. The movie of Region 1 is provided as supplementary information (Movie S1). Figure 7 shows

selected TEM images from the time-lapsed series of all three regions. After the reduction treatment, the sample was cooled to room temperature and the electron microscope evacuated to reestablish a base vacuum of  $1.9 \cdot 10^{-6}$  mbar. Under these conditions, TEM images were acquired of the three regions and of reference regions, which had not previously been illuminated by the electron beam.

The TEM images in Figure 7 reveal that the first appearance of copper nanoparticles occurred within the first few minutes at the reduction conditions. Due to the finite image SNR and resolution, it is possible that the particles had nucleated at earlier times and subsequently had grown beyond the size of 3 nm which is detectable in the TEM images. That is, the particle size at the first observation by TEM is likely larger than the critical size associated with the copper nanoparticle formation. Once formed, the nanoparticles remained immobile. This finding suggests that the continued growth (Figure 7) cannot be a result of particle migration and coalescence under the present conditions.<sup>15</sup> Instead, the observations suggest that the nanoparticles grew by the attachment of smaller copper species, which are formed during the reduction treatment and which are sufficiently mobile to reach a nanoparticle. As the copper nanoparticles appear to have formed homogeneously across the precursor material, this

mobility was probably limited to diffusion distances on the order of the final spacing between the nanoparticles, which is roughly 10 nm. Moreover, a close-up inspection of particles near the precursor agglomerate edge did not indicate any marked preference for specific nucleation sites.<sup>7e</sup> Thus, these observations suggest that the copper nanoparticles tended to nucleate homogeneously and grew by attachment of copper species from their vicinity.

To develop a kinetic description of these dynamic observations, the role of the actual electron illumination, which is shown in Figure 1, is addressed. This assessment is done by comparison of the particle evolution and final PSD of the three regions (Region 1, 2 and 3) to each other and by comparison of the final PSDs of the three regions to the PSD of reference regions (Figure 7). The PSDs of the three regions (Region 1, 2 and 3) were visually similar and their deviations were within the statistical error ( $p_{(\text{same mean size})} > 0.025$ , Table S4). Thus the accumulated electron dose used in the present experiment did not affect the final nanoparticle size. The PSDs of the three regions (Region 1, 2 and 3) were also visually and statistically similar to the reference regions, (Figure 7D) indicating that the applied pre-illumination scheme and dose-rate were also of inferior importance for the final nanoparticle size. Moreover, the stage of particle evolution was evaluated by tracking 25 visually distinguishable particles per region. Figure 8 shows the stage of particle evolution as a function of time for the three regions. Since only particles that were clearly visible throughout the experiment were measured, this analysis was biased towards larger particles resulting in a final average particle size close to 10 nm, instead of 8 nm (Figure 7). The progress of particle formation for the three regions (Region 1, 2 and 3) was close to identical, despite the different electron doses. Specifically, region 3 was imaged for the first time after 7 min at 1 mbar H<sub>2</sub> and 280 °C and the particle formation had progressed to the same extent as for Region 1, which had been continuously illuminated. This indicates that the electron illumination during reduction did not have a measurable influence on the evolution of the sample.

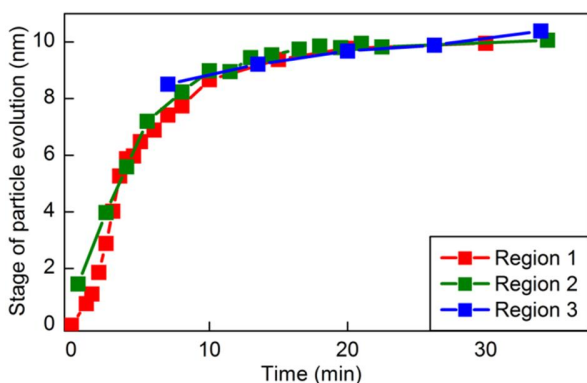


Figure 8. The stage of copper particle evolution versus time for reduction of copper phyllosilicate in 1 mbar H<sub>2</sub> at 280 °C. The stage of particle evolution is obtained from the time-resolved TEM images of Region 1-3 (Figure 7).

Quantitative information for the kinetic models is obtained from measuring the sizes of the 25 individual par-

ticles in region 1 at different stages of the reduction, as shown in Figure 9 (black dots, see Figure S5 for corresponding particles). At the time for first appearance, all particles were larger than 3.4 nm. Most particles were detected after 2 to 6 minutes and all particles had appeared within 15 minutes. After its appearance, a particle grew initially fast and later slower until it had reached its final size within the following 10 minutes.

### Kinetic models for the nanoparticle formation

The TEM observations made *in situ* of nanoparticle formation provide information about the time for the first observation of a nanoparticle and about its subsequent growth. This dynamic information is hereafter compared with two kinetic models that are consistent with the observed dynamic behavior of the nanoparticles. For both models, it is assumed that the reduction process starts as the temperature reached 280 °C, because particle formation did not occur below 250 °C in the experiments and because the heating rate is fast (30 °C/min) (Figure 3). Furthermore, variations in temperature over time or over different locations are considered negligible because the particle size evolved similarly in different areas (Figure 7, 8).

### Nucleation-and-growth model

The first model considers the reduction of the phyllosilicate as a first order and irreversible reaction that feeds reduced mobile copper species to a reservoir, which leads to a classical nucleation-and-growth scenario (e.g. DeBenedetti,<sup>16</sup> LaMer and Dinegar,<sup>17</sup> see Supporting Information). That is, as the concentration of reduced species exceeds the saturation concentration, copper nuclei larger than a critical size are formed and subsequently grow by addition of diffusing reduced species. The concentration of these mobile reduced species is assumed to be uniform throughout the system, except for a diffusive boundary layer surrounding each particle (mean field approximation). As nucleation in this model is a statistical event, the model is consistent with a homogeneous distribution of nanoparticles. In the model, the size evolution of all particles was fitted with only two adjustable parameters, namely the kinetic constant of the reduction and the diffusion coefficient of the reduced species (see Supporting Information). The best fit of the model to the data in Figure 9 was obtained with a kinetic constant of 0.64 min<sup>-1</sup> and a diffusion coefficient of  $\sim 5 \cdot 10^{-19}$  m<sup>2</sup>/s. With these parameters the model accounts reasonably for the observed nucleation times as well as for the growth of the nanoparticle size (See Figure 9, green lines and Figure S7).

However, the model has some implications that are physically improbable. Because nucleation does not occur until after a few minutes in the reduction treatment, a large fraction of the copper atoms must be present as mobile reduced copper species in the early phase (Figure S6). The peak amount of mobile reduced copper species exceeds 20% of all copper present, corresponding to a surface concentration of  $\sim 15$  Cu atoms/nm<sup>2</sup> or about 100%

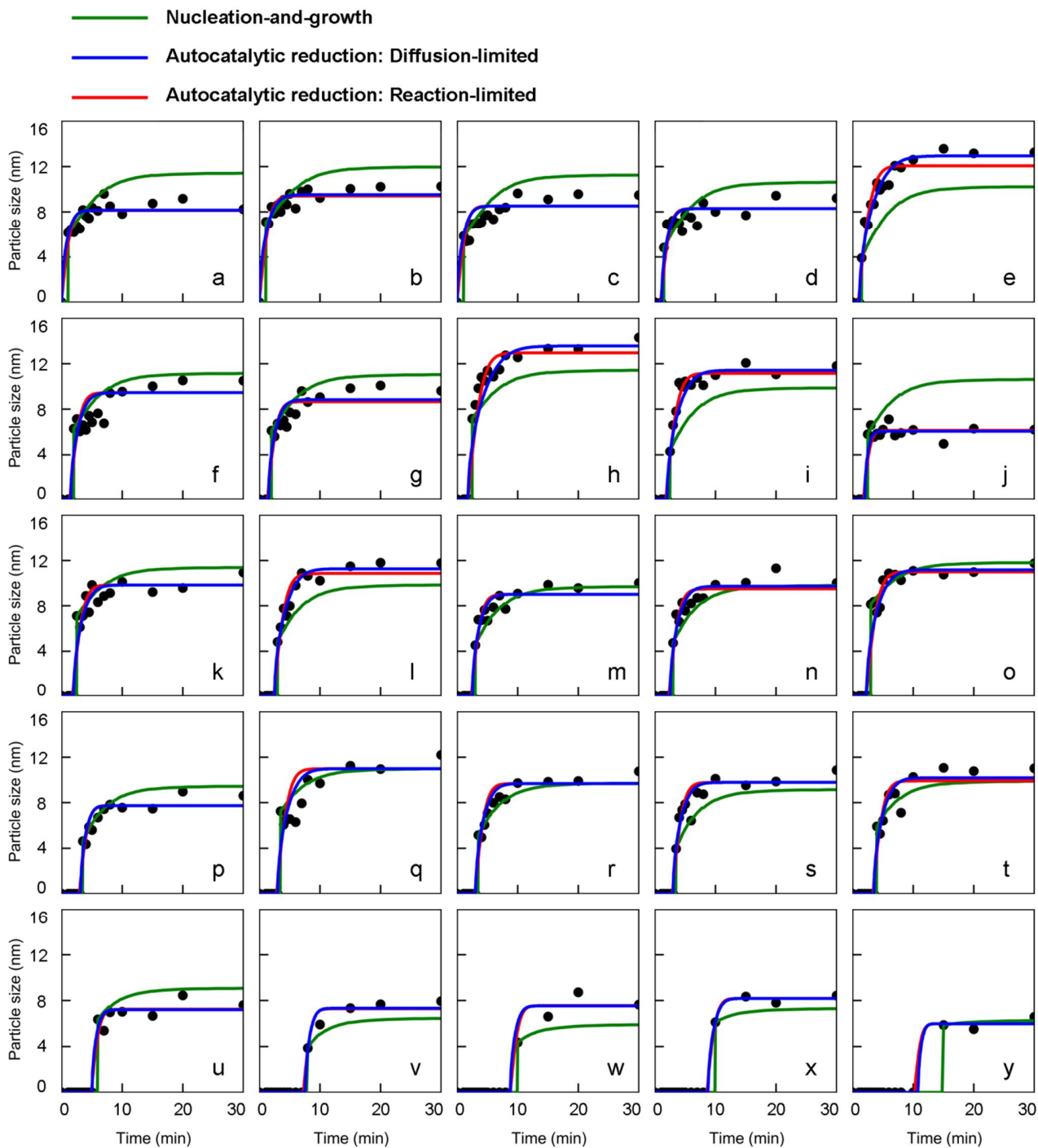


Figure 9. Size evolutions of the 25 copper particles selected in Region 1. The measured particle size is shown as black dots, the fitted nucleation-and-growth model is shown in green and the fitted autocatalytic model is shown in red (reaction-limited) and in blue (diffusion-limited).

of a monolayer. Such a high surface concentration is physically unrealistic. Another inconsistency of the model results from the mean-field approximation, which imposes that the chemical environment of all nanoparticles is the same at any given time. As a consequence the final size of the particles should depend only on the nucleation time, which is contradicted by the data since it exhibits a considerable scatter in the relation between nucleation time and final particle size

(Figure 10). At last, it is expected that the reduction rate is sensitive to the  $H_2$  pressure while the diffusion of reduced copper species is not. Since in the nucleation-and-growth model the ratio between the reduction rate and the diffusion coefficient determines the final particle size and density, the model predicts a higher particle density and smaller particle sizes at higher  $H_2$  pressures. However, this prediction resulting from the nucleation-and-growth model is inconsistent with the experimental

observation that the final particle size is insensitive to the  $H_2$  pressure at 1 mbar and 200 mbar.

### Autocatalytic model

In the light of the high and homogeneous particle density (Figure 7) and the inability of the mean field approximation proved unable to explain the scatter in the relation between nucleation time and final particle size, it seems inconsistent that a nanoparticle is able to grow from mobile species originating from a distance far away. Rather, a nanoparticle captures species from a limited spatial zone in its vicinity ( $< \text{few (tens) of nanometer}$ ). Therefore the second model includes the additional assumption that the copper phyllosilicate is made up of regions, referred to as boxes, which do not exchange copper species. The structural characterization of the copper phyllosilicate shows that the material consists of agglomerations of platelets in the range of 5 - 20 nm in width and thickness and up to 100 nm in length (Figure 2). Logically, diffusion of copper species within a platelet is easier than from one platelet to another. It is thus probable that the copper particles effectively only grow from the copper phyllosilicate present in a certain volume. The final size of a particle is therefore related to the size of its surrounding copper phyllosilicate box. For example, an 8 nm copper particle would contain as many copper atoms as a copper phyllosilicate cubic box of size 17 nm. Depending on the exact dimensions of a copper phyllosilicate platelet this means that the phase transformation resulted into one or a few copper particles per platelet, which is also observed experimentally.<sup>7e</sup>

Since the appearance of particles seemed to be randomly occurring throughout the agglomerate and specific nucleation sites seemed to be absent, homogeneous nucleation was considered. In that light, every copper ion in a box is assumed to have a given probability of being reduced per unit of time resulting in a particle nucleus. As shown in the Supporting Information, such a nucleation phenomenon is governed by Poisson statistics. As a consequence, the probability of early nucleation is higher in larger boxes corresponding to larger final particle sizes, which is in qualitative agreement with Figure 9. The reduction probability obtained from a maximum-likelihood analysis of the data is  $5.42 \times 10^{-6} \text{ min}^{-1} \text{ ion}^{-1}$  (see supporting information). Based on that value, and using the final particle size to estimate the corresponding box volume, the overall nucleation probabilities were calculated as a function of time and they are shown in Figure 10. Most of the particles have a probability between 0.1 and 0.9 of having nucleated at the observed time. It has to be stressed that the Poisson model captures both the relation between the final size and the nucleation time, and the scatter in the data resulting from the inherently statistical nature of the process. The model assumes that only one particle nucleates in each box and that no secondary nucleation takes place. However, for large boxes corresponding to final particle sizes of about 13 nm, secondary nucleation should occur with a probability as large as 90% (see Supporting Information). Secondary nuclei are therefore

assumed to coalesce with the primary particle. Although no mobility of particles larger than 3.4 nm was observed, diffusion and coalescence of much smaller particles consisting of one or a few copper atoms can be expected to be fast.<sup>15</sup>

It is particularly interesting to observe that the statistical reduction rate of each ion before nucleation ( $5.42 \times 10^{-6} \text{ min}^{-1}$ ) is orders of magnitude lower than the overall reduction rate, which is of the order of  $0.64 \text{ min}^{-1}$  according to the kinetic constant of the nucleation-and-growth model. This difference suggests that an autocatalytic process may be at play, by which the reduction is catalyzed by the newly formed copper particles. Autocatalytic reduction is often observed in the synthesis of supported metal catalysts<sup>2, 18</sup> and it has been shown that the reduction of CuO is autocatalytic.<sup>19</sup>

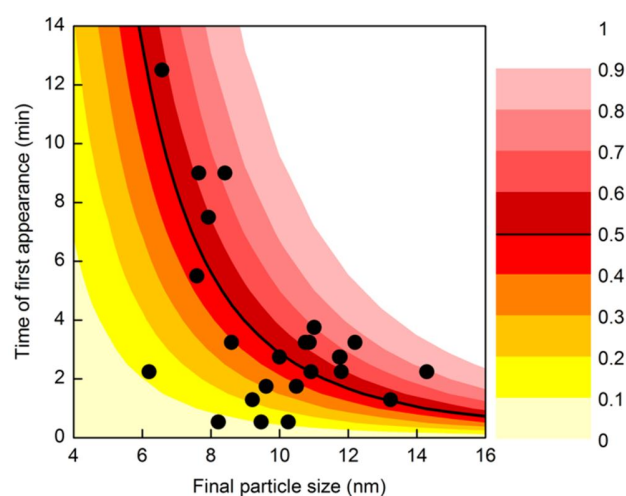


Figure 10. Observed time of first appearance of a particle against the observed final particle size (black dots). The colored regions indicate the cumulative probability according to Poisson statistics for nucleation to occur at a specific time for a given box size. Box sizes are expressed as the corresponding final particle sizes to aid the comparison with the observed experimental data.

To model the growth of the nucleated particles, it is therefore assumed that the autocatalytic process starts as soon as a particle nucleus has been formed. In principle, particle growth during autocatalytic reduction could be either diffusion-limited or reaction-limited.<sup>20</sup> Both limiting cases were therefore considered in models fitted to the data. In the reaction-limited model (Red lines in Figure 9, autocatalytic model<sub>reaction-limited</sub>) the reduction and hence growth of the particles is assumed to be catalyzed by the copper surface and therefore proportional to the average  $\text{Cu}^{2+}$  concentration in the box.<sup>18</sup> The best fit of the model was obtained with a kinetic constant of  $\sim 0.45 \text{ nm/min}$ , which corresponds to about 2 atomic layers per min. In the diffusion-limited model (Blue lines in Figure 9, autocatalytic model<sub>diffusion-limited</sub>) the reduction rate is high and all of the copper ions are considered to have the same mobility. The diffusion coefficient derived from fitting the model to the experimental data is  $4.5 \times 10^{-19} \text{ m}^2/\text{s}$ , which is typical for solid

state diffusion.<sup>21</sup> Extrapolated to 280 °C, coefficients around  $1 \times 10^{-16} \text{ m}^2/\text{s}$  have been found for the diffusion of  $\text{Cu}^+$  ions in sodium enriched silica.<sup>22</sup> Gonella et al. have reported that the diffusion of  $\text{Cu}^{2+}$  is about two orders of magnitude slower than that of  $\text{Cu}^+$ .<sup>23</sup>

The experimental results are well described by both the diffusion-limited and the reaction-limited model and do not allow to distinguish between the two. In conclusion, the autocatalytic model seems to slightly better describe all of the observations in Figure 7 compared to the nucleation-and-growth model. Therefore the autocatalytic model seems to be a more attractive model for describing the reduction mechanism. It is plausible that initial particle growth is reaction-limited since the surrounding area is not yet depleted of copper. Analogous to this, the final stage of particle growth is more likely to be diffusion-limited since at that time the surrounding area is depleted of copper. Thus, a combination of the two limiting autocatalytic models could be possible for describing the observations.

## CONCLUSION

*In situ* TEM was used to follow the phase transformation of copper phyllosilicate to silica-supported copper particles during reduction with 1 mbar  $\text{H}_2$  at 280 °C. Similar particle size distributions after reduction in the TEM and in a plug-flow reactor were obtained, validating that the phase transformation inside the microscope was representative for the phase transformation in a plug-flow reactor. Based on an assessment of the electron beam illumination prior to and during reduction, a procedure was developed for time-resolved imaging of the dynamical changes of the copper phyllosilicate that are inherent to the reduction process. After an induction time of a few minutes, particles with a size larger than 3.4 nm were detected throughout the sample and grew in about 10 minutes to their final size of about 8 nm. Particle mobility was not observed indicating that growth of particles larger than 3.4 nm occurred via the diffusion of mobile copper species (likely  $\text{Cu}^{2+}$  ions) and their attachment to the copper particles. The size evolution of the particles was measured and was well described by a two-step reduction mechanism with either diffusion-limited or reaction-limited particle growth. It is concluded that reduction of copper phyllosilicate in  $\text{H}_2$  to silica supported copper particles is autocatalytic and occurs via the diffusion of copper species over a limited distance of a few (tens) of nanometers to the copper particles. Thus, with careful optimization of the imaging strategy, time-resolved TEM provided unique mechanistic and kinetic information about the nucleation and growth of nanoparticles that is representative for large scale nanomaterial synthesis.

## ASSOCIATED CONTENT

Supporting Information

Figures S1-S11, Tables S1-S11, a movie with time-lapsed TEM images during reduction at 280 °C at 1mbar  $\text{H}_2$  of Region 1, and a description of the kinetic models.

This material is available free of charge via the Internet at <http://pubs.acs.org>.

## AUTHOR INFORMATION

### Corresponding Author

\* E-mail: [sth@topsoe.dk](mailto:sth@topsoe.dk).

### Notes

The authors declare no competing financial interest.

## ACKNOWLEDGMENTS

The project was supported financially by Haldor Topsoe A/S. The authors also acknowledge Haldor Topsoe A/S for access to its *in situ* TEM facility. CJG is a research associate at the Funds for Scientific Research (F.R.S.-FNRS, Belgium). KPdj acknowledges the European Research Council, EU FP7 ERC Advanced Grant no. 338846. PEDj acknowledges The Netherlands Organization for Scientific Research NWO-Vici program. CFE and IC gratefully acknowledge The Danish National Research Foundation's Center for Individual Nanoparticle Functionality, supported by the Danish National Research Foundation (DNRF54).

## REFERENCES

- (1) (a) Schüth, F.; Hesse, M.; Unger, K. K. Precipitation and coprecipitation. In *Handbook of Heterogeneous Catalysis*, Ertl, G.; Knözinger, H.; Schüth, F.; Weitkamp, J., Eds. Wiley-VCH Verlag GmbH & Co. KGaA: Weinheim, 2008; (b) Behrens, M. *Catal. Today* 2015, 246, 46-54; (c) de Jong, K. P.; (Ed.). *Synthesis of solid catalysts*. Wiley-VCH: Weinheim, 2009; (d) Yin, Y.; Alivisatos, A. P. *Nature* 2005, 437, 664-670; (e) Peng, Z.; Kisielowski, C.; Bell, A. T. *Chem. Commun.* 2012, 48, 1854-1856.
- (2) Mondloch, J. E.; Bayram, E.; Finke, R. G. *J. Mol. Catal. A: Chem.* 2012, 355, 1-38.
- (3) (a) Gontard, L. C.; Chang, L. Y.; Hetherington, C. J.; Kirkland, A. I.; Ozkaya, D.; Dunin-Borkowski, R. E. *Angew. Chem. Int. Ed.* 2007, 46, 3683-3685; (b) Zhu, Y.; Ramasse, Q. M.; Brorson, M.; Moses, P. G.; Hansen, L. P.; Kisielowski, C. F.; Helveg, S. *Angew. Chem. Int. Ed.* 2014, 53, 10723-10727.
- (4) (a) Boyes, E. D.; Gai, P. L. *Ultramicroscopy* 1997, 67, 219-232; (b) Sharma, R.; Crozier, P. A. Environmental transmission electron microscopy in nanotechnology. In *Handbook of microscopy for nanotechnology*, Yao, N.; Wang, Z. L., Eds. Kluwer Academic Publishers: New York, 2005; pp 531-565; (c) Hansen, P. L.; Helveg, S.; Datye, A. K. *Adv. Catal.* 2006, 50, 77-95; (d) Creemer, J. F.; Helveg, S.; Hoveling, G. H.; Ullmann, S.; Molenbroek, A. M.; Sarro, P. M.; Zandbergen, H. W. *Ultramicroscopy* 2008, 108, 993-8; (e) de Jonge, N.; Ross, F. M. *Nature Nanotech.* 2011, 6, 695-704.
- (5) (a) Woehl, T. J.; Evans, J. E.; Arslan, I.; Ristenpart, W. D.; Browning, N. D. *ACS nano* 2012, 6, 8599-8610; (b) Liao, H. G.; Zheng, H. *J. Am. Chem. Soc.* 2013, 135, 5038-5043; (c) Williamson, M. J.; Tromp, R. M.; Vereecken, P. M.; Hull, R.; Ross, F. M. *Nat. Mater.* 2013, 2, 532-536.
- (6) (a) Banerjee, R.; Crozier, P. A. *J. Phys. Chem. C* 2012, 116, 11486-11495; (b) Li, P.; Liu, J.; Nag, N.; Crozier, P. *Appl. Catal., A* 2006, 307, 212-221; (c) Li, P.; Liu, J.; Nag, N.; Crozier, P. A. *Surf. Sci.* 2006, 600, 693-702; (d) Hayden, T. F.; Dumesic, J. A.; Sherwood, R. D.; Baker, R. T. K. *J. Catal.* 1987, 105, 299-318; (e) Li, P.; Liu, J.; Nag, N.; Crozier, P. A. *J. Catal.* 2009, 262, 73-82; (f) Hansen, L. P.; Johnson, E.; Brorson, M.; Helveg, S. *J. Phys. Chem. C* 2014, 118, 22768-22773; (g) Li, P.; Liu, J.; Nag, N.; Crozier, P. A. *J. Phys. Chem. B* 2005, 109, 13883-13890.
- (7) (a) Zhu, S.; Gao, X.; Zhu, Y.; Fan, W.; Wang, J.; Li, Y. *Catal. Sci. Technol.* 2015, 5, 1169-1180; (b) Simonov, M. N.; Zaikin, P. A.; Simakova, I. L. *Appl. Catal., B* 2012, 119-120, 340-347; (c) Gong, J.; Yue, H.; Zhao, Y.; Zhao, S.; Zhao, L.; Lv, J.; Wang, S.; Ma, X. *J. Am. Chem. Soc.* 2012, 134, 13922-13925; (d) Chen, L.; Guo, P.; Qiao, M.; Yan, S.; Li, H.; Shen, W.; Xu, H.; Fan, K. *J. Catal.* 2008, 257, 172-180;

- (e) van den Berg, R.; Zečević, J.; Sehested, J.; Helveg, S.; de Jongh, P. E.; de Jong, K. P. *Catal. Today* 2015, doi:10.1016/j.cattod.2015.08.052; (f) Behrens, M.; Studt, F.; Kasatkin, I.; Kuhl, S.; Havecker, M.; Abild-Pedersen, F.; Zander, S.; Girgsdies, F.; Kurr, P.; Knief, B. L.; Tovar, M.; Fischer, R. W.; Nørskov, J. K.; Schlögl, R. *Science* 2012, 336, 893-897; (g) Hansen, J. B.; Hojlund Nielsen, P. E. Methanol Synthesis. In *Handbook of Heterogeneous Catalysis*, Ertl, G.; Knozinger, H.; Schuth, F.; Weltkamp, J., Eds. Wiley-VCH: 2008; pp 2920-2949.
- (8) (a) Toupance, T.; Kermarec, M.; Lambert, J.-F.; Louis, C. *J. Phys. Chem. B* 2002, 106, 2277-2286; (b) van der Grift, C. J. G.; Elberse, P. A.; Mulder, A.; Geus, J. W. *Appl. Catal.* 1990, 59, 275-289.
- (9) Huang, Z.; Cui, F.; Xue, J.; Zuo, J.; Chen, J.; Xia, C. *J. Phys. Chem. C* 2010, 114, 16104-16113.
- (10) Jinschek, J. R.; Helveg, S. *Micron* 2012, 43, 1156-1168.
- (11) ANOVA analysis performed using Analysis ToolPak in Excel 2010.
- (12) (a) Egerton, R. F. *Ultramicroscopy* 2013, 127, 100-108; (b) Kuwauchi, Y.; Yoshida, H.; Akita, T.; Haruta, M.; Takeda, S. *Angew. Chem. Int. Ed.* 2012, 51, 7729-7733; (c) Hølse, C.; Elkjær, C. F.; Nierhoff, A.; Sehested, J.; Chorkendorff, I.; Helveg, S.; Nielsen, J. H. *J. Phys. Chem. C* 2015, DOI: 10.1021/jp510015v.
- (13) Kisielowski, C.; Wang, L.-W.; Specht, P.; Calderon, H. A.; Barton, B.; Jiang, B.; Kang, J. H.; Cieslinski, R. *Phys. Rev. B* 2013, 88, 024305.
- (14) Helveg, S.; Lauritsen, J. V.; Lægsgaard, E.; Stensgaard, I.; Nørskov, J. K.; Clausen, B. S.; Topsøe, H.; Besenbacher, F. *Phys. Rev. Lett.* 2000, 84, 951-954.
- (15) Wynblatt, P.; Gjostein, N. A. *Prog. Solid State Chem.* 1976, 9, 21-58.
- (16) Debenedetti, P. G. *Metastable liquids: concepts and principles*. Princeton University Press: New Jersey, 1996.
- (17) LaMer, V. K.; Dinegar, R. H. *J. Am. Chem. Soc.* 1950, 72, 4847-4854.
- (18) Watzky, M. A.; Finke, R. G. *J. Am. Chem. Soc.* 1997, 119, 10382-10400.
- (19) (a) Tieman, M. J.; Barnes, P. A.; Parkes, G. M. B. *J. Phys. Chem. B* 1999, 103, 338-345; (b) Pease, R. N.; Taylor, H. S. *J. Am. Chem. Soc.* 1921, 43, 2179-2188.
- (20) Aiken, J. D.; Finke, R. G. *J. Am. Chem. Soc.* 1998, 120, 9545-9554.
- (21) Heitjans, P.; Kärger, J. *Diffusion in condensed matter*. Springer-Verlag: Berlin-Heidelberg, 2005.
- (22) Kaufmann, J.; Rüssel, C. *J. Non-Cryst. Solids* 2010, 356, 1158-1162.
- (23) Gonella, F.; Quaranta, A.; Padovani, S.; Sada, C.; D'Acapito, F.; Maurizio, C.; Battaglin, G.; Cattaruzza, E. *Appl. Phys. A* 2004, 81, 1065-1071.

